The Nanogranular Origin of Concrete Creep: A Nanoindentation Investigation of Microstructure and Fundamental Properties of Calcium-Silicate-Hydrates

by

Matthieu Vandamme

Ingénieur de l'Ecole Polytechnique (2002)
Diplôme des Etudes Approfondies Solides, Structures et Systèmes Mécaniques (2003)
Ingénieur de l'Ecole Nationale des Ponts et Chaussées (2004)

Submitted to the Department of Civil and Environmental Engineering
in partial fulfillment of the requirements for the degree of

Doctor of Philosophy

at the

MASSACHUSETTS INSTITUTE OF TECHNOLOGY

June 2008

Signature of Author . . . .
Department of Civil and Environmental Engineering
May 1, 2008

Certified by . . . .
Franz-Josef Ulm
Professor of Civil and Environmental Engineering
Thesis Supervisor

Accepted by . . . .
Daniele Veneziano
Chairman, Departmental Committee for Graduate Students

The Nanogranular Origin of Concrete Creep: A Nanoindentation Investigation of Microstructure and Fundamental Properties of Calcium-Silicate-Hydrates

by

Matthieu Vandamme

Submitted to the Department of Civil and Environmental Engineering
on May 1, 2008, in partial fulfillment of the
requirements for the degree of
Doctor of Philosophy in the field of Structures and Materials

Abstract

With an annual per capita consumption of one cubic meter, concrete is the most manufactured material on Earth. But concrete subject to sustained load creeps, like chewing gum, at a rate that deteriorates the durability and lifespan of concrete infrastructure. While it is generally agreed that concrete creep originates from the complex viscous behavior of nanometer-sized building blocks of concrete, the calcium-silicate-hydrates (C-S-H), the origin of concrete creep is still an enigma and the creep properties of C-S-H have never been measured directly since C-S-H cannot be recapitulated ex situ in bulk form.

This thesis develops a comprehensive nano-investigation approach to the assessment of the microstructure and the mechanical stiffness, strength and creep properties of the fundamental building block C-S-H. This is achieved by extending the realm of classical indentation analysis of homogeneous solids to highly heterogeneous, linear-viscoelastic, cohesive-frictional materials. Applied to and validated for a wide range of sub-stoichiometric cement pastes of different composition and processing conditions, the link between material composition, microstructure and nanomechanical stiffness, strength and creep properties of cement-based materials is assessed. It is found that C-S-H, exhibiting a unique nanogranular behavior, exists in (at least) three structurally distinct but compositionally similar forms (Low-Density, High-Density and Ultra-High Density) which are characterized by packings close to limit packing densities. It is found that at the nanoscale all C-S-H phases exhibit a logarithmic creep whose magnitude depends only on the packing of 5-nanometer sized particles and not on mix proportions, processing conditions, etc. Logarithmic creep is an intrinsic creep property of C-S-H. We suggest that the C-S-H creep rate ($\sim 1/t$) is due to rearrangement of C-S-H particles similar to the compaction of vibrated particles, for which the free volume dynamics theory of granular physics provides a strong argument in favor of its justification. Finally, we show that the logarithmic creep measured by an indentation test in some minutes time at nanoscales is as exact as macroscopic creep tests carried out over years. This supports the simple idea that large time scales can be accessed by looking at small length scales, which is of great engineering importance.

Thesis Supervisor: Franz-Josef Ulm
Title: Professor of Civil and Environmental Engineering

Contents

List of Figures

13

15

17

19

Acknowledgments

I thank Prof. Franz-Josef Ulm for his financial support in complement to the Schoettler Scholarship and for his guidance during my doctoral studies at MIT. I learnt a lot, and not only about Science.

To my wife Marina and my family I express my deepest gratitude for their continuous support without which the outcome of this work may have been very different.

I am grateful also to my committee members (Prof. Van Vliet, Dr. Germaine and Prof. Coussy) for their fruitful advice along those years.

Thank you to my office mates Matt, Jong Min, Emilio, Georgios, Sophie, Mahalia, Benjamin, Jimmy, Chris, Rouzbeh, Alberto and Zenzile, who all made this experience a lot more enjoyable. Special thanks to Mahalia and Zenzile for having run tests for me, and to Chris and Jimmy for having both run tests for me and proofread this work. Thank you also to the director of the Nanolab Dr. Schwartzman for his help, and to the staff of the CEE department (particularly Donna, Donna, Patty and Sheila) for their efficiency and their kindness.

I gratefully acknowledge that this work was made possible by the funding provided by Lafarge and the French ministry of Ecology, Energy, Sustainable Development and Regional Development.

Part I

General Presentation

Chapter 1

Introduction

1.1 Industrial Context

With an annual per capita consumption of one cubic meter, concrete made of Portland cement is the material the most manufactured on Earth. Portland cement concrete is durable, strong (its compressive strength can be greater than 100 MPa), and relatively cheap. Every day, about ten times more concrete is used than all other construction materials together [162], and the consumption of Portland cement is increasing by more than 5% a year [172]. Since the raw materials necessary to produce Portland cement are abundant on Earth, this trend is unlikely to be reversed in the near future. But concrete creeps. Concrete creep can lead to unacceptable deformations or cause the prestress in a bridge to vanish. Over the lifespan of civil engineering structures (typically 50 years), the occurrence of creep may require expensive repair. This repair comes at a high cost. Concrete creep is partly responsible for an estimated 78.8 billion dollars required annually for highway and bridge maintenance in the United States alone [190].

1.2 Research Motivation

Concrete is an intriguing material. The man-made result of mixing water with cement clinker, sand and aggregates, concrete develops in a few hours from a liquid state to a solid state, becoming eventually as hard as rock. By nature, concrete is highly heterogeneous over a large range of length scales: It is a multiscale heterogeneous material (Fig. 1-1). At the macroscale of

Level III
Concrete

Level II
Cement Paste

Level I
C-S-H Matrix

Level 0
C-S-H Solid

Log[m]

> -2

-5/-4

-7/-6

-9

1 cm

10 μm

100 nm

Cement paste
+ aggregates

C-S-H matrix + other
hydration products +
unhydrated clinker

C-S-H solid + pores

C-S-H solid phase
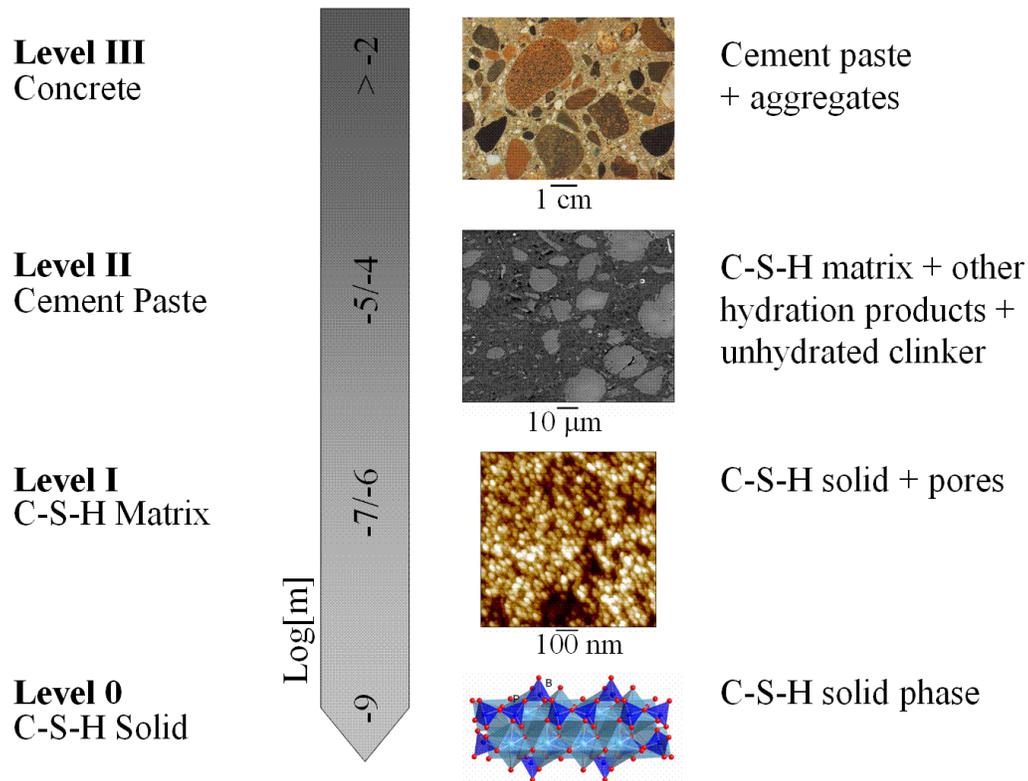
Figure 1-1: Multiscale structure thought model of concrete (adapted from [184]). Image credits: level 0 from [154], level I from [135], level II from [128] and level III from [106]

engineering applications, concrete is composed of aggregates and cement paste. At a microscale, the cement paste itself is heterogeneous, made of several hydration products, the most prominent being the Calcium-Silicate-Hydrates (C-S-H) phases. At a nanoscale, the different C-S-H phases are a mix of solid and pores.

Concrete creep, that is the time-dependent behavior of concrete under sustained load, is complex. This complexity is recognized to stem from the viscous response of C-S-H [3]. However, concrete creep has been classically investigated at the macroscopic scale for engineering design purposes (e.g., [132], [83], [15], [113]). The physical origin of concrete creep is still unknown, as the time-dependent response of C-S-H has never been measured directly. In addition, a question (seemingly) as simple as 'how the C-S-H solid fills the space', i.e., how solid and pores are distributed within the C-S-H matrix is still the subject of debate [145]. We will refer to this

distribution of solid within the C-S-H matrix as the *microstructure* of C-S-H. In contrast, at a scale above, we will refer to the spatial organization of the hydration products and unhydrated clinker in the paste as the *structure* of the paste. Given the characteristic size of the C-S-H phases (a few microns), the measurement of their mechanical properties cannot be performed by conventional macroscopic testing, but requires the use of nanomechanical testing techniques such as nanoindentation.

This research aims to answer the following questions:

Why do cementitious materials creep? And how do elastic, strength and creep properties of cementitious materials relate to the microstructure of C-S-H?

The ultimate goal of this research, therefore, is to implement the materials science paradigm for concrete creep; that is, to link composition and microstructure to material performance.

1.3 Research Objectives

A comprehensive approach is presented to address the scientific challenge. The approach is composed of experimental investigation, theory, numerical simulations and modeling. The effect of the microstructure of C-S-H on the elastic, strength, and creep properties of the material from the nanometer scale to the macroscopic scale is studied. The approach is guided by the following four research objectives:

Objective 1: *Develop the analytical tools that allow the measurement of mechanical properties by indentation testing for cementitious materials.* Cementitious materials are multiphase viscous cohesive–frictional materials. We shall build and extend here classical indentation analysis for elasto-plastic materials and multiphase cohesive–frictional materials [57], to account for the viscous behavior of the indented material as a prerequisite for our experimental investigation. This approach is based on continuum mechanics.

Objective 2: *Develop the analytical tools that allow the assessment of the microstructure of C-S-H by indentation testing.* Considering the C-S-H solid as a cohesive–frictional material, a method to obtain the distribution of porosities within the C-S-H matrix is developed. This approach is based on micromechanics.

28

Objective 3: *Assess the effect of mix proportions on the microstructure of C-S-H.* A nanoindentation testing campaign on a variety of cement pastes is performed to quantify the effect of mix proportions on the elastic and strength properties of the paste from the nanometer range to the macroscopic scale. Emphasis is placed on linking the microstructure of C-S-H to elastic and strength properties.

Objective 4: *Assess the time-dependent properties of C-S-H.* The final objective of this study is to study the creep behavior of C-S-H and to link this behavior to microstructure. We here combine the newly developed tools of time-dependent indentation analysis with the microstructural information gained by nanoindentation.

1.4 Industrial and Scientific Benefits

Associated with the research objectives are some industrial and scientific benefits. They include:

- Fundamental understanding of the effect of mix design on microstructure and mechanical properties of cementitious materials.

- Assessment of the viscous properties of the individual hydration products in hardened cement-based materials.

- Quick measurement of the long-term creep behavior of cementitious materials.

1.5 Outline of Thesis

This thesis is divided into six Parts. The first Part deals with the presentation of the topic.

Parts II and III deal with indentation analysis and develop the analytical tools necessary to link indentation data to meaningful material properties. Part II focuses on homogeneous solids. In particular, Chapter 2 studies how existing tools which already exist to back-calculate the elastic and strength properties of cohesive–frictional materials from indentation data can be extended when the indented material also exhibits a time-dependent behavior. Chapter 3 develops the tools, that allow the assessment of viscous properties by indentation means.

In contrast to Part II, Part III focuses on heterogeneous solids with heterogeneities which result either from the microstructure or from the multiphasic composition. More specifically,

Chapter 4 deals with a porous material whose solid phase manifests itself at a scale much smaller than the scale of indentation analysis. An indentation technique is developed which allows the linking of indentation data to constitutive properties and microstructural information of the solid phase. In contrast, Chapter 5 deals with a multiphase composite whose spatial heterogeneities are much larger than the scale of indentation analysis. Statistical indentation techniques are complemented or developed to allow the determination of the intrinsic phase properties of the composite as well as its homogenized properties. Together, the developments of Part II and III enable the characterization of highly heterogeneous materials from their microstructural level to their macroscopic level.

Part IV is devoted to the application of the tools of indentation analysis to cement-based materials. Chapter 6 introduces a multiscale thought model on the structure of cementitious materials that will guide the experimental investigation. Chapter 7 deals with the validation of the tools of indentation analysis developed in Parts II and III for cement-based materials.

Part V deals with the experimental investigation of the link between mix proportions, microstructure and mechanical performance for cement-based materials. Chapter 8 assesses the effect of mix proportions on microstructure by considering sub-stoichiometric cement pastes with a wide range of mix proportions. Chapter 9 focuses on the link between microstructure and creep properties.

The sixth Part, i.e., Chapter 10, summarizes the results of this study and gives suggestions for further research.

Part II

Indentation Analysis of Homogeneous Solids

Chapter 2

Assessment of Time-Independent Elastic and Strength Properties by Indentation

Indentation analysis aims at linking indentation data to meaningful mechanical properties. The second Part of this report deals with the indentation analysis of homogeneous solids. It is composed of two Chapters: The first deals with indentation analysis of time-independent elastic and strength properties; the second with time-dependent properties. In particular, this Chapter reviews the classical tools of indentation analysis of homogeneous solids that allow for the extraction of elastic and strength properties of the indented material. This review defines a basis for original developments presented in forthcoming Chapters, and the analytical developments presented here will be of critical importance for the experimental investigation of the fundamental properties of cement-based materials.

2.1 Introduction

An indentation test consists in pushing an indenter tip of known geometry and mechanical properties orthogonally to the surface of the material of interest (Fig. 2-1). During the indentation test, the load P applied to the indenter tip and the depth h of the indenter with respect to the indented surface are continuously monitored, and a $P - h$ curve is recorded (Fig.
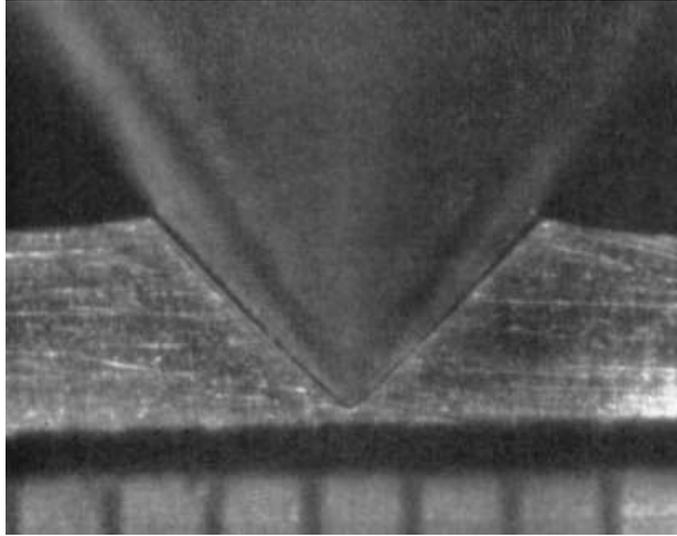
Figure 2-1: Indentation on duralumin with a tungsten carbide conical indenter (from [170]).

2-2). The experimental indentation data is traditionally condensed into two parameters: The indentation modulus M and the indentation hardness H. Based on continuum contact theory, the indentation modulus has been classically related to the elasticity content of the indented half-space and the indentation hardness to strength properties. The underlying concept, which allows these indentation properties to be linked to material properties, is the self-similarity of the indentation test. The focus of this Chapter is to review recent developments in indentation analysis of elastic, elasto-plastic and visco-elasto-plastic materials which enable M (Section 2.3) and H (Section 2.4) to be linked to the elastic and strength properties of the indented material, respectively.

2.2 Self-Similarity of Indentation Tests

One salient feature of indentation analysis is the self-similarity of the indentation test. A time-developing phenomenon is called self-similar if the spatial distributions of its properties at various moments of time can be obtained from one another by a similarity transformation [7]. Thus the self-similarity of a problem often simplifies its investigation. In indentation testing, self-similarity implies that the displacement fields at any load P can be inferred from
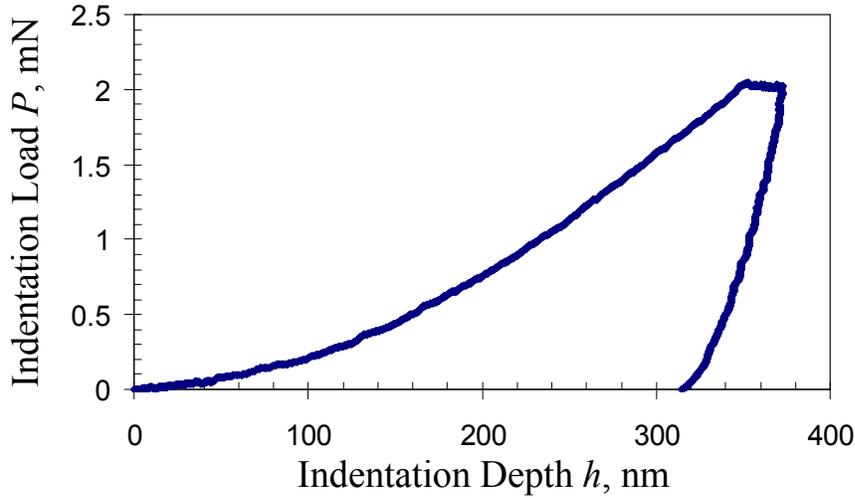
Figure 2-2: Typical indentation load P versus indentation depth h response of a nanoindentation test on cement paste.

the displacement fields at a given load P_0. The conditions under which indentation problems are self-similar were stated explicitly by Borodich et al. [23] [24]:

1. The shape of the indenter probe must be described by a homogeneous function whose degree is greater than or equal to unity.

2. The constitutive relationships of the indented material must be homogeneous with respect to the strains or the stresses.

3. During the contact process, the loading at any point must be progressive. That is, as soon as the indentation load is decreased, the indentation test loses its self-similarity.

2.2.1 Geometry of Indenter Probes and Geometric Similarity

The most common indenter probes are (Fig. 2-3):

- The flat punch indenter probe, which is rarely used in actual indention testing, but which is (as we will demonstrate) important from a theoretical point of view. The contact surface between the probe and the indented surface is constant over the entire indentation process, which greatly simplifies the analysis of the indentation contact problem (Section 2.3.1).

34
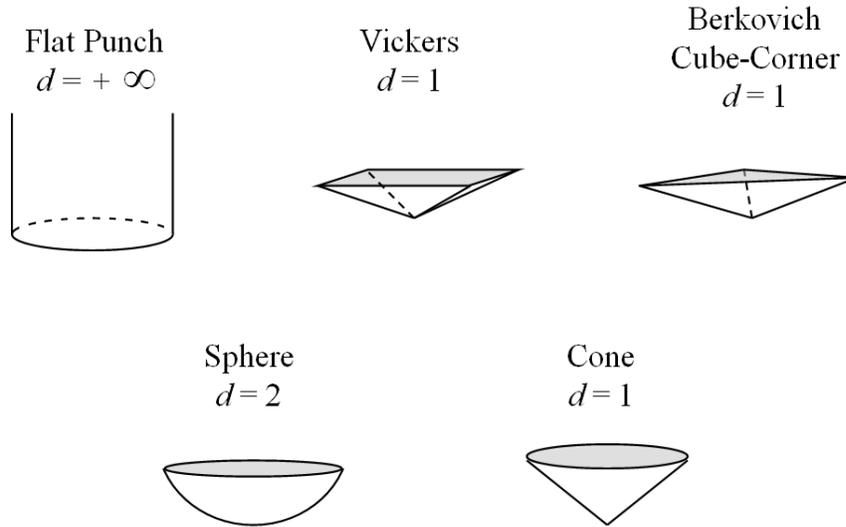
Figure 2-3: Probes of different geometries and the degree d of the homogeneous function describing their geometry.

- The spherical indenter probe, which is used mostly for soft materials. At small load magnitudes, it is possible to solicit the indented material in its elastic range only.

- Pyramidal indenter probes (such as the Berkovich, Vickers, or Cube-Corner indenter probe), which are the most used indenter shapes. The sharp geometry allows for the testing of volumes of materials smaller than is the case with probes of other geometries. However, this sharp geometry generates stress concentrations at the probe tip, so that the indented material is solicited plastically even at low load magnitudes. Among all pyramidal probes, the three-sided Berkovich pyramidal probe is the most common, and it is the one we will use almost exclusively in our experimental investigation.

For all mentioned probes, within a Cartesian coordinate system $Ox_1x_2x_3$, whose origin is at the tip of the probe, with x_3 going into the depth of the probe (Figure 2-4), the height z of the surface of the probe verifies:

$$z(\lambda x_1, \lambda x_2) = \lambda^d z(x_1, x_2) \text{ with } \lambda > 0 \qquad (2.1)$$

Probe type	d	B
Flat punch	$\to \infty$	$1/(a^n)$
Spherical	2	$1/(2R)$
Pyramidal	1	$\cot(\theta^{eq})$
Conical	1	$\cot(\theta)$

Table 2.1: Degree d of the homogeneous function and proportionality factor B for several indenter probes.

Probe type	Equivalent half-cone angle θ^{eq}
Berkovich	70.32°
Vickers	70.32°
Cube Corner	42.28°

Table 2.2: Equivalent half-cone angle θ for several pyramidal probes.

where d is the degree of the homogeneous function. For axisymmetric probes, Equation (2.1) can be condensed into:

$$z(r) = Br^d \tag{2.2}$$

where r is the radius of the probe at a given height z, and B is a proportionality factor that represents the radius at unit radius (Figure 2-4). The degree d and the proportionality factor B for all probes considered is given in Table 2.1.

Two objects which can be transformed into each other by dilation or contraction are 'geometrically similar'. Applied to indenter geometries, two spheres of different radii - and therefore all spherical indenter probes - are geometrically similar to each other. Likewise, all flat punch indenter probes are geometrically similar. In contrast, pyramidal and conical indenters are invariant when contracted or dilated. That is, pyramidal and conical indenters are similar to themselves. They are said to be 'geometrically self-similar'.

Making use of this geometric self-similarity, the non-axisymmetric pyramidal probes are often approximated, for the purpose of indentation analysis, by axisymmetric cones of same degree $d = 1$, which greatly simplifies the indentation analysis as shown later on (Section 2.3.1). This is achieved by means of an equivalent half-cone angle (or cone opening angle), which ensures that the pyramidal probe and the cone have the same cross-sectional area S at a given height z. The equivalent half-cone angles of common pyramidal probes are given in Table 2.2.
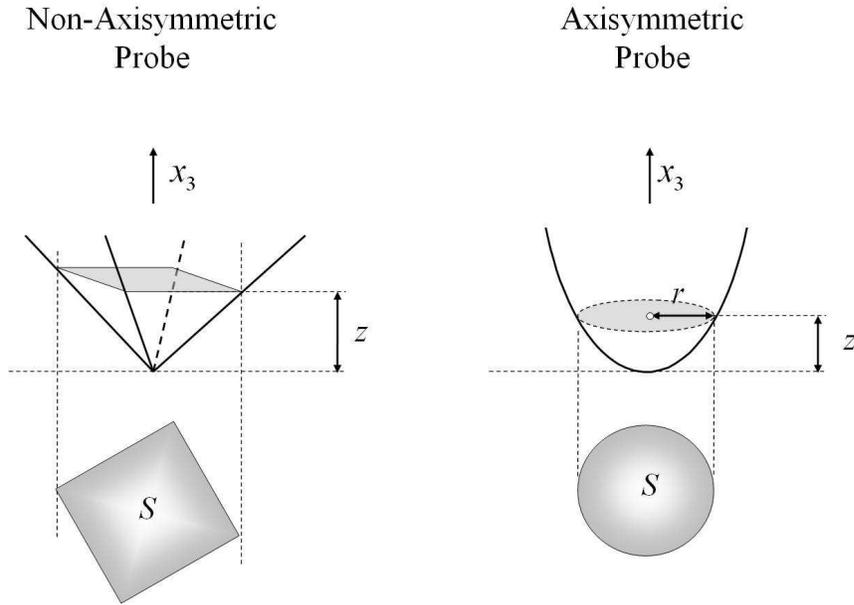
Figure 2-4: Parameters defining the geometry of an indenter probe. z is the height, S the cross-sectional area. For an axisymmetric probe, r is the radius.

2.2.2 Material Behavior

For the indentation problem to be self-similar, the constitutive relationships of the indented material need to be homogeneous with respect to the strains (or strain rates) or stresses; which means that the operator of constitutive relations F (and thus the stress tensor $\boldsymbol{\sigma}(\boldsymbol{\varepsilon})$) must scale as:

$$\boxed{F(\lambda \boldsymbol{\varepsilon}) = \lambda^{\kappa} F(\boldsymbol{\varepsilon})} \tag{2.3}$$

where $\boldsymbol{\varepsilon}$ is the strain tensor, and κ is the degree of the homogeneous constitutive function F. We note:

- Linear and non-linear elasticity satisfy this requirement, provided that [22]:

$$\boldsymbol{\sigma} = \mathbb{C}(\boldsymbol{\varepsilon}) : \boldsymbol{\varepsilon}; \ \mathbb{C}(\lambda \boldsymbol{\varepsilon}) = \lambda^{\kappa-1} \mathbb{C}(\boldsymbol{\varepsilon}) \tag{2.4}$$

where $\mathbb{C}(\boldsymbol{\varepsilon})$ is the secant stiffness tensor; and $\kappa = 1$ in the case of linear elasticity.

- Viscoelasticity also satisfies the requirement (2.3), provided that both the elastic and

viscous behaviors are linear with regard to the applied stress. In fact, in this case, the time-dependent response as represented by the stress convolution integral scales as [50] [157]:

$$\boldsymbol{\sigma}\left(\lambda\boldsymbol{\varepsilon}(t)\right) = \lambda\mathcal{F}(\boldsymbol{\varepsilon}(t)); \ \mathcal{F}(\boldsymbol{\varepsilon}(t)) = \int_0^t \mathbb{C}(t-\tau) : \frac{d}{d\tau}\boldsymbol{\varepsilon}\left(\tau\right)d\tau \qquad (2.5)$$

where $\mathcal{F}$ is a linear operator, and thus $\kappa = 1$; and where $\mathbb{C}(t)$ is the time-dependent stiffness tensor.

- The condition is also satisfied for a rigid plastic limit behavior, for which the stress derives from the dissipation function (or support function) $\boldsymbol{\sigma} : \mathbf{d} = \pi\left(\mathbf{d}\right)$; [70]:

$$\boldsymbol{\sigma} = \frac{\partial\pi}{\partial\mathbf{d}}\left(\mathbf{d}\right) \qquad (2.6)$$

where $\pi\left(\mathbf{d}\right)$ is a homogeneous function of degree 1 w.r.t. the strain rate tensor $\mathbf{d}$, such that:

$$\pi\left(\lambda\mathbf{d}\right) = \lambda\,\pi\left(\mathbf{d}\right) \qquad (2.7)$$

In this case, which will be considered in more detail in Section 2.4, it is readily understood that yield design solutions applied to indentation analysis satisfy the self-similarity condition (2.3), with $\kappa = 0$.

But not all materials satisfy Equation (2.3). An instance of such a material is a linear–elastic perfectly–plastic material, for which $\kappa = 1$ within the elastic domain, while $\kappa = 0$ at the limit of the elastic domain corresponding to the strength limit. That is, there is no unique value of κ for which Equation (2.3) holds for all strain levels eventually present in the indentation test, and indentations performed on linear–elastic perfectly–plastic materials are, therefore, not self-similar. More generally, whenever the material response of the indented half-space is not uniformly governed by the same class of material behavior identified by the constituent coefficient κ, the non-homogeneous stress distribution within the indented half-space may entail a loss of self-similarity of the indentation test. We keep this in mind for later developments.
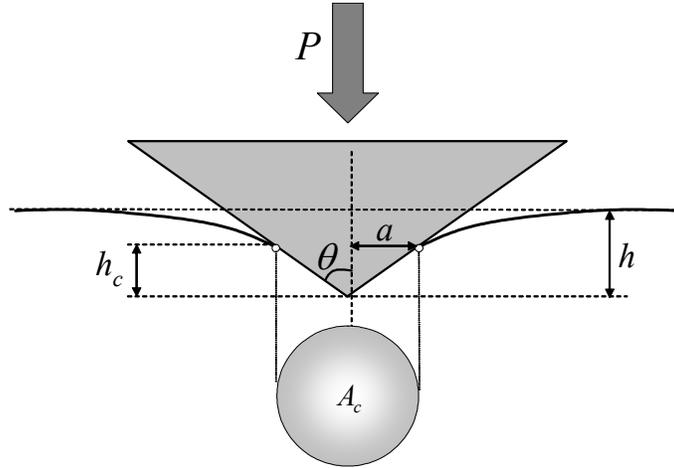
Figure 2-5: Geometry of an indentation test. P is the indentation load, h the indentation depth, h_c the contact depth, A_c the projected area of contact, and a the contact radius.

2.2.3 Self-Similar Scaling Relations

Provided relations (2.1) and (2.3) are satisfied, the loading phase of an indentation test possesses self-similarity. That is, given a known indentation response, represented by load P_0, indentation depth h_0, contact depth $(h_c)_0$ and projected area of contact $(A_c)_0$ (see Figure 2-5), the indentation response (P, h, h_c, A_c) is obtained from a similarity transformation [21]:

$$\frac{P}{P_0} = \left(\frac{h}{h_0}\right)^{\frac{2+\kappa(d-1)}{d}} \tag{2.8}$$

For instance, for elastic behavior ($\kappa = 1$), $P \propto h$ for a flat punch and $P \propto h^{3/2}$ for a spherical indenter. In turn, for a conical or pyramidal indentation ($d = 1$), $P \propto h^2$ irrespective of the material behavior. This provides a strong argument in favor of using the Berkovich indenter, as self-similarity will prevail irrespective of the constitutive relations.

Another relation obtained from the self-similarity of the indentation test is [21]:

$$\frac{h}{h_0} = \left(\frac{A_c}{(A_c)_0}\right)^{\frac{d}{2}} \tag{2.9}$$

A combination of the previous two scaling relations readily shows that average pressure

39

below the indenter —that is the hardness $H = P/A_c$— scales as:

$$\frac{H}{H_0} = \left(\frac{h}{h_0}\right)^{\frac{\kappa(d-1)}{d}} \tag{2.10}$$

Hence, for any rigid plastic behavior ($\kappa = 0$) or for any pyramidal or conical indenter shape, the hardness is constant throughout the loading process, and does not depend on the applied load.

Finally, noting that $A_c = \pi a^2$, where a is the contact radius, Eq. (2.9) can be rewritten as:

$$\frac{a^d}{h} = cst. \tag{2.11}$$

or equivalently, for axisymmetric probes, for which the contact radius a and the contact depth h_c are linked by $h_c = Ba^d$ (Eq. (2.2)):

$$\frac{h_c}{h} = cst. \tag{2.12}$$

Thus, provided self-similarity of the indentation test, the contact height –to– indentation depth ratio h_c/h does not depend on the load P. This result is of critical importance for indentation analysis and forms much of the basis of indirect methods of determination of the projected area of contact A_c in the contact problem.

2.3   Indentation Modulus

The indentation modulus M is defined by:

$$S \overset{def}{=} \frac{2}{\sqrt{\pi}} M \sqrt{A_c} \tag{2.13}$$

where $S = dP/dh$ is the contact stiffness measured during unloading (Fig. 2-6), and A_c the projected area of contact between the indenter tip and the indented material (Fig. 2-5). This definition, or manner of reporting the data, was introduced by Bulychev, Alekhin and Shorshorov [32], and Eq. (2.13) is therefore often referred to as the BASh formula. The focus of this Section is to link the indentation modulus M to the elastic properties of the indented material. We

40
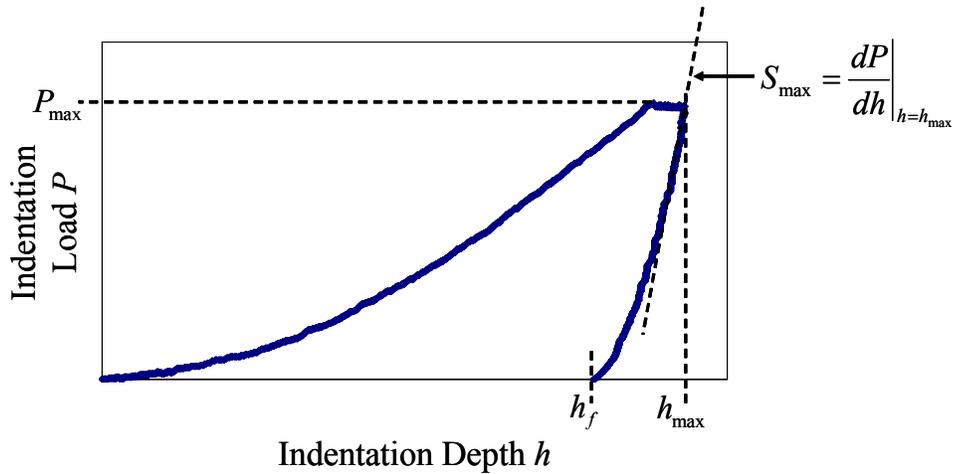
Figure 2-6: Parameters used to describe an indentation test. $P_{\max}$ is the maximum load, $h_{\max}$ the maximum depth, h_f the residual depth, and $S_{\max}$ the contact stiffness at maximum depth.

start with an elastic material, follow with a cohesive-frictional elasto-plastic material, then a linear viscoelastic material, and finally a cohesive-frictional linear viscoelastic material.

2.3.1   Linear Elastic Material

Consider an indentation on a linear elastic isotropic material, defined by the elastic constants, bulk modulus K_0 and shear modulus G_0. The loading and unloading branches of an elastic indentation overlap (Fig. 2-7). With $\kappa = 1$, the indentation test is assumed to possess perfect self-similarity.

Dimensional Analysis

A straightforward dimensional analysis [30] of the quantities involved in an indentation test performed on a linear elastic material allows us to reduce the four independent variables (bulk and shear modulus, K_0 and G_0, indentation depth h, and indenter shape factor B of dimension
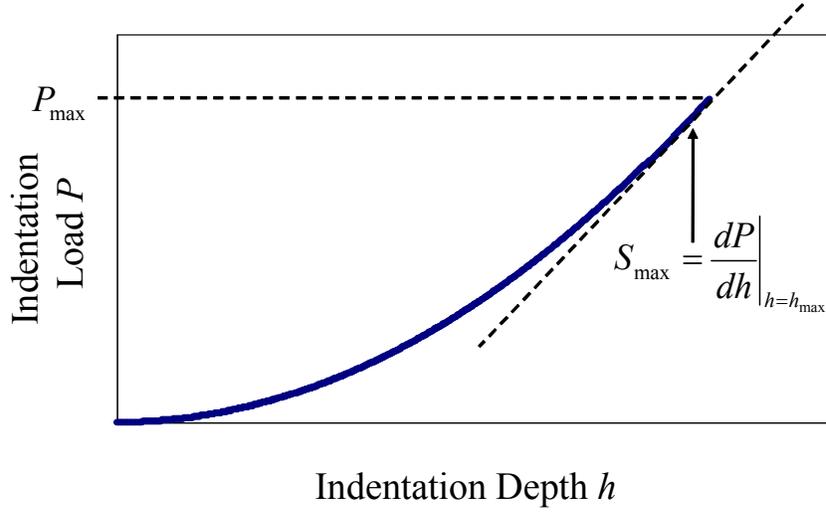
Figure 2-7: Typical $P-h$ curve for an indentation on an elastic material. $P_{\max}$ is the maximum load and $S_{\max}$ the contact stiffness at maximum depth. The loading and unloading branches overlap.

function $[B] = L^{1-d}$) to two; that is:

$$P = f(K_0, G_0, h, B) \tag{2.14}$$

$$\Downarrow$$

$$\frac{P}{G_0 h^2} = \Pi_\alpha \left(\Pi_1 = \frac{K_0}{G_0}; \Pi_2 = \frac{B}{h^{1-d}} \right) \tag{2.15}$$

where the bulk-to-shear modulus ratio $K_0/G_0 = 2(1+\nu)/(3(1-2\nu))$ is recognized as related to the Poisson's ratio ν. For any pyramidal or conical indenter shape $(d=1)$ we readily confirm the scaling relation (2.8), while the self-similarity implies that for other indenter shapes $(d \neq 1)$:

$$\frac{P}{G_0 h^2} = \Pi_2^{-1/d} \Pi'_{el} (\Pi_1^* = \nu) \tag{2.16}$$

That is,

$$P = \frac{h^{1/d+1}}{B^{1/d}} G_0 \, \Pi'_{el} (\Pi_1^* = \nu) \tag{2.17}$$

42

The contact stiffness thus reads:

$$S = \frac{dP}{dh} = \left(1 + \frac{1}{d}\right)\left(\frac{h}{B}\right)^{1/d} G_0 \, \Pi'_{el} \left(\Pi_1^* = \nu\right) \tag{2.18}$$

It has two components: One relating to the probe geometry (the term $(1 + 1/d)\,(h/B)^{1/d}$), and the other to the elastic properties of the indented half-space, $G_0 \, \Pi'_{el} \left(\Pi_1^* = \nu\right)$. A determination of both terms requires some refined analysis based on contact mechanics.

The Galin-Sneddon Solution

Indentation problems are contact mechanics problems: Two bodies (an indenter and a material half-space) interact mechanically through an area of contact (which is not known a priori except for the specific case of flat punch indentation). Because of the unknown area of contact, the governing equations of a contact mechanics problem are non–linear by nature even if the material behavior is linear. Hertz in 1881 was the first to analytically solve a contact mechanics problem, namely the contact of two elastic spheres [90]. The indentation of an elastic half-space by a rigid indenter was first solved by Love for a flat punch [117] and for a conical punch [118]. The general solution for a rigid axisymmetric indenter of arbitrary shape is due to Galin [76] developed in 1953 in the former USSR. His solution was presented in the USA by Sneddon [167], and is now known as the Galin-Sneddon solution.

The Galin-Sneddon solution is derived under the assumption of small perturbations, i.e., under the assumptions of both small displacements and small deformations. The geometry of the problem is defined in Figure 2-5. The boundary conditions are as follows:

- Outside the area of contact, the surface of the indented material is stress-free.

- Inside the area of contact, the contact between the indenter tip and the surface of the indented material is frictionless. Therefore, everywhere at the surface of the indented material, the stress vector can only have a $z-$component. Inside the area of contact, the z-component of the displacement of the surface of the indented material is imposed by the shape of the indenter.

The solution of the problem so described can be performed with several methods, one being

the use of Hankel transforms (two-dimensional Fourier transforms) on the polar coordinates ρ and θ. As a result of the derivation, for an indenter of monomial shape $z = Br^d$ (Section 2.2.1), the indentation load is linked to the indentation depth by:

$$P = \frac{2}{(\sqrt{\pi}B)^{1/d}} M_0 \frac{d}{d+1} \left[\frac{\Gamma\left(\dfrac{d}{2} + \dfrac{1}{2}\right)}{\Gamma\left(\dfrac{d}{2} + 1\right)} \right]^{1/d} h^{1+1/d} \tag{2.19}$$

where $\Gamma(x)$ is the Euler Gamma function, $\Gamma(x) = \int_0^\infty t^{x-1} \exp(-t) \, dt$, and M_0 is the plane stress modulus:

$$M_0 = \frac{E_0}{1 - \nu^2} = 4G_0 \frac{3K_0 + G_0}{3K_0 + 4G_0} \tag{2.20}$$

The solution also yields the contact depth –to– indentation depth ratio h_c/h:

$$\frac{h_c}{h} = \frac{1}{\sqrt{\pi}} \frac{\Gamma\left(\dfrac{d}{2} + \dfrac{1}{2}\right)}{\Gamma\left(\dfrac{d}{2} + 1\right)} \tag{2.21}$$

As expected from the self-similarity of the indentation test (Section 2.2.3), h_c/h for a given indenter probe is found to be constant. A differentiation of Equation (2.19) with respect to the indentation depth h combined with Equation (2.21) yields the BASh-Formula (2.13):

$$S = \frac{2}{\sqrt{\pi}} M_0 \sqrt{A_c} \tag{2.22}$$

Since h_c/h is known, the contact depth h_c, and consequently the projected area of contact A_c, can be calculated from the measured indentation depth h. Thus, all variables in the BASh formula (2.13) are obtained from the indentation test, and the indentation modulus M_0 of the indented material can be calculated.

In addition to the $P - h$ relationship (2.19), the analytical solution also provides the displacement field $\underline{u}$ and the stress field $\boldsymbol{\sigma}$ in the elastic half-space. In the specific case of conical indentation, these fields at the surface of the indented material read in cylindrical coordinates

44

[167]:

$$u_\rho(\rho \ < \ a, 0) = \frac{1-2\nu}{4(1-\nu)}\frac{\rho}{\tan\theta}\left[\ln\left(\frac{\rho/a}{1+\sqrt{1-(\rho/a)^2}}\right) - \frac{1-\sqrt{1-(\rho/a)^2}}{(\rho/a)^2}\right] \quad (2.23)$$

$$u_z(\rho \ < \ a, 0) = \frac{1}{\tan\theta}\left[a\sin^{-1}\left(\frac{a}{\rho}\right) + \sqrt{\rho^2 - a^2} - \rho\right] \quad (2.24)$$

$$\sigma_{zz}(\rho \ < \ a, 0) = \frac{1}{2\tan\theta}\frac{E_0}{1-\nu^2}\cosh^{-1}\left(\frac{a}{\rho}\right) \quad (2.25)$$

Equation (2.25) shows a stress singularity for $\rho = 0$ right below the tip of an infinitely sharp cone.

Relevance of Assumption of Small Perturbations

The Galin-Sneddon solution assumes small perturbations, that is small displacements and small deformations. Given that infinite stresses (and therefore infinite strains) occur at the tip of a conical indenter (see Equation (2.25)), the assumption of small deformations is surely not valid. Furthermore, by assuming small displacements the initial and actual configurations are merged, and the boundary conditions are expressed in the initial configuration for the derivation of the Galin-Sneddon solution. With an indenter of half-cone angle θ, the surface of the indented material rotates by $\pi/2 - \theta$ inside the area of contact, which translates to about $20°$ for a Berkovich probe and about $48°$ for a Cube Corner probe! Thus the assumption of small displacements is not valid either, and the assumption of small perturbations has true theoretical restrictions when it comes to indentation analysis. On the other hand, the question of interest for day-to-day indentation analysis is the deviation of the Galin-Sneddon solution from the actual finite strain and large displacement elastic indentation solution. From the point of view of dimensional analysis of the elastic problem (Section 2.3.1), this deviation will depend only on the Poisson's ratio and the indenter geometry; thus for conical indentation:

$$S = \beta(\nu, \theta)\frac{2}{\sqrt{\pi}}M_0\sqrt{A_c} \quad (2.26)$$

where the β-factor captures all deviations from the Galin-Sneddon solution. The β-factor for elastic indentation was studied numerically by Hay et al. [87], who found that the β-factor is always greater than unity (see Figure 2-8a). They showed that β differs from unity because

the displacement of the surface below the indenter has a non-zero radial component for any compressible material. The Galin-Sneddon solution, which is first-order in nature, disregards this radial displacement. Taking into account the radial displacement and performing a new analytical derivation, Hay et al. proposed the following expression for β, which is displayed in Figure 2-8b:

$$\beta(\nu,\theta) = \pi \frac{\dfrac{\pi}{4} + 0.1548\dfrac{1-2\nu}{4(1-\nu)}\cot\theta}{\left[\dfrac{\pi}{2} - 0.8312\dfrac{1-2\nu}{4(1-\nu)}\right]^2} \qquad (2.27)$$
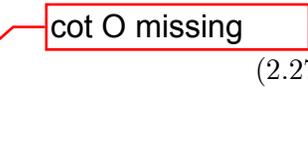
The correction factor depends on both the half-cone angle θ and the Poisson's ratio ν of the indented material. $\beta(\nu = 0.5, \theta) = 1$ for any half-cone angle θ. For an incompressible material, the displacement of the surface has no radial component and the BASh formula (2.13) requires no correction.

Finite Elasticity of Indenter Probe

The Galin-Sneddon solution was derived under the assumption of a rigid indenter probe. From a practical point of view, the probe is never rigid. Although stiffer than many materials, probes are often made of diamond, which has a finite Young's modulus, $E_{in} \simeq 1,141$ GPa [62], and Poisson's ratio $\nu_{in} = 0.07$ [62]. Hertz's original contact solution between two elastic spheres already accounted for the different elasticity of the two bodies; from which:

$$\frac{1}{M_0} = \frac{1 - \nu_{in}^2}{E_{in}} + \frac{1 - \nu^2}{E_0} \qquad (2.28)$$

The finite elasticity of the indenter tip is accounted for by approximating the tip-material system as two springs in series with respective plane-stress stiffnesses $E_{in}/(1 - \nu_{in}^2)$ and $E_0/(1 - \nu^2)$ [137].

2.3.2 Cohesive-Frictional Elasto-Plastic Material

Consider next an indentation test into an elasto-plastic material. A typical $P - h$ curve of an elasto-plastic material is displayed in Figure 2-9, showing– as expected– that the loading and unloading branches do not overlap. This Section reports on recent developments that show
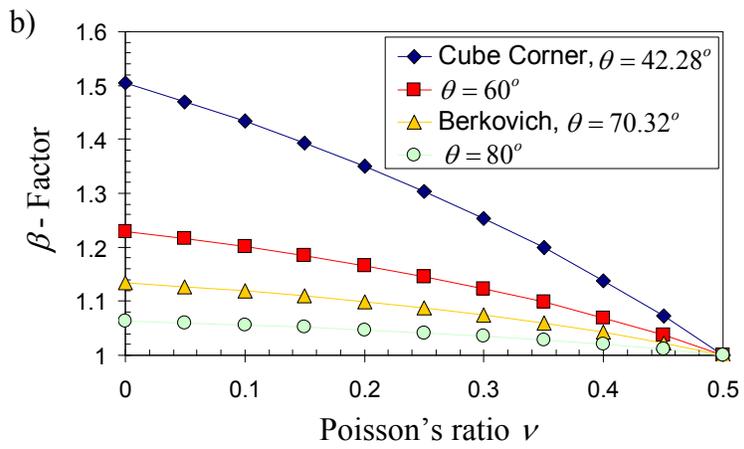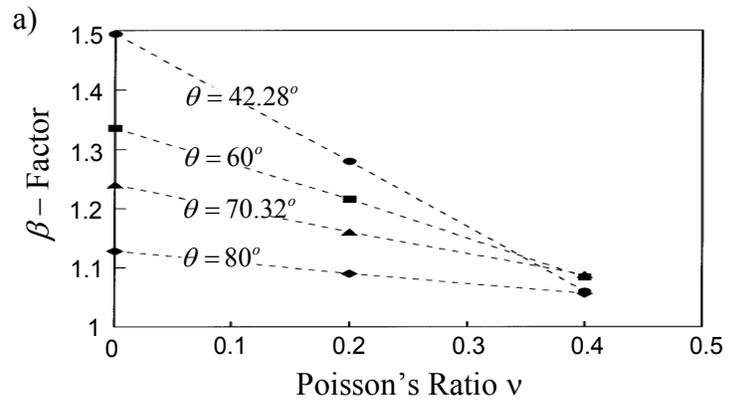
Figure 2-8: Correction factor β for elastic conical indentation (a) derived from numerical simulations (adapted from [87]) (b) obtained from Equation (2.27).
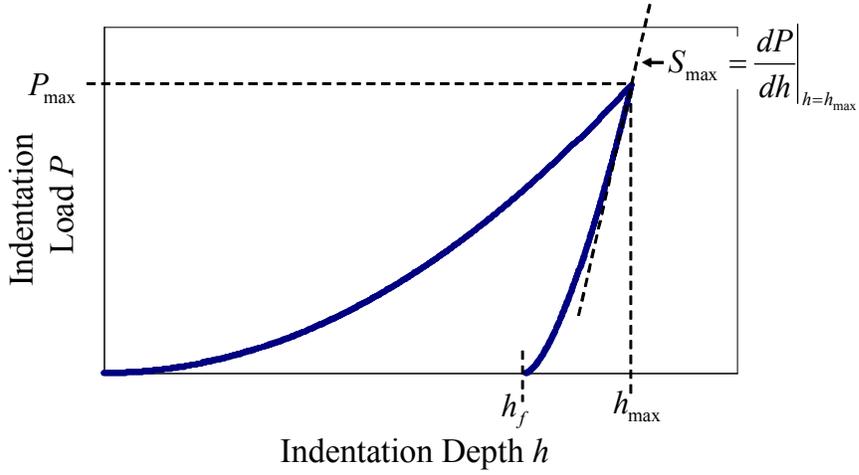
Figure 2-9: Typical $P - h$ curve for an indentation on an elasto-plastic material. $P_{\max}$ is the maximum load, $h_{\max}$ the maximum depth, h_f the residual depth and $S_{\max}$ the contact stiffness at maximum depth.

that the BASh formula (2.13), derived for the elastic case, can still be applied to the unloading branch of the elasto-plastic material response to extract the elasticity content.

Dimensional Analysis

In addition to the set of variables (2.14), the dimensional analysis of the unloading branch of an indentation test on an elasto-plastic material behavior requires additional variables [48] [57], namely strength properties and a reference indentation depth at which unloading occurs. For the purpose of this analysis, we consider the material to be a cohesive-frictional elasto-plastic material whose strength domain is described by the cohesion C and the friction coefficient μ. Analogous to (2.14) and (2.15), application of the Π-theorem [30] yields:

$$P = f_U\left(M_0, \nu, C, \mu, h, h_{\max}, B\right) \tag{2.29}$$

$$\Downarrow$$

$$\frac{P}{M_0 h^2} = \Pi_\beta\left(\nu; \frac{C}{G}; \mu; \frac{h}{h_{\max}}; \frac{B}{h_{\max}^{1-d}}\right) \tag{2.30}$$

48

where M_0 is the plane-stress modulus (2.20). Differentiation and evaluation at $h = h_{\max}$ of Eq. (2.30) yields:

$$
\begin{aligned}
\frac{S}{M_0 h_{\max}} &= 2\Pi_\beta + h_{\max} \left.\frac{\partial \Pi_\beta}{\partial h}\right|_{h=h_{\max}} \\
&= \Pi_\gamma \left(\nu; \frac{C}{G}; \mu; \frac{h}{h_{\max}} = 1; \frac{B}{h_{\max}^{1-d}}\right)
\end{aligned}
\tag{2.31}
$$

Furthermore, in elasto-plastic indentation, because of the loss of self-similarity (see Section 2.2.2), the projected area of contact is no longer independent of the material behavior. Performing a similar dimensional analysis for the area of contact during loading yields:

$$
A_c = f_{A_c} \left(M_0, \nu, C, \mu, h, B\right)
\tag{2.32}
$$

$$
\Downarrow
$$

$$
\frac{A_c}{h^2} = \Pi_\delta \left(\nu; \frac{C}{M_0}; \mu; \frac{B}{h^{1-d}}\right)
\tag{2.33}
$$

Eq. (2.33) is valid during the entire loading phase and consequently at $h = h_{\max}$ as well. Therefore a combination of Eqs. (2.31) and (2.33) yields a new invariant:

$$
\frac{S}{M_0 \sqrt{A_c}} \overset{h=h_{\max}}{=} \frac{\Pi_\gamma \left(\nu; \frac{C}{M_0}; \mu; \frac{B}{h_{\max}^{1-d}}\right)}{\sqrt{\Pi_\delta \left(\nu; \frac{C}{M_0}; \mu; \frac{B}{h_{\max}^{1-d}}\right)}} \equiv \Pi_\epsilon \left(\nu; \frac{C}{M_0}; \mu; \frac{B}{h_{\max}^{1-d}}\right)
\tag{2.34}
$$

From a comparison of Eq. (2.34) with the BASh formula (2.13), we readily find that $\Pi_\epsilon = 2/\sqrt{\pi}$ in elastic indentation, and $\Pi_\epsilon = 2\beta \left(\nu, B/h_{\max}^{1-d} = \cot\theta\right)/\sqrt{\pi}$ (according to (2.26)) when large elastic deformation and displacement are taken into account. In the case of an elasto-plastic behavior, dimensional analysis reveals that the β correction factor may also depend on the strength–to–stiffness ratio, C/M_0, and the friction coefficient, μ. This conjecture was numerically investigated by Cheng and Cheng [45] [46] for conical indentation ($d = 1, \theta = 68°$) on elasto-plastic cohesive materials ($\mu = 0$) with a wide range of yield strength –to– Young's modulus ratios, $\sigma_y/E = (C/G) \times (1 + \nu)^{-1}$, Poisson's ratios, ν, and strain hardening exponent n (Fig 2-10). They found that the β correction factor in elasto-plastic indentation is almost insensitive to the plastic properties of the material and of a similar order as the elastic large

deformation/large displacement correction factor β (Section 2.3.1); that is:

$$\beta = \frac{\sqrt{\pi}}{2}\Pi_\epsilon = 1.08 \pm 0.04 \qquad (2.35)$$

This result provides strong evidence that the indentation modulus M_0 assessed by the the BASh formula (2.13) is a function of the elastic properties of the indented material only[1]. Bolshakov and Pharr [19] also performed numerical simulations of conical indentations on cohesive materials with and without strain hardening, but considered a cone of half-cone angle of $70.3°$, which is the equivalent half-cone angle of Berkovich probes. They found that $\beta \simeq 1.07$ works for most materials, although this value may rise for materials with large E/σ_y ratios. Therefore, considering a value of $\beta = 1.06 \pm 0.06$ is probably safe, and disregarding the effect of the β-factor on the BASh formula (2.13) may lead to overestimating the indentation modulus $M_0 = E_0/(1 - \nu^2)$ merely by $6\% \pm 6\%$.

Effective Indenter

One could argue that, for an elasto-plastic material, the indentation modulus, M_0, is a function solely of the elastic properties, if the unloading branch of an indentation test is (almost) only elastic, and if the reloading after unloading is also elastic (Figure 2-11). It is useful, however, to remind ourselves that the very concept of the indentation modulus derives from elastic indentation analysis based on the self-similarity of the indentation test (see Section 2.2), while indentation into an elasto-plastic half-space does not possess this self-similarity due to the non-uniqueness of the constituent coefficient κ in elasto-plastic indentation analysis ($\kappa = 1$ in elastic domain, $\kappa = 0$ for the strength limit; see Section 2.2.2). The concept of the 'effective indenter' introduced by Pharr and Bolshakov [147] implicitly addresses this loss of self-similarity in elasto-plastic indentation analysis.

The concept of the effective indenter (see Figure 2-12) is based on the premise that the specific pressure distribution below an indenter during elastic unloading and reloading of an

---

[1]The result may not come as a surprise, as Cheng and Cheng's investigation considered a cohesive material behavior (with and without hardening). Cohesive materials are plastically incompressible. The plastic component of the indentation response, therefore, is not expected to increase the inaccuracy of the BASh formula due to the small perturbation assumption. In contrast, the additional incompressible plastic deformation in a zone below the indenter is expected to correct for possible errors induced by the elastic compressibility.
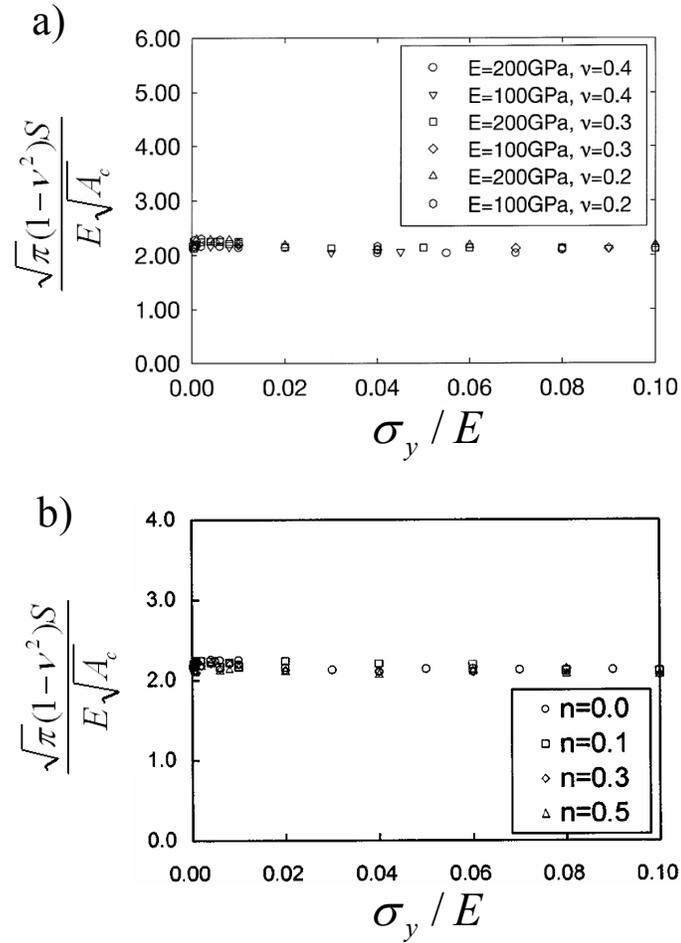
Figure 2-10: A relationship between $\dfrac{(1-\nu^2)S}{Ea}$ and σ_y/E for conical indentation $(\theta = 68^o)$ of an elasto-plastic cohesive half-space (a) for a material with no strain hardening (from [46]) and (b) for a material with strain hardening (from [45]). σ_y is the yield strength, n the strain hardening exponent.
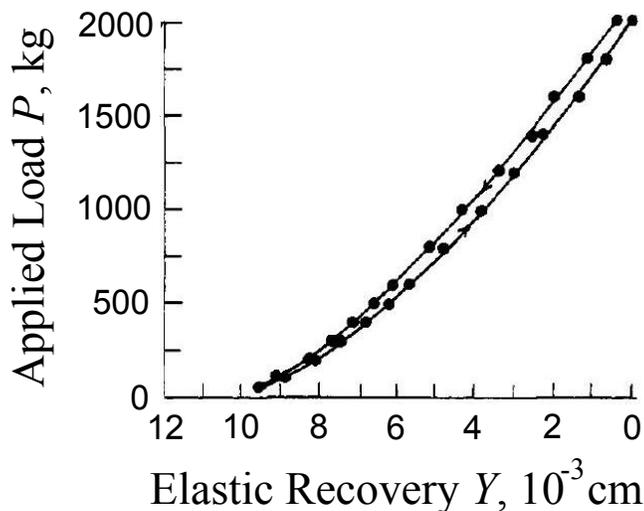
Figure 2-11: Unloading-reloading cycle of a conical indentation ($\theta = 68^o$) on duralumin. After a few cycles the loop becomes very narrow (from [170]).

elasto-plastic half-space is that of an effective indenter of unknown geometry, which creates, for the same load, the same specific pressure distribution. In terms of the self-similarity properties discussed in Section 2.2, this concept, therefore, shifts the non-uniqueness of the constituent coefficient κ in elasto-plastic indentation analysis to the indenter geometry, i.e., the probe geometry coefficient d (see Section 2.2.1). An argument in favor of its justification is the observation that the "elastic" $P - (h - h_f)$ curve of the unloading of the elasto-plastic indent with the real indenter is the same as the $P - h_{el}$ curve of the loading of the elastic indent of unknown geometry. Experimentally, Pharr and Bolshakov observed that the unloading phase of Berkovich indentation tests on a range of elasto-plastic materials can be well fit with a power function [147]:

$$P \simeq c(h - h_f)^m \qquad (2.36)$$

with the power exponent $1.2 \leq m \leq 1.6$. Equating $P \simeq c(h - h_f)^m$ of the real indenter with $P \simeq c(h_{el})^m$ of the equivalent indenter, while assuming geometric self-similarity of the effective indenter shape, an application of the scaling relation (2.8) from Section 2.2.3 with

52
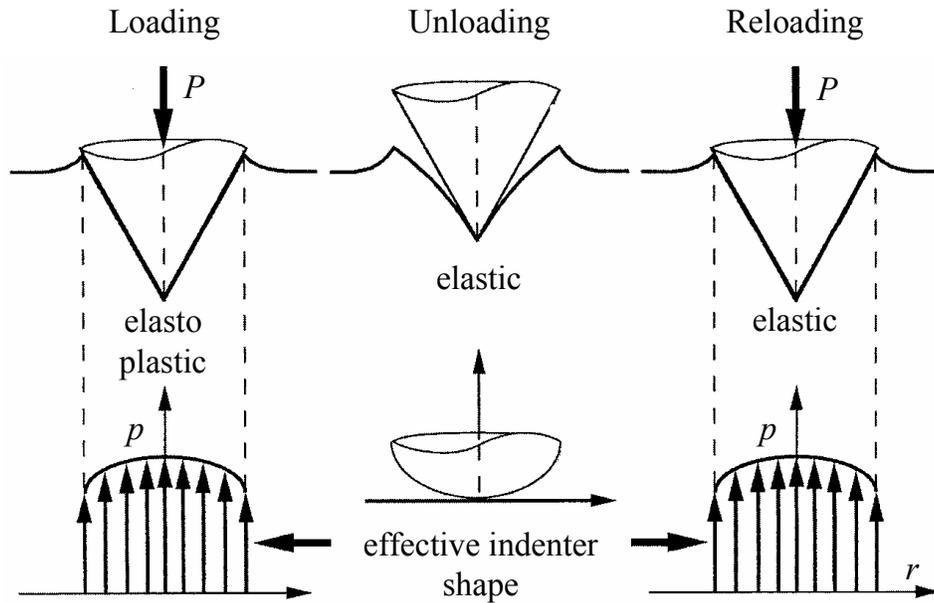
Figure 2-12: Schematic representation of pressure distributions below the indenter and concept of the effective indenter (adapted from [147]).

$\kappa = 1$ provides an estimate of d:

$$d \stackrel{\kappa=1}{=} \frac{1}{m-1} \in \left[\frac{5}{3}; 5 \right] \tag{2.37}$$

The range of values so obtained is clearly greater than $d = 1$ that characterizes conical and pyramidal probes; and comes the closest, according to [147], to an equivalent paraboloid shape, for which $d = 2$. It should, however, be noted that the equivalent indenter, if it were to exist, would most likely not be self-similar. Otherwise said, the effective indenter concept provides a pragmatic way to circumvent an intrinsically difficult situation of elasto-plastic indentation analysis, which is the loss of self-similarity. This loss of self-similarity, however, seems to have a second order effect on the accuracy of the BASh formula (2.13) in extracting an indentation modulus that relates to the elasticity content of the indented elasto-plastic material.
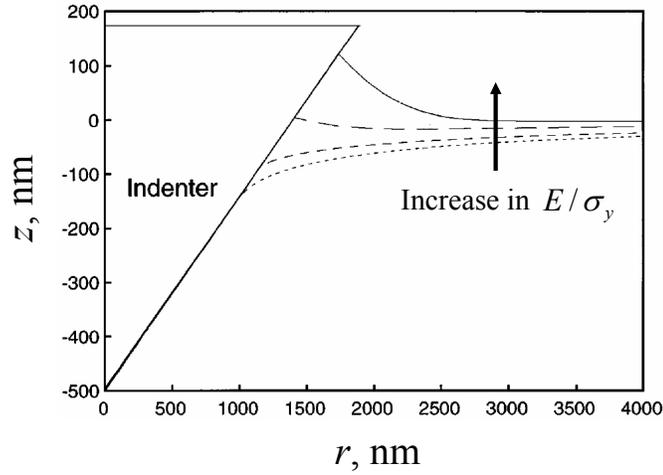
Figure 2-13: Increase in the contact depth –to– indentation depth ratio h_c/h due to plastic phenomena for conical indentation in elastic perfectly plastic materials (adapted from [19]). In conical elastic indentation, $h_c/h = 2/\pi$. In elasto-plastic indentation, the greater the Young's modulus –to– yield strength ratio E/σ_y, the greater h_c/h. When $h_c/h > 1$, the material is said to 'pile-up'.

Oliver and Pharr Method

There is, however, one fundamental difference between elastic and elasto-plastic indentation analysis, which is the determination of the projected area of contact A_c that is required as input for the use of the BASh formula (2.13). In fact, while elastic indentation solution provides a direct means to determine the area of contact from the contact depth –to– indentation depth ratio h_c/h provided by the Galin-Sneddon solution (i.e., Eq. (2.21)), the h_c/h ratio in elasto-plastic indentation is a priori unknown (Figure 2-13). Traditionally the projected area of contact A_c was approximated by the area of the residual imprint of the test, and the residual imprint was measured optically after the indent was performed. Stillwell and Tabor showed for metals that the remaining imprint was a good estimate of the projected area of contact at maximum depth [170]. But measuring the residual imprint after each indent is both time-consuming and difficult at small scales. This brought about indirect methods of the determination of the projected area of contact A_c at maximum load, among which the most prominent is the method proposed by Oliver and Pharr in 1992 [137].

The Oliver and Pharr method provides an indirect estimate of the projected area of contact

54
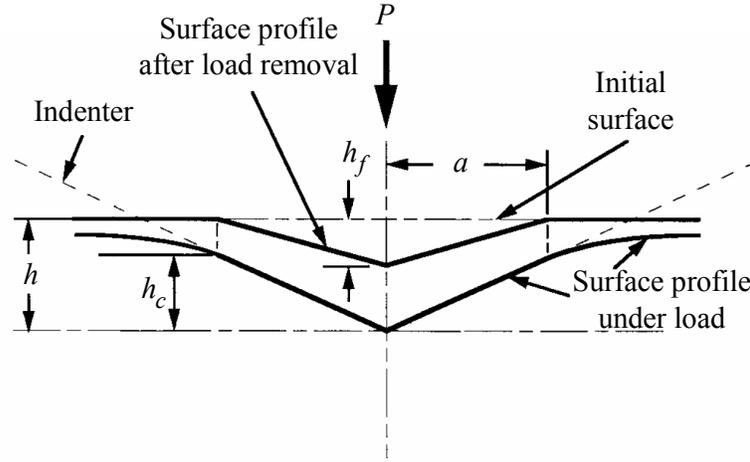
Figure 2-14: Determination of the projected contact area with the Oliver and Pharr method (from [137]).

at maximum load from the shape of the unloading curve. It is based on the concept of the effective indenter shape (Section 2.3.2): It considers the unloading curve $P \propto (h - h_f)^m$ and elastic response $P \propto (h_{el})^m$ obtained with an indenter of parabolic shape. For such a probe, the *elastic* contact depth –to– indentation depth ratio is obtained from (2.21):

$$\frac{h_c}{h}(d=2) = \frac{1}{\sqrt{\pi}} \frac{\Gamma\left(\frac{3}{2}\right)}{\Gamma(2)} = \frac{1}{2} \qquad (2.38)$$

The Oliver and Pharr method is based on the assumption that the elastic contact depth - to - indentation depth ratio $h_c/h = 1/2$ for parabolic probes applies also to the elastic unloading of the elasto-plastic indentation:

$$h_c - h_f = \frac{1}{2}(h_{\max} - h_f) \qquad (2.39)$$

where h_f is the residual indentation depth (Fig. 2-14).

Both $h_{\max}$ and h_f are data available from the test, so that Eq. (2.39) provides an indirect means to determine the contact depth h_c, and thus the projected area of contact A_c. Furthermore, since the measurement of the residual depth h_f is sensitive to surface roughness, an expression is sought in which h_f does not appear. The effective indenter being close to a

paraboloid, the load-depth relation during unloading is:

$$P \simeq c(h - h_f)^{3/2} \tag{2.40}$$

which, after differentiation with respect to h and evaluation at $h = h_{\max}$, yields:

$$h_{\max} - h_f = 2\frac{P}{S} \tag{2.41}$$

Combining Eqs. (2.39) and (2.41) yields:

$$\boxed{\frac{h_c}{h_{\max}} = 1 - \varepsilon\frac{P_{\max}}{Sh_{\max}}} \tag{2.42}$$

where $\varepsilon = 3/4$. Since the maximum indentation load $P_{\max}$, the contact stiffness S and the maximum indentation depth $h_{\max}$ are all available from the test, Eq. (2.42) provides a convenient way to estimate the contact depth h_c, and thus the projected area of contact A_c. From an experimental point of view, the effective indenter is not truly a paraboloid (see Equation (2.36)). But slightly modifying the shape of the effective indenter and repeating the derivation presented earlier in this Section does not change much the value of ε (for a cone, e.g., $\varepsilon = 0.72$); and keeping a value of $\varepsilon = 0.75$ for all tests is recommended [137].

Though a powerful tool in indentation analysis, the Oliver and Pharr method has one limitation. It can only capture 'sink-in' phenomena, for which $h_c/h < 1$, but not 'pile-up', for which the contact depth is greater than the indentation depth, and which has been observed experimentally, especially in sharp indentation and for some plastically dilating materials (Fig. 2-13). Despite this limitation, for Berkovich indentation on cementitious materials, Constantinides verified experimentally that the Oliver and Pharr method provides a good estimate of the projected area of contact [57].

2.3.3 Linear Viscoelastic Materials

The focus of this Section is to study the effect of a time-dependent behavior on the measurable unloading slope S, and thus on the measurable indentation modulus M. The importance of considering a time-dependent material behavior on the indentation unloading response is readily

depicted by Figure 2-15. In fact, due to creep, a bulge can appear in the unloading branch of the $P - h$ curve, and the initial unloading slope can become negative, $S(h_{\max}) < 0$. The use of a negative slope in the BASh formula (2.13) implies a negative indentation modulus M and thus, according to (2.20), a negative Young's modulus or shear modulus, which is not admissible. The aim of this Section is to identify, analytically, the influence of a time-dependent behavior on the measured contact stiffness, and to derive test conditions for which this influence becomes negligible. To this aim, we consider the indented material to be linear viscoelastic in the sense of Eq. (2.5); that is, both the elastic and the viscoelastic behavior are linear w.r.t. the stress at a material scale, and the indentation problem possesses perfect self-similarity. To investigate the phenomena at stake, we first introduce a general method for solving linear viscoelastic indentation problems.

Linear Viscoelastic Contact Problems

Most viscoelastic indentation solutions originate from the method of functional equations developed for linear viscoelastic contact problems by Radok in 1957 [152] and completed by Lee and Radok in 1960 [112]. The method of functional equations is an extension of the s-multiplied Laplace transform method, as formulated by Lee in 1955 [111]. The s-multiplied Laplace transform method consists in eliminating the explicit time dependence of the viscoelastic problem by replacing all time dependent moduli by their Laplace transform multiplied by the Laplace parameter s. The corresponding elasticity problem is then solved in the Laplace domain. The solution, obtained in the Laplace domain, is then translated back into the time domain.

The s-multiplied Laplace transform method, however, is restricted to boundary value problems, in which the displacement and stress boundary conditions are fixed in time. This is not the case in indentation problems (except for the flat punch problem), in which the area of contact changes with time, hence changing a part of the stress boundary outside the area of contact into a displacement boundary inside the area of contact, and *vice versa*. This restriction of the s-multiplied Laplace transform was lifted by Lee and Radok [152] [112], who introduced and developed the method of functional equations for linear viscoelastic problems with time dependent boundary conditions. If the boundary conditions are not explicitly expressed within the set of equations describing the contact problem, the use of the Laplace transform is valid as
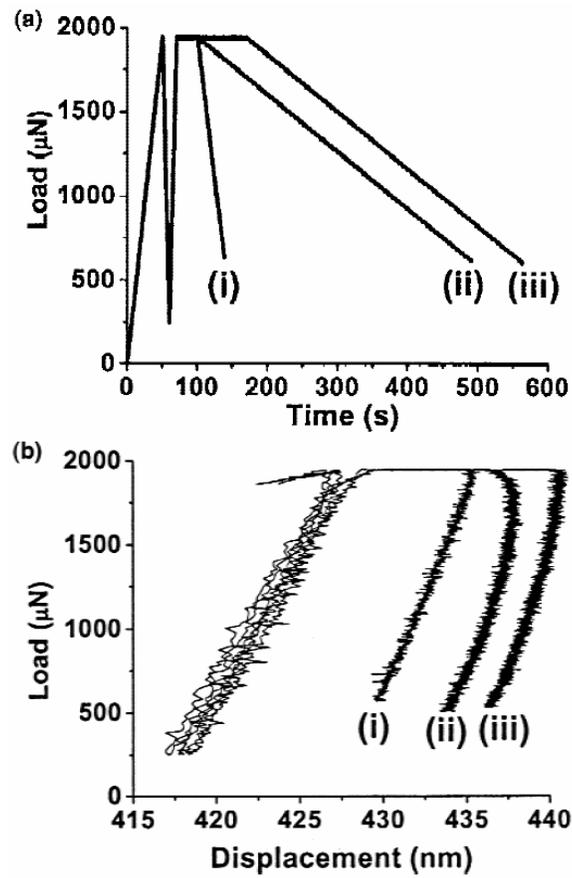
Figure 2-15: Effect of creep on the unloading curve for Berkovich indentation on Aluminum (from [75]). (a) Load cases and (b) resulting unloading curves. For some load cases, a negative unloading slope at maximum depth can be observed.

a mere mathematical tool without physical meaning, and the method of functional equations can be equated with the s-multiplied Laplace transform method.

For indentation problems, the method of functional equations remains valid as long as the area of contact (or, equivalently for viscoelastic materials, the penetration depth) increases monotonically [112]. The restriction of the method to monotonically increasing area of contact haunted many researchers (e.g., Hunter's 1960 solution for spherical indentation [94]) and was finally removed in 1966 by Ting [180], who developed implicit equations for the general case of indentation in any linear viscoelastic material by any axisymmetric indenter and for any load history. However, it is a challenge to employ Ting's implicit formulation, except to a few very specific load histories, indenter shapes and material behaviors. This explains why Radok's method of functional equations is still attractive today [44] [43] [191]. Finally, due to the employment of the method of functional equations and its restriction to monotonically increasing areas of contact, most solutions cannot address the question of how viscous phenomena affect the measured contact stiffness and hence the extracted elasticity properties. However, we show in Appendix A that the method of functional equations remains valid at the onset of unloading and can therefore be used to study the effect of viscosity on the measured contact stiffness S.

Effect of Viscosity on Measurement of Contact Stiffness

When applying indentation analysis to an experimental curve, the measured contact stiffness S_U is the slope of the experimental $P - h$ curve at the onset of unloading by:

$$S_U = \left. \frac{dP}{dh} \right|_{h=h_{\max}} \tag{2.43}$$

As observed in Figure 2-15, because of viscous effects the measured contact stiffness can differ from the elastic contact stiffness S, defined by:

$$S = \frac{2}{\sqrt{\pi}} M_0 \sqrt{A_c} \tag{2.44}$$

where M_0 is the elastic indentation modulus. The aim of this Section is to analytically identify the difference.

The time-dependent behavior of the indented material is described by its bulk relaxation
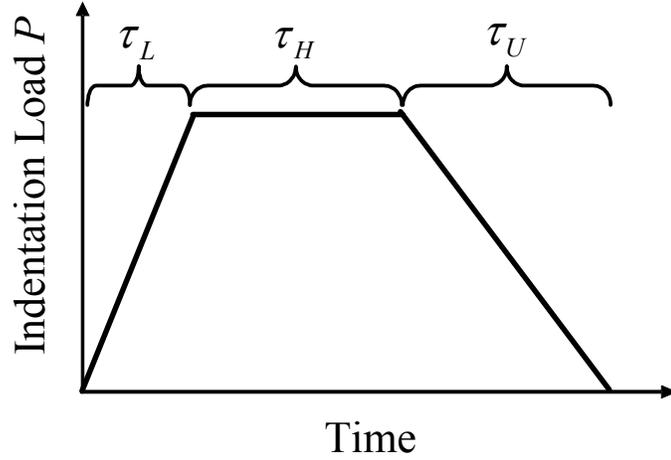
Figure 2-16: Trapezoidal load case considered for indentation on a linear viscoelastic material.

modulus $K(t)$ and by its shear relaxation modulus $G(t)$. $K(t = 0) = K_0$ is the instantaneous elastic bulk modulus and $G(t = 0) = G_0$ is the instantaneous elastic shear modulus of the indented material. The elastic indentation modulus M_0 is linked to the elastic bulk and shear moduli K_0 and G_0 (see Equation (2.20)):

$$M_0 = 4G_0 \frac{3K_0 + G_0}{3K_0 + 4G_0} \qquad (2.45)$$

A rigid axisymmetric indenter of arbitrary shape indents the material of interest, according to a trapezoidal load case. The load is increased linearly for a time of duration τ_L, then kept constant at its maximum value $P_{\max}$ for a time τ_H, and finally decreased linearly to zero over a time τ_U (see Figure 2-16).

The viscoelastic problem is solved by applying the s-multiplied Laplace transform to the Galin-Sneddon solution (2.3.1):

$$\widehat{h^{1+1/d}}(s) = \frac{(\sqrt{\pi}B)^{1/d}}{2} \frac{d+1}{d} \left[\frac{\Gamma(d/2+1)}{\Gamma(d/2+1/2)} \right]^{1/d} \frac{\widehat{P}(s)}{s\widehat{M}(s)} \qquad (2.46)$$

where s is the Laplace parameter and $\widehat{f}(s)$ is the Laplace transform of $f(t)$. The above equation

can be rewritten as:

$$\widehat{h^{1+1/d}}(s) = \widehat{g(s)}s\widehat{P(s)} \tag{2.47}$$

where $g(t)$ depends on the indented material properties and on the indenter shape, but not on the loading profile. $g(t)$ is defined in the Laplace domain by:

$$\widehat{g(s)} = \frac{(\sqrt{\pi}B)^{1/d}}{2}\frac{d+1}{d}\left[\frac{\Gamma(d/2+1)}{\Gamma(d/2+1/2)}\right]^{1/d}\frac{1}{s^2\widehat{M(s)}} \tag{2.48}$$

If we remind ourselves that a multiplication in the Laplace domain corresponds to a convolution in the time-domain [157], Eq. (2.48) reads in the time-domain:

$$h^{1+1/d}(t) = \int_{\tau=0}^{t} g(t-\tau)\frac{dP(\tau)}{d\tau}d\tau \tag{2.49}$$

$$= \begin{cases} h_H(t) = \dfrac{P_{\max}}{\tau_L}\displaystyle\int_{\tau=0}^{\tau_L} g(t-\tau)d\tau & \text{during holding} \\[3mm] h_U(t) = \dfrac{P_{\max}}{\tau_L}\displaystyle\int_{\tau=0}^{\tau_L} g(t-\tau)d\tau - \dfrac{P_{\max}}{\tau_U}\displaystyle\int_{\tau=\tau_L+\tau_H}^{t} g(t-\tau)d\tau & \text{during unloading} \end{cases}$$

where the solution during unloading, since derived with the s-multiplied Laplace transform method (see Appendix A), is only valid at the onset of unloading, i.e., at $t = (\tau_L + \tau_H)^+$. The rate of penetration of the indenter at respectively the end of the holding phase, $\dot{h}_H(t^- = \tau_L + \tau_H)$, and at the onset of the unloading phase, $\dot{h}_U(t^+ = \tau_L + \tau_H)$ are obtained from a differentiation of Eq. (2.49) with respect to time:

$$\dot{h}_H(t = \tau_L + \tau_H) = \frac{P_{\max}}{\left(1+\frac{1}{d}\right)h_{\max}^{1/d}\tau_L}\int_{\tau=0}^{\tau_L} \dot{g}(t-\tau)d\tau \tag{2.50}$$

$$\dot{h}_U(t = \tau_L + \tau_H) = \dot{h}_H(t = \tau_L + \tau_H) - \frac{P_{\max}}{\left(1+\frac{1}{d}\right)h_{\max}^{1/d}\tau_U}g(0) \tag{2.51}$$

where $g(0)$ can be obtained from Equation (2.48) by evoking the final value theorem which links the short-term behavior of a function to its Laplace transform [134], $f(t = 0^+) =$

$\lim_{s \to +\infty} s\widehat{f}(s)$. That is:

$$g(0) = \frac{(\sqrt{\pi}B)^{1/d}}{2} \frac{d+1}{d} \left[\frac{\Gamma(d/2+1)}{\Gamma(d/2+1/2)} \right]^{1/d} \frac{1}{M_0} = \left(1 + \frac{1}{d}\right) h_{\max}^{1/d} \frac{\sqrt{\pi}}{2M_0} \tag{2.52}$$

where we made use of Eqs. (2.19) and (2.21). Eq. (2.51) thus becomes:

$$\dot{h}_U(t = \tau_L + \tau_H) - \dot{h}_H(t = \tau_L + \tau_H) = -\frac{P_{\max}\sqrt{\pi}}{2\tau_U M_0 \sqrt{A_c}} \tag{2.53}$$

Finally, using Equations (2.43) and (2.44), and noting that $S_U = dP/dh = P_{\max}/(\dot{h}_U \tau_U)$, the above equation is rewritten as:

$$\boxed{\frac{1}{S} = \frac{1}{S_U} + \frac{\dot{h}_H}{|\dot{P}|}} \tag{2.54}$$

where $S_U = dP/dh$ is the apparent (measured) contact stiffness (2.43), while S is the elastic contact stiffness (2.44), i.e., the contact stiffness one would measure if the unloading phase was unbiased w.r.t. time-dependent properties; $\dot{h}_H$ is the rate of penetration of the indenter at the end of the holding phase, and $\dot{P}$ the rate of unloading. Eq. (2.54) was first obtained by Feng and Ngan [75] for conical indentation and a specific rheological model. However, as our derivation shows, it holds for any axisymmetric indenter and any linear viscoelastic material; i.e., for any self-similar linear viscoelastic indentation problem.

Eq. (2.54) is of great importance to the extraction of the true elasticity content from the measured unloading slope of a viscoelastic material. It shows that the occurrence of viscosity during unloading leads to an underestimation of the elastic contact compliance $1/S \leq 1/S_U$. Consequently, if no bulge is present in the experimental $P - h$ curve, a direct application of the BASh formula with S_U would lead to overestimating the indentation modulus of the indented material. Equation (2.54) suggests two ways of minimizing the viscous effects on the measured contact stiffness:

- Increase of the unloading rate $|\dot{P}| = P_{\max}/\tau_U$, which is equivalent to a decrease of the duration τ_U of the unloading phase.

- Decrease of the indentation creep rate $\dot{h}_H$ at the end of the holding phase. Since the creep rate of any solid material decreases with time, decreasing $\dot{h}_H$ can be achieved by increasing the duration of the holding phase τ_H. Chudoba and Richter [51] provided

62

experimental evidence for this suggestion, recommending that the holding phase should be 'long enough such that the creep rate has decayed to a value where the depth increase in one minute is less than one percent of the indentation depth'. This recommendation is about the duration of the holding phase only, whereas Equation (2.54) clearly shows that the effect of the viscosity on the measured contact stiffness depends on the unloading rate and on the elastic properties of the indented material as well.

Hence, an appropriate correction of the unloading slope in view of the application of the BASh formula to extract the instantaneous indentation modulus M_0 from an indentation test on a linear viscoelastic material should read as:

$$\frac{1}{M_0} = \beta \left(\frac{1}{S_U} + \frac{\dot{h}_H}{|\dot{P}|} \right) \frac{2}{\sqrt{\pi}} \sqrt{A_c} \qquad (2.55)$$

where the correction factor $\beta = \beta(\nu, \theta)$ accounts for the deviations from the Galin-Sneddon solution due to large deformation and displacements (Section 2.3.1).

2.3.4 Cohesive-Frictional Linear Viscoelastic Material

We cannot conclude this discussion of the indentation modulus without considering a viscoelastic-plastic behavior, i.e., a combination of the behaviors discussed in Sections 2.3.1, 2.3.2 and 2.3.3. A typical indentation curve is displayed in Figure 2-2. A significant difference between the loading and unloading branches is observed, which is characteristic of a plastic behavior. In addition, at constant maximum load, an increase in depth versus time (here the load was held at its maximum for 5 s) is observed, which is characteristic of a time-dependent behavior. Such a combination of elastic, viscous and plastic behavior is expected to entail a loss of the self-similarity of the indentation test due to the varying values of the constituent coefficient κ for different stress levels ($\kappa = 1$ for linear viscoelasticity, $\kappa = 0$ for the strength limit; see Section 2.2.2). On the other hand, it can be argued that this difficulty is akin to the elasto-plastic indentation analysis discussed in Section 2.3.2 and that the viscoelastic solution (2.54) should therefore be applicable to cohesive–frictional linear viscoelastic materials as well. Feng and Ngan [75] showed experimentally that Eq. (2.54) remains valid for Berkovich indentation on a wide range of metals, i.e., cohesive materials, provided that the area of contact is correctly

estimated. It is reasonable to extend this reasoning to cohesive-frictional viscoelastic materials, for which it should be possible to determine the instantaneous indentation modulus M_0 from Eq. (2.55) by means of a holding phase that is 'long enough' and/or an unloading rate $|\dot{P}|$ that is 'fast enough', so that:

$$\frac{S\,\dot{h}_H}{|\dot{P}|} \approx \frac{S_U \dot{h}_H}{|\dot{P}|} \ll 1 \tag{2.56}$$

But how long the holding phase and how fast the unloading rate should be depends on the viscous properties of the indented material, which are a priori not known. In other words, in order to extract meaningful elastic properties from the unloading curve of an indentation test on a cohesive–frictional linear viscoelastic material, the indentation rate $\dot{h}_H$ at the end of the holding phase and the unloading rate $|\dot{P}|$ need to be specified.

2.4   Indentation Hardness

The indentation hardness H is the average pressure below the indenter:

$$\boxed{H \stackrel{def}{=} \frac{P}{A_c}} \tag{2.57}$$

where P is the load applied to the indenter, and A_c the projected area of contact between the indenter tip and the indented material (Figure 2-5). The concept of hardness can be found as early as in the 18th century in the work of Réaumur (1683–1757) and Mohs (1773–1839) as a means of material classification. The first example of engineering application of indentation methods using the material hardness appeared in the work of the Swedish engineer Brinell, published in a 1900 international congress in Paris [26]. Pushing a small ball of hardened steel or tungsten carbide against the surface of the specimen, Brinell empirically correlated the shape of the resulting permanent impression (indentation) with the strength of the metal alloys. The merits of Brinell's proposal were quickly appreciated by contemporaries: Meyer (1908), O'Neill (1944) and Tabor (1951) suggested empirical relations to transform indentation data into meaningful mechanical properties. For metals, Tabor suggested a rule-of-thumb relation between indentation hardness H and tensile strength σ_y [173]:

$$H/\sigma_y \simeq 3 \tag{2.58}$$

64

Based on this classical result, the indentation hardness is often interpreted as a snapshot of the strength or plastic properties of the indented material. But indentation hardness is not a material property and its physical meaning is still subject to debate [48]. The main issue with using indentation hardness or indentation analysis to back-calculate plastic or strength properties is the non-uniqueness of the solution of the reverse analysis. Indeed, for cohesive materials with work-hardening, very different material properties (yield strength-to-Young's modulus ratio and work-hardening exponent) can yield identical indentation hardness values, and even identical loading curves (Figure 2-17).

2.4.1 Dimensional Analysis

To motivate the forthcoming developments, consider the loading phase of an indentation test on a cohesive-frictional elasto-plastic material. Similar to the dimensional analysis performed in Section 2.3.2, we consider the two dependent variables in the contact problem [48] which define the hardness, namely indentation force P and projected area of contact A_c:

$$P = f_L(h, M_0, \nu, C, \mu, B) \tag{2.59a}$$

$$A_c = g(h, M_0, \nu, C, \mu, B) \tag{2.59b}$$

Application of the Π-theorem to (2.59) yields the dimensionless relations:

$$\frac{P}{Ch^2} = \Pi_P\left(\nu, \frac{C}{M_0}, \mu, \frac{B}{h^{1-d}}\right) \tag{2.60a}$$

$$\frac{A_c}{h^2} = \Pi_{A_c}\left(\nu, \frac{C}{M_0}, \mu, \frac{B}{h^{1-d}}\right) \tag{2.60b}$$

A substitution of (2.60) in (2.57) readily yields a new invariant, the hardness–to–solid cohesion ratio:

$$\frac{H}{C} = \frac{\Pi_P}{\Pi_{A_c}} = \Pi_H\left(\nu, \frac{C}{M_0}, \mu, \frac{B}{h^{1-d}}\right) \tag{2.61}$$

For conical indentation $(d = 1, B = \cot\theta)$ we verify that the hardness does not depend on the indentation depth h. In contrast, a comparison with the hardness scaling relation (2.10) for other self-similar indenter shapes $(d \neq 1)$ readily reveals that the dimensionless relation Π_H is
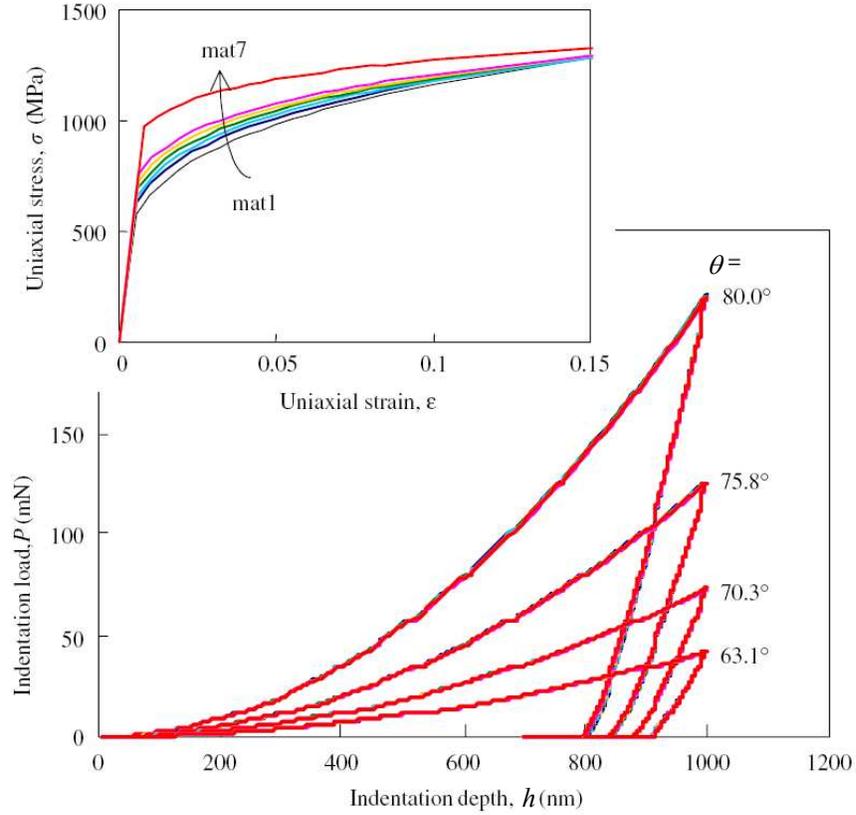
Figure 2-17: Set of materials with indistinguishable $P - h$ curves in conical indentation, even when the half-cone angle θ is varied (from [42]). The materials have distinct uniaxial stress-strain curves (see inset). The material properties (E(GPa), ν, σ_y(MPa), n) are (104.23, 0.499, 574.4, 0.2434), (113.4, 0.40, 627.6, 0.2173), (116.9, 0.35, 659.4, 0.2038), (120.0, 0.30, 691.8, 0.1913), (122.2, 0.25, 725.5, 0.1784), (123.9, 0.20, 762.8, 0.1653), and (127.5, 0.0, 947.2, 0.1047) respectively for mat1 to mat7. σ_y is the yield strength and n is the work-hardening exponent.

66

of the form:

$$\Pi_H \left(\nu, \frac{C}{M_0}, \mu, \frac{B}{h^{1-d}} \right) = \left(\frac{B}{h^{1-d}} \right)^{\kappa/d} \Pi_H^* \left(\nu, \frac{C}{M_0}, \mu \right) \tag{2.62}$$

In this general case, therefore, there is no unique link between material properties and hardness, as the constitutive behavior affects both the value of the constitutive coefficient κ and the arguments of the dimensionless function Π_H^*. Fortunately, for specific indenter geometries and constitutive behaviors a unique link between the indentation hardness H and the strength properties of the indented material can be established. The following Sections review some relevant cases which we will use in our experimental investigation. The presentation is restricted to conical indentation, which is representative as well for pyramidal indenter probes. In such a case, Eq. (2.62) becomes:

$$\boxed{\frac{H}{C} = \Pi_H \left(\nu, \frac{C}{M_0}, \mu, \theta \right)} \tag{2.63}$$

2.4.2   Rigid Cohesive-Frictional Material

This Section reviews the application of yield design solutions in hardness indentation analysis. Such solutions can be found early on in the indentation literature. From slip-line field solutions for indentation in a rigid cohesive plastic solid by a frictionless rigid wedge, Tabor [173] suggested a hardness (H) versus yield strength (σ_y) relationship of the form (2.58), $H/\sigma_y \simeq 3$. Lockett [116] and Chitkara and Butt [49] developed yield design solutions for conical indentations in cohesive rigid-plastic solids (without and with friction at the indenter-material interface). More recently, using the upper bound theorem of yield design, Ganneau et al. [78] [185] [77] developed a dual indentation approach which allows the determination of cohesion and friction of a Mohr-Coulomb solid from the dependence of the hardness-to-cohesion ratio on the cone angle:

$$\frac{H}{C} = \Pi_H' \left(\mu, \theta \right) \tag{2.64}$$

where $\mu = \tan \varphi$ is the Coulomb friction coefficient. More generally, the application of yield design solutions to indentation hardness analysis is based on the premise that the material half-space, in response to the application of the indentation load P, has exhausted its capacity to store externally supplied work into recoverable energy, which is equivalent to assuming a rigid plastic behavior. As a consequence, the hardness relates, by design, only to the strength

67

properties of the indented material. The remaining part of this Section reports recent developments of such a solution for a cohesive-frictional material whose strength behavior is governed by the Drucker-Prager strength model. It is inspired by the contributions of Cariou and Ulm [33], and Gathier and Ulm [80].

Bulk Frictional Behavior: Mohr-Coulomb, Drucker-Prager Criterion and Regularization

Two important strength criteria which model pressure-sensitive frictional behavior in stress space are the Mohr-Coulomb criterion and the Drucker-Prager criterion. The Mohr-Coulomb criterion is a surface traction criterion reading:

$$f\left(\underline{T} = \boldsymbol{\sigma} \cdot \underline{n}\right) = |T_t| + \mu\, T_n - C \leq 0 \tag{2.65}$$

where $T_t = \underline{t} \cdot (\boldsymbol{\sigma} \cdot \underline{n})$ is the tangential shear stress on the material surface oriented by unit outward normal $\underline{n}$, and $T_n = \underline{n} \cdot (\boldsymbol{\sigma} \cdot \underline{n})$ is the normal stress acting on this surface. The two parameters of the criterion are C, the Mohr-Coulomb cohesion, and $\mu = \tan\varphi$, the Mohr-Coulomb friction coefficient, where φ is defined as the Mohr-Coulomb friction angle. The Mohr-Coulomb criterion may also be expressed as a function of the principal stresses, $\sigma_I \geq \sigma_{II} \geq \sigma_{III}$:

$$f\left(\boldsymbol{\sigma}\right) = \sigma_I - \sigma_{III} + \left(\sigma_I + \sigma_{III}\right)\sin\varphi - 2C\cos\varphi \leq 0 \tag{2.66}$$

The Drucker-Prager criterion can be viewed as a Mohr-Coulomb criterion on the deviatoric stress plane defined by the orientation of the hydrostatic axis, i.e., $\underline{n} = \frac{1}{\sqrt{3}}\left(\underline{u}_I + \underline{u}_{II} + \underline{u}_{III}\right)$, with $\underline{u}_J$, the eigenvectors of the stress tensor, corresponding to principal stress directions. In contrast to the Mohr-Coulomb criterion, which depends only on the minimum and maximum principal stresses, the Drucker-Prager criterion involves all three principal stresses. The confining stress on the deviator stress plane is the mean stress, $\sigma_m = \frac{1}{3}I_1 = \frac{1}{3}\mathrm{tr}\left(\boldsymbol{\sigma}\right) = \frac{1}{3}\left(\sigma_I + \sigma_{II} + \sigma_{III}\right)$. The shear stress magnitude on the deviator plane is expressed by the second invariant of the stress deviator, $\mathbf{s} = \boldsymbol{\sigma} - \sigma_m\mathbf{1}$, defined as

$$J_2 = \frac{\sigma_d^2}{2} = \frac{\mathbf{s}:\mathbf{s}}{2} = \frac{\mathrm{tr}\left(\mathbf{s}\cdot\mathbf{s}\right)}{2} \tag{2.67}$$

68
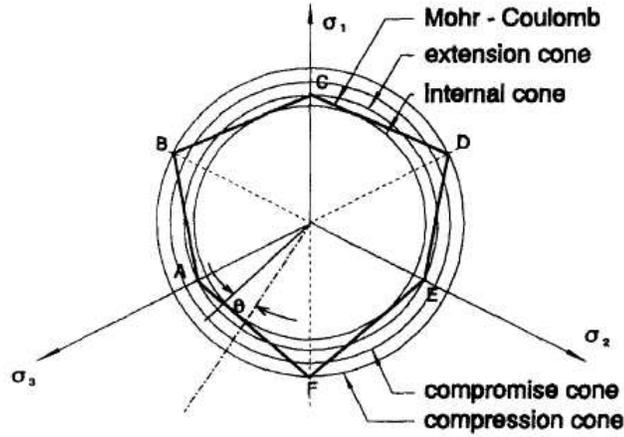
Figure 2-18: Correspondance between the Mohr-Coulomb and the Drucker-Prager criterion in the deviatoric stress plane (from [161]).

The Drucker-Prager criterion then reads as a function of these two stress invariants:

$$f\left(\boldsymbol{\sigma}\right) = \sqrt{J_2} + \alpha_s\,\sigma_m - c_s \leq 0 \tag{2.68}$$

where α_s is the Drucker-Prager friction coefficient, and c_s is the Drucker-Prager cohesion. It is important to note that there is a limit on the choice of the Drucker-Prager friction coefficient,

$$\alpha_s < \sqrt{\frac{3}{4}} \tag{2.69}$$

Indeed, it has been shown that this value corresponds to a friction angle of $\varphi = 90°$ for the corresponding Mohr-Coulomb criterion [67].

It is possible to link the Drucker-Prager friction coefficient α_s to the Mohr-Coulomb friction coefficient $\tan\varphi$ by considering the deviator plane representation of both criteria (Eqs. 2.66 and 2.68), as shown in Figure 2-18. Considering respectively the internal cone and the compression cone of the Drucker-Prager criterion [161] yields the following links between the material properties of the Drucker-Prager material (c_s, α_s) and of the Mohr-Coulomb criterion

69
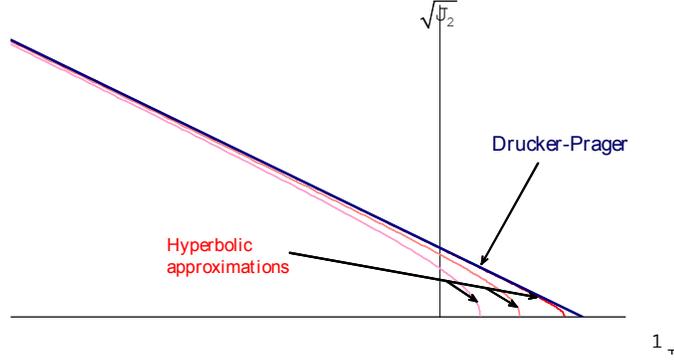
Figure 2-19: Approximation of a Drucker-Prager strength domain by a family of hyperbolic strength domains (from [80]).

$(C, \sin \varphi)$:

$$\text{Compression Cone} \qquad C = c_s \frac{3 - \sin \varphi}{2\sqrt{3} \cos \varphi} \qquad \sin \varphi = \frac{3\alpha_s}{\alpha_s + 2\sqrt{3}}$$

(2.70)

$$\text{Internal Cone} \qquad C = c_s \sqrt{\frac{3 + (\sin \varphi)^2}{3 (\cos \varphi)^2}} \qquad \sin \varphi = \sqrt{\frac{3\alpha_s^2}{3 - \alpha_s^2}}$$

Finally, from a practical point of view, the Drucker-Prager model involves only regular functions of the principal stresses, and it is usually easier to handle than the Mohr-Coulomb criterion. In fact, the Drucker-Prager strength criterion (2.68) can be regularized as the limit case of a hyperbolic criterion:

$$\boxed{f(\boldsymbol{\sigma}) = 1 - \left(\frac{\sigma_m - S_0}{A}\right)^2 + \left(\frac{\sigma_d}{\sqrt{2}B}\right)^2 \leq 0}$$

(2.71)

The Drucker-Prager criterion is obtained by letting (Fig. 2-19):

$$\begin{cases} B = \alpha_s A \\ S_0 = \dfrac{c_s}{\alpha_s} \\ A \to 0 \end{cases}$$

(2.72)

There exists a dual approach to define the strength of a material within the context of yield design theory. It is based on the premise that the material, at plastic collapse, has exhausted

its capacity to store the external work rate into recoverable elastic energy. As a consequence, it is entirely dissipated in the form of heat. This leads to introducing the support function $\pi(\mathbf{d})$ as the maximal possible value of the locally dissipated work rate or maximum dissipation capacity of the material:

$$\pi(\mathbf{d}) = \sup_{\boldsymbol{\sigma}^* \in G} \boldsymbol{\sigma}^* : \mathbf{d} \tag{2.73}$$

where G denotes the strength domain. It is then possible to show that if $\boldsymbol{\sigma}$ is the stress on the boundary of G maximizing the work rate (i.e., $\boldsymbol{\sigma} : \mathbf{d} = \pi(\mathbf{d})$), then $\boldsymbol{\sigma}$ and $\mathbf{d}$ are linked by:

$$\boldsymbol{\sigma} = \frac{\partial \pi}{\partial \mathbf{d}}(\mathbf{d}) \tag{2.74}$$

The π function is obtained from the following set of equations:

$$\mathbf{d} = \overset{\circ}{\lambda} \frac{\partial f}{\partial \boldsymbol{\sigma}}(\boldsymbol{\sigma}) \tag{2.75a}$$

$$f(\boldsymbol{\sigma}) = 0 \tag{2.75b}$$

$$\boldsymbol{\sigma} : \mathbf{d} = \pi(\mathbf{d}) \tag{2.75c}$$

The $6 + 1 + 1 = 8$ equations allow solving for the 8 unknowns: $\pi(\mathbf{d})$, $\overset{\circ}{\lambda}$ and $6 \times \sigma_{ij}$ at the boundary of the strength domain. In particular, in the case of the hyperbolic strength criterion (2.71), we make use of the fact that:

$$\frac{\partial f}{\partial \boldsymbol{\sigma}}(\boldsymbol{\sigma}) = \frac{1}{3}\frac{\partial f}{\partial \sigma_m}(\sigma_m, \sigma_d)\mathbf{1} + \frac{\partial f}{\partial \sigma_d}(\sigma_m, \sigma_d)\frac{\mathbf{s}}{\sigma_d} \tag{2.76}$$

Thus Eq. (2.75a) gives:

$$\begin{cases} \sigma_m - S_0 &= -\dfrac{A^2}{2\overset{\circ}{\lambda}}d_v \\[2mm] \mathbf{s} &= \dfrac{B^2}{\overset{\circ}{\lambda}}\boldsymbol{\delta} \end{cases} \tag{2.77}$$

While the value of $\overset{\circ}{\lambda}$ is given by Eq. (2.75b):

$$\left(\overset{\circ}{\lambda}\right)^2 = \left(\frac{Ad_v}{2}\right)^2 - \left(\frac{B}{\sqrt{2}}d_d\right)^2 \tag{2.78}$$

71

It follows:

$$\pi\left(\mathbf{d}\right) = \pi\left(d_v, d_d\right) = S_0 d_v - \sqrt{\left(A d_v\right)^2 - \left(\sqrt{2} B d_d\right)^2} \qquad (2.79)$$

with $d_v = \operatorname{tr}\mathbf{d} = I_1'$ and $d_d = \sqrt{\boldsymbol{\delta} : \boldsymbol{\delta}} = \sqrt{2 J_2'}$. Letting (2.72) in (2.79) yields $\pi\left(\mathbf{d}\right) = \left(c_s/\alpha_s\right)\, d_v$, which is the $\pi-$ function of a Drucker-Prager material [158]. We readily verify that $\pi\left(\mathbf{d}\right)$ is a homogeneous function of degree 1 (i.e., $\pi\left(\lambda\mathbf{d}\right) = \lambda\pi\left(\mathbf{d}\right)$) and that the stress $\boldsymbol{\sigma}$ on the boundary of the strength domain is:

$$\boldsymbol{\sigma} = \frac{\partial \pi}{\partial \mathbf{d}}\left(\lambda\mathbf{d}\right) = \frac{\partial \pi}{\partial \mathbf{d}}\left(\mathbf{d}\right) \qquad (2.80)$$

Equation (2.80) shows that the constitutive coefficient κ of the constitutive operator (2.3) that links stresses to strain rates in yield design, $\left(F\left(\lambda\mathbf{d}\right) = \lambda^\kappa F\left(\mathbf{d}\right)\right)$ is $\kappa = 0$.

Yield Design Approach

Yield design is based on the following two ideas [61] [158]:

1. Plastic collapse occurs once the material system can not further develop, in response to a prescribed loading, stress fields which are statically compatible with the external loading and plastically admissible with the strength of the material. The material system can not sustain any additional load by means of stresses in the structure which satisfy equilibrium and which do not exceed the local material strength.

2. Plastic collapse occurs when the work rate supplied from the outside can no longer be stored as recoverable (free) energy into the system. As a consequence, this work rate is entirely dissipated in the form of heat. During plastic collapse, the material locally dissipates the externally applied work at the highest possible rate. Any additional supplied work is dissipated through plastic yielding in the material bulk and/or (eventually) along narrow bands of surfaces of discontinuity.

In the case of an indentation test on a rigid plastic material, the external work rate $\delta\mathcal{W}$ provided to the system by the indenter is:

$$\delta\mathcal{W} = P\mathring{h} \qquad (2.81)$$

where P is the indentation load and $\mathring{h}$ the rate of penetration of the probe into the material. In the absence of surfaces of discontinuity, the principle of virtual work rate provides the link between the external work rate and the internal work rate realized by the stress field $\boldsymbol{\sigma}$ along the strain rate field $\mathbf{d}\,(\underline{u}^*)$ in the indented half-space Ω:

$$P\mathring{h} = \int_\Omega \boldsymbol{\sigma} : \mathbf{d}\,(\underline{u}^*)\ d\Omega \tag{2.82}$$

where the strain rate $\mathbf{d}\,(\underline{u}^*)$ is linked to the velocity field $\underline{u}^*$ by:

$$\mathbf{d}\,(\underline{u}^*) = \frac{1}{2}\left(\operatorname{grad}\underline{u}^* + {}^T\operatorname{grad}\underline{u}^*\right) \quad \forall \underline{x} \in \Omega \tag{2.83}$$

The determination of the indentation load P at plastic collapse requires solving, or at least estimating numerically, the fields $\boldsymbol{\sigma}$ and $\mathbf{d}$ at plastic collapse for a given penetration rate $\mathring{h}$, under the following constraints:

- At plastic collapse, the strain rate $\mathbf{d}\,(\underline{u}^*)$ follows an associated flow rule:

$$\mathbf{d}\,(\underline{u}^*) = \mathring{\lambda}\frac{\partial f\,(\boldsymbol{\sigma})}{\partial\boldsymbol{\sigma}} \quad \forall \underline{x} \in \Omega \tag{2.84}$$

  where $\mathring{\lambda}$ is a plastic multiplier which must satisfy:

$$\mathring{\lambda} \geq 0;\ f\,(\boldsymbol{\sigma}) \leq 0;\ \mathring{\lambda}f\,(\boldsymbol{\sigma}) = 0 \quad \forall \underline{x} \in \Omega \tag{2.85}$$

- The velocity field must be kinematically admissible. Considering a frictionless contact between the indenter probe and the indented material, the velocity field must satisfy the boundary conditions:

$$\underline{U}\,(\underline{x}) \cdot \underline{n} \quad = \quad -\mathring{h}\sin\,(\theta)\ \text{ inside the area of contact} \tag{2.86}$$

$$|\underline{U}\,(\underline{x})| \quad \to \quad 0 \quad \text{for } |\underline{x}| \to \infty \tag{2.87}$$

- The stress field $\boldsymbol{\sigma}\,(\underline{x})$ must satisfy the strength criterion defined by Eqs. (2.71) and (2.72) and simultaneously the weak form of the equilibrium condition $\operatorname{div}\boldsymbol{\sigma}\,(\underline{x}) = 0$ as expressed

by Eq. (2.82).

The contact condition (2.86) implies that the yield design solution $P\mathring{h}$ is proportional to $\mathring{h}$. In other words, $\mathring{h}$ is a dummy variable which we set equal to $\mathring{h} = 1$ so that (2.82) yields the sought expression that links the hardness (2.57) to the dissipation capacity of the material half-space:

$$\boxed{H = \frac{P}{A_c} = \frac{1}{A_c} \int_\Omega \boldsymbol{\sigma} : \mathbf{d} \left(\underline{u}^*\right) d\Omega; \ \mathring{h} = 1} \tag{2.88}$$

Estimating the stress and velocity fields solutions of the problem described above was achieved using the Limit Analysis Solver, developed by Borges [20] [148]. It is based on a finite element discretization of the model material domain. An axisymmetric mesh is loaded by a conical indenter with the equivalent half-cone angle of a Berkovich tip. The Limit Analysis Solver employs both stresses and velocities as degrees of freedom and requires that the stress fields satisfy equilibrium and the chosen strength criterion, and that the velocity fields be kinematically admissible and obey an associated flow rule. On this basis, the principle of limit analysis is to directly find a numerical estimate of the stress and velocity fields which obey these conditions of plasticity. The discrete simulation results were fitted with a continuous function of the form (2.64):

$$\frac{H}{c_s} = \Pi_H \left(\alpha_s, \theta = 70.32^\circ\right) = A(1 + B\alpha_s + (C\alpha_s)^3 + (D\alpha_s)^{10}) \tag{2.89}$$

which provided:

$$\begin{cases} A = 4.76438 \\ B = 2.5934 \\ C = 2.1860 \\ D = 1.6777 \end{cases} \tag{2.90}$$

For the specific case of a frictionless material $(\alpha_s = 0)$, for which the tensile strength σ_y is linked to the cohesion c_s by $\sigma_y = \sqrt{3}c_s$, Eq. (2.89) yields:

$$\frac{H}{\sigma_y} = \frac{1}{\sqrt{3}}\Pi_H \left(\alpha_s = 0, \theta = 70.32^\circ\right) \simeq 2.75 \tag{2.91}$$

This value is in very good agreement with Tabor's rule of thumb (2.58).

2.4.3 Cohesive–Frictional Elasto-Plastic and Viscoelastic-Plastic Material

The yield design solution is strictly speaking only valid if the strength–to–stiffness ratio is zero and if the loading rate is infinitely fast so that neither the elastic properties nor the viscous effects affect the hardness–strength property relation. From comprehensive finite element simulations of conical indentation ($\theta = 68°$) of frictionless (Von Mises) elasto-plastic solids, Cheng and Cheng [48] concluded that the hardness–to–strength ratio is not affected by the elastic properties provided that $\sigma_y/E < 10^{-2}$ (Fig. 2-20), in which case:

$$\frac{H}{\sigma_y} = \frac{1}{\sqrt{3}}\Pi_H \left(\alpha_s = 0, \frac{\sigma_y}{E} < 10^{-2}, \theta = 68°\right) \simeq 2.7 \tag{2.92}$$

which is in very good agreement with the yield design solution (2.91). For $\sigma_y/E > 10^{-2}$, the effect of the elasticity leads to a deviation from yield design solution in function of the stiffness–to–strength ratio and the Poisson's ratio (Fig. 2-20). Cheng and Cheng results can reasonably be extended to cohesive frictional materials by considering that yield design approaches are relevant provided that the cohesion –to– stiffness ratio c_s/M_0 is small enough. This is the case for most geomaterials, for which $c_s/G_0 \sim 10^{-3} - 10^{-6}$.

Viscous effects can also have an effect on the indentation hardness. This is readily understood by considering an indentation test on a visco-elasto-plastic material. During the holding phase, during which the indentation load is kept constant at its maximum value $P_{\max}$, the time-dependent behavior of the indented material calls for a time dependent indentation rate, which pushes the tip deeper into the indented material. As a consequence, the area of contact increases over time, and the hardness, according to its definition (2.57), decreases during the holding phase. Chudoba and Richter [51] did indeed report a time-dependent indentation hardness which decreases with increasing holding duration (Figure 2-21). Therefore, for the hardness to be representative of the plastic properties the indentation test should be as short as possible. On the other hand, if the holding phase is too short, the measurable contact stiffness S_U due to viscous effects is greater than the actual elastic contact stiffness S (Section 2.3.3, Eq. (2.54)), which leads to an overestimation of the projected area of contact from Eq. (2.42) and thus an underestimation of the indentation hardness. In other words, two opposing trends need to be taken into account in the accurate determination of the strength properties from hardness
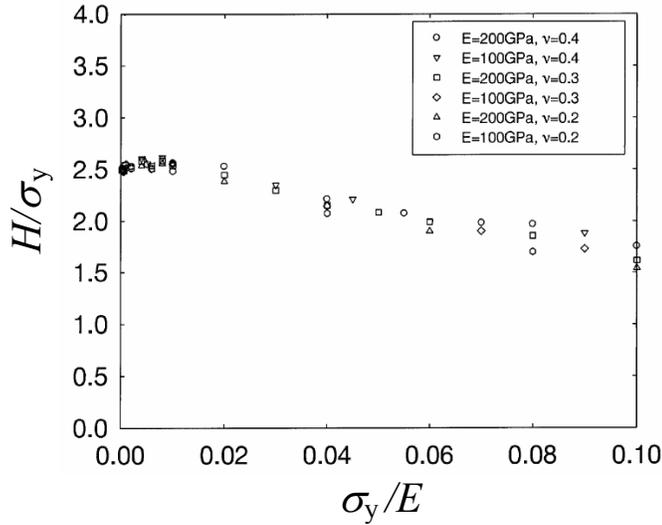
Figure 2-20: Relationship between H/σ_y and σ_y/E determined by finite element calculations of conical indentation ($\theta = 68^o$) on frictionless (Von Mises) elasto-plastic materials (adapted from [46]).

measurements on a cohesive–frictional viscoelastic material: The shorter the indentation test the more representative is the hardness of plastic properties only, while for the indentation hardness to be correctly measured, the projected area of contact must be accurately estimated, for which reason the holding phase should not be too short.

2.5 Chapter Summary

Indentation aims to provide, by contact testing, bulk mechanical properties. The review of current tools of continuum indentation analysis in this Chapter shows that the two indentation quantities, indentation modulus M and indentation hardness H, are linked respectively to elastic and strength properties as long as the projected area of contact at the onset of unloading is correctly estimated. This area of contact is usually estimated with the Oliver and Pharr method (Section 2.3.2). The BASh formula (2.13) enables the indentation modulus M to be linked to the elastic properties, while yield design approaches provide the link between the indentation hardness H and the strength properties of the indented material (Section 2.4).

A preliminary investigation of the effect of a time-dependent behavior on M and H shows
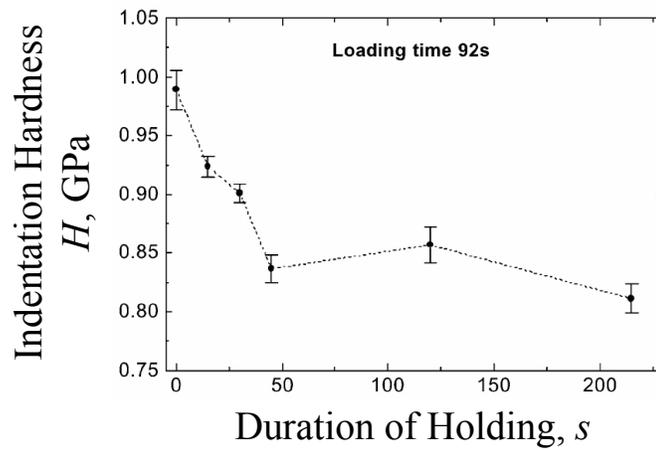
Figure 2-21: Effect of duration of holding on the measured hardness for an aluminum layer on a BK7 glass (from [51]).

that viscosity may have a non-negligible effect. In particular, the application of the Oliver and Pharr method to estimate the projected area of contact requires that viscous effects be negligible during unloading so that the measured indentation modulus M and indentation hardness H are indeed representative of the elastic and strength properties of the indented material. The focus of the next Chapter is precisely to develop the analytical tools that shall allow the extraction of these viscous properties of a solid from an indentation test.

Chapter 3

Assessment of Time-Dependent Properties by Indentation

This Chapter presents original developments of indentation analysis for homogeneous materials exhibiting a time-dependent behavior. Following the approach in Chapter 2, the focus will be first on linear viscoelastic materials (linear w.r.t. stresses) before investigating the effect of plastic deformation on the indentation response. By analogy with uniaxial relaxation and creep tests we consider both indentation relaxation and indentation creep tests, in which respectively the indentation depth h (Section 3.2) or the indentation load P is kept constant in time (Section 3.3). The overall goal of these original developments is to identify the viscous properties that can be assessed by indentation relaxation and indentation creep testing. These analytical developments will form the backbone of the identification of the fundamental viscous properties of cement-based materials presented later in this report.

3.1 Preliminaries on Viscoelastic Indentation Analysis

A first encounter of viscoelastic indentation analysis based on the method of functional equations was presented in Section 2.3.3. As a reminder, the method of functional equations for indentation analysis remains valid as long as the indentation depth (and thus the area of contact) does not decrease. The principle of solving linear viscoelastic indentation problems by means of the s-multiplied Laplace transform method consists in eliminating the explicit time

dependence of the viscoelastic problem by replacing all time dependent moduli by their Laplace transform multiplied by the Laplace parameter s. The corresponding elasticity problem is then solved in the Laplace domain. The solution, obtained in the Laplace domain, is then translated back into the time domain. The method of functional equations has been used by several researchers to solve the viscoelastic indentation problem for specific rheological models and indenter probe geometries, e.g., for flat punch indentation [44], for spherical indentation [43] [140], or for conical indentation [65] [191].

3.1.1 Continuum Material Scale

On a material scale of the continuum, we assume a linear viscoelastic behavior of the indented material defined by the bulk relaxation modulus $K(t)$ and the shear relaxation modulus $G(t)$. For such a linear material, the volume and deviator stress histories, $\boldsymbol{\sigma}_v(t) = \frac{1}{3}(\operatorname{tr}\boldsymbol{\sigma})\mathbf{1}$ and $\boldsymbol{\sigma}_d(t) = \boldsymbol{\sigma} - \boldsymbol{\sigma}_v(t)$ relate to the volume and deviator strain histories $\boldsymbol{\varepsilon}_v = (\operatorname{tr}\boldsymbol{\varepsilon})\mathbf{1}$ and $\boldsymbol{\varepsilon}_d = \boldsymbol{\varepsilon} - \frac{1}{3}\boldsymbol{\varepsilon}_v$ by the stress convolution integrals [157]:

$$\boldsymbol{\sigma}_v(t) = \int_0^t K(t-\tau)\frac{d}{d\tau}\boldsymbol{\varepsilon}_v(\tau)\,d\tau \tag{3.1a}$$

$$\boldsymbol{\sigma}_d(t) = \int_0^t 2G(t-\tau)\frac{d}{d\tau}\boldsymbol{\varepsilon}_d(\tau)\,d\tau \tag{3.1b}$$

The Laplace transformations of the stress convolution integrals of linear isotropic viscoelasticity read [50]:

$$\widehat{\boldsymbol{\sigma}_v(s)} = s\,\widehat{K(s)}\,\widehat{\boldsymbol{\varepsilon}_v(s)} \tag{3.2a}$$

$$\widehat{\boldsymbol{\sigma}_d(s)} = s\,2\widehat{G(s)}\,\widehat{\boldsymbol{\varepsilon}_d(s)} \tag{3.2b}$$

where $\widehat{f(s)}$ is the Laplace transform of $f(t)$, and s the Laplace parameter. Hence, $\widehat{\boldsymbol{\sigma}_v(s)}$, $\widehat{\boldsymbol{\sigma}_d(s)}$, $\widehat{\boldsymbol{\varepsilon}_v(s)}$ and $\widehat{\boldsymbol{\varepsilon}_d(s)}$ denote the Laplace transforms of $\boldsymbol{\sigma}_v(t)$, $\boldsymbol{\sigma}_v(t)$, $\boldsymbol{\varepsilon}_v(t)$ and $\boldsymbol{\varepsilon}_d(t)$, whereas $\widehat{K(s)}$ and $\widehat{G(s)}$ represent the Laplace transforms of the bulk relaxation modulus $K(t)$ and the shear relaxation modulus $G(t)$.

The compliance counterparts of $K(t)$ and $G(t)$ are the bulk creep compliance $J^v(t)$ and the shear creep compliance $J^d(t)$, which appear in the strain convolution integrals [157]:

$$\varepsilon_v(t) = \int_0^t J^v(t-\tau)\frac{d}{d\tau}\boldsymbol{\sigma}_v(\tau)\,d\tau \tag{3.3a}$$

$$\varepsilon_d(t) = \int_0^t \frac{J^d(t-\tau)}{2}\frac{d}{d\tau}\boldsymbol{\sigma}_d(\tau)\,d\tau \tag{3.3b}$$

The Laplace transforms of the strain convolution integrals read:

$$\widehat{\varepsilon_v(s)} = s\,\widehat{J^v(s)}\,\widehat{\boldsymbol{\sigma}_v(s)} \tag{3.4a}$$

$$\widehat{\varepsilon_d(s)} = s\,\frac{\widehat{J^d(s)}}{2}\,\widehat{\boldsymbol{\sigma}_d(s)} \tag{3.4b}$$

From a comparison of (3.2) and (3.4), it is readily found that $J^v(t)$ and $J^d(t)$ are linked to $K(t)$ and $G(t)$ in the Laplace domain [157]:

$$\left(s\widehat{J^v(s)}\right)^{-1} = s\widehat{K(s)} \tag{3.5a}$$

$$\left(s\widehat{J^d(s)}\right)^{-1} = s\widehat{G(s)} \tag{3.5b}$$

A similar relation for indentation relaxation and indentation creep testing is still missing, and it is one focus of this Chapter to derive such relations for viscoelastic indentation testing carried out either under constant indentation depth conditions (indentation relaxation), or under constant indentation force conditions (indentation creep).

3.1.2 Indentation Scale

Analogously to (3.1) and (3.2), the application of the correspondence principle of viscoelasticity to the elastic indentation force relation (2.19) yields:

$$P(t) = \phi \int_0^t M(t-\tau)\frac{d}{d\tau}h^{1+1/d}(\tau)\;d\tau \tag{3.6}$$

$$\Downarrow$$

$$\widehat{P(s)} = \phi\,s\,\widehat{M(s)}\;\widehat{h^{1+1/d}}(s) \tag{3.7}$$

where ϕ (of dimension $[\phi] = L^{1-1/d}$) condenses the indenter specific geometry parameters of the elastic solution (2.19):

$$\phi = \frac{2}{(\sqrt{\pi}B)^{1/d}} \frac{d}{d+1} \left[\frac{\Gamma(d/2+1/2)}{\Gamma(d/2+1)} \right]^{1/d} \tag{3.8}$$

where $d \geq 0$ is the degree of the homogeneous function describing the probe geometry, and B the shape function of the indenter at unit radius (see Tab. 2.1). In turn, the indentation modulus M in viscoelastic indentation is time-dependent. Application of the correspondence principle to the elastic indentation modulus $M_0 \rightarrow M(t)$ defined by (2.20) yields:

$$\boxed{M(t) \rightarrow s\,\widehat{M(s)} = 4s\,\widehat{G(s)}\frac{3s\widehat{K(s)} + s\widehat{G(s)}}{3s\widehat{K(s)} + 4s\widehat{G(s)}}} \tag{3.9}$$

where $\widehat{K(s)}$ and $\widehat{G(s)}$ represent the Laplace transforms of the bulk relaxation modulus $K(t)$ and the shear relaxation modulus $G(t)$ of the indented material, as defined by (3.2). The indentation modulus $M(t) \rightarrow s\,\widehat{M(s)}$ carries all the material scale viscoelastic constitutive information, while $P(t) \rightarrow \widehat{P(s)}$ and $\widehat{h^{1+1/d}}(s)$ specify the time-dependent load conditions. The next two Sections will deal separately with indention relaxation and indentation creep testing.

3.2   Indentation Relaxation Test

3.2.1   Contact Relaxation Modulus

Consider first an indentation relaxation test defined by Heaviside displacement loading:

$$h(t) = h_{\max}\mathcal{H}(t) \tag{3.10}$$

where $h_{\max}$ is the maximum indentation depth, and $\mathcal{H}(t)$ is the Heaviside function. What is measured in such a test is the relaxation of the indentation load $P(t)$. An inspection of the elastic solution (2.19) and viscoelastic solution (3.6) suggests looking for a force relaxation solution $P(t)$ of the form:

Indenter shape	d	B	$m(t)$
Cone (Berkovich)	1	$\cot(\theta)$	$\dfrac{\pi\cot(\theta)}{2h_{max}^2}P(t)$
Sphere	2	$1/(2R)$	$\dfrac{3}{4\sqrt{R}h_{max}^{3/2}}P(t)$
Flat punch	$\to\infty$	$1/(a^n)$	$\dfrac{P(t)}{2ah_{max}}$

Table 3.1: Expression of $m(t)$ for several indenter shapes.

$$m(t) \stackrel{def}{=} \frac{1}{\phi h_{\max}^{1+1/d}}P(t) \tag{3.11}$$

where the modulus $m(t)$ —by design— provides a means to assess the force relaxation $P(t)$. Expressions of $m(t)$ for several indenter shapes are developed in Table 3.1.

Consider then the Laplace transform of (3.11):

$$\widehat{m(s)} = \frac{1}{\phi h_{\max}^{1+1/d}}\widehat{P(s)} \tag{3.12}$$

A combination of Eqs. (3.7), (3.12) and (3.9), while noting that the Laplace transform of $h(t)^\alpha = h_{\max}^\alpha \mathcal{H}(t)$ is $\widehat{h^\alpha(s)} = h_{\max}^\alpha/s$, yields:

$$\widehat{m(s)} = s\,\widehat{M(s)}\frac{\widehat{h^{1+1/d}(s)}}{h_{\max}^{1+1/d}} \stackrel{\mathcal{H}(t)}{=} \widehat{M(s)} \tag{3.13}$$

and after back translation into the time domain:

$$m(t) \stackrel{\mathcal{H}(t)}{=} M(t) \tag{3.14}$$

The modulus $m(t)$ corresponds to the time–dependent indentation modulus $M(t)$ that would be measured in an indentation relaxation test of a linear viscoelastic material subjected to a Heaviside displacement load history. By analogy with the uniaxial relaxation moduli, it is thus appropriate to refer to $M(t)$ as the *contact relaxation modulus*. In such a test, $M(t=0) = M_0$ corresponds to the instantaneous elastic indentation modulus, so that the normalized indenta-

tion force relaxation history can be measured from:

$$\frac{M(t)}{M_0} \overset{\mathcal{H}(t)}{=} \frac{P(t)}{P_0} \tag{3.15}$$

where $P_0 = P_{\max}$.

Consider then a displacement load history:

$$h(t) = h_{\max}\mathcal{F}(t) \tag{3.16}$$

where $\mathcal{F}(t) = h(t)/h_{\max}$ is the normalized displacement load history satisfying $\frac{d}{dt}\mathcal{F}(t) \geq 0$ (see Section 2.3.3). Noting for this case that $\widehat{h^{1+1/d}}(s) = h_{\max}^{1+1/d} \ \widehat{\mathcal{F}^{1+1/d}}(s)$, the Laplace expression (3.13) of the contact relaxation modulus becomes:

$$\widehat{m(s)} = s \ \widehat{M(s)}\frac{\widehat{h^{1+1/d}}(s)}{h_{max}^{1+1/d}} \overset{\mathcal{F}(t)}{=} s \ \widehat{M(s)} \ \widehat{\mathcal{F}^{1+1/d}}(s) \tag{3.17}$$

Recalling that a multiplication by s in the Laplace domain corresponds to a differentiation in the time domain, and that a multiplication in the Laplace domain corresponds to a convolution product in the time domain [157], Eq. (3.17) can be back-transformed into the time domain:

$$m(t) = \frac{P(t)}{\phi h_{\max}^{1+1/d}} = \int_0^t M(t-\tau)\frac{d}{d\tau}\left(\mathcal{F}(t)^{1+1/d}\right) d\tau \tag{3.18}$$

The above developments show that the viscoelastic force relaxation solution $P(t)$ can easily be found from the applied displacement $h(t)$ if the contact relaxation modulus $M(t)$ is known.

3.2.2 Illustration for Some Classical Linear Viscoelastic Behaviors

Equations (3.11) and (3.14) link time-dependent indentation data to the viscoelastic properties of the indented material. The contact relaxation modulus so defined is independent of the indenter shape, and $M(t)$ thus provides a snapshot of the linear viscoelastic behavior of the solid. By way of illustration, we derive in this Section the expressions of the contact relaxation modulus $M(t)$ for some classical 'textbook-type' viscoelastic materials [119], namely the three-parameter Maxwell Model, the four-parameter Kelvin-Voigt model, and the five-parameter
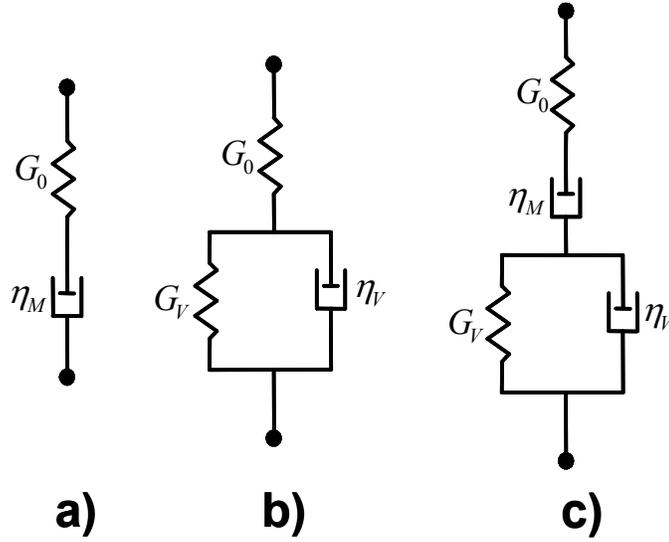
Figure 3-1: Three deviatoric creep models. (a) The three-parameter Maxwell model. (b) The four-parameter Kelvin-Voigt model. (c) The five-parameter Maxwell-Kelvin-Voigt model.

Maxwell-Kelvin-Voigt model (Fig. 3-1$(a - c)$). For purposes of illustration, only deviatoric creep is considered, meaning that the volumetric part is time-independent, $K(t) = K_0$. In the Laplace domain, this translates into:

$$\widehat{K(s)} = \frac{K_0}{s} \tag{3.19}$$

Three-parameter Maxwell Model

The three-parameter Maxwell deviatoric creep model (Figure 3-1a) is obtained by introducing a Maxwell unit of viscosity η_M into the shear behavior. The expression of the viscous evolution law in the time domain reads:

$$2\dot{\boldsymbol{\varepsilon}}^d(t) = \frac{\dot{\boldsymbol{\sigma}}^d(t)}{G_0} + \frac{\boldsymbol{\sigma}^d(t)}{\eta_M} \tag{3.20}$$

which, in the Laplace domain, yields:

$$2\widehat{\boldsymbol{\varepsilon}^d(s)} = \frac{\widehat{\boldsymbol{\sigma}^d(s)}}{G_0} + \frac{\widehat{\boldsymbol{\sigma}^d(s)}}{s\eta_M} \tag{3.21}$$

Applying a Laplace transform to the constitutive equation of linear viscoelasticity (3.1b) gives:

$$\widehat{\boldsymbol{\sigma}^d(s)} = s2\widehat{G(s)}\widehat{\boldsymbol{\varepsilon}^d(s)} \tag{3.22}$$

A combination of the two equations above enables an expression for the shear relaxation modulus $\widehat{G(s)}$ of the three-parameter Maxwell model to be obtained in the Laplace domain:

$$\widehat{G(s)} = \left(\frac{s}{G_0} + \frac{1}{\eta_M} \right)^{-1} \tag{3.23}$$

Finally, a combination of Equations (3.19) and (3.18) yields an expression of the contact relaxation modulus in the Laplace domain:

$$\widehat{M(s)} = \eta_M G_0 \left(\frac{1}{s\eta_M + G_0} + \frac{9K_0}{3K_0 G_0 + s\eta_M(3K_0 + 4G_0))} \right) \tag{3.24}$$

which, with the use of standard Laplace tables (e.g., [134]), can be translated back into the time-domain:

$$M(t) = M_0 - \frac{E_0}{2(1+\nu_0)} \left(1 - e^{\left(-\frac{E_0}{2(1+\nu_0)\eta_M} t \right)} \right) - \frac{E_0}{2(1-\nu_0)} \left(1 - e^{\left(-\frac{E_0}{6(1-\nu_0)\eta_M} t \right)} \right) \tag{3.25}$$

Four-parameter Kelvin-Voigt Model

The four-parameter Kelvin-Voigt deviatoric creep model (Figure 3-1b) is obtained by introducing into the shear behavior a Kelvin-Voigt unit, i.e., a spring of stiffness G_V in parallel with a dashpot of viscosity η_V. This model can be defined as well by its delayed shear stiffness $G_\infty = (1/G_0 + 1/G_V)^{-1}$. The viscous evolution law reads:

$$G_0 G_V 2\boldsymbol{\varepsilon}^d(t) + G_0 \eta_V 2\dot{\boldsymbol{\varepsilon}}^d(t) = (G_0 + G_V)\boldsymbol{\sigma}^d(t) + \eta_V \dot{\boldsymbol{\sigma}}^d(t) \tag{3.26}$$

whence the shear relaxation modulus $\widehat{G(s)}$ in the Laplace domain:

$$\widehat{G(s)} = \left(\frac{s}{G_0} + \frac{s}{G_V + s\eta_V} \right)^{-1} \tag{3.27}$$

A combination of Equations (3.19) and (3.27) yields an expression of the contact relaxation modulus $\widehat{M(s)}$ in the Laplace domain which can be translated back into the time-domain. The result of this calculation is given in Table 3.2.

Five-parameter Maxwell-Kelvin-Voigt Model

A combination in series of the Kelvin-Voigt unit with the Maxwell unit (Figure 3-1c) yields a 5-parameter deviatoric creep model for which the viscous deformation is given by:

$$G_0\eta_V\eta_M\,2\ddot{\boldsymbol{\varepsilon}}^d\,(t)+G_0G_V\eta_M\,2\dot{\boldsymbol{\varepsilon}}^d\,(t) = \eta_M\eta_V\,\ddot{\boldsymbol{\sigma}}^d\,(t)+(G_0\eta_V+G_0\eta_M+G_V\eta_M)\,\dot{\boldsymbol{\sigma}}^d\,(t)+G_0G_V\,\boldsymbol{\sigma}^d\,(t) \tag{3.28}$$

whence the shear relaxation modulus $\widehat{G(s)}$ in the Laplace domain:

$$\widehat{G(s)} = \left(\frac{1}{G_0} + \frac{1}{s\eta_M} + \frac{1}{G_V + s\eta_V}\right)^{-1} \tag{3.29}$$

A combination of Equations (3.19) and (3.29) yields an expression of the contact relaxation modulus $\widehat{M(s)}$ in the Laplace domain which can be translated back into the time-domain. The result of this calculation is given in Table 3.2.

3.2.3   Effect of Plasticity on Contact Relaxation Modulus

The indented material is now assumed to be not only linear viscoelastic, but also plastic. Plastic deformations cannot be avoided below a sharp punch (e.g., below a Berkovich tip) and often also occur below spherical and flat punches. Plastic deformations result in a decrease in load at a given depth. As a consequence, Equation (3.11) underestimates the contact relaxation modulus. In other words, when plastic phenomena occur, Equation (3.11) gives time-dependent properties which are not material properties since they depend on the uncontrolled amount of plasticity exhibited during the test and therefore on both the load case and the indenter geometry [182]. To overcome this limitation, Zhang and Zhang [201] proposed a procedure based on an effective flat punch indenter.

Here we show, for a Heaviside displacement, that the plasticity that occurs during an instantaneous displacement loading can be separated from the time-dependent creep deformation

Rheological model for deviatoric creep behavior	Contact relaxation modulus $M(t)$
Maxwell	$M_0 - \dfrac{E_0}{2(1+\nu_0)}\left(1 - e^{\left(-\frac{E_0}{2(1+\nu_0)\eta_M}t\right)}\right) - ...$ $... - \dfrac{E_0}{2(1-\nu_0)}\left(1 - e^{\left(-\frac{E_0}{6(1-\nu_0)\eta_M}t\right)}\right)$
Kelvin-Voigt	$M_0 - \dfrac{E_0^2}{2(1+\nu_0)(E_0 + 2G_V(1+\nu_0))}\left(1 - e^{-\frac{t}{T_4}}\right) - ...$ $... - \dfrac{E_0^2}{2(1-\nu_0)(E_0 + 6G_V(1-\nu_0))}\left(1 - e^{-\frac{t}{T_5}}\right)$
Combined Maxwell-Kelvin-Voigt	$\dfrac{E_0}{2(1+\nu_0)}\dfrac{1}{\frac{1}{T_8} - \frac{1}{T_9}}\left(\begin{array}{c}\left(\frac{1}{T_2} - \frac{1}{T_9}\right)e^{-\frac{t}{T_9}} + \\ \left(\frac{1}{T_8} - \frac{1}{T_2}\right)e^{-\frac{t}{T_8}}\end{array}\right) + ...$ $... + \dfrac{E_0}{2(1-\nu_0)}\dfrac{1}{\frac{1}{T_6} - \frac{1}{T_7}}\left(\begin{array}{c}\left(\frac{1}{T_2} - \frac{1}{T_7}\right)e^{-\frac{t}{T_7}} + \\ \left(\frac{1}{T_6} - \frac{1}{T_2}\right)e^{-\frac{t}{T_6}}\end{array}\right)$

Table 3.2: Analytical expressions of the contact relaxation modulus $M(t)$ for the three deviatoric creep models described in Figure 3-1.

$T_2 = \eta_V/G_V$;

$T_4 = 2\eta_V(1+\nu_0)/(E_0 + 2G_V(1+\nu_0))$;

$T_5 = 6\eta_V(1-\nu_0)/(E_0 + 6G_V(1-\nu_0))$;

$T_6 = 12(1-\nu_0)\eta_M\eta_V/(E_0(\eta_M + \eta_V) + 6\eta_M G_V(1-\nu_0) + (E_0^2(\eta_V + \eta_M)^2 + 36\eta_M^2 G_V^2(1-\nu_0)^2 + 12\eta_M G_V E_0(\eta_M - \eta_V)(1-\nu_0))^{1/2})$;

$T_7 = 12(1-\nu_0)\eta_M\eta_V/(E_0(\eta_M + \eta_V) + 6\eta_M G_V(1-\nu_0) - (E_0^2(\eta_V + \eta_M)^2 + 36\eta_M^2 G_V^2(1-\nu_0)^2 + 12\eta_M G_V E_0(\eta_M - \eta_V)(1-\nu_0))^{1/2})$

during the relaxation phase such that the measured force relaxation response $P(t)$ can be directly linked to the contact relaxation function $M(t)$ by Eq. (3.15):

$$\boxed{M(t) = M_0\frac{P(t)}{P(0^+)} = M_0\frac{P(t)}{P_{\text{max}}}} \qquad (3.30)$$

where $M_0 = M(t = 0)$ is the instantaneous indentation modulus of the tested material and $P(0^+) = P_{\text{max}}$ is the maximum force recorded in the relaxation test, immediately after application of the Heaviside displacement. The proof presented next is valid for any type of time-independent plasticity and any axisymmetric indenter.

Analytical Proof

Let $\boldsymbol{\sigma}_0$, $\boldsymbol{\varepsilon}_0$, $\boldsymbol{\varepsilon}_0^p$ and $\underline{\xi}_0$ be the stress, total strain, plastic strain and displacement solution fields generated instantaneously by the Heaviside step indentation displacement (applied at $t = 0^+$). The half-space behaves elasto-plastically during the infinitely fast loading. We tentatively assume that no further plastic deformation occurs during the relaxation phase $t > 0^+$, so that the half-space behaves viscoelastically after loading. This assumption will be verified later on. Dividing the stress and strain tensors into their deviatoric (superscript d) and spherical parts (superscript v), the viscoelastic behavior of the solid during the relaxation phase is governed by the hereditary integral functions:

$$\begin{aligned}\boldsymbol{\sigma}^d(t) &= 2\int_{0^+}^t G(t-\tau)\frac{d}{d\tau}(\boldsymbol{\varepsilon}^d(\tau) - (\boldsymbol{\varepsilon}_0^p)^d)dt \\ \boldsymbol{\sigma}^v(t) &= \int_{0^+}^t K(t-\tau)\frac{d}{d\tau}(\boldsymbol{\varepsilon}^v(\tau) - (\boldsymbol{\varepsilon}_0^p)^v)dt\end{aligned} \qquad (3.31)$$

We restrict ourselves to a plastic linear viscoelastic half-space characterized by a time-invariant Poisson's ratio, as frequently admitted in viscoelastic indentation analysis [103] [141], which implies:

$$\nu(t) = \nu \Rightarrow K(t) \propto G(t) \qquad (3.32)$$

The stresses, strains and displacements need to satisfy at all times the following field equations:

$$\boldsymbol{\varepsilon}(t) = (1/2)\left[\boldsymbol{\nabla}\underline{\xi}(t) +^t\left(\boldsymbol{\nabla}\underline{\xi}(t)\right)\right]$$
$$\underline{\mathrm{div}}\left(\boldsymbol{\sigma}(t)\right) = \underline{0} \tag{3.33}$$

and the following boundary and frictionless contact conditions:

$$\text{Out of the area of contact } A_c: \qquad \boldsymbol{\sigma}(t) \cdot \underline{e}_z = \underline{0}$$
$$\text{Within the area of contact } A_c: \quad \begin{cases} (\boldsymbol{\sigma}(t) \cdot \underline{n}) \cdot \underline{t} = \underline{0} \\ \underline{\xi}(t) \cdot \underline{n} = -h_{max} + Br^n \end{cases} \tag{3.34}$$

where $(\underline{n}, \underline{t})$ stand for the outward unit normal and tangential vectors of the half-space. At $t = 0^+$, the solution fields $\boldsymbol{\sigma}_0$, $\boldsymbol{\varepsilon}_0$ and $\underline{\xi}_0$ satisfy the field equations (3.33) and the boundary conditions (3.34), while the constitutive relations (3.31) read:

$$\boldsymbol{\sigma}_0^d = 2G_0(\boldsymbol{\varepsilon}_0^d - (\boldsymbol{\varepsilon}_0^p)^d) \tag{3.35}$$
$$\boldsymbol{\sigma}_0^v = K_0(\boldsymbol{\varepsilon}_0^v - (\boldsymbol{\varepsilon}_0^p)^v) \tag{3.36}$$

where $G_0 = G(0)$ and $K_0 = K(0)$ are respectively the elastic shear and bulk moduli of the indented half-space.

During the relaxation phase $(t > 0^+)$, for which the applied displacement is constant, the area of contact between the indenter and the half-space is also assumed constant. Using Equation (3.32), the following displacement, stress and strain fields are readily found to satisfy the set of governing equations (3.31), (3.33) and (3.34):

$$\underline{\xi}(t) = \underline{\xi}_0$$
$$\boldsymbol{\varepsilon}(t) = \boldsymbol{\varepsilon}_0 \text{ and } \boldsymbol{\varepsilon}^p(t) = \boldsymbol{\varepsilon}_0^p$$
$$\boldsymbol{\sigma}^d(t) = [G(t)/G(0)]\,\boldsymbol{\sigma}_0^d = 2G(t)(\boldsymbol{\varepsilon}_0^d - (\boldsymbol{\varepsilon}_0^p)^d) \tag{3.37}$$
$$\boldsymbol{\sigma}^v(t) = [K(t)/K(0)]\,\boldsymbol{\sigma}_0^v = K(t)(\boldsymbol{\varepsilon}_0^v - (\boldsymbol{\varepsilon}_0^p)^v)$$

Moreover, since $G(t)$ and $K(t)$ are decreasing functions, the maximum stresses are reached at $t = 0^+$, which justifies a posteriori the assumption that no plasticity occurs after loading. Therefore the fields (3.37) are the solution of the relaxation indentation test in a plastic linear viscoelastic solid with time-invariant Poisson's ratio, and the assumption of a time-invariant

89

area of contact between the indenter and the half-space over the relaxation phase is justified.

On this basis, the force relaxation history $P(t)$ for the plastic linear viscoelastic half-space is derived:

$$P(t) = \int_{A_c} (\boldsymbol{\sigma}(\underline{t}) \cdot \underline{n}) \cdot \underline{e}_z dA = \int_{A_c} \frac{G(t)}{G(0)} (\boldsymbol{\sigma}_0 \cdot \underline{n}) \cdot \underline{e}_z dA = \frac{G(t)}{G(0)} P(0^+) = \frac{G(t)}{G(0)} P_{max} \qquad (3.38)$$

where $P(0^+)$ is the maximum indentation force recorded immediately after the Heaviside displacement loading. The viscoelastic relaxation solution in the Laplace domain and then in the time domain, for a time-invariant Poisson's ratio, is:

$$\widehat{M(s)} = M_0 \frac{\widehat{G(s)}}{\widehat{G(0)}} \Rightarrow M(t) = M_0 \frac{G(t)}{G(0)} \qquad (3.39)$$

Finally, a combination of (3.38) and (3.39) yields the sought-after relation (3.30) which links the indentation relaxation function $M(t)$ to the load history $P(t)$.

Strictly speaking, the analytical proof holds for a time-invariant Poisson's ratio (3.32). This condition is not fulfilled with the often considered deviatoric creep cases, for which the Poisson's ratio $\nu(t)$ is time-dependent since:

$$\widehat{K(s)} = K_0 \Rightarrow \widehat{\nu(s)} = \frac{3K_0 - 2\widehat{G(s)}}{6K_0 + 2\widehat{G(s)}} \Rightarrow \nu(t) \neq cst \qquad (3.40)$$

Nevertheless, for an incompressible material with deviatoric creep, the Poisson's ratio $\nu(t) = 0.5$ is indeed time-invariant, and Equation (3.30) holds.

Numerical Validation

To confirm the validity of Equation (3.30), numerical simulations of conical indentation relaxation tests on a linear viscoelasto–plastic finite element model are performed.

The numerical simulations are carried out with ABAQUS (Dassault Systemes, Nanterre, France) in large displacements. An axisymmetric mesh refined in several steps around the indenter probe is used. The included half-cone angle is $\theta = 70.32°$, which is the equivalent cone angle of the three-sided pyramidal Berkovich indenter (Section 2.2.1). The displacement of the indenter probe is imposed, and the load applied to the indenter $P(t)$ is output from the

numerical simulation. To minimize distortions due to the finite size of the meshed domain, the simulations are performed with free and fixed boundary conditions at the mesh ends to evaluate the influence of boundary effects on the simulation. For all simulations, a change in boundary conditions induces a change in load $P(t)$ less than 0.5%. To simulate an instantaneous loading, viscous properties are dismissed during the loading phase. As a result, the displacement history applied to the indenter corresponds to a Heaviside function.

The viscous behavior of the indented material is modeled by a deviatoric Maxwell creep model, characterized by its viscosity η_M (Figure 3-1a). Two instantaneous Poisson's ratios are used in the simulations: $\nu_0 = 0.499$ to model an incompressible material and $\nu_0 = 0.25$ to model a compressible material. The incompressible plastic flow is modeled with an associated Von Mises plasticity model. The yield strength-to-Young's modulus ratio is $\sigma_y/E_0 = 10^{-3}$, which is a lower bound value for most materials [5].

The indentation modulus $M_0 = E_0/(1-\nu_0^2)$ and the maximum displacement h_{max} are input in the numerical simulation. The resulting load history $P(t)$ is output from the numerical simulation. From Equation (3.30), the normalized contact relaxation function $M(t)/M_0 = P(t)/P_{max}$ is calculated. The numerical relaxation function is then compared with the linear viscoelastic analytical solution for a deviatoric Maxwell creep model (Table 3.2):

$$M(t) = M_0 - \frac{E_0}{2(1+\nu_0)}\left(1 - e^{\left(-\frac{E_0 t}{2(1+\nu_0)\eta_M}\right)}\right) - \frac{E_0}{2(1-\nu_0)}\left(1 - e^{\left(-\frac{E_0 t}{6(1-\nu_0)\eta_M}\right)}\right)$$

$$\Downarrow \tag{3.41}$$

$$\frac{M(t)}{M_0} = G_0\left[e^{-\frac{G_0 t}{\eta_M}} + \frac{9K_0}{3K_0 + 4G_0}e^{-\frac{3K_0 G_0 t}{\eta_M(3K_0 + 4G_0)}}\right].$$

The comparison of the numerical and analytical results is displayed in Figure 3-2. For an incompressible material, independent of the plasticity Equation (3.30) yields a perfect evaluation of the indentation relaxation function of the indented material. A discrepancy of less than 7% is observed in the case of a compressible material. Since this discrepancy is observed for both the viscoelastic and the plastic viscoelastic materials, this discrepancy is attributed to the
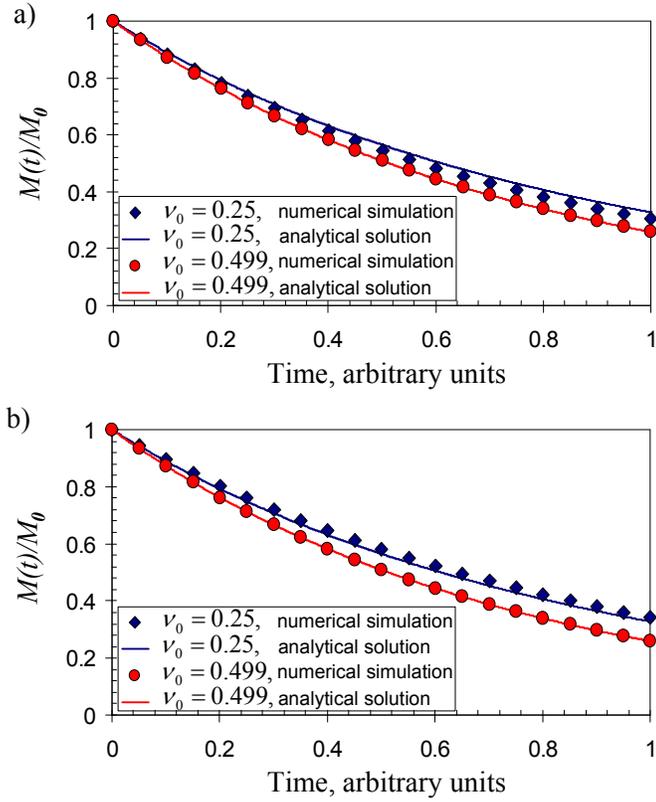
Figure 3-2: Normalized contact relaxation modulus $M(t)/M_0$ versus time for two different Poisson's ratios, calculated from numerical simulations combined with Eq. (3.30) and from linear viscoelastic analytical solutions Eq. (3.41). (a) Linear viscoelastic material with no plasticity and (b) plastic linear viscoelastic material with Von Mises plasticity.

assumption of small perturbations under which the elastic solution is derived (see Section 2.3.1), and its effect is captured by the β-factor (see Section 2.3.2). Nevertheless, Equation (3.30) gives very satisfactory results and provides a tool to access, from an indentation relaxation test and within the range of the β-factor, the contact relaxation modulus $M(t)$ unbiased by plastic effects.

3.3   Indentation Creep Test

Most indenters are load-controlled, and thus indentation creep tests are easier to perform experimentally than indentation relaxation tests. The focus of this Section, therefore, is on indentation creep tests, in which the indentation load is held at its maximum value $P_{\max}$ while monitoring the indentation depth $h(t)$. Following previous developments, we first investigate the indentation creep response of a linear viscoelastic material (Section 3.3.1) to define the time-dependent material properties that can be assessed by indentation creep testing. Then, in Section 3.3.3, a plastic linear viscoelastic material behavior is considered.

3.3.1   Contact Creep Compliance

Consider a Heaviside step loading:

$$P(t) = P_{\max}\mathcal{H}(t) \tag{3.42}$$

where $P_{\max}$ is the maximum load, and $\mathcal{H}(t)$ the Heaviside step function. An inspection of the elastic solution (2.19) and viscoelastic solution (3.6) suggests looking for a depth solution $h(t)$ of the form:

$$\boxed{l(t) \overset{def}{=} \frac{\phi}{P_{\max}}h^{1+1/d}(t)} \tag{3.43}$$

where the probe geometry factor ϕ of dimension $[\phi] = L^{1-1/d}$ is given by (3.8). $l(t)$ is homogeneous to a compliance, $[l] = [m]^{-1}$. Expressions of $l(t)$ for several indenter shapes are developed in Table 3.3.

Indenter shape	d	B	$l(t)$
Cone (Berkovich)	1	$\cot(\theta)$	$\dfrac{2\tan(\theta)}{\pi P_{\max}}h^2(t)$
Sphere	2	$1/(2R)$	$\dfrac{4\sqrt{R}}{3P_{\max}}h^{3/2}(t)$
Flat punch	$\to \infty$	$1/(a^n)$	$\dfrac{2a}{P_{\max}}h(t)$

Table 3.3: Expression of $l(t)$ for several indenter shapes.

Consider then the Laplace transform of (3.43):

$$\widehat{l(s)} = \frac{\phi}{P_{\max}}\widehat{h^{1+1/d}}(s) \tag{3.44}$$

A combination of Eqs. (3.7), (3.44) and (3.9), while recalling that the Laplace transform of the Heaviside load function is $\widehat{P(s)} = P_{\max}/s$, yields:

$$\widehat{l(s)} = s\widehat{L(s)}\frac{\widehat{P(s)}}{P_{\max}} \stackrel{\mathcal{H}(t)}{=} s\widehat{L(s)} \tag{3.45}$$

where:

$$\boxed{\left(s\widehat{L(s)}\right)^{-1} = s\widehat{M(s)}} \tag{3.46}$$

Akin to the uniaxial creep compliance–relaxation modulus relations (3.5), expression (3.46) establishes, in the Laplace domain, the link between the contact relaxation modulus $\widehat{M(s)}$ and the *contact creep compliance*, $\widehat{L(s)}$. In fact, a back-transformation of (3.45) into the time domain shows that the compliance $l(t)$ that is measured –by means of Eq. (3.43)– in an indentation creep test on a linear viscoelastic material is the contact creep compliance:

$$\boxed{l(t) \stackrel{\mathcal{H}(t)}{=} L(t)} \tag{3.47}$$

This contact creep compliance $L(t)$ is defined in the Laplace domain by (3.46) and (3.9), which allows one to link indentation data (Eq. (3.43)) to meaningful viscoelastic material properties.

Moreover, for any monotonically increasing load history, $P(t) = P_{\max}\mathcal{F}(t)$, for which the area of contact increases (see Section 2.3.3), the contact creep compliance $L(t)$ provides a means

94

to calculate the indentation creep response in both Laplace and time domains:

$$\widehat{l(s)} = \frac{\phi \widehat{h^{1+1/n}}(s)}{F_{\max}} = s\,\widehat{L(s)}\,\widehat{\mathcal{F}(s)}$$

$$\Downarrow \tag{3.48}$$

$$l(t) = \frac{\phi h^{1+1/n}(t)}{F_{\max}} = \int_0^t L(t-\tau)\frac{d}{d\tau}\mathcal{F}(\tau)d\tau$$

where $\widehat{\mathcal{F}(s)}$ is the Laplace transform of the normalized loading history $\mathcal{F}(t) = F(t)/F_{\max}$, satisfying $\frac{d}{dt}\mathcal{F}(t) \geq 0$. The above developments show that the depth solution $h(t)$ can easily be found from the applied displacement $h(t)$ once the contact creep compliance $L(t)$ is known. $L(t)$ depends neither on the load case, nor on the geometry of the indenter, but depends only on the viscous properties of the indented material. That is, the contact creep compliance $L(t)$ provides a snapshot of the linear viscoelastic behavior of the indented half-space.

3.3.2 Illustration for Some Linear Viscoelastic Models

Deviatoric Rheological Models

For purposes of illustration of the contact creep compliance $L(t)$, we consider the three deviatoric creep models shown in Figure 3-1.[1] For each model, $\widehat{K(s)}$ and $\widehat{G(s)}$ are available (see Section 3.2.2). Therefore, the contact creep compliance $\widehat{L(s)}$ can be calculated with Equation (3.46) and then translated back into the time domain. By way of example, a linear viscoelastic material with deviatoric creep governed by a Maxwell unit of viscosity η_M (Figure 3-1a) is considered. The shear creep compliance $J^d(t)$ is given by:

$$J^d(t) = \frac{1}{G_0} + \frac{t}{\eta_M} \tag{3.49}$$

A substitution of $\widehat{K(s)} = K_0/s$ and $\widehat{G(s)} = (s/G_0 + 1/\eta_M)^{-1}$ into (3.46) allows the determination of the contact creep compliance in the Laplace space:

$$\widehat{L(s)} = \frac{G_0 + K_0}{4sK_0G_0} + \frac{1}{4s^2\eta_M} - \frac{G_0\eta_M}{4K_0(3K_0G_0 + (3K_0 + G_0)s\eta_M)} \tag{3.50}$$

---

[1] The results here presented have been published in [191].

95

Rheological model used for the deviatoric creep behavior	Contact creep compliance $L(t)$
Maxwell unit	$\dfrac{1}{M_0} + \dfrac{t}{4\eta_M} + \dfrac{(1-2\nu_0)^2}{4E_0}\left(1 - e^{-\frac{E_0}{3\eta_M}t}\right)$
Kelvin-Voigt unit	$\dfrac{1}{M_0} + \dfrac{1}{4G_V}\left(1 - e^{-\frac{G_V}{\eta_V}t}\right) + \dfrac{(1-2\nu_0)^2}{4(E_0+3G_V)}\left(1 - e^{-\frac{E_0+3G_V}{3\eta_V}t}\right)$
Combined	$\dfrac{5-4\nu_0}{4E_0} + \dfrac{t}{4\eta_M} + \dfrac{1}{4G_V}\left(1 - e^{-\frac{t}{T_2}}\right) - ...$
Maxwell-Kelvin-Voigt unit	$... - \dfrac{(1-2\nu_0)^2}{4E_0(\frac{1}{T_1}-\frac{1}{T_3})}\left[(\dfrac{1}{T_2}-\dfrac{1}{T_3})e^{-\frac{t}{T_3}} + (\dfrac{1}{T_1}-\dfrac{1}{T_2})e^{-\frac{t}{T_1}}\right]$

Table 3.4: Analytical expressions of the contact creep compliance $L(t)$ for the three deviatoric creep models described in Figure 3-1.
$T_1 = 6\eta_M\eta_V/(E_0(\eta_M+\eta_V) + 3\eta_M G_V + (E_0^2(\eta_V+\eta_M)^2 + 6E_0\eta_M G_V(\eta_M-\eta_V) + 9\eta_M^2 G_V^2)^{1/2})$;
$T_2 = \eta_V/G_V$;
$T_3 = 6\eta_M\eta_V/(E_0(\eta_M+\eta_V) + 3\eta_M G_V - (E_0^2(\eta_V+\eta_M)^2 + 6E_0\eta_M G_V(\eta_M-\eta_V) + 9\eta_M^2 G_V^2)^{1/2})$

and, after back-transformation into the time domain:

$$\widehat{L(s)} \to L(t) = \frac{1}{M_0} + \frac{t}{4\eta_M} + \frac{(1-2\nu_0)^2}{4E_0}\left(1 - e^{-\frac{E_0 t}{3\eta_M}}\right) \tag{3.51}$$

Interestingly, Equation (3.51) shows that, although the shear creep compliance is linear with respect to time, the contact creep compliance is not. The contact creep compliance is linear with respect to time only at large times, i.e., after a transient period. A characteristic duration of this transient period is the time constant $3\eta_M/E_0$. For an incompressible material ($\nu_0 = 0.5$), the transient term vanishes, and the contact creep compliance, akin to the shear creep compliance, is linear with regard to time.

Using the same methodology, solutions of the form (3.51) are developed for the other rheological models, namely the 4-parameter Kelvin-Voigt model (Figure 3-1b) and the 5-parameter combined Maxwell-Kelvin-Voigt model (Fig. 3-1c). These solutions are summarized in Table 3.4.

Deviatoric Logarithmic Creep

It will turn out useful, for application to cement-based materials, to consider a material that exhibits logarithmic creep. To simplify the derivation, the material is assumed incompressible (i.e., $K_0 \gg G_0$). The viscous behavior is assumed to be restricted to the shear component only,

such that:

$$K(t) = K_0 \rightarrow \widehat{K(s)} = K_0/s \tag{3.52}$$

The shear creep compliance of the indented material is a logarithmic function of time:

$$J^d(t) = \frac{1}{G_0} + \frac{\ln(t/\tau + 1)}{C} \tag{3.53}$$

where τ is a characteristic time of the viscous phenomenon, while C —homogeneous to a modulus— governs the magnitude of the logarithmic creep. The Laplace transform of Eq. (3.53) reads [134]:

$$\widehat{J^d(s)} = \frac{1}{s}\left(\frac{1}{G_0} - \frac{1}{C}e^{s\tau}\,\mathrm{Ei}(-s\tau)\right) \tag{3.54}$$

where Ei is the exponential integral, defined by:

$$\mathrm{Ei}(x) = \int\limits_{-\infty}^{x} \frac{e^{-t}}{t}dt \tag{3.55}$$

From Equation (3.5b) $\widehat{G(s)}$ is calculated:

$$\widehat{G(s)} = \frac{1}{s^2\widehat{J^d(s)}} = \frac{1}{s}\left(\frac{1}{G_0} - \frac{1}{C}e^{s\tau}\,\mathrm{Ei}(-s\tau)\right)^{-1} \tag{3.56}$$

Substituting (3.52) and (3.56) into (3.9), and the result into (3.46), yields the expression of the contact creep compliance for logarithmic creep; first in the Laplace domain:

$$\widehat{L(s)} = \frac{1}{4s^2\widehat{G(s)}}\frac{3\widehat{K(s)} + 4\widehat{G(s)}}{3\widehat{K(s)} + \widehat{G(s)}} \tag{3.57}$$

$$= \frac{1}{4s}\left(\frac{1}{G_0} - \frac{1}{C}e^{s\tau}\,\mathrm{Ei}(-s\tau)\right) \tag{3.58}$$

$$= \frac{1}{sM_0} - \frac{1}{4sC}e^{s\tau}\,\mathrm{Ei}(-s\tau) \tag{3.59}$$

Then, in the time domain:

$$\boxed{L(t) = \frac{1}{M_0} + \frac{\ln(t/\tau + 1)}{4C}} \tag{3.60}$$

Therefore, a logarithmic creep at a material scale entails a logarithmic contact creep compliance $L(t)$, and vice versa: A logarithmic contact creep compliance can be attributed to a logarithmic material creep.

Lastly, if the assumption of an incompressible material (3.52) is relaxed, the derivation here performed becomes much more complex. Similar to the Maxwell creep model (see Section 3.3.2), a transient phase appears, during which the contact creep compliance is not logarithmic with respect to time. The duration of this transient phase must be on the order of τ, which is the only time scale involved in the problem.

3.3.3 Effect of Plasticity on Contact Creep Compliance

The focus of this Section is an investigation of the effects of plastic deformation on the linear viscoelastic contact creep compliance. As plastic deformations below the probe result in an increase in depth at a given load, Equation (3.43) may eventually overestimate the contact creep compliance [192]. Except for highly creeping materials [165] and for spherical indentations at very low loads [140] [142], for which plastic deformations are negligible compared to viscous deformations, and for which the creep compliance of a material can be extracted with confidence using viscoelastic solutions, neglecting the plastic deformations leads in general to an erroneous determination of the viscous properties of the material. To overcome this limitation, several approaches were recently proposed. Oyen and Cook [143] [144] [60], as well as Yang and Zhang [198], suggested that the total indentation depth be split into an elastic, a plastic and a viscous part. But their model remains one-dimensional and does not solve the plastic-viscoelastic problem at the material level. Implicitly evoking the material constitutive level, Zhang et al. [200] [201] proposed the measurement of viscous parameters by means of loading-unloading-reloading cycles combined with the concept of the effective indenter introduced by Pharr and Bolshakov (see Section 2.3.2). But the shape of the effective indenter is a priori unknown, and the experimental implementation of such a method requires several tests, which makes this method unappealing for day-to-day indentation creep analysis.

Here we show that the measured indentation depth response $h(t)$ is linked to the contact creep compliance $L(t)$ by:

$$\boxed{\dot{L}(t) = \frac{2a(t)\dot{h}(t)}{P_{\max}}} \qquad (3.61)$$

where $a(t)$ is the radius of the projected area of contact between the probe and the indented surface. The proof presented next is valid for any type of time-independent plasticity and any axisymmetric indenter. One should note that for a linear viscoelastic material Equation (3.61) is valid, as can be readily observed from a differentiation of Equation (3.43).

Analytical Proof

Instead of a 'usual' indentation creep test (for which the load is increased to $P_{\max}$ and kept constant), consider the following thought experiment with the following load history (see Figure 3-3):

- Instantaneous loading to $P_{\max}$.

- Complete instantaneous unloading.

- Instantaneous reloading to $P_{\max}$.

- Creep phase at $P_{\max}$.

The indentation depth $h(t)$ over the creep phase of the thought experiment is the same as over the creep phase of a 'usual' indentation creep test. The reloading-creep phase is assumed to exhibit no plasticity. Under this assumption, which will be discussed later on, the viscoelastic reloading-creep phase can be itself considered as an indentation creep test in a linear viscoelastic material. The effect of plasticity (plastic deformations having taken place during the preliminary loading-unloading cycle) on this indentation creep test is two-fold:

- The indentation is performed by a probe of known geometry on a surface which is plastically deformed (by the preliminary loading-unloading cycle) and thus of unknown geometry.

- The plastic deformations (which occurred during the preliminary loading-unloading cycle) lead to a build-up of self-equilibrated residual stresses in the indented half-space.

99
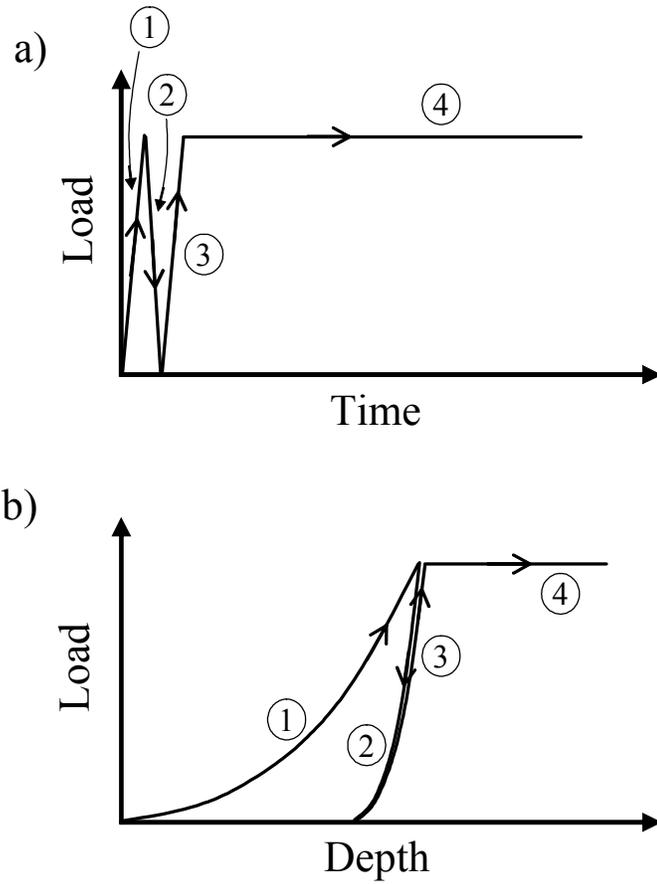
Figure 3-3: (a) Load versus time curve and (b) load versus depth curve of the thought experiment. (1) instantaneous loading. (2) instantaneous unloading. (3) instantaneous reloading. (4) creep phase.

In what follows, we will first discard the effects of residual stresses and show later how they may eventually affect the creep response.

Analytical Proof in the Absence of Residual Stresses In the absence of residual stresses, the effect of plasticity on the reloading-creep phase is limited to the deformation of the surface of the indented half-space. Therefore the reloading-creep phase is a linear viscoelastic indentation on a non-flat surface. The method of functional equations (see Section 2.3.3) is used to convert the reloading-creep phase into an equivalent elastic problem. The equivalent elastic problem is the elastic indentation of a surface of unknown geometry, which itself is equivalent to the elastic indentation of a flat surface by an indenter of unknown geometry. The relation between the contact radius a and the indentation depth h is defined as:

$$a = f(h) \tag{3.62}$$

where $f(h)$ is an unknown function. From an application of the BASh-formula (2.13) to the equivalent elastic problem, the indentation stiffness S is linked to the indentation depth h:

$$S = \frac{dP}{dh} = 2M_0 a = 2M_0 f(h) \tag{3.63}$$

which, after integration, becomes:

$$P = 2M_0 F(h) \tag{3.64}$$

where $F(h)$ is the primitive of $f(h)$ for which $F(0) = 0$. Therefore, the contact creep compliance $L(t)$ is linked to the experimental data by:

$$L(t) = \frac{2F(h(t))}{P_{\max}} \tag{3.65}$$

Finally, after differentiation, the sought-after relation (3.61) is obtained:

$$\dot{L}(t) = \frac{d}{dt}\left(\frac{2F(h)}{P_{max}}\right) = \frac{2f(h)\dot{h}(t)}{P_{max}} = \frac{2a(t)\dot{h}(t)}{P_{max}} \tag{3.66}$$

101

This relation links the measured creep indentation data $h(t)$ to the rate expression of the contact creep compliance, $\dot{L}(t)$, which is insensitive to the plasticity that occurred during the loading phase. The stress, strain and displacement field solutions of the reloading-creep phase with no residual stress, which will later be needed, are denoted by $\boldsymbol{\sigma}^s(t)$, $\boldsymbol{\varepsilon}^s(t)$ and $\underline{\xi}^s(t)$.

Analytical Proof in the Presence of Residual Stresses   The residual stresses consecutive to the infinitely fast loading-unloading cycle of the thought experiment are now taken into account. We restrict ourselves to a linear viscoelasto-plastic half-space characterized by a time-invariant Poisson's ratio (see Eq. (3.32)). A loading-unloading cycle with no further reloading is first considered. Let $\boldsymbol{\sigma}_0^r$, $\boldsymbol{\varepsilon}_0^r$ and $\underline{\xi}_0^r$ be the residual stress and the resulting total strain and displacement generated by the instantaneous loading-unloading cycle in the elasto-plastic half-space. Following the reasoning of Section 3.2.3, we show that the stress $\boldsymbol{\sigma}^r(t)$, strain $\boldsymbol{\varepsilon}^r(t)$ and displacement $\underline{\xi}_0^r$ fields are solutions of the residual stress problem:

$$\begin{aligned}
\underline{\xi}^r(t) &= \underline{\xi}_0^r \\
\boldsymbol{\varepsilon}^r(t) &= \boldsymbol{\varepsilon}_0^r \\
(\boldsymbol{\sigma}^r)^d(t) &= 2G(t)(\boldsymbol{\varepsilon}_0^r)^d \\
(\boldsymbol{\sigma}^r)^v(t) &= K(t)(\boldsymbol{\varepsilon}_0^r)^v
\end{aligned} \tag{3.67}$$

The creep phase of the thought experiment presented earlier in this Section is now considered, and we show that the stress $\boldsymbol{\sigma}^s(t) + \boldsymbol{\sigma}^r(t)$, strain $\boldsymbol{\varepsilon}^s(t) + \boldsymbol{\varepsilon}_0^r$ and displacement $\underline{\xi}^s(t) + \underline{\xi}_0^r$ are the solution fields. Indeed, since $(\underline{\xi}^s(t), \boldsymbol{\sigma}^s(t))$ and $(\underline{\xi}_0^r, \boldsymbol{\sigma}^r(t))$ both verify the field equations (3.31) and (3.33), by linearity their sum does as well. Moreover, the solution to the creep test with no residual stresses $(\underline{\xi}^s(t), \boldsymbol{\sigma}^s(t))$ satisfies the boundary condition (3.34) of the creep problem, whereas the solution to the residual stress problem $(\underline{\xi}_0^r, \boldsymbol{\sigma}^r(t))$ satisfies zero boundary condition everywhere. Therefore, their sum still satisfies the boundary condition (3.34) of the creep problem, and $(\underline{\xi}^s(t) + \underline{\xi}_0^r, \boldsymbol{\sigma}^s(t) + \boldsymbol{\sigma}^r(t))$ is thus the solution of an indentation creep test in a linear visco-elasto-plastic material.

The presence of residual stresses due to the loading-unloading cycle introduces only a constant offset in the indenter probe displacement (with regard to the indenter probe displacement in the absence of residual stresses) and has no influence on the indenter penetration rate. There-

fore, relation (3.61) remains valid and can be applied to plastic linear viscoelastic indentation creep tests.

Numerical Validation

To confirm the validity of Equation (3.61), numerical simulations of conical and parabolic indentation creep tests on a linear-viscoelasto–plastic finite element model are performed. The numerical simulations are carried out with ABAQUS (Dassault Systemes, Nanterre, France) in large displacements. An axisymmetric mesh refined in several steps around the indenter probe is used. To better capture the evolution of the area of contact over the creep phase, extra refinement of the mesh is introduced around the eventual edge of the area of contact during the creep phase. For most simulations, the half-cone angle of the probe is $\theta = 70.32°$, which is the equivalent half-cone angle of the Berkovich probe (see Section 2.2.1). For two simulations, the half-cone angle of the probe is $\theta = 42.28°$, which is the equivalent half-cone angle of the Cube Corner probe (see Section 2.2.1). To simulate an instantaneous loading, viscous properties are dismissed during the loading phase.

The viscous behavior of the indented material is modeled with the deviatoric Maxwell creep model (Fig. 3-1a), characterized by a viscosity η_M. The instantaneous Poisson's ratio is $\nu_0 = 0.499$. The incompressible plastic flow is modeled with an associated Von Mises plasticity model. The yield strength-to-Young's modulus ratio σ_y/E_0 is varied from 10^{-2} to 10^{-1}. The duration of the creep phase is equal to three times the characteristic viscous time $(1-\nu_0^2)\eta_M/E_0$.

The indentation modulus $M_0 = E_0/(1 - \nu_0^2)$ and the maximum load $P_{\max}$ are input into the numerical simulation. The depth history $h(t)$ and contact radius $a(t)$ are output from the numerical simulation. With Eq. (3.61), the rate $\dot{L}^{num}(t)$ of the contact creep function is determined. $\dot{L}^{num}(t)$ is then compared with the linear viscoelastic analytical solution (3.51) of the deviatoric Maxwell creep model:

$$\dot{L}^{an}(t) = \frac{1}{4\eta_M}\left[1 + \frac{(1 - 2\nu_0)^2}{3}e^{-\frac{E_0 t}{3\eta_M}}\right] \tag{3.68}$$

For all simulations, $\dot{L}^{num}(t)/\dot{L}^{an}(t)$ is constant within $\pm 2\%$ over the holding (creep) phase. $\dot{L}^{num}(t)/\dot{L}^{an}(t)$ is displayed in Figure 3-4 versus M_0/H, where $H = P_{\max}/A_c$ is the hardness
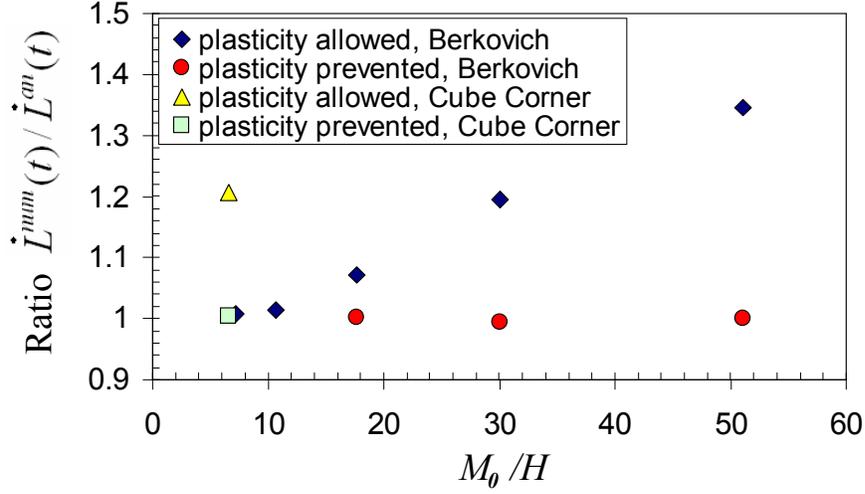
Figure 3-4: Ratio of the contact creep compliance rate $\dot{L}^{num}(t)$ obtained from the numerical simulations and Eq. (3.61) to the contact creep compliance rate $\dot{L}^{an}(t)$ obtained from the analytical solution (3.68) versus M_0/H for Berkovich and Cube Corner indentation. When plasticity is prevented during the holding phase (red circles and green squares), plasticity is still allowed during the holding phase.

calculated at the end of the loading phase.

On average, Equation (3.61) overestimates the contact creep compliance rate. This overestimation depends on the half-cone angle and is more pronounced for the Cube Corner probe. The overestimation increases with an increasing M_0/H ratio, i.e., with a decreasing σ_y/E_0 ratio. At most, an overestimation of about 36% is obtained for the simulation with $M_0/H \simeq 51$. On the other hand, for 'low' M_0/H ratios ($M_0/H \leq 10$) Equation (3.61) gives an almost perfect evaluation of the contact creep compliance rate. To find the reason for the discrepancy of Equation (3.61) new simulations were run in which plasticity was prevented during the creep phase: For any σ_y/E_0 ratio, Equation (3.61) is then in perfect agreement with the analytical solution (3.68), for both Berkovich and Cube Corner probes. This observation proves that plastic phenomena do occur *during* the creep phase, and lead to overestimating the contact creep compliance rate by Eq. (3.61). The occurrence of plastic phenomena during the creep phase is somewhat surprising. Indeed, over the creep phase, the area of contact between the probe and the indented surface increases and, as a result, the average stress below the indenter, i.e.,

104
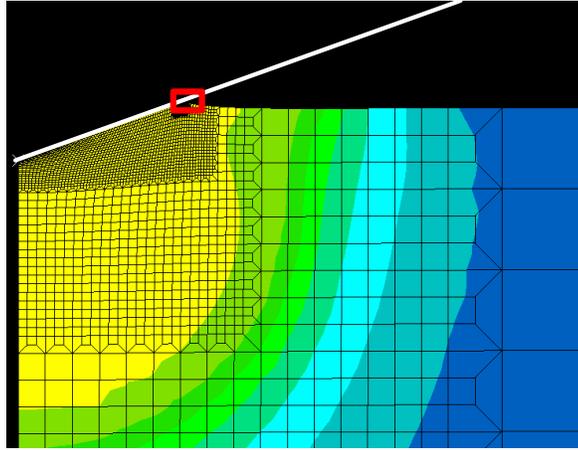
Figure 3-5: Deformed mesh and Von Mises stresses during the creep phase for the numerical simulation with $\sigma_y/E_0 = 10^{-2}$. The plastic phenomena occurring during the creep phase take place in the rectangle.

the hardness H, decreases. The plastic deformations occur in a very localized fashion, around the edge of the area of contact (Fig. 3-5). For the linear-viscoelasto–plastic simulations, the fineness of the mesh around the contact edge was modified, which had no effect on the ratio displayed in Figure 3-4. This observation suggests that the occurrence of plastic phenomena over the creep phase is not a numerical artifact.

The simulation with $\sigma_y/E_0 = 10^{-2}$ (i.e., the most plastic case simulated) was repeated with a parabolic indenter. When preventing plasticity over the creep phase, we find $\dot{L}^{num}(t)/\dot{L}^{an}(t) = 0.989 \pm 0.5\%$, which confirms that the validity of Equation (3.61) is not restricted to a given indenter geometry.

In short, for any indenter shape, Equation (3.61) provides a link between experimental data and the contact creep compliance rate, even when instantaneous plasticity occurs during the loading phase. However, Equation (3.61) does not correct for the occurrence of plasticity during the creep phase.

Specific Case of Short Indentation Creep Tests

For short creep phases the change in contact radius over the creep phase can be neglected. To the first order, the contact radius is thus constant over the creep phase, i.e., $a(t) \approx a_U$, where

a_U is the contact radius just before unloading. Under this approximation, Equation (3.61) becomes:

$$\dot{L}(t) = \frac{2a_U \dot{h}(t)}{P_{max}} \qquad (3.69)$$

where $\dot{h}(t)$ and P_{max} are readily available from experimentation, and a_U can be estimated with the Oliver and Pharr method (see Section 2.3.2).

3.4   Chapter Summary

Indentation analysis aims at linking indentation data to meaningful material properties. Based on original linear viscoelastic solutions developed in this Chapter, we propose such meaningful material properties for time-dependent materials in the form of the contact relaxation modulus $M(t)$ and the contact creep compliance $L(t)$, which can be accessed by an indentation relaxation test and an indentation creep test, respectively. Both, $M(t)$ and $L(t)$, are material properties which depend neither on the shape of the indenter probe nor on the load profile ($P_{\max}$ for an indentation creep test, $h_{\max}$ for an indentation relaxation test). Simple formulas (Eqs. (3.30) and (3.69)) were derived which enable the measurement of $M(t)$ and $L(t)$ even when plasticity occurs during loading. Such a derivation was mandatory since plastic phenomena occur below a sharp Berkovich tip even at small loads.

The time-dependent properties of the indented material are measured during the holding phase of the creep or relaxation test. Consequently, for the measurement to be reliable, the holding phase should be "long enough". In contrast, we concluded in Section 2.4.3 that the holding phase should be as short as possible for the indentation hardness to be representative of the strength properties of the indented material. Those two requirements are clearly antagonistic. Therefore, depending on whether emphasis is placed on the measurement of the strength or of the creep properties, different loading profiles may be required.

This Part was devoted to the development of the theoretical basis for the indentation analysis of homogeneous cohesive–frictional linear viscoelastic solids. On this basis, it is possible to extend the tools of indentation analysis to heterogeneous and multiphase materials. This is shown in the next Part of this report.

Part III

Indentation Analysis of Heterogeneous Solids

Chapter 4

Assessment of Microstructure by Indentation

This third Part of the thesis deals with indentation analysis of heterogeneous solids having heterogeneities that result either from microstructure or from multiphasic composition. The analytical tools developed in this Part will play a critical role in achieving the objective of this thesis, which is the implementation of the Materials Science paradigm between composition, microstructure and performance for cement-based materials, which by nature are highly heterogeneous, multiscale and multiphase materials. This Part is composed of two Chapters: This Chapter develops an indentation technique that allows linking continuum indentation quantities obtained by indentation of a porous material, namely indentation modulus M_0, indentation hardness H, and contact creep compliance $L\left(t\right)$ or contact relaxation modulus $M\left(t\right)$, to constitutive properties and microstructural information of the solid phase that manifests itself at a scale much smaller than that of indentation analysis. This will be achieved by using the tools of linear and non-linear microporomechanics to homogenize elastic, strength and viscous properties [70]. The next Chapter will carry the analysis on to account for the multiphase structure of materials in indentation analysis.

4.1 Introduction

4.1.1 Problem Formulation

Consider an indentation test into a porous material composed of a solid phase and an (empty) pore space (Fig. 4-1). The constitutive behavior of the solid phase is characterized by a set of mechanical properties (elastic modulus m_s, Poisson's ratio ν_s, cohesion c_s, friction coefficient α_s and contact creep compliance $l_s(t)$ or equivalently contact relaxation modulus $m_s(t)$) which is the same throughout the studied domain. The characteristic size of the porosity or solid particle, say d, is assumed to be much smaller than the size of the indentation depth h. As a result, the indentation modulus M_0, the indentation hardness H, and the contact creep compliance $L(t)$ or equivalently the contact relaxation modulus $M(t)$, which are extracted from the indentation test using the tools developed in Chapters 2 and 3, are *composite* properties. The goal of the indentation analysis of such a heterogeneous material is to link the measurable composite indentation properties $(M_0, H, L(t))$ to constituent properties of the solid phase $(m_s, \nu_s, c_s, \alpha_s, l_s(t))$ and microstructural information, such as the volume fractions (porosity φ, solid concentration or solid packing density $\eta = 1 - \varphi$), pore– and/or particle aspect ratio, and matrix–pore morphology versus granular morphology, as displayed in Figure 4-1. – This seems quite a daunting task given the large number of constituent and morphological properties compared to the number of measurable composite indentation properties.

4.1.2 Scale Separability in Microporomechanics Indentation Analysis

Continuum micromechanics, or more precisely microporomechanics [70], is an extremely powerful tool to achieve just this, namely linking composite properties of a representative elementary volume (*rev*) to constituent properties and microstructural morphology. This *rev* is an intermediate mechanical system whose characteristic size $\mathcal{L}$ is situated in-between the microstructural scale characterized by the size of the heterogeneity d and the characteristic size of mechanical solicitation, which in the case of an indentation test in a semi-infinite half-space is defined by the indentation depth h or the contact radius a. In order to apply the tools of continuum
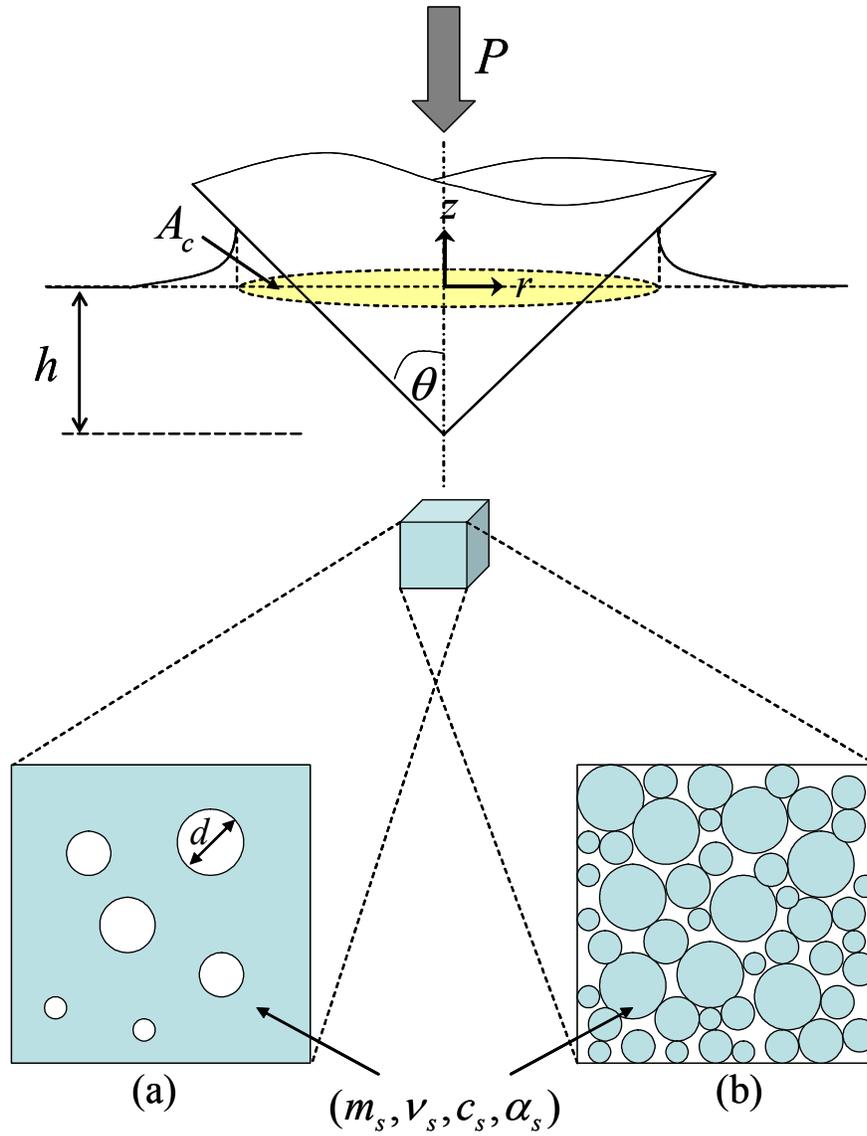
Figure 4-1: Conical indentation in a porous material composed of a solid phase and pore space: (*a*) Matrix–porosity morphology and (*b*) perfectly disordered, polycrystal morphology (adapted from [33]).

micromechanics, these scales must satisfy the scale separability condition:

$$d \ll \mathcal{L} \ll (a, h)$$ (4.1)

where:

- The condition $d \ll \mathcal{L}$ ensures that the *rev* include enough heterogeneities so that the composite response at the scale of the *rev* is representative of the material in a statistical sense.

- The condition $\mathcal{L} \ll (a, h)$ ensures that the tools of differential calculus used in Chapters 2 and 3 to derive the relationships linking indentation data to mechanical properties remain valid.

Scale separability in indentation testing is quite easy to ensure, as one can monitor the indentation depth h via the indentation load. Thus a combination of continuum microme-chanics and indentation analysis based on the scale-separability conditions (4.1) is a powerful approach to probing the microstructure of the indented heterogeneous material. This is shown in forthcoming Sections for the composite indentation modulus M_0 (Section 4.2), the composite indentation hardness H (Section 4.3), and finally for the contact creep compliance $L(t)$ (Section 4.4). Along the way we introduce the necessary tools of linear and non-linear micromechanics for stiffness, strength and viscous properties.

4.2 Indentation Modulus–Packing Density Scaling Relations

4.2.1 Dimensional Analysis

Consider the indentation modulus M determined from an indentation test by means of the BASh formula (2.13):

$$M \stackrel{def}{=} S\frac{\sqrt{\pi}}{2\sqrt{A_c}}$$ (4.2)

where $S = (dP/dh)_{h=h_{\max}}$ is the initial contact stiffness measured during unloading, and A_c the projected area of contact between the indenter tip and the indented material determined, for instance, with the Oliver and Pharr method. The indentation test conditions are such that the

111

indentation modulus M is representative of the elasticity content of the indented material only, as discussed in detail in Section 2.3[1]. Consider then that M is the indentation modulus of a two-phase (solid plus pore) composite that satisfies the scale separability conditions (4.1). The indentation modulus M thus depends on the elastic properties of the solid phase (m_s, ν_s) and on the microstructure (packing density η and morphology); that is, in a dimensionless form:

$$\boxed{\frac{M}{m_s} = \Pi_M(\nu_s, \eta, X)} \tag{4.3}$$

where X is a yet-to-be specified dimensionless morphology parameter that characterizes the microstructure of the solid-pore composite. Based on linear homogenization theory, the focus of this Section is to identify the dimensionless elasticity function Π_M for different pore morphologies characterized by parameter X.

4.2.2 Brief Reminder of Elements of Linear Homogenization Theory

This Section provides a brief introduction to the tools of linear micromechanics[2].

Briefly, we recall that continuum micromechanics based on the scale separability conditions (4.1) involves two scales: The microscale, where the composite is heterogeneous, and the macroscale, where the composite behaves mechanically in a homogeneous manner. Microscopic and macroscopic quantities are defined in Table 4.1. The macroscopic quantities $A(\underline{X})$ are defined as the local average of the microscopic ones $a(\underline{x})$. If $\Omega(\underline{X})$ is the *rev* centered at point $\underline{X}$, then for any quantities $A(\underline{X})$ and $a(\underline{x})$ we have:

$$A(\underline{X}) = \langle a(\underline{x}) \rangle_{\Omega(\underline{X})} = \frac{1}{|\Omega|} \int_{\Omega(\underline{X})} a(\underline{x}) \, d\underline{x} \tag{4.4}$$

The aim of linear homogenization theory is to find from the local distribution of microscopic stiffness tensors $\mathbb{C}(\underline{x})$, which link the local stress $\boldsymbol{\sigma}(\underline{x})$ to the local strain $\boldsymbol{\varepsilon}(\underline{x})$ by $\boldsymbol{\sigma}(\underline{x}) = \mathbb{C}(\underline{x}) : \boldsymbol{\varepsilon}(\underline{x})$, the homogenized stiffness tensor $\mathbb{C}^{\text{hom}}$, which links the macroscopic stress $\boldsymbol{\Sigma}(\underline{X})$ to the

---

[1] For this reason, we now drop the subscript M_0, assuming in all what follows that M is representative of the true elastic properties of the indented material.

[2] Inspired from the presentation of B. Gathier [80].

	Microscopic quantities	Macroscopic quantities
Position	$\underline{x}$	$\underline{X}$
Strain	$\boldsymbol{\varepsilon}\left(\underline{x}\right)$	$\mathbf{E}\left(\underline{X}\right)$
Stress	$\boldsymbol{\sigma}\left(\underline{x}\right)$	$\boldsymbol{\Sigma}\left(\underline{X}\right)$
Energy	$\omega\left(\underline{x}\right)$	$\mathcal{W}\left(\underline{X}\right)$

Table 4.1: Microscopic and macroscopic quantities.

macroscopic strain $\mathbf{E}\left(\underline{X}\right)$:

$$\boldsymbol{\Sigma}\left(\underline{X}\right) = \mathbb{C}^{\text{hom}} : \mathbf{E}\left(\underline{X}\right) \tag{4.5}$$

It is common in homogenization theory to work with regular strain or stress boundary conditions [70]:

- For fixed $\mathbf{E}$, the displacement is prescribed at the boundary $\partial\Omega$ of the *rev*:

$$\underline{\xi} = \mathbf{E} \cdot \underline{x} \qquad \text{on } \partial\Omega \tag{4.6}$$

- For fixed $\boldsymbol{\Sigma}$, the stress vector is prescribed at the boundary $\partial\Omega$ of the *rev*:

$$\boldsymbol{\sigma} \cdot \underline{n} = \boldsymbol{\Sigma} \cdot \underline{n} \qquad \text{on } \partial\Omega \tag{4.7}$$

For regular boundary conditions, and by neglecting the effect of an externally applied load density so that $\text{div}\,\boldsymbol{\sigma} = \underline{0}$, the Hill lemma [91] applies:

$$\langle \boldsymbol{\sigma} : \boldsymbol{\varepsilon} \rangle = \langle \boldsymbol{\sigma} \rangle : \langle \boldsymbol{\varepsilon} \rangle \tag{4.8}$$

which stipulates that the macroscopic energy $\mathcal{W}\left(\underline{X}\right) = \boldsymbol{\Sigma}\left(\underline{X}\right) : \mathbf{E}\left(\underline{X}\right)$ is indeed the volume average of the microscopic strain energy $\omega\left(\underline{x}\right)$.

Localization Tensor

From now on we restrict ourselves to regular displacement boundary conditions of the form (4.6). In this case, due to the linearity of all microscopic material behaviors, the microscopic

strain $\varepsilon\left(\underline{x}\right)$ is proportional to the applied macroscopic strain $\mathbf{E}\left(\underline{X}\right)$:

$$\varepsilon\left(\underline{x}\right) = \mathbb{A}\left(\underline{x}\right) : \mathbf{E} \tag{4.9}$$

where $\mathbb{A}\left(\underline{x}\right)$ is called the strain concentration or strain localization tensor. Then the stress field reads:

$$\boldsymbol{\sigma}\left(\underline{x}\right) = \mathbb{C}\left(\underline{x}\right) : \mathbb{A}\left(\underline{x}\right) : \mathbf{E} \tag{4.10}$$

So that:

$$\boldsymbol{\Sigma} = \langle\boldsymbol{\sigma}\left(\underline{x}\right)\rangle_{\Omega} = \langle\mathbb{C}\left(\underline{x}\right) : \mathbb{A}\left(\underline{x}\right)\rangle_{\Omega} : \mathbf{E} \tag{4.11}$$

A comparison of Eqs. (4.11) and (4.5) yields the expression for the homogenized stiffness tensor:

$$\mathbb{C}^{\text{hom}} = \langle\mathbb{C}\left(\underline{x}\right) : \mathbb{A}\left(\underline{x}\right)\rangle_{\Omega} \tag{4.12}$$

Determining the homogenized stiffness tensor is hence reduced to the determination of the strain localization tensor $\mathbb{A}\left(\underline{x}\right)$. Estimates of the strain localization tensor are obtained by considering the problem known today as the Eshelby inclusion problem, presented next.

Eshelby Inclusion Problem

In 1957, Eshelby [72] considered the case of an isolated ellipsoidal inclusion $(\mathcal{I})$ with constant elasticity tensor $\mathbb{C}_1$ embedded in an infinite medium with a different elasticity tensor $\mathbb{C}_0$ and subjected to a uniform strain $\mathbf{E}^{\infty}$ at infinity (Figure 4-2).

The domain occupied by the inclusion is defined by:

$$\mathcal{I} = \left\{ \underline{x} \in \mathbb{R}^3 \,|\, \underline{x} \cdot \left({}^t\mathbf{A} \cdot \mathbf{A}\right)^{-1} \cdot \underline{x} \leq 1 \right\} \tag{4.13}$$

where $\mathbf{A}$ is a second order tensor. If $\underline{e}_1$, $\underline{e}_2$, $\underline{e}_3$ are the directions of the main axis and a_1, a_2, a_3 are the half lengths of the axis, then:

$$\mathbf{A} = a_1\,\underline{e}_1 \otimes \underline{e}_1 + a_2\,\underline{e}_2 \otimes \underline{e}_2 + a_3\,\underline{e}_3 \otimes \underline{e}_3 \tag{4.14}$$

114
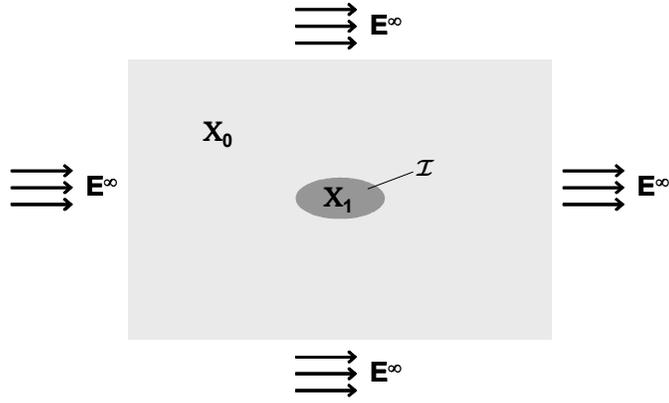
Figure 4-2: Eshelby problem: Ellipsoidal inclusion ($\mathcal{I}$) embedded in an infinite elastic medium (from [80]).

and the equation of the ellipsoid is:

$$\left(\frac{x_1}{a_1}\right)^2 + \left(\frac{x_2}{a_2}\right)^2 + \left(\frac{x_3}{a_3}\right)^2 \leq 1 \tag{4.15}$$

Eshelby showed that the strain field inside the inclusion is constant and that the value of the strain inside the inclusion is:

$$\forall \underline{x} \in \mathcal{I}, \quad \boldsymbol{\varepsilon}\left(\underline{x}\right) = \left(I + \mathbb{P}_0 : \left(\mathbb{C}_1 - \mathbb{C}_0\right)\right)^{-1} : \mathbf{E}^{\infty} \tag{4.16}$$

where:

$$\mathbb{P}_0 = \frac{\det \mathbf{A}}{4\pi} \int_{||\underline{v}||=1} \frac{\underline{v} \overset{s}{\otimes} \left(\underline{v} \cdot \mathbb{C}_0 \cdot \underline{v}\right)^{-1} \overset{s}{\otimes} \underline{v}}{\left(\underline{v} \cdot \left({}^t\mathbf{A} \cdot \mathbf{A}\right)^{-1} \cdot \underline{v}\right)^{\frac{3}{2}}} dS \tag{4.17}$$

is the Hill tensor. The Hill tensor depends only on the shape of the inclusion and not on its size.

If the reference medium is isotropic,

$$\mathbb{C}_0 = 3K_0 \, \mathbb{J} + 2G_0 \, \mathbb{K} \tag{4.18}$$

and if the inclusion is a sphere (i.e. $\mathbf{A} = \mathbf{1}$), then

$$\mathbb{P}_0 = \frac{1}{3K_0 + 4G_0} \mathbb{J} + \frac{3}{5G_0} \frac{K_0 + 2G_0}{3G_0 + 4G_0} \mathbb{K} \tag{4.19}$$

where $\mathbb{J}$ and $\mathbb{K}$ are the fourth-order tensors defined by:

$$\mathbb{J} = \mathbf{I} \otimes \mathbf{I}; \quad \mathbb{K} = \mathbb{I} - \mathbb{J} \tag{4.20}$$

where $\mathbf{I}$ is the second order unit tensor.

From Eq. (4.17), expressions for the Hill tensor can also be derived for more complicated material behaviors (e.g., for an anisotropic reference medium [110]) and other shapes of inclusions (e.g., ellipsoidal inclusions in an isotropic reference medium [72] [9]).

The Eshelby inclusion problem can be used to obtain estimates of the homogenized stiffness tensor $\mathbb{C}^{\mathrm{hom}}$, as described next.

Estimates of Homogenized Stiffness Tensor

Here the composite material is assumed to be made of N phases, and the inclusions are assumed to be spherical. The i-th phase $(i \in \{1, .., N\})$ is characterized by the stiffness tensor $\mathbb{C}_i$ and occupies the volume Ω_i and a volume fraction ϕ_i of the composite. Using Eshelby's result (4.16), the mean strain tensor in each inclusion of phase i is estimated by:

$$\langle \varepsilon\, (\underline{x}) \rangle_{\Omega_i} = (I + \mathbb{P}_0 : (\mathbb{C}_i - \mathbb{C}_0))^{-1} : \mathbf{E}^\infty \tag{4.21}$$

In the above expression, the strain $\mathbf{E}^\infty$ 'felt' by the inclusion and the stiffness tensor $\mathbb{C}_0$ of the embedding medium must be determined. $\mathbf{E}^\infty$ is determined by enforcing the regular strain boundary condition:

$$\mathbf{E} = \langle \varepsilon\, (\underline{x}) \rangle_\Omega \tag{4.22}$$

Making use of Eq. (4.21) yields:

$$\mathbf{E} = \sum_{i=1}^N \phi_i \, (I + \mathbb{P}_0 : (\mathbb{C}_i - \mathbb{C}_0))^{-1} : \mathbf{E}^\infty \tag{4.23}$$

116

It follows:

$$\mathbf{E}^{\infty} = \left[\sum_{i=1}^{N} \phi_i \left(I + \mathbb{P}_0 : (\mathbb{C}_i - \mathbb{C}_0) \right)^{-1} \right]^{-1} : \mathbf{E} \qquad (4.24)$$

Therefore, from Eq. (4.16), the mean strain in each inclusion of phase i is:

$$\langle \varepsilon(\underline{x}) \rangle_{\Omega_i} = \left(I + \mathbb{P}_0 : (\mathbb{C}_i - \mathbb{C}_0) \right)^{-1} : \left[\sum_{i=1}^{N} \phi_i \left(I + \mathbb{P}_0 : (\mathbb{C}_i - \mathbb{C}_0) \right)^{-1} \right]^{-1} : \mathbf{E} \qquad (4.25)$$

A comparison of Eqs. (4.25) and (4.9) yields the expression of the mean strain localization tensor:

$$\langle \mathbb{A}(\underline{x}) \rangle_{\Omega_i} = \left(I + \mathbb{P}_0 : (\mathbb{C}_i - \mathbb{C}_0) \right)^{-1} : \left[\sum_{i=1}^{N} \phi_i \left(I + \mathbb{P}_0 : (\mathbb{C}_i - \mathbb{C}_0) \right)^{-1} \right]^{-1} \qquad (4.26)$$

and, finally, the expression of the homogenized stiffness tensor $\mathbb{C}^{\text{hom}}$:

$$\mathbb{C}^{\text{hom}} = \sum_{i=1}^{N} \phi_i \mathbb{C}_i : \langle \mathbb{A}(\underline{x}) \rangle_{\Omega_i} \qquad (4.27)$$

$$= \left[\sum_{i=1}^{N} \phi_i \mathbb{C}_i : \left(I + \mathbb{P}_0 : (\mathbb{C}_i - \mathbb{C}_0) \right)^{-1} \right] : \left[\sum_{i=1}^{N} \phi_i \left(I + \mathbb{P}_0 : (\mathbb{C}_i - \mathbb{C}_0) \right)^{-1} \right]^{-1} \qquad (4.28)$$

In Eq. (4.28) the stiffness tensor $\mathbb{C}_0$ (and consequently $\mathbb{P}_0$) of the embedding medium remains still to be determined and depends on the morphology of the composite considered:

- If the composite has a clear matrix–inclusion morphology (see Figure 4-1a), it is reasonable to consider that the embedding medium is the matrix. Such an estimate of the homogenized stiffness tensor $\mathbb{C}^{\text{hom}}$ is called the Mori-Tanaka estimate $\mathbb{C}^{MT}$ [130]. Assuming that the phase 1 is the matrix, letting $\mathbb{C}_0 \to \mathbb{C}_1$ in Eq. (4.28) yields the Mori-Tanaka estimate:

$$\mathbb{C}^{MT} = \left[\sum_{i=1}^{N} \phi_i \mathbb{C}_i : \left(I + \mathbb{P}_1 : (\mathbb{C}_i - \mathbb{C}_1) \right)^{-1} \right] : \left[\sum_{i=1}^{N} \phi_i \left(I + \mathbb{P}_1 : (\mathbb{C}_i - \mathbb{C}_1) \right)^{-1} \right]^{-1} \qquad (4.29)$$

- If no phase in the composite plays the role of a matrix (see Figure 4-1b), one can consider that the embedding medium is the homogenized medium itself. Such an estimate of the homogenized stiffness tensor $\mathbb{C}^{\text{hom}}$ is called the self-consistent (or polycrystal) estimate

117

$\mathbb{C}^{SC}$, which originated independently from Hershey [89] and Kröner [107]. Granular materials are well captured by a self-consistent model. Letting $\mathbb{C}_0 \to \mathbb{C}^{\text{hom}} = \mathbb{C}^{SC}$, the self-consistent estimate is found by solving:

$$\mathbb{C}^{SC} = \left[\sum_{i=1}^{N}\phi_i\mathbb{C}_i : \left(I + \mathbb{P}^{SC} : \left(\mathbb{C}_i - \mathbb{C}^{SC}\right)\right)^{-1}\right] : \left[\sum_{i=1}^{N}\phi_i \left(I + \mathbb{P}^{SC} : \left(\mathbb{C}_i - \mathbb{C}^{SC}\right)\right)^{-1}\right]^{-1} \tag{4.30}$$

We now have all the theoretical tools necessary to assess the link between indentation modulus M and microstructure for the solid-pore composite presented in Figure 4-1.

4.2.3 Matrix–Pore Inclusion Morphology

We start with the matrix-pore inclusion morphology (Figure 4-1a), which is well captured by the Mori-Tanaka scheme [130]. The isotropic solid phase of the solid-pore composite occupies the volume fraction (packing density) $\phi_S = \eta$ of the composite and is characterized by the elastic stiffness tensor $\mathbb{C}_s = 3k_s \mathbb{J} + 2g_s \mathbb{K}$. In contrast, the pore occupies the volume fraction $\phi_V = \varphi = 1 - \eta$ of the composite and obviously has no stiffness. Solving Eq. (4.29) for $N = 2$ with the solid as matrix ($K_1 = k_s$, $G_1 = g_s$ and $\phi_1 = \eta$) and the pores as inclusion ($K_2 = 0$, $G_2 = 0$ and $\phi_2 = \varphi$) yields the homogenized bulk modulus K^{MT} and shear modulus G^{MT}:

$$K^{MT} = g_s\mathcal{K}^{MT}; \mathcal{K}^{MT} = 4\frac{\eta}{3\left(1-\eta\right) + 4/\gamma_s} \tag{4.31}$$

$$G^{MT} = g_s\mathcal{M}^{MT}; \mathcal{M}^{MT} = \frac{\eta(8/\gamma_s + 9)}{6\left(1-\eta\right)\left(2/\gamma_s + 1\right) + 8/\gamma_s + 9} \tag{4.32}$$

where $\gamma_s = k_s/g_s = 2\left(1+\nu_s\right)/3\left(1-2\nu_s\right) > 0$. Recalling that the indentation modulus relates to the bulk and shear modulus by (2.20):

$$M^{MT} = 4G^{MT}\frac{3K^{MT} + G^{MT}}{3K^{MT} + 4G^{MT}} \tag{4.33}$$

a dimensionless expression of the form (4.3) is obtained that links the indentation modulus to constituent properties (m_s, ν_s) and microstructure (solid concentration η) [184]:

$$\Pi_M^{MT} = \frac{M^{MT}}{m_s} = \frac{1}{2}\frac{(7 - 5\nu_s)(-13\varphi + 2\varphi\nu_s + 15\varphi\nu_s^2 - 14 + 10\nu_s)(1 - \varphi)}{(7 - 5\nu_s + 5\varphi + 5\varphi\nu_s)(-8\varphi + 10\varphi\nu_s - 7 + 5\nu_s)} \tag{4.34}$$

118

where $m_s = 4g_s(3k_s + g_s)/(3k_s + 4g_s)$ is the plane-stress modulus of the solid phase. Figure 4-3a displays the normalized indentation modulus M/m_s versus solid packing density η. The normalized indentation modulus M/m_s shows very little sensitivity to the Poisson's ratio ν_s of the solid phase.

4.2.4 Granular Morphology with Spherical Particles

Consider next a granular morphology of the solid phase with spherical pores and spherical solid particles (Figure 4-1b). Solving Eq. (4.30) for $N = 2$ with the solid as the first phase ($K_1 = k_s$, $G_1 = g_s$ and $\phi_1 = \eta$) and the pores as the second ($K_2 = 0$, $G_2 = 0$ and $\phi_2 = \varphi$) yields the homogenized bulk modulus K^{SC} and shear modulus G^{SC} :

$$
\begin{aligned}
K^{SC} \ = \ & \frac{1}{2} \frac{k_s}{9\,\varphi\,k_s + (12 - 20\,\varphi)\,g_s}\big(3\,\varphi\,(3 - \varphi)\,k_s + (24 + 20\,\varphi^{\,2} - 56\,\varphi)\,g_s \\
& \dots\ -\varphi\,\sqrt{81\,k_s^2 - 168\,\varphi\,k_s g_s - 54\,k_s^2\,\varphi + 144\,g_s\,k_s + 400\,\varphi^{\,2}\,g_s^{\,2}} \\
& \dots\ \overline{-120\,k_s\,\varphi^{\,2}\,g_s - 320\,\varphi\,g_s^{\,2} + 9\,k_s^{\,2}\,\varphi^2 + 64\,g_s^{\,2}}\ \big)
\end{aligned}
\tag{4.35}
$$

$$
\begin{aligned}
G^{SC} \ = \ & \frac{1}{16}\big((8 - 20\,\varphi)\,g_s + (3\,\varphi - 9)\,k_s \\
& \dots\ +\sqrt{81\,k_s^2 - 168\,\varphi\,k_s\,g_s - 54\,k_s^{\,2}\,\varphi + 144\,g_s\,k_s + 400\,\varphi^{\,2}\,g_s^{\,2}} \\
& \dots\ \overline{-120\,k_s\varphi^{\,2}\,g_s - 320\,\varphi\,g_s^{\,2} + 9\,k_s^{\,2}\,\varphi^2 + 64\,g_s^{\,2}}\ \big)
\end{aligned}
\tag{4.36}
$$

and eventually the homogenized indentation modulus M in the dimensionless form (4.3) [57]:

$$
\Pi_M^{SC} = \frac{M^{SC}}{m_s} = \mathcal{M}^{SC}\frac{\left(9(1 - \varphi)\gamma_s + 4\mathcal{M}^{SC} + 3\gamma_s\right)(3\gamma_s + 4)}{4\left(4\mathcal{M}^{SC} + 3\gamma_s\right)(3\gamma_s + 1)}
\tag{4.37}
$$

where $\gamma_s = 2\left(1 + \nu_s\right)/3\left(1 - 2\nu_s\right) > 0$, and $\mathcal{M}^{SC}$ is the composite shear–to–solid shear moduli ratio:

$$
\begin{aligned}
\mathcal{M}^{SC} \ = \ & \frac{1}{2} - \frac{5}{4}\varphi - \frac{3}{16}\gamma_s\,(3 - \varphi) \\
& +\frac{1}{16}\sqrt{\begin{aligned} &144\,(1 - \gamma_s) - 480(1 - \varphi) + 400(1 - \varphi)^2 + \dots \\ &\dots + 408\gamma_s(1 - \varphi) - 120\gamma_s(1 - \varphi)^2 + 9\gamma_s^2\,(3 - \varphi)^2 \end{aligned}}
\end{aligned}
\tag{4.38}
$$

Figure 4-3b displays the normalized indentation modulus M/m_s versus the packing density

119

a)

b)
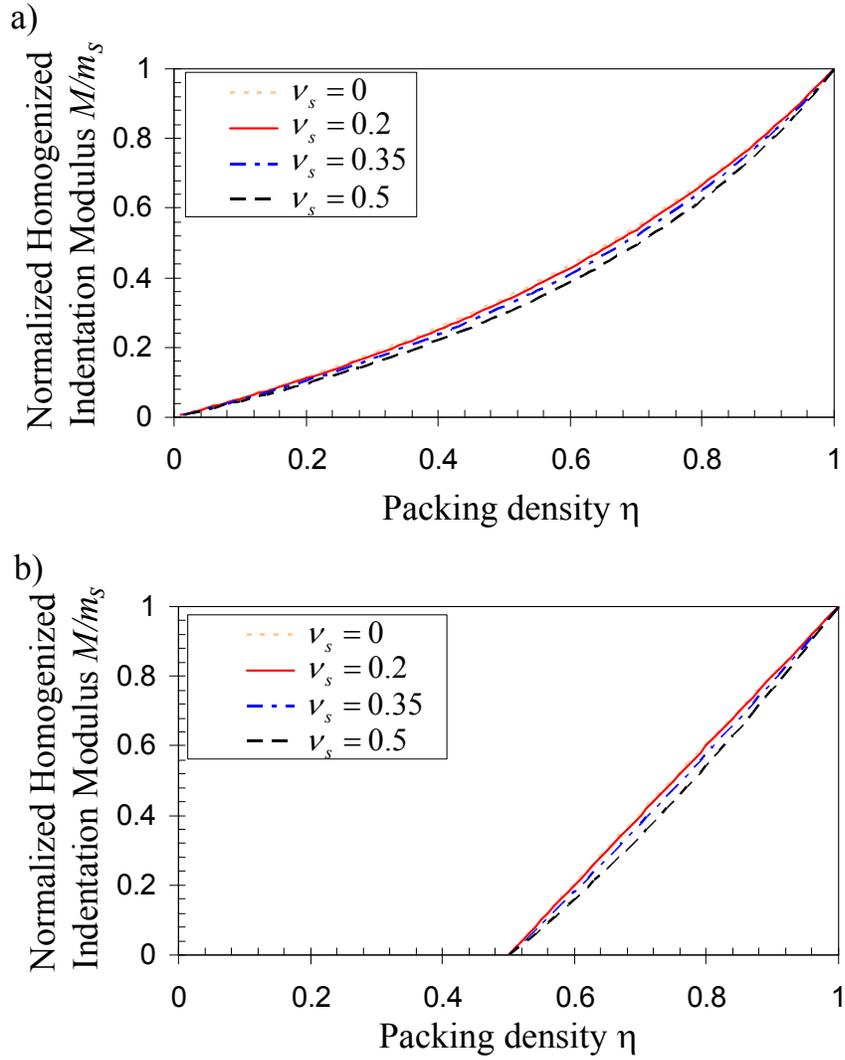
Figure 4-3: Normalized homogenized indentation modulus M/m_s versus packing density η (a) for a Mori-Tanaka scheme and (b) for a self-consistent scheme.

$\eta = 1 - \varphi$. Similarly to the matrix-pore morphology, the normalized indentation modulus M/m_s shows very little sensitivity to the Poisson's ratio ν_s of the solid phase; however a comparison between Figures 4-3a and 4-3b shows that the choice of morphology strongly affects the relationship between indentation modulus and packing density. While the matrix–pore inclusion morphology leads to a continuous M/m_s scaling for the entire packing density range $\eta \in [0,1]$, the spherical granular morphology is characterized by a percolation threshold of $\eta_0 = 1/2$, below which the composite material has no stiffness. In terms of the dimensionless relation (4.3), the relevant morphology parameter X appears to be the percolation threshold:

$$\boxed{\frac{M}{m_s} = \Pi_M(\nu_s, \eta, X = \eta_0)} \tag{4.39}$$

with $\eta_0 = 0$ for a matrix–pore inclusion morphology, and $\eta_0 = 1/2$ for a polycrystal morphology with spherical particles. As we will see here below, the identification of the percolation threshold as the key morphological parameter for randomly oriented particles holds even for different particle shapes.

4.2.5 Granular Morphology with Aspherical Particles

In this Section, the morphology of the composite is assumed to be granular, the solid particles being aspherical and randomly oriented in the composite. The presentation is inspired by the work of Sanahuja et al. [160]. To capture the asphericity of the solid particles spheroids are considered, defined by their aspect ratio r^s (see Figure 4-4). The aspect ratio r^s of a spheroid is defined as the ratio of the length of the symmetry axis over the diameter in the symmetry plane. Particles with $r^s < 1$ are oblate spheroids, particles with $r^s > 1$ are prolate spheroids. In contrast, the pore inclusions are still considered spherical.

Since solid inclusions and pore inclusions now have different shapes, the corresponding expressions of the Hill tensor (4.17) are also different. Since the pore inclusions are assumed spherical, Eq. (4.26) is still valid to calculate the mean strain localization tensor in the pore inclusions, but the mean strain localization tensor in the aspherical solid inclusions must be calculated again so that Eq. (4.27) can be solved.

The Hill-tensor for spheroids can be found in the literature (e.g., [9]). It now depends on
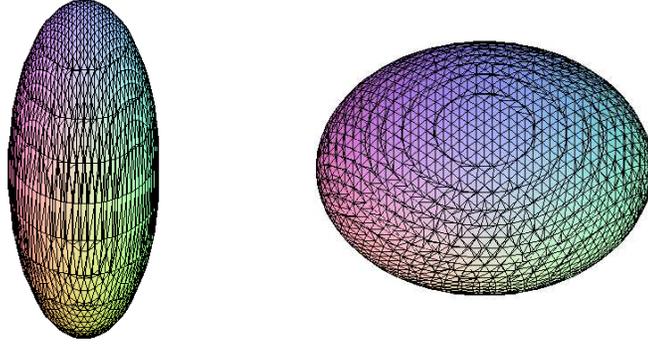
Figure 4-4: Prolate spheroid with $r^s = 3$ (left) and oblate spheroid with $r^s = 1/3$ (right).

the orientation $\mathbb{P}_0(\theta, \phi)$ and so does the solution of the Eshelby inclusion problem [160]:

$$\varepsilon(\theta, \phi) = (I + \mathbb{P}_0(\theta, \phi) : (\mathbb{C}_i - \mathbb{C}_0))^{-1} : \mathbf{E}^\infty \tag{4.40}$$

The strain localization tensor $\mathbb{A}_S$ in the solid and the mean strain (4.21) must be carefully calculated. Considering a random orientation of the solid spheroids, the mean strain in the solid inclusions is now calculated over the solid volume Ω_S as [160]:

$$\langle \varepsilon\left(\underline{x}\right)\rangle_{\Omega_S} = \mathbb{A}_s\left(\underline{x}\right) : \mathbf{E}^\infty \tag{4.41}$$

$$= \left[\int\limits_{\phi=0}^{2\pi}\int\limits_{\theta=0}^{\pi} (I + \mathbb{P}_0(\theta, \phi) : (\mathbb{C}_i - \mathbb{C}_0))^{-1} \frac{\sin\theta}{4\pi} d\theta d\phi\right] : \mathbf{E}^\infty \tag{4.42}$$

Once this calculation is performed, the strain localization tensor is known in both the solid and pore inclusions. Then Eq. (4.27) can be used to calculate the homogenized stiffness tensor. However, the calculation of Eq. (4.42) requires extensive use of Maple[3], and its result is too lengthy to be reasonably printed. Nevertheless, it is thus possible to obtain the link between homogenized indentation modulus and microstructure for various packing densities η and aspect ratios r^s of the solid particles.

The results of this calculation, which are displayed in Figure 4-5, show that the percolation

---

[3]The numerical implementation was performed by Alberto J. Ortega during his PhD at MIT.

a) Percolation Threshold vs Aspect Ratio r_s of the Solid Particles

Legend:
- △ Buchalter & Bradley (1994)
- ■ Coelho et al. (1997)
- ◆ Sherwood (1997)
- — Self-Consistent Model

b) Normalized Homogenized Indentation Modulus M/m_s vs Packing density η

Legend:
- $r_s = 1$
- $r_s = 0.5$
- $r_s = 0.25$
- $r_s = 0.1$
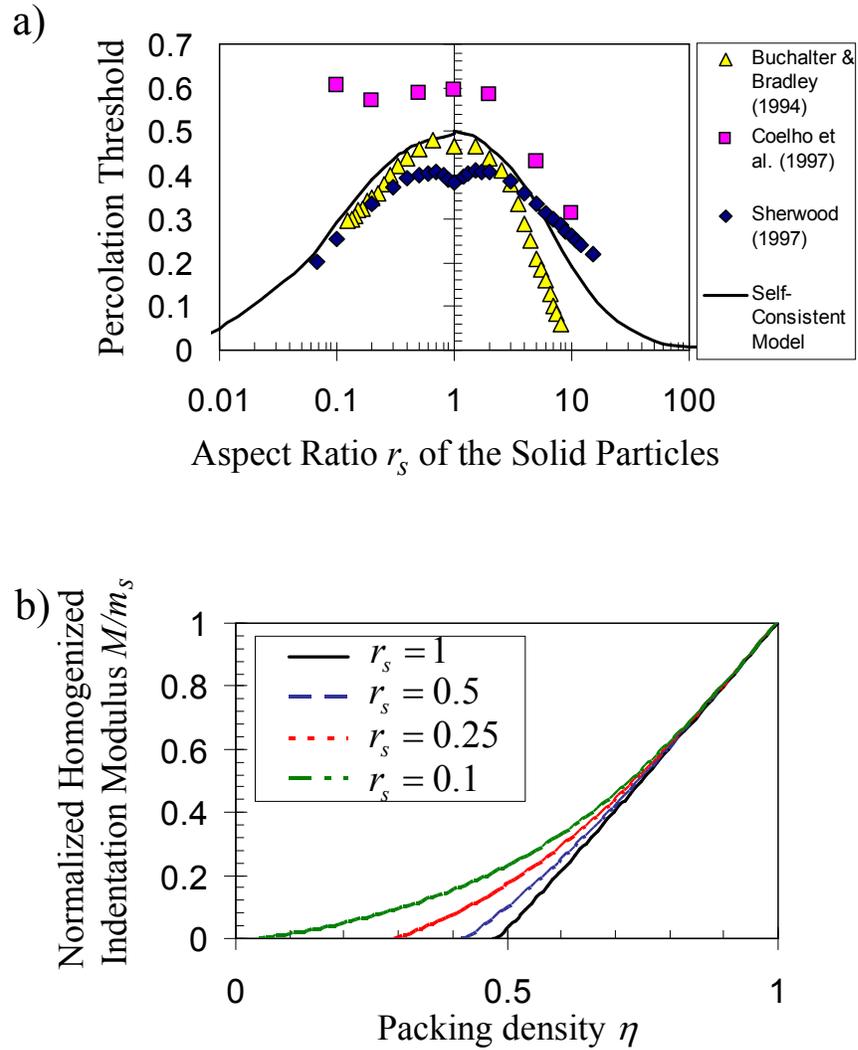
Figure 4-5: Effect of the solid particle aspect ratio r^s of the solid particles (a) on the percolation threshold and (b) on the indentation modulus–packing density $(M/m_s - \eta)$ scaling relations.

threshold of a randomly oriented polycrystal material depends on the particle shape, which is in very good agreement with granular physics results. Indeed, the packing of particles is a focus of attention in the granular physics community, and several researchers have attempted to understand the packing of ellipsoids. Onoda and Liniger [139] determined that the random-loose packing fraction of uniform spheres at the limit of zero gravitational force is 0.555 ± 0.005, which corresponds to a sphere packing at its rigidity-percolation threshold. Buchalter and Bradley [29] performed Monte Carlo simulations of the pouring of oblate and prolate ellipsoids, and showed that increased asphericity (prolate and oblate) yields lower percolation thresholds. Similar results have been obtained by Coelho et al. [53] and Sherwood [164] using a sequential deposition algorithm of rigid particles of different shapes. The results obtained with the polycrystal model, therefore, are quantitatively in very good agreement with granular physics results, as shown in Figure 4-5(a). This confirms, if need still be, that the self-consistent model of linear micromechanics, which originated independently from Hershey [89] and Kröner [107], recognizes the percolation threshold associated with granular materials. Kröner's original work considered a perfectly random distribution of contact surfaces between particles. This averaged random contact may be represented, mechanically, by a sphere. For the spherical case, the percolation threshold of the polycrystal model is $\eta_0 = 1/2$ (Fig. 4-3b). While a sphere itself is a 'perfectly disordered' particle shape in the context of the self-consistent model [199], non-spherical shapes introduce some order to the system, leading to a percolation threshold below $\eta_0 < 0.5$.

This dependence of the percolation threshold on the particle shape affects the indentation modulus – packing density scaling particularly around the percolation threshold (Fig. 4-5b), that is for loosely packed granular materials close to the minimum packing density at which the material is able to sustain a load. In contrast, for higher packing densities, the effect of the particle size on the modulus–packing density scaling vanishes, and above a packing density of $\eta \simeq 0.6$ the shape of the solid particles has virtually no effect on the scaling of the indentation modulus with the packing density η. Otherwise said, for highly packed systems ($\eta > 0.6$), micromechanics alone cannot resolve order in the particle shape when understanding and predicting the mechanical response of the composite response, as the influence of the particle shape is negligible in linking mechanical properties to microstructure. In this case, it

seems prudent to consider a spherical particle morphology for micromechanics analysis of the indentation modulus of a highly packed system.

Finally, the unique link between particle shape and percolation threshold for randomly oriented granular materials (i.e., see Fig. 4-5b) proves that the key morphological parameter that affects the indentation modulus – packing density scaling is the percolation threshold, which varies as a function of the particle shape, $\eta_0 = \eta_0(r_s)$, between $\eta_0 = 0$ for a matrix–inclusion morphology and $\eta_0 = 1/2$ for spherical solid particles.

4.3 Hardness–Packing Density Scaling Relations

4.3.1 Dimensional Analysis

Consider the indentation hardness of an indentation test:

$$H = \frac{P}{A_c} \tag{4.43}$$

The hardness is assumed to be representative of only the strength properties of the indented material, as discussed in detail in Section 2.4. Consider then that H is the indentation hardness of a two-phase (solid plus pore) composite that satisfies the scale separability condition (4.1). The composite indentation hardness H thus depends on the strength properties of the solid phase (cohesion c_s, friction coefficient α_s; see Section 2.4.2) and on the microstructure (packing density η and percolation threshold $X = \eta_0$); that is, in a dimensionless form:

$$\boxed{\frac{H}{h_s} = \Pi_H(\alpha_s, \eta, X = \eta_0, \theta)} \tag{4.44}$$

where $h_s = \lim_{\eta \to 1} H$ is the asymptotic hardness of a cohesive–frictional solid phase that obeys the Drucker-Prager criterion (Section 2.4.2). This asymptotic value does not depend on the morphology of the solid phase, but relates only to the solid's cohesion c_s and friction coefficient α_s through relation (2.89), which we recall:

$$\frac{h_s}{c_s} = A(1 + B\alpha_s + (C\alpha_s)^3 + (D\alpha_s)^{10}) \tag{4.45}$$

with:

$$\begin{cases} A = 4.76438 \\ B = 2.5934 \\ C = 2.1860 \\ D = 1.6777 \end{cases}$$

This Section reports recent results of indentation analysis of the hardness–packing density scaling relation Π_H for Berkovich indentation ($\theta = 70.32°$). Based on the scale separability condition (4.1), the analysis is performed in two steps: (1) Homogenization of the strength behavior of the composite at the scale of the *rev*; (2) determination of the hardness–packing density scaling from indentation yield design analogous to the approach presented in Section 2.4.2. These steps are detailed below. Along the way, a brief introduction to the elements of non-linear strength homogenization is presented, which is inspired by the work of Gathier [80].

4.3.2 Elements of Strength Homogenization Theory

The goal of strength homogenization is to derive the macroscopic strength domain of a heterogenous material from knowledge of the microscopic strength domains of the different material phases that make up a composite material. Yield design theory provides a useful framework for strength homogenization.

Yield Design Formulation

Yield design aims to find the macroscopic load, $\boldsymbol{\Sigma}$, corresponding to the plastic collapse of the composite material. The strength domain of phase i is denoted by G_i. The behavior of each phase at plastic collapse is assumed to follow the principle of maximum dissipation, linking the stress, $\boldsymbol{\sigma}$, on the boundary of G_i to the strain rate, $\mathbf{d}$, by:

$$\boldsymbol{\sigma} = \frac{\partial \pi_i(\mathbf{d})}{\partial \mathbf{d}} \tag{4.46}$$

where $\pi_i(\mathbf{d})$ is the maximum dissipation capacity of phase i:

$$\pi_i(\mathbf{d}) = \sup_{\boldsymbol{\sigma}^* \in G_i} \boldsymbol{\sigma}^* : \mathbf{d} \tag{4.47}$$

Then, subjecting a representative elementary volume of the composite material (*rev*) to a homogeneous strain rate boundary condition and recalling the static admissibility of the stress field solution to the problem formulated in strain rates, we can summarize the equations of the problem as follows:

$$\underline{\mathrm{div}}(\boldsymbol{\sigma}) = 0 \qquad\qquad \text{in } V \qquad\qquad (4.48\text{a})$$

$$\boldsymbol{\sigma} = \frac{\partial \pi_i}{\partial \mathbf{d}}(\mathbf{d}) \qquad\qquad \text{in } V_i \qquad\qquad (4.48\text{b})$$

$$\mathbf{d} = \frac{1}{2}\left(\mathbf{grad}\,\underline{v} + {}^t\mathbf{grad}\,\underline{v}\right) \qquad\qquad \text{in } V \qquad\qquad (4.48\text{c})$$

$$\underline{v} = \mathbf{D} \cdot \underline{x} \qquad\qquad \text{on } \partial V \qquad\qquad (4.48\text{d})$$

Then, from convex analysis [61] [158], we can show that the maximum dissipation capacity of the system:

$$\Pi^{\mathrm{hom}}\left(\mathbf{D}\right) = \sup_{\boldsymbol{\Sigma} \in G^{\mathrm{hom}}} \boldsymbol{\Sigma} : \mathbf{D}$$
$$\text{with} \qquad \boldsymbol{\Sigma} = \langle \boldsymbol{\sigma} \rangle_V = \overline{\boldsymbol{\sigma}} \qquad\qquad (4.49)$$

is the solution to the variational problem:

$$\Pi^{\mathrm{hom}}\left(\mathbf{D}\right) = \inf_{\underline{v}^* \in \mathcal{K}(\mathbf{D})} \overline{\pi\left(\mathbf{d}\left(\underline{v}^*\right), \underline{x}\right)} \qquad\qquad (4.50)$$

where $\mathcal{K}\left(\mathbf{D}\right)$ is the set of kinematically admissible strain rates:

$$\mathcal{K}\left(\mathbf{D}\right) = \{\underline{v}^*\left(\underline{x}\right) | \underline{v}^*\left(\underline{x}\right) = \mathbf{D} \cdot \underline{x} \quad \text{on } \partial V\} \qquad\qquad (4.51)$$

Analogously to the microscopic quantities, we obtain the following relation between the macroscopic stress at plastic collapse, $\boldsymbol{\Sigma}$, and the macroscopic strain rate, $\mathbf{D}$:

$$\boldsymbol{\Sigma} = \frac{\partial \Pi^{\mathrm{hom}}}{\partial \mathbf{D}} \qquad\qquad (4.52)$$

LCC Homogenization Method

Consequently, the aim of our strength homogenization approach is to estimate the solution to system (4.48). It is important to note that the plastic behavior of each phase (4.48b) introduces

127

a strong non-linearity to the problem and prevents the use of linear micromechanics techniques. Methods based on Effective Strain Rates have been recently proposed [10], [159]. In order to be less restrictive, however, we employ the more general concept of Linear Comparison Composite (LCC), introduced by Castañeda [35] [36] [37].

The principle of the LCC approach is to approximate the non-linear behavior by a linear one with suitably chosen stiffness parameters. We consider a fictitious comparison composite in which the behavior of each phase is given by:

$$\boldsymbol{\sigma} = \mathbb{C}_i : \mathbf{d} + \boldsymbol{\tau}_i \tag{4.53}$$

The corresponding strain rate energy of the composite material is:

$$\omega_0 \left(\underline{x}, \mathbf{d} \right) = \sum_i \chi \left(\underline{x} \right) \ \omega_i \left(\mathbf{d} \right)$$
$$\text{with} \quad \omega_i \left(\mathbf{d} \right) = \frac{1}{2} \mathbf{d} : \mathbb{C}_i : \mathbf{d} + \boldsymbol{\tau}_i : \mathbf{d} \tag{4.54}$$

Then, recalling the classical inequality

$$\inf_x \left(f \left(x \right) + g \left(x \right) \right) \geq \inf_x \left(f \left(x \right) \right) + \inf_x \left(g \left(x \right) \right) \tag{4.55}$$

and applying it to $\omega_0 = \pi + \omega_0 - \pi$, we obtain

$$\inf_{\underline{v}^* \in \mathcal{K}(\mathbf{D})} \overline{\omega_0 \left(\underline{x}, \mathbf{d} \left(\underline{v}^* \right) \right)} \geq \inf_{\underline{v}^* \in \mathcal{K}(\mathbf{D})} \overline{\pi \left(\underline{x}, \mathbf{d} \left(\underline{v}^* \right) \right)} + \inf_{\underline{v}^* \in \mathcal{K}(\mathbf{D})} \overline{\omega_0 \left(\underline{x}, \mathbf{d} \left(\underline{v}^* \right) \right) - \pi \left(\underline{x}, \mathbf{d} \left(\underline{v}^* \right) \right)} \tag{4.56}$$

where we recognize $\Pi^{\text{hom}} \left(\mathbf{D} \right)$:

$$\Pi^{\text{hom}} \left(\mathbf{D} \right) \leq \inf_{\underline{v}^* \in \mathcal{K}(\mathbf{D})} \overline{\omega_0 \left(\underline{x}, \mathbf{d} \left(\underline{v}^* \right) \right)} - \inf_{\underline{v}^* \in \mathcal{K}(\mathbf{D})} \overline{\omega_0 \left(\underline{x}, \mathbf{d} \left(\underline{v}^* \right) \right) - \pi \left(\underline{x}, \mathbf{d} \left(\underline{v}^* \right) \right)} \tag{4.57}$$

The first term of the right hand side is the macroscopic strain rate energy $\mathcal{W}_0 \left(\mathbf{D} \right)$ of the LCC:

$$\mathcal{W}_0 \left(\mathbf{D} \right) = \mathcal{W}_0 \left(\mathbf{D} \right) = \inf_{\underline{v}^* \in \mathcal{K}(\mathbf{D})} \overline{\omega_0 \left(\underline{x}, \mathbf{d} \left(\underline{v}^* \right) \right)} \tag{4.58}$$

The second term can be overestimated by:

$$-\inf_{\underline{v}^* \in \mathcal{K}(\mathbf{D})} \overline{\omega_0\left(\underline{x}, \mathbf{d}\left(v^*\right)\right) - \pi\left(\underline{x}, \mathbf{d}\left(v^*\right)\right)} \geq \sum_i \phi_i \, \mathcal{V}_i \tag{4.59}$$

where $\mathcal{V}_i$ is constant in each phase of volume fraction ϕ_i:

$$\mathcal{V}_i = \sup_{\mathbf{d}} \overline{\pi_i\left(\mathbf{d}\right) - \omega_i\left(\mathbf{d}\right)} \tag{4.60}$$

Finally, we obtain the following upper bound for Π^{hom}:

$$\Pi^{\mathrm{hom}}\left(\mathbf{D}\right) \leq \mathcal{W}_0\left(\mathbf{D}\right) + \sum_i \phi_i \, \mathcal{V}_i \tag{4.61}$$

The goal, therefore, is to find the stiffness parameters of the comparison composite that lead to the lowest possible upper bound, thus yielding the best possible estimate of Π^{hom}. Preserving a true upper bound status, however, may sometimes prove difficult, and we can replace the infima or maxima by stationary points [37]. The resulting estimates are then stationary variational estimates and not bounds in general. This new estimate, $\widetilde{\Pi}^{\mathrm{hom}}$, reads:

$$\widetilde{\Pi}^{\mathrm{hom}}\left(\mathbf{D}\right) = \operatorname*{stat}_{\mathbb{C}_i, \boldsymbol{\tau}_i} \left[\mathcal{W}_0\left(\mathbf{D}\right) + \sum_i \phi_i \, \mathcal{V}_i \right] \tag{4.62}$$

with

$$\mathcal{V}_i = \operatorname*{stat}_{\mathbf{d}} \left\{ \pi_i\left(\mathbf{d}\right) - \omega_i\left(\mathbf{d}\right) \right\} \tag{4.63}$$

There are usually different points of stationarity, which is why each particular case must be analyzed separately [37]. The method is summarized in 3 main steps:

1. Compute the expression of the macroscopic strain rate energy, $\mathcal{W}_0\left(\mathbf{D}\right)$, in the Linear Comparison Composite. This expression is obtained from linear micromechanics.

2. Compute, for each phase, the expression of $\mathcal{V}_i$, which measures the non-linearity of the original material and contains information on the local strength domain.

3. Formulate the stationarity equations (Eqs. 4.62 and 4.63) and solve the system in terms of $\mathbb{C}_i$ and $\boldsymbol{\tau}_i$. The corresponding estimate of the macroscopic plastic dissipation capacity,

$\widetilde{\Pi}^{\text{hom}}(\mathbf{D})$, allows generation of the macroscopic strength criterion (Eq. 4.52).

This methodology is applied next for the two-phase solid-pore composite of interest.

4.3.3 Application to the Solid–Pore Composite

Here a two-phase solid-pore composite is considered. The solid phase strength properties are governed by a Drucker-Prager model of cohesion c_s and friction coefficient α_s. For reasons of convexity, the strength domain is described by the regularized hyperbolic criterion (2.71):

$$f(\boldsymbol{\sigma}) = 1 - \left(\frac{\sigma_m - S_0}{A}\right)^2 + \left(\frac{\sigma_d}{\sqrt{2}B}\right)^2 \leq 0 \tag{4.64}$$

where $\sigma_m = \frac{1}{3}I_1 = \frac{1}{3}tr(\boldsymbol{\sigma})$ and $\sigma_d = \sqrt{2J_2} = \sqrt{\mathbf{S}:\mathbf{S}}$ with $\mathbf{S} = \boldsymbol{\sigma} - \sigma_m\mathbf{1}$. The dual definition of the strength domain in terms of the π function is given by (2.79):

$$\pi(\mathbf{d}) = \pi(d_v, d_d) = S_0 d_v - \sqrt{(Ad_v)^2 - \left(\sqrt{2}Bd_d\right)^2} \tag{4.65}$$

where $d_v = \text{tr}\,\mathbf{d} = I_1'$ and $d_d = \sqrt{\boldsymbol{\delta}:\boldsymbol{\delta}} = \sqrt{2J_2'}$. The Drucker-Prager model is obtained from (2.72):

$$\begin{cases} B = \alpha_s\,A \\ S_0 = \dfrac{c_s}{\alpha_s} \\ A \to 0 \end{cases} \tag{4.66}$$

Step 1: Strain Rate Energy Function $\mathcal{W}_0(\mathbf{D})$ of the Linear Comparison Composite

The first step in solving the strength homogenization problem is to determine the strain rate energy function $\mathcal{W}_0(\mathbf{D})$ of the linear comparison composite (LCC). Consider the porous composite composed of a solid phase (volume fraction η) and porosity $\varphi = 1 - \eta$. It is convenient to apply a two-phase description of the microscopic stiffness $\mathbb{C}(\underline{x})$ and prestress $\boldsymbol{\tau}(\underline{x})$, with spatial distribution within the *rev* given by:

$$\mathbb{C}(\underline{x}) = \begin{cases} \mathbb{C}_s = 3k_s\mathbb{J} + 2g_s\mathbb{K} & \text{in } V_s \\ 0 & \text{in } V_p \end{cases} ; \ \boldsymbol{\tau}(\underline{x}) = \begin{cases} \tau\mathbf{1} & \text{in } V_s \\ 0 & \text{in } V_p \end{cases} \tag{4.67}$$

where V_s stands for the domain occupied by the solid phase and V_p stands for the domain occupied by the voids.

Using Levin's theory [70], the corresponding macroscopic stress equation of state reads [80]:

$$\boldsymbol{\Sigma} = \mathbb{C}^{\text{hom}} : \mathbf{D} + \mathbf{T} \tag{4.68}$$

where $\mathbb{C}^{\text{hom}}$ and $\mathbf{T}$ are respectively the macroscopic stiffness tensor and the macroscopic pre-stress given by:

$$\mathbb{C}^{\text{hom}} = \overline{\mathbb{C}\left(\underline{x}\right) : \mathbb{A}\left(\underline{x}\right)} = \mathbb{C}_s : \eta \overline{\mathbb{A}}^s = 3K^{\text{hom}}\mathbb{J} + 2G^{\text{hom}}\mathbb{K} \tag{4.69a}$$

$$\mathbf{T}^I = \overline{\boldsymbol{\tau}\left(\underline{x}\right) : \mathbb{A}\left(\underline{x}\right)} = \tau\mathbf{1} : \eta \overline{\mathbb{A}}^s = \tau\mathbf{1} : \mathbb{C}_s^{-1} : \mathbb{C}^{\text{hom}} = \tau\frac{K^{\text{hom}}}{k_s}\mathbf{1} \tag{4.69b}$$

with:

$$K^{\text{hom}} = \eta \, K_s \, \mathbb{J} : \overline{\mathbb{A}}^s = G \, \mathcal{K}\left(\frac{k_s}{g_s}, \eta, \eta_0\right) \tag{4.70a}$$

$$G^{\text{hom}} = \eta \, G \, \mathbb{K} : \overline{\mathbb{A}}^s = G\mathcal{M}\left(\frac{k_s}{g_s}, \eta, \eta_0\right) \tag{4.70b}$$

where $\mathbb{A}\left(\underline{x}\right)$ is the fourth-order strain (rate) localization tensor and $\overline{\mathbb{A}}^s$ the volume average of $\mathbb{A}\left(\underline{x}\right)$ over the solid phase. The second part of the equalities are readily obtained from dimensional analysis, where k_s/g_s is the bulk–to–shear modulus ratio of the solid phase, while the dimensionless functions $\mathcal{K}$ and $\mathcal{M}$ are morphological factors which depend on the solid's bulk–to–shear modulus ratio, the pore morphology, and the solid concentration η, as detailed later on.

The strain rate energy function $\mathcal{W}_0\left(\mathbf{D}\right)$ is obtained by an application of linear homogenization theory. The resulting strain rate energy function for the solid–void composite is [80]:

$$\begin{aligned}
\mathcal{W}_0\left(D_v, D_d\right) &= \frac{1}{2}K^{\text{hom}}D_v^2 + G^{\text{hom}}D_d^2 + \frac{K^{\text{hom}}}{k_s}\tau D_v + \frac{1}{2k_s}\left(\frac{K^{\text{hom}}}{k_s} - \eta\right)\tau^2 \tag{4.71}\\
&= \frac{1}{2}g_s \, \mathcal{K}D_v^2 + g_s \, \mathcal{M}D_d^2 + \frac{g_s}{k_s}\mathcal{K}\tau D_v + \frac{1}{2k_s}\left(\frac{g_s}{k_s}\mathcal{K} - \eta\right)\tau^2
\end{aligned}$$

where $D_v = \text{tr}\left(\mathbf{D}\right)$ and $D_d = \sqrt{\boldsymbol{\Delta} : \boldsymbol{\Delta}}$ with $\boldsymbol{\Delta} = \mathbf{D} - \frac{1}{3}D_v\mathbf{1}$.

Step 2: $\mathcal{V}$ Function

The second step consists of determining the $\mathcal{V}$ function (Eq. 4.63) for the solid phase ($\mathcal{V}$ for the pore space is zero). This requires the expression of the π-function (Eq. 2.79) along with an expression for the strain rate energy of the solid:

$$\omega_s\left(\mathbf{d}\right) = \frac{1}{2}k_s d_v^2 + g_s d_d^2 + \tau d_v \tag{4.72}$$

Then, applying the stationarity condition to the $\mathcal{V}$ function implies that:

$$k_s d_v + \tau \;=\; S_0 - \frac{A^2 d_v}{\sqrt{\left(A d_v\right)^2 - \left(\sqrt{2}B d_d\right)^2}} \tag{4.73a}$$

$$2 g_s d_d \;=\; \frac{2B^2 d_d}{\sqrt{\left(A d_v\right)^2 - \left(\sqrt{2}B d_d\right)^2}} \tag{4.73b}$$

The microscopic stiffness components k_s and g_s of the linear comparison composite must be positive. Introduction of the prestress provides a means to ensure that k_s and g_s are positive by requiring that:

$$\tau \;=\; S_0 - \frac{2A^2 d_v}{\sqrt{\left(A d_v\right)^2 - \left(\sqrt{2}B d_d\right)^2}} \tag{4.74a}$$

$$k_s \;=\; \frac{A^2}{\sqrt{\left(A d_v\right)^2 - \left(\sqrt{2}B d_d\right)^2}} > 0 \tag{4.74b}$$

$$g_s \;=\; \frac{B^2}{\sqrt{\left(A d_v\right)^2 - \left(\sqrt{2}B d_d\right)^2}} > 0 \tag{4.74c}$$

Then we have just two independent parameters for the behavior of the comparison composite, τ and g_s; since:

$$\frac{k_s}{g_s} = \frac{A^2}{B^2} = const. \tag{4.75}$$

and for the Drucker-Prager case (Eqs. (4.66)):

$$\frac{k_s}{g_s} = \frac{A^2}{B^2} = \frac{1}{\alpha_s^2} \tag{4.76}$$

These expressions yield the sought-after expression of $\mathcal{V}$ for the hyperbolic criterion as a function of the independent parameters τ and g_s:

$$\mathcal{V}_s = \left(\frac{B\left(S_0 - \tau\right)}{2A}\right)^2 \frac{1}{g_s} - \frac{1}{2}\frac{B^2}{g_s} \tag{4.77}$$

In the Drucker-Prager case (Eqs. 4.66), $\mathcal{V}_s$ becomes:

$$\mathcal{V}_s = (c_s - \alpha\tau)^2 \frac{1}{4g_s} \tag{4.78}$$

Step 3: Stationarity of $\widetilde{\Pi}^{\mathrm{hom}}$

The third step consists in exploring the stationarity of $\widetilde{\Pi}^{\mathrm{hom}}$, i.e., Eq. (4.62). Note, however, that Eq. (4.75) reduces the degrees of freedom from three $(k_s, g_s, \boldsymbol{\tau})$ to two $(g_s, \boldsymbol{\tau})$, such that:

$$\widetilde{\Pi}^{\mathrm{hom}} = \underset{G,\boldsymbol{\tau}}{\mathrm{stat}}\left[\mathcal{W}_0\left(D_v, D_d\right) + \eta\mathcal{V}_s\right] \tag{4.79}$$

The condition is explicitly expressed as:

$$\frac{\partial\widetilde{\Pi}^{\mathrm{hom}}}{\partial g_s} = \frac{\partial K}{\partial g_s}\frac{\partial\mathcal{W}_0}{\partial g_s} + \frac{\partial\mathcal{W}_0}{\partial g_s} + \eta\frac{\partial\mathcal{V}_s}{\partial g_s} = 0 \tag{4.80a}$$

$$\frac{\partial\widetilde{\Pi}^{\mathrm{hom}}}{\partial\tau} = \frac{\partial\mathcal{W}_0}{\partial\tau} + \eta\frac{\partial\mathcal{V}_s}{\partial\tau} = 0 \tag{4.80b}$$

Using Eq. (4.71) and Eq. (4.77) in Eq. (4.80b) while making use of Eq. (4.75) yields:

$$\tau = \frac{A^2\left(2\mathcal{K}g_s D_v - \eta S_0\right)}{\eta A^2 - 2\mathcal{K}B^2} \tag{4.81}$$

Then, substituting Eq. (4.81) into Eq. (4.80a) gives:

$$g_s^2 = \frac{B^2}{A^2}\frac{\eta\left(\eta A^2\left(S_0^2 - A^2\right) + \mathcal{K}B^2\left(2A^2 - S_0^2\right)\right)}{\left(\eta\mathcal{K}A^2 D_v^2 + \left(2\eta\mathcal{M}A^2 - 4\mathcal{K}\mathcal{M}B^2\right)D_d^2\right)} \tag{4.82}$$

Finally, using the values of (g_s, τ) corresponding to the stationarity of $\widetilde{\Pi}^{\mathrm{hom}}$ in Eq. (4.79) provides the following estimate for $\widetilde{\Pi}^{\mathrm{hom}}$:

$$\boxed{\widetilde{\Pi}^{\mathrm{hom}} = \Sigma_0^{\mathrm{hom}} D_v - \mathrm{sign}\left(2\mathcal{K}B^2 - \eta A^2\right)\sqrt{\left(A^{\mathrm{hom}}\right)^2 D_v^2 + 2\left(B^{\mathrm{hom}}\right)^2 D_d^2}} \qquad (4.83)$$

where:

$$\left(A^{\mathrm{hom}}\right)^2 = \frac{\eta^2 B^2 \mathcal{K}\left(\eta A^2\left(S_0^2 - A^2\right) + B^2\left(2A^2 - S_0^2\right)\mathcal{K}\right)}{\left(\eta A^2 - 2\mathcal{K}B^2\right)^2} \qquad (4.84\mathrm{a})$$

$$\left(B^{\mathrm{hom}}\right)^2 = \frac{\eta B^2 \mathcal{M}\left(\eta A^2\left(S_0^2 - A^2\right) + B^2\left(2A^2 - S_0^2\right)\mathcal{K}\right)}{A^2\left(\eta A^2 - 2B^2 \mathcal{K}\right)} \qquad (4.84\mathrm{b})$$

$$\Sigma_0^{\mathrm{hom}} = \frac{\eta B^2 \mathcal{K}}{2\mathcal{K}B^2 - \eta A^2} S_0 \qquad (4.84\mathrm{c})$$

A comparison of Eq. (4.83) with Eq. (2.79) readily reveals that Eq. (4.83) is the Π function of a hyperbolic criterion provided that $2\mathcal{K}B^2 - \eta A^2 > 0$. In return, for $2\mathcal{K}B^2 - \eta A^2 < 0$, the function $\widetilde{\Pi}^{\mathrm{hom}}$ corresponds to an elliptical strength criterion:

$$\boxed{\frac{\left(\Sigma_m - \Sigma_0^{\mathrm{hom}}\right)^2}{\left(A^{\mathrm{hom}}\right)^2} + \frac{\left(\Sigma_d/\sqrt{2}\right)^2}{\left(B^{\mathrm{hom}}\right)^2} = 1} \qquad (4.85)$$

More generally, depending on the sign of the term $\left(B^{\mathrm{hom}}\right)^2$, the strength criterion can be either an ellipse $\left(\left(B^{\mathrm{hom}}\right)^2 > 0\right)$ or a hyperbola $\left(\left(B^{\mathrm{hom}}\right)^2 < 0\right)$, as displayed in Figure 4-6.

From its definition (4.84b), it is recognized that the sign of $\left(B^{\mathrm{hom}}\right)^2$ depends on the sign of $\eta A^2 - 2\mathcal{K}B^2$, that is:

$$\mathrm{sign}\left(\left(B^{\mathrm{hom}}\right)^2\right) = \mathrm{sign}\left(\eta A^2 - 2\mathcal{K}B^2\right) = \begin{cases} -1 & \text{Hyperbolic Criterion} \\ 0 & \text{Limit Parabola} \\ +1 & \text{Elliptical Criterion} \end{cases} \qquad (4.86)$$

In the Drucker-Prager case (Eqs. 4.66), the strength homogenization factors (Eq. 4.84)
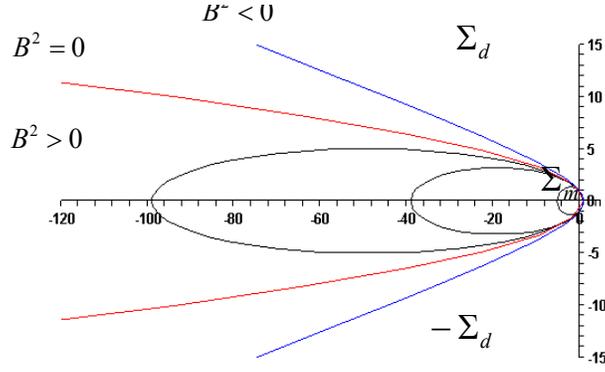
Figure 4-6: Illustration of strength criterion: Elliptical criterion, $\left(B^{\mathrm{hom}}\right)^2 > 0$, limit parabola $\left(B^{\mathrm{hom}}\right)^2 = 0$, and hyperbola $\left(B^{\mathrm{hom}}\right)^2 < 0$. In the $\Sigma_m \times \Sigma_d$ plane, the criterion is a half-ellipse, half-parabola and half-hyperbola, and full drawing here to negative values, $-\Sigma_d$, is for illustration only. (from [34]).

simplify:

$$\left(\frac{A^{\mathrm{hom},I}}{c_s}\right)^2 = \frac{\eta^2 \mathcal{K}\left(\eta - \alpha_s^2 \mathcal{K}\right)}{\left(\eta - 2\alpha_s^2 \mathcal{K}\right)^2} \tag{4.87a}$$

$$\left(\frac{B^{\mathrm{hom},I}}{c_s}\right)^2 = \frac{\eta \mathcal{M}\left(\eta - \alpha_s^2 \mathcal{K}\right)}{\eta - 2\alpha_s^2 \mathcal{K}} \tag{4.87b}$$

$$\frac{\Sigma_0^{\mathrm{hom},I}}{c_s} = \frac{\eta \alpha_s \mathcal{K}}{2\mathcal{K}\alpha_s^2 - \eta} \tag{4.87c}$$

and the class of criterion is now determined by the sign of $X = 2\alpha_s^2 \mathcal{K} - \eta$: $X > 0$ for an hyperbole, $X < 0$ for an ellipse:

$$\eta - 2\alpha_s^2 \mathcal{K}\left(\frac{k_s}{g_s} = \frac{1}{\alpha_s^2}, \eta\right)\begin{cases} < 0 & \text{Hyperbolic Criterion} \\ = 0 & \text{Limit Parabola} \\ > 0 & \text{Elliptical Criterion} \end{cases} \tag{4.88}$$

135

Pore Morphology Factors

We are left with specifying the pore morphology factors:

$$\frac{K^{\text{hom}}}{g_s} = \mathcal{K}\left(\frac{k_s}{g_s}, \eta, \eta_0\right) \tag{4.89}$$

$$\frac{G^{\text{hom}}}{g_s} = \mathcal{M}\left(\frac{k_s}{g_s}, \eta, \eta_0\right) \tag{4.90}$$

Their determination is based on linear homogenization theory, in which the solid's bulk –to–shear modulus ratio is replaced by relation (4.76). The two 'limit' morphologies depicted in Figure 4-1 are considered:

- For a matrix–pore morphology (Fig. 4-1a), characterized by a percolation threshold $\eta_0 = 0$, the results of linear homogenization for a Mori-Tanaka scheme, (4.31) and (4.32), yield:

$$\mathcal{K}^{MT} = \mathcal{K}\left(\frac{k_s}{g_s} = \frac{1}{\alpha_s^2}, \eta, \eta_0 = 0\right) = \frac{4\eta}{3(1-\eta) + 4\alpha_s^2} \tag{4.91}$$

$$\mathcal{M}^{MT} = \mathcal{M}\left(\frac{k_s}{g_s} = \frac{1}{\alpha_s^2}, \eta, \eta_0 = 0\right) = \frac{\eta\left(9 + 8\alpha_s^2\right)}{15 - 6\eta + (20 - 12\eta)\alpha_s^2} \tag{4.92}$$

- For a polycrystal morphology (Fig. 4-1b), characterized by a percolation threshold $\eta_0 = 1/2$, the results of linear homogenization for a self-consistent scheme, (4.35) and (4.36), yield:

$$\mathcal{K}^{SC} = \mathcal{K}\left(\frac{k_s}{g_s} = \frac{1}{\alpha_s^2}, \eta, \eta_0 = 0.5\right) = \frac{4\eta\,\mathcal{M}_{sc}}{4\alpha_s^2\,\mathcal{M}_{sc} + 3\left(1-\eta\right)} \tag{4.93}$$

$$\mathcal{M}^{SC} = \mathcal{M}\left(\frac{k_s}{g_s} = \frac{1}{\alpha_s^2}, \eta, \eta_0 = 0.5\right) = \frac{1}{2} - \frac{5}{4}\left(1-\eta\right) - \frac{3}{16\alpha_s^2}\left(2+\eta\right) \tag{4.94}$$
$$+ \frac{1}{16\alpha_s^2}\sqrt{144\left(\alpha_s^4 - \alpha_s^2\right) - 480\alpha_s^4\eta + 400\alpha_s^4\eta^2 + 408\alpha_s^2\eta - 120\alpha_s^2\eta^2 + 9\left(2+\eta\right)^2}$$

The description of the homogenized strength domain of the solid–pore composite is then complete.

4.3.4 Hardness–Packing Density Scaling Relations for Specific Pore Morpho–logies

The strength criterion of the *rev* can now be used for the determination of hardness–packing density scaling relations (4.44) in functions of the solid's friction coefficient and the pore morphology. To make this mapping of the normalized hardness, the numerical Limit Analysis Solver presented in Section 2.4.2 is employed.[4] In order to map the values of the hardness/cohesion ratio for any parameter of the system, we vary $\alpha_s \in [0, \sqrt{3/4}[$ and $\eta \in [0.5, 1]$. This mapping covers the entire range of both the elliptical strength domain, $\eta \in [\eta_0, \eta_{cr}[$, and the hyperbolic strength domain, $\eta \in \,]\eta_{cr}, 1]$, according to:

$$\eta - \eta_{cr}\left(\alpha_s, \eta_0\right) \begin{cases} > 0 & \text{Hyperbolic Criterion} \\ = 0 & \text{Limit Parabola} \\ < 0 & \text{Elliptical Criterion} \end{cases} \tag{4.95}$$

where $\eta - \eta^{cr}\left(\alpha_s, \eta_0\right)$ is the critical packing density, which depends on the pore morphology:

- For the matrix–pore morphology ($\eta_0 = 0$):

$$\eta_{cr}^{MT} = 1 - \frac{4}{3}\alpha_s^2 \leq 1 \tag{4.96}$$

- For the self-consistent morphology ($\eta_0 = 1/2$):

$$\eta_{cr}^{SC} = 1 - \frac{1}{2}\frac{\sqrt{81 + 432\alpha_s^2 + 1216\alpha_s^4} - \left(9 + 16\alpha_s^2\right)}{3 + 20\alpha_s^2} \leq 1 \tag{4.97}$$

The Limit Analysis Solver would not converge, however, for high values of α_s (i.e., $\alpha_s > 1/\sqrt{3} = 0.577\,35$). The reason for this computational limitation is unknown. Hence, all results below are strictly valid for $\alpha_s \in [0, \sqrt{1/3}[$.

Figure 4-7 presents a sampling of results for both the matrix–pore morphology (Fig. 4-7a) and the polycrystal morphology (Fig. 4-7b) in terms of relationships between packing density and hardness–to–cohesion ratios for various friction coefficients, α_s. Similar results were first

---

[4]The numerical implementation was performed by Prof. Lavinia A. Borges.

obtained by Cariou et al. [34] by employing an upper bound yield design approach for an elliptical strength criterion based on the work of Barthélémy and Dormieux [10].

It is possible to derive fitting functions that summarize the discrete simulation results in closed form expressions to be used for data analysis. The format of the scaling relations is chosen in the following form:

$$\frac{H}{h_s} = \Pi_1 (\eta, \eta_0) + \alpha_s (1 - \eta) \; \Pi_2 (\alpha_s, \eta, \eta_0) \qquad (4.98)$$

where the first part, $\Pi_1 (\eta, \eta_0)$, is the frictionless portion of the function, while the second part, $\alpha_s (1 - \eta) \Pi_2 (\alpha_s, \eta, \eta_0)$, captures the effect of the solid friction on the normalized hardness-packing density scaling relation. Depending on the pore morphology, the following fitted expressions for $\Pi_1 (\eta)$ and $\Pi_2 (\alpha, \eta)$ were obtained [80]:

- For the matrix–pore morphology ($\eta_0 = 0$):

$$\Pi_1^{MT} (\eta) = \eta \left(1 + a (1 - \eta) + b (1 - \eta)^2 + c (1 - \eta) \eta^3 \right) \qquad (4.99)$$
$$\Pi_2^{MT} (\alpha_s, \eta) = \alpha_s \eta^2 \left(d + e (1 - \eta) + f (1 - \eta) \alpha_s + g \alpha_s^3 \right)$$

  with
$$\text{MT:} \begin{cases} a = -1.2078 & d = 8.7145 \\ b = 0.4907 & e = -40.6615 \\ c = -1.7257 & f = 74.0617 \\ & g = -64.094 \end{cases}$$

- For the polycrystal morphology representing a perfectly disordered porous material ($\eta_0 = 1/2$):

$$\Pi_1^{SC} (\eta) = \frac{\sqrt{2 (2\eta - 1)} - (2\eta - 1)}{\sqrt{2} - 1} \left(1 + a (1 - \eta) + b (1 - \eta)^2 + c (1 - \eta)^3 \right) \qquad (4.100)$$
$$\Pi_2^{SC} (\alpha_s, \eta) = \frac{2\eta - 1}{2} \left(d + e (1 - \eta) + f (1 - \eta) \alpha_s + g \alpha_s^3 \right)$$

a)
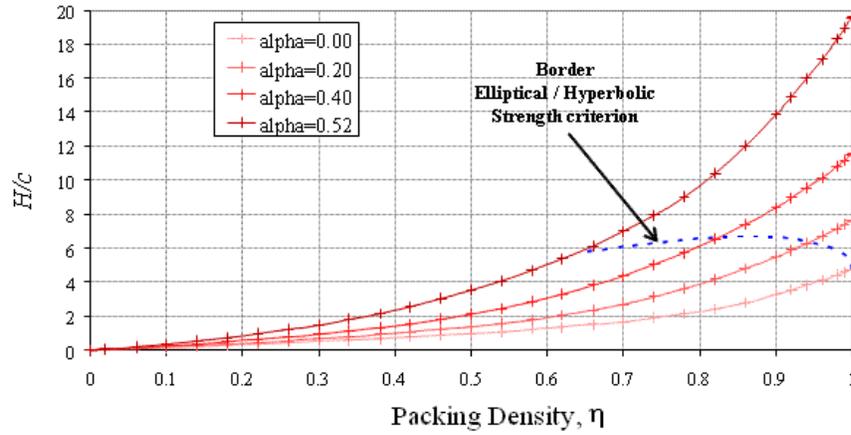
b)
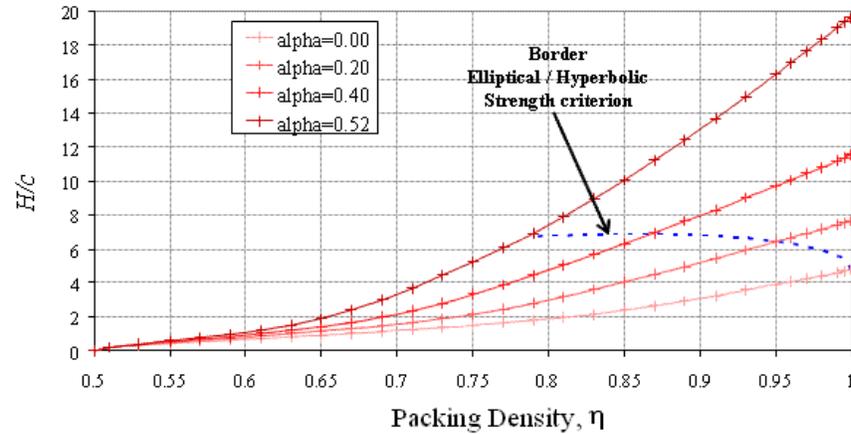
Figure 4-7: Scaling of the indentation hardness –to– cohesion ratio H/c_s of the porous composite with the packing density η and the solid friction coefficient α_s (a) using a Mori-Tanaka scheme and (b) using a Self-Consistent scheme (from [80]).

with

$$\text{SC:} \begin{cases} a = -5.3678 & d = 6.7374 \\ b = 12.1933 & e = -39.5893 \\ c = -10.3071 & f = 34.3216 \\ & g = -21.2053 \end{cases}$$

With relationships between packing density, cohesive-frictional strength parameters, and indentation hardness in place and well approximated by smooth, closed-form fitting functions, an inverse approach to analysis of nanoindentation results is possible.

4.4 Scaling of Creep Properties with Packing Density

This Section focuses on identifying the link between the creep properties of the composite and the microstructure. Within the framework of linear viscoelasticity, the solving of the viscoelastic problem is performed with the s-multiplied Laplace transform method presented in Section 2.3.3.

4.4.1 Dimensional Analysis

Consider an indentation creep test on a linear viscoelastic material. The indentation test provides access to the contact creep compliance $L(t)$ from Eqs. (3.43) and (3.47) or in rate form from Eq. (3.61):

$$L(t) = \frac{\phi h^{1+1/d}(t)}{P_{\max}} = \int_0^t \frac{2a(t)\dot{h}(t)}{P_{\max}} dt \tag{4.101}$$

where ϕ given by (3.8) condenses the indenter specific geometry parameters, $P_{\max}$ is the indentation load in a Heaviside loading, and $a(t)$ is the contact radius. For purpose of argument, we assume that the test conditions are such that the contact creep compliance characterizes the true viscoelastic properties of the indented material as discussed in detail in Chapter 3. In particular, to simplify subsequent derivations we assume that the material exhibits no plastic deformation.

Consider then, as throughout this Chapter, that $L(t)$ is the contact creep compliance of a viscoelastic solid-pore composite material which respects the scale separability conditions (4.1). Since the pore space is assumed to be empty (drained conditions), the composite viscous

behavior expressed by $L(t)$ results from the viscoelastic response of the solid phase. The contact creep compliance $L(t)$ thus depends on the solid's contact creep compliance $\ell_s(t)$, the solid's Poisson's ratio $\nu_s(t)$ (which may or may not be time-dependent), and on microstructure and morphology parameters (packing density η, percolation threshold η_0):

$$\frac{L(t)}{\ell_s(t)} = \Pi_{L(t)}(\nu_s(t), \eta, \eta_0) \tag{4.102}$$

In a similar manner, consider an indentation relaxation test, which gives access to the contact relaxation modulus $M(t)$ from (3.11) or (3.30):

$$M(t) = \frac{P(t)}{\phi h_{\max}^{1+1/d}} = M_0 \frac{P(t)}{P_{\max}} \tag{4.103}$$

where M_0 is the instantaneous elastic indentation modulus, $P_{\max}$ the instantaneous indentation force, and $P(t)$ the force relaxation history. For a solid-pore composite material, the contact relaxation modulus $M(t)$ depends on:

$$\frac{M(t)}{m_s(t)} = \Pi_{M(t)}(\nu_s(t), \eta, \eta_0) \tag{4.104}$$

where $m_s(t)$ is the solid's contact relaxation modulus.

4.4.2 Time–Independent Poisson's Ratio of the Solid Phase

In the case of a time-independent Poisson's ratio of the solid phase (as frequently admitted in viscoelastic indentation analysis [103] [141])[5], the dimensionless functions $\Pi_{L(t)}$ and $\Pi_{M(t)}$ defined by (4.102) and (4.104) are readily recognized to be time-independent as well. In particular, $\Pi_M(\nu_s = cst, \eta, \eta_0)$ is recognized as the normalized instantaneous elastic indentation modulus defined by (4.3). To determine function $\Pi_L(\nu_s = cst, \eta, \eta_0)$ we take the s-multiplied

---

[5]As a reminder, a time-independent Poisson's ratio means that $K(t) \propto G(t)$; that is the time-dependent bulk relaxation and shear relaxation moduli have the same time dependency. In the Laplace domain a constant Poisson's ratio means $\widehat{\nu_s}(s) \propto 1/s$ so that $s\widehat{\nu_s}(s) = c$, where c is a constant.

Laplace transform of (4.102) and (4.104):

$$s \, \widehat{L(s)} \;=\; s \, \widehat{\ell_s(s)} \; \Pi_L(\nu_s = cst, \eta, \eta_0) \tag{4.105}$$

$$s \, \widehat{M(s)} \;=\; s \, \widehat{m_s(s)} \; \Pi_M(\nu_s = cst, \eta, \eta_0) \tag{4.106}$$

If we remind ourselves that $L(t)$ and $M(t)$, as well as $\ell_s(t)$ and $m_s(t)$, are related, in the Laplace domain, by Eq. (3.46), it follows:

$$\left(s\widehat{L(s)}\right)^{-1} = s\widehat{M(s)}; \quad \left(s\widehat{\ell_s(s)}\right)^{-1} = s \, \widehat{m_s(s)}$$

$$\Downarrow \tag{4.107}$$

$$\frac{1}{\Pi_L(\nu_s = cst, \eta, \eta_0)} = \Pi_M(\nu_s = cst, \eta, \eta_0)$$

Thus, for a time-independent Poisson's ratio of the solid phase, the following deserves attention:

1. The creep rate of the composite, $\dot{L}(t)$, scales linearly with the solid's creep rate, i.e.,

$$\boxed{\dot{L}(t) = \frac{1}{\Pi_M(\nu_s, \eta, \eta_0)} \dot{\ell}_s(t)} \tag{4.108}$$

For instance, if the contact creep rate of the solid phase is governed by a Maxwell unit, $\dot{\ell}_s \propto 1/\varsigma_s$, then the contact creep rate of the composite is also governed by a Maxwell unit, $\dot{L} \propto 1/\varsigma^{\mathrm{hom}}$, and the viscosities are related by:

$$\frac{\varsigma^{\mathrm{hom}}}{\varsigma_s} = \Pi_M(\nu_s, \eta, \eta_0) \tag{4.109}$$

Similarly, if the contact creep behavior of the solid phase is logarithmic with respect to time $(l_s(t) = 1/m_s + \ln(t/\tau + 1)/(4C_s)$, see Section 3.3.2) with a creep rate governed by the modulus C_s, then the contact creep behavior of the composite is also logarithmic w.r.t. time with a creep rate magnitude governed by the modulus C:

$$\frac{C}{C_s} = \Pi_M(\nu_s, \eta, \eta_0) \tag{4.110}$$

2. The scaling with the packing density of the composite creep and relaxation properties of

the composite, $L(t)$ and $M(t)$, is provided by the elastic indentation modulus – packing density scaling relations $\Pi_M(\nu_s, \eta, \eta_0)$; that is by Eq. (4.34) for a matrix–pore inclusion morphology ($\eta_0 = 0$) and by Eq. (4.37) for a perfectly disordered granular morphology ($\eta_0 = 1/2$). The composite indentation creep magnitude, therefore, should scale with the composite indentation stiffness; for instance:

$$\frac{\varsigma^{\text{hom}}}{M} = \frac{\varsigma_s}{m_s}; \text{ for Maxwell creep} \tag{4.111}$$

$$\frac{C}{M} = \frac{C_s}{m_s}; \text{ for logarithmic creep} \tag{4.112}$$

Phase

4.4.3 Deviatoric Creep of the Solid Creep

The time-dependent behavior of the solid phase is now assumed to be restricted to its shear component and governed by a Maxwell unit of shear viscosity, $\varsigma_s/4$. The factor $1/4$ is introduced so that the viscosity of the solid's *contact* creep compliance at large times is ς_s (see Section 3.3.2; Eq. (3.51)). The bulk relaxation modulus $K_s(t)$ and the shear creep compliance $J_s^d(t)$ of the solid phase are:

$$k_s(t) = k_s \to \widehat{k_s(s)} = \frac{k_s}{s} \tag{4.113}$$

$$J_s^d(t) = \frac{1}{g_s} + \frac{4t}{\varsigma_s} \to \widehat{J_s^d(s)} = \frac{1}{sg_s} + \frac{4}{s^2\varsigma_s} \tag{4.114}$$

so that:

$$\widehat{g_s(s)} = \frac{4}{s^2 J_s^d(s)} = \frac{1}{s^2}\left(\frac{1}{sg_s} + \frac{4}{s^2\varsigma_s}\right)^{-1} \tag{4.115}$$

The solution of the viscoelastic problem is found in the Laplace domain by applying an s-multiplied Laplace transform to the solution of any linear elastic homogenization scheme (i.e., Eqs. (4.31) and (4.32) for the Mori-Tanaka scheme or Eqs. (4.35) and (4.36) for the self-consistent scheme). Here, we are particularly interested in the asymptotic behavior at large times -when the effect of transient creep becomes negligible. The asymptotic behavior of the

143

creep properties defined by Eqs. (4.113) and (4.114) is:

$$\lim_{s \to 0^+} \widehat{k_s(s)} = +\infty \tag{4.116}$$

$$\lim_{s \to 0^+} \widehat{g_s(s)} = \varsigma_s/4 \tag{4.117}$$

We readily verify that the solid's contact relaxation modulus, in the Laplace domain, for large times is:

$$\lim_{s \to 0^+} \widehat{m_s(s)} = \lim_{s \to 0^+} \left(4\widehat{g_s(s)} \frac{3\widehat{k_s(s)} + \widehat{g_s(s)}}{3\widehat{k_s(s)} + 4\widehat{g_s(s)}} \right) = \varsigma_s \tag{4.118}$$

We now want to determine the composite contact relaxation modulus, i.e., the homogenized viscosity ς^{hom}, for large times. To this end, we note that the homogenized bulk relaxation modulus $K^{\text{hom}}(t)$ and the homogenized shear relaxation modulus verify in the Laplace domain:

$$\lim_{s \to 0^+} s\, \widehat{K^{\text{hom}}(s)} = \mathcal{K}_0 \lim_{s \to 0^+} s\, \widehat{g_s(s)} \tag{4.119}$$

$$\lim_{s \to 0^+} s\, \widehat{G^{\text{hom}}(s)} = \mathcal{M}_0 \lim_{s \to 0^+} s\, \widehat{g_s(s)} \tag{4.120}$$

where $\mathcal{K}_0 = \mathcal{K}\,(\nu_s = 0.5, \eta, \eta_0)$ and $\mathcal{M}_0 = \mathcal{M}\,(\nu_s = 0.5, \eta, \eta_0)$ are the elastic pore morphology factors (4.89) and (4.89) evaluated for an incompressible solid phase. Finally, substituting (4.119) and (4.120) into (3.9) yields the contact relaxation modulus in the Laplace domain in the form:

$$
\begin{aligned}
\lim_{s \to 0^+} s\widehat{M(s)} &= \lim_{s \to 0^+} \left(4s\widehat{G^{\text{hom}}(s)} \frac{3s\widehat{K^{\text{hom}}(s)} + s\widehat{G^{\text{hom}}(s)}}{3s\, \widehat{K^{\text{hom}}(s)} + 4s\, \widehat{G^{\text{hom}}(s)}} \right) \tag{4.121}\\
&= \mathcal{M}_0 \frac{3\mathcal{K}_0 + \mathcal{M}_0}{3\mathcal{K}_0 + 4\mathcal{M}_0} \lim_{s \to 0^+} s\, \widehat{m_s(s)}\\
&= \Pi_M(\nu_s = 0.5, \eta, \eta_0) \lim_{s \to 0^+} s\, \widehat{m_s(s)} \tag{4.122}
\end{aligned}
$$

or equivalently, for large times:

$$\boxed{\frac{\varsigma^{\text{hom}}}{\varsigma_s} = \Pi_M(\nu_s = 0.5, \eta, \eta_0)} \tag{4.123}$$

144

Therefore, after a transient phase, the contact creep compliance of the composite at large times is governed by a Maxwell unit of viscosity ς^{hom} that relates to the shear viscosity ς_s of the solid by the elastic scaling relation of an incompressible material. As a consequence, and in contrast to the case of a time-independent Poisson's ratio, the viscosity ς^{hom} of a composite composed of a solid exhibiting deviatoric creep no longer scales linearly with the indentation modulus, as in Eq. (4.111), but by:

$$\frac{\varsigma^{\text{hom}}}{M} = \frac{\Pi_M(\nu_s = 0.5, \eta, \eta_0)}{\Pi_M(\nu_s, \eta, \eta_0)} \frac{\varsigma_s}{m_s} \tag{4.124}$$

To evaluate the order of this non-linearity we consider the two characteristic pore morphologies of the solid-pore composite depicted in Figure 4-1 and calculate:

$$\Pi_M(\nu_s = 0.5, \eta, \eta_0) = \mathcal{M}_0 \frac{3\mathcal{K}_0 + \mathcal{M}_0}{3\mathcal{K}_0 + 4\mathcal{M}_0}$$

where:

- In the case of a matrix–pore inclusion morphology ($\eta_0 = 0$):

$$\mathcal{K}_0^{MT} = \lim_{\nu \to 0.5} \mathcal{K}(\nu_s = 0.5, \eta, \eta_0 = 0) = \frac{4\eta}{3(1 - \eta)} \tag{4.125}$$

$$\mathcal{M}_0^{MT} = \lim_{\nu \to 0.5} \mathcal{M}(\nu_s = 0.5, \eta, \eta_0 = 0) = \frac{3\eta}{5 - 2\eta} \tag{4.126}$$

Thus:

$$\Pi_M^{MT}(\nu_s = 0.5, \eta, \eta_0 = 0) = \frac{3}{4} \frac{(23 - 11\eta)\,\eta}{(5 - 2\eta)(8 - 5\eta)} \tag{4.127}$$

- In the case of a perfectly disordered porous material ($\eta_0 = 1/2$):

$$\mathcal{K}_0^{SC} = \lim_{\nu \to 0.5} \mathcal{K}(\nu_s = 0.5, \eta, \eta_0 = 1/2) = \frac{4\eta\,(2\eta - 1)}{(1 - \eta)(2 + \eta)} \tag{4.128}$$

$$\mathcal{M}_0^{SC} = \lim_{\nu \to 0.5} \mathcal{M}(\nu_s = 0.5, \eta, \eta_0 = 1/2) = \frac{3\,(2\eta - 1)}{2 + \eta} \tag{4.129}$$

Thus,

$$\Pi_M^{SC}(\nu_s = 0.5, \eta, \eta_0 = 0) = \frac{3}{4} \frac{(2\eta - 1)(3\eta + 1)}{(\eta + 2)} \tag{4.130}$$

A comparison of Figures 4-8a and 4-8b shows that the scaling of ς^{hom}/M with the packing
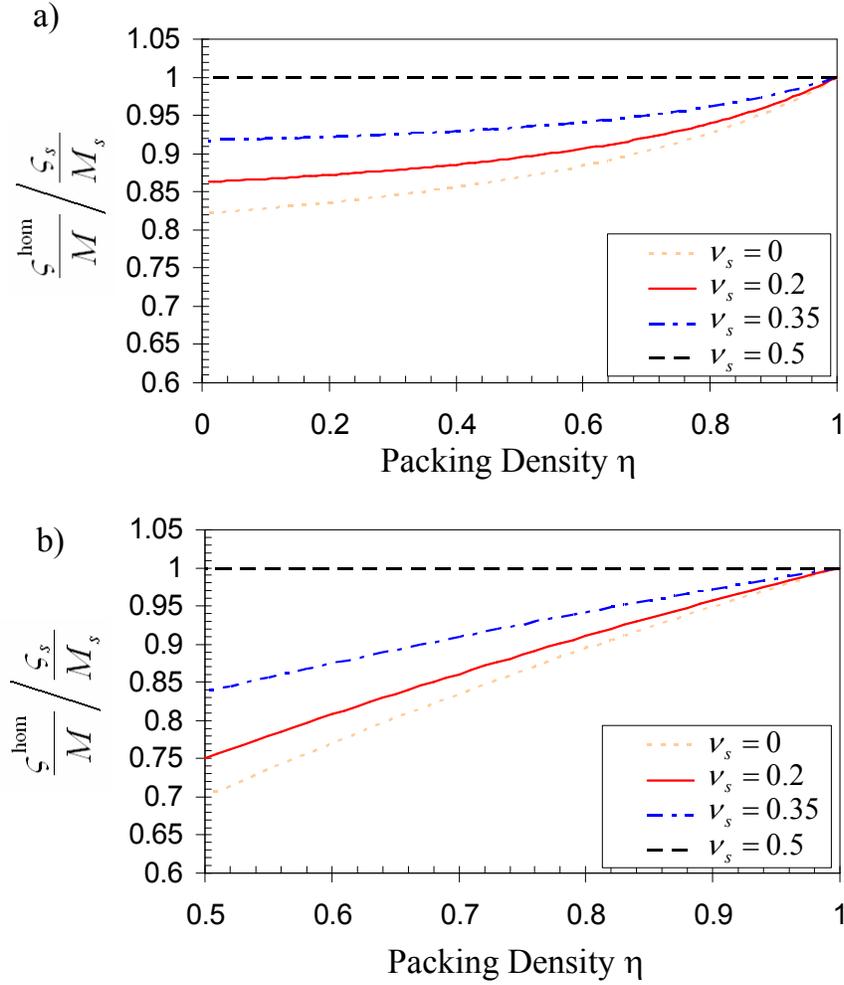
Figure 4-8: Evidence of the non-linearity of the $\varsigma^{\mathrm{hom}}/M$ versus ς_s/m_s scaling for (a) a matrix-pore inclusions morphology and (b) a granular morphology. ν_s is the instantaneous elastic Poisson's ratio.

density η strongly depends on the morphology: for a matrix-pore inclusions morphology this scaling relation is convex for all elastic Poisson's ratios, whereas, for a granular morphology, this scaling relation is concave for all elastic Poisson's ratios.

4.5 Concluding Remarks: Probing Microstructure by Indentation Testing

While classical indentation analysis proceeds by applying a continuum scale model to indentation data, an extension of this method to composite materials is possible. In this Chapter, we showed that the indentation modulus M, the indentation hardness H and the contact creep compliance $L(t)$ determined from an indentation test on a two phase solid-pore composite have one thing in common: The microstructure. It is on this basis that it becomes possible to link indentation data of a composite material to constituent properties of the solid phase and microstructural morphology information. The packing density scaling relations for different morphologies derived in this Chapter provide a wealth of information about the link between the microstructure and the elasticity, strength and creep properties of the composite that are accessible by indentation testing. In other words, an indentation test provides a means of probing the microstructure. In a forward application, the developed packing density relations allow one to predict the indentation response of the composite based on known constituent properties and known microstructural information. But the true advantage of the scaling relation is in its inverse application, that is the determination of the microstructure and/or the constituent properties from a contact experiment.

Assuming that no information is available at the microscopic scale, six unknowns have to be determined: Two strength properties of the solid phase (c_s and α_s, or h_s and α_s), two elastic parameters (m_s, ν_s), one porosity or packing density ($\eta = 1 - \varphi$) and the morphology (characterized by its packing density η_0 at percolation). Those six unknowns are to be compared with only two measurements (M and H) provided by an indentation test.[6] The problem is clearly ill-posed.

---

[6]The contact creep compliance and solid viscous properties are for now disregarded in this reverse analysis, since an indentation test designed to correctly assess the strength properties will most likely be too short in duration to provide a reliable measurement of the creep properties (see Chapter 3).

Let us now perform a large number N of indentations at different locations on the surface of the composite. Since the solid properties and morphology are assumed constant within the sample, while the packing density can vary locally, $N+5$ unknowns now have to be determined: Five mechanical and morphological properties of the solid, and N local packing densities. Those $N+5$ unknowns are to be compared with the $2N$ measurements provided by N indentation tests. Hence, in an inverse application, $N \geq 5$ indentation tests are required to determine from experimental (M, H) values the solid properties $(m_s, \nu_s, c_s, \alpha_s)$, the percolation threshold η_0 and the N packing densities η. Therefore, provided the existence of a unique solid phase present in the porous microstructure, the scaling relations are a versatile tool to probe the microstructure sensed by the large array of grid indentation tests, typically $2N \gg N+5$; and a full assessment of the mechanical and morphological properties of the solid phase is theoretically possible by reverse analysis. We will extensively employ this method for cement-based materials as a means to identify the microstructure and constituent properties.

Chapter 5

Statistical Indentation Analysis of Multiphase Materials

This Chapter deals with the indentation analysis of multiphase composite materials. By multiphase composites, we mean materials that exhibit a spatial heterogeneity of the material properties as a consequence of microstructure or composition, or both. This spatial heterogeneity of properties calls for statistical indentation techniques that enable (1) the assessment of the mechanical properties of each individual phase and (2) the quantification of the effect of this spatial heterogeneity on stiffness, strength and creep properties of the composite material. These techniques complement the micromechanics-based indentation analysis developed in Chapter 4. In fact, in contrast to the solid–pore composite that exhibits a heterogeneity at a scale much smaller than the indentation depth (see Section 4.1.2), the focus of this Chapter is on indentation depths much smaller than the characteristic size of the heterogeneity (Figure 5-1). With this focus in mind, the first Part of this Chapter complements recent developments of Constantinides et al. [57] [54] of the grid-indentation technique, and the second Part presents original developments of a self-consistent indentation technique that allows the determination of composite indentation properties from the heterogeneous indentation response of a multiphase material.
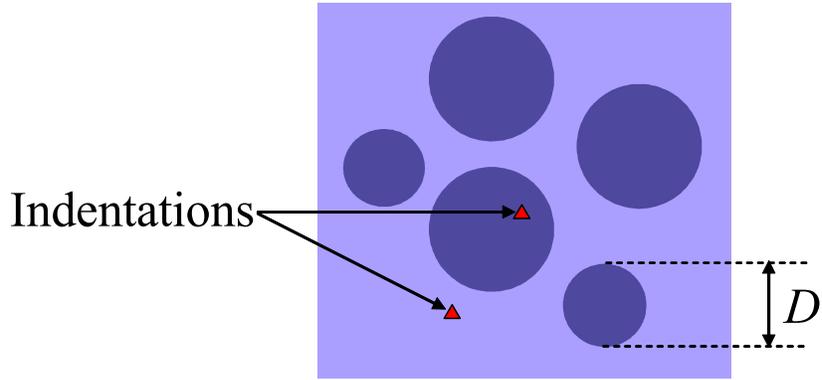
Figure 5-1: Principle of statistical indentation analysis: The characteristic size of the indents is smaller than the characteristic size of the material heterogeneities of the multiphase material.

5.1   Problem Statement

To motivate the forthcoming developments, consider an indentation test on a multiphase material. The characterize size of the heterogeneity (e.g., particle size) is denoted by D. We want to determine the characterize size d_s of the material volume that is activated by the indentation test on the multiphase material. This size d_s can be roughly associated with a half-sphere surrounding the indenter, as the iso-values of the stress field show (Fig. 5-2a). The indentation response will depend mostly on the material within a distance d_s from the indenter tip. If $d_s < D$ an indentation test may probe only one phase and therefore characterize its intrinsic phase properties (Fig. 5-3).

The size d_s of the volume of material probed by the indentation test depends on the indentation depth h, on the geometry of the indenter (for instance, equivalent half-cone angle θ of a Berkovich indenter), on the properties of the indented material (indentation modulus M, Poisson's ratio ν, hardness H, friction angle α, contact creep compliance $L(t)$), and on the characteristic size of the heterogeneity, D. A straightforward dimensional analysis of the problem yields:

$$\frac{d_s}{h} = \Pi_{d_s}\left(\theta, \frac{M}{H}, \nu, \alpha, \frac{L(\tau \leq t)}{H}, \frac{h}{D}\right) \tag{5.1}$$

The first five invariants are material properties (eventually of the composite material), while the last invariant, h/D, links the indentation depth to a characteristic material scale, the

150

a)

b)
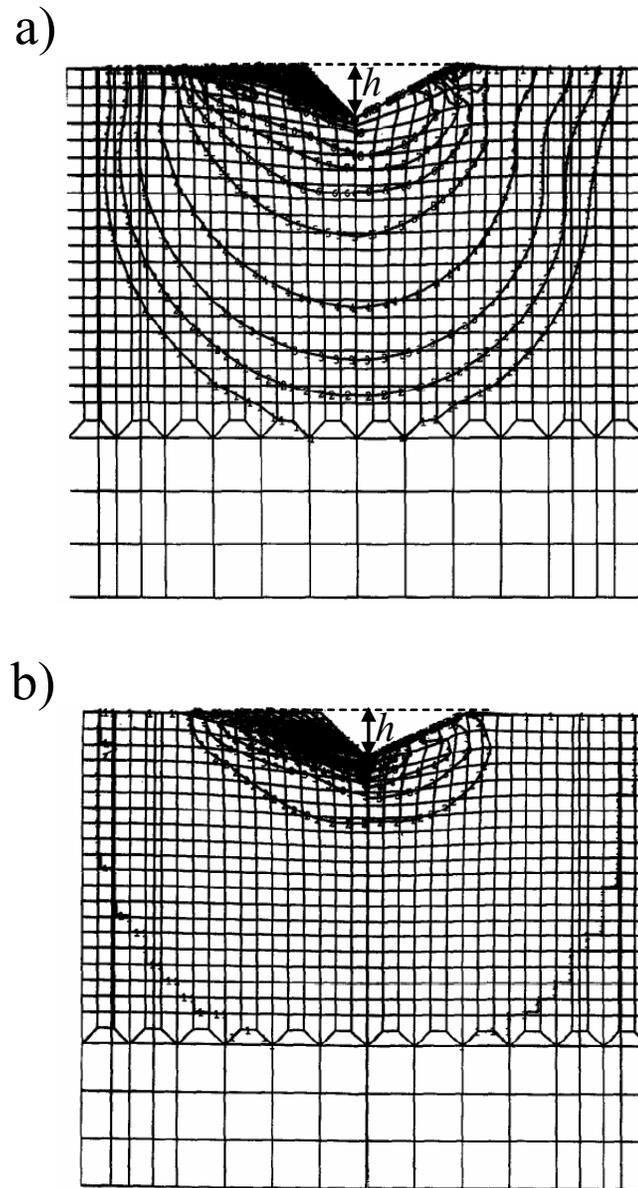
Figure 5-2: Numerical simulation of Berkovich indentation on an elasto-plastic material with linear hardening (from [109]). (a) Von Mises effective stress and (b) effective plastic strain. The simulations were performed in three dimensions.
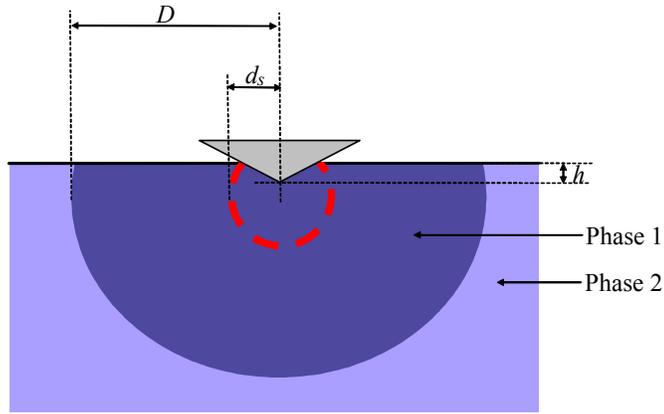
Figure 5-3: Characterization of intrinsic phase properties from shallow indentation depths. The red circle is a schematic of the volume of material probed during the indentation test.

characteristic size of the heterogeneity. In the case $h/D \to 0$ this invariant skips out of the set of dimensionless quantities. It follows:

$$h/D \to 0 \Rightarrow d_s \propto h \tag{5.2}$$

In this case, h is the sole length scale in the infinite half-space, and the problem respects the condition of self-similarity. The indentation properties $(M, H, L(t))$ extracted with a test $h \ll D$ are representative of the elasticity, strength and creep properties of the phase of size D. In contrast, the properties extracted with a test $h/D \gg 1$ sample the composite response, as discussed in Section 4.1.2.

The focus of this Chapter is two-fold:

1. For the case $h/D \ll 1$, to develop a statistical indentation technique that allows the assessment of phase properties of multiphase composite materials, and

2. To link the heterogeneity of the indentation data to homogeneous composite indentation properties representative of the behavior of the composite at scales $h/D \gg 1$.

5.2 Grid–Indentation Technique for Multiphase Materials

Recognizing the high heterogeneity of multiphase materials, application of the indentation technique is a challenge, as it is difficult to choose to indent on a specific material phase with sufficient repeatability. To address this challenge, it is advantageous to perform large grids of indentations on heterogeneous samples. Then, if the indentation depth is chosen properly, each indentation test may be treated as an independent statistical event, and statistical techniques may be applied to analyze the results. This is the fundamental idea of the grid-indentation technique [57] [54].

To illustrate its purpose, consider the following thought-experiment:

> Consider an infinite half-space composed of two materials of different mechanical properties. Provided that the indentation depth is much smaller than the characteristic size of the two phases, a random indentation on the sample surface provides access to either of the phase properties, with a probability that equals the surface fraction the two phases occupy on the sample surface. By contrast, an indentation to a depth much larger than the characteristic size of the two phases samples mechanically the composite response.

This thought-experiment illustrates how the classical tools of instrumented indentation can be extended to heterogeneous materials through a careful choice of the indentation depth which depends on the size of the elementary components. It calls for a statistical analysis of a large array of indentation tests and a subsequent statistical deconvolution of the indentation results. This Section reports on recent developments of and improvements to the grid-indentation technique.

5.2.1 Choice of Depth of Indentation

The choice of a critical depth h_{crit} below which intrinsic phase properties can reliably be measured by indentation was studied both analytically and numerically (for a detailed review, see [57] [54]). Numerical simulations of conical indentations on (almost) rigid perfectly plastic biphasic systems were performed by Durst et al. [71], who focused on the measurement of the indentation hardness. They considered phases of different shapes (Fig. 5-4). Their simulations

153

show that, if $a < 0.7D$ (where a is the contact radius), the indentation hardness of the indented phase is correctly measured. Their simulations also show that this criterion is almost the same for a particle embedded in a matrix and a thin film on a substrate; that is, h_{crit} is almost independent on the shape of the indented phase and depends only on its characteristic size D. This result may be due to the quasi-spherical shape of the material volume probed by indentation (see Fig. 5-2a). But a criterion for a reliable measurement of the indentation modulus may be more stringent than the one obtained by Durst et al. since the material volume that is solicited elastically below the indenter is much larger than the volume solicited plastically (see Figure 5-2b).

Constantinides et al. [57] [54] employ the thin-film analogy[1] to determine a critical h/D ratio below which the elastic properties of the indented composite do not diverge more than 10% from the elastic properties of the phase (here the film; see Fig. 5-5):

$$\boxed{\frac{h}{D} < \frac{1}{10}}$$

(5.3)

This result, which holds for both 'hard-on-soft' and 'soft-on-hard' composites with elastic mismatch ratios comprised within $1/5 \le E_{substrate}/E_{film} < 5$, is expected to hold for the measurement of the indentation hardness and for other shapes of the indented phase as well. The

---

[1]The indentation analysis of a film-substrate composite (Figure 5-4c) aims to link the measured composite modulus E_{eff} to the elastic moduli E_{film} and $E_{substrate}$ of the film and the substrate, respectively:

$$E_{eff} = E_{film} + (E_{substrate} - E_{film})\Psi$$

where Ψ is a weight function that depends on the ratio of the contact radius a to the film thickness a/d_s. For moduli mismatch ratio $E_{film}/E_{substrate}$ between 0.5 and 2, Gao et al. [79] derived the following closed-form solution:

$$\Psi^G = 1 - \left[\frac{2}{\pi}\tan^{-1}\left(\frac{D}{a}\right) + \frac{1}{2\pi(1-\nu)}\left((1-2\nu)\left(\frac{D}{a}\right)\ln\left(\frac{1+(D/a)^2}{(D/a)^2}\right) - \frac{(D/a)}{1+(D/a)^2}\right)\right]$$

Using the auxiliary functions introduced by Sneddon and Ting [180] [168], Perriot and Barthel [146] empirically extended the previous equation to a wider range of modulus mismatch ratios $E_{film}/E_{substrate}$ between 0.01 and 100:

$$\Psi^{PB} = \left[1 + \left(\frac{D}{a}k\right)^{1.27}\right]^{-1}$$

where:

$$\log(k) = -0.093 + 0.792\log\left(\frac{E_{substrate}}{E_{film}}\right) + 0.05\left(\log\left(\frac{E_{substrate}}{E_{film}}\right)\right)^2$$
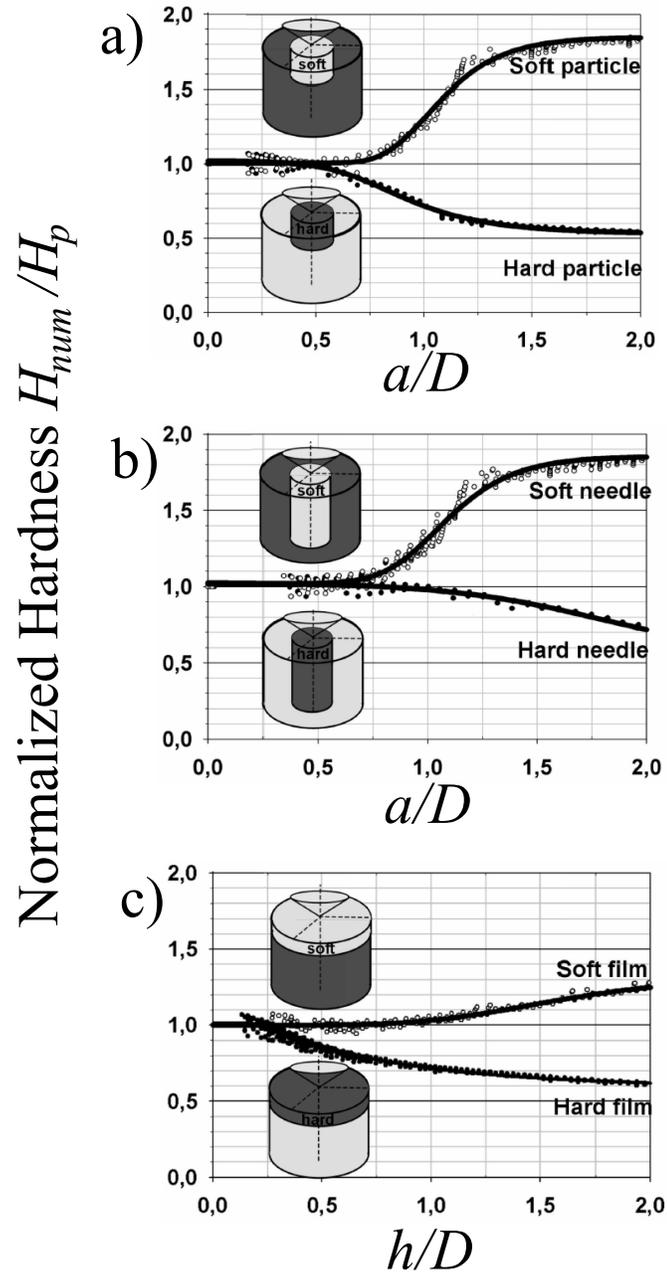
Figure 5-4: Normalized indentation hardnesses obtained from numerical simulations of conical indentations on a biphasic material (adapted from [71]). The indented phase is (a) a particle, (b) a needle, and (c) a film. H_p is the indentation hardness of the indented phase, H_{num} is the indentation hardness output from the numerical simuation, a is the contact radius and h is the indentation depth. d_s is the characteristic size of the indented phase, i.e., the radius and depth of the particle, or the radius of the needle, or the thickness of the film.
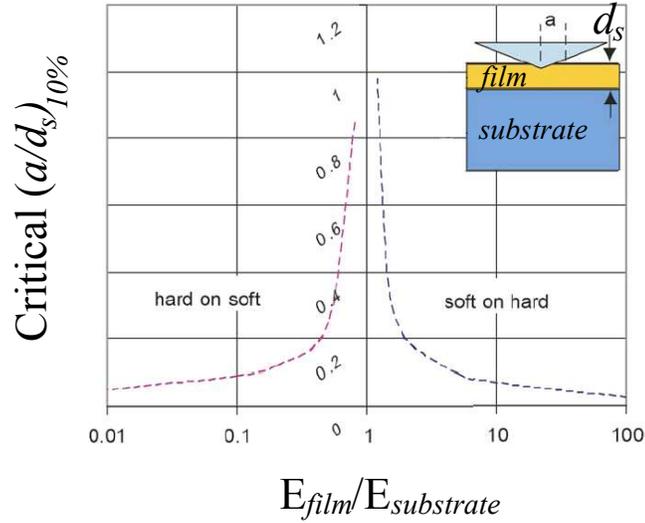
Figure 5-5: Critical a/d_s ratio versus $E_{substrate}/E_{film}$ according to Perriot and Barthel [146] for which the composite modulus E_{eff} is within 10% of the film modulus E_{film} (from [54]).

relevance of this criterion, also known as Buckle's rule-of-thumb, has been shown experimentally for titanium – titanium monoboride composites [54] .

To measure the indentation properties of a specific phase in the heterogeneous material, one may think of optically targeting the phase of interest and performing an indentation test at the exact chosen location. But such an approach is likely to fail, since an optical image is only a two-dimensional representation of a three-dimensional structure: it may well be that just below the surface another phase is present and that the measured response is a composite response. The grid indentation technique presented next precisely addresses this issue.

5.2.2   Principle of Grid-Indentation Technique

Since one may never be sure that one indentation test provides the sought-after intrinsic indentation properties of a given phase and not a composite response, the main idea of the grid-indentation technique is to perform a large array of indentations tests on a sample surface and analyze the results statistically.

To introduce the quantities that are measured by the technique, reconsider the introductory thought experiment of a grid-indentation campaign of a two-phase composite. A large number

of indentations is performed at random locations on the surface of the two-phase material (Fig. 5-6a). The indentations are shallow enough to ensure that the criterion (5.3) is respected. Although a few indentations may measure a composite response, criterion (5.3) ensures that a large majority of the indentations will probe the intrinsic properties of the two phases. It is intuitively appealing to display the experimental results as histograms (or frequency plots) of the measured indentation properties (indentation modulus M, indentation hardness H, etc.), which in the case of the two-phase composite material display two peaks (Fig. 5-6c). The mean value of each peak represents the mean phase property.

The area below each curve of the histogram is a measure of the percentage of all indentations performed on the corresponding phase, and is therefore a measure of the surface fraction of each phase. For a perfectly disordered material, surface fractions and volume fractions are identical, which is known at the Delesse principle [66]. Therefore, the volume fraction of each phase of the heterogeneous material can also be obtained by an analysis of the experimental frequency plot.

The randomness of the location of the indentations ensures that the measured properties are not correlated from indentation to indentation. If the indented material is perfectly disordered, this zero correlation can also be ensured by performing the indentations on a grid, as long as the spacing between indentations is greater than the characteristic size D of the phases (Fig. 5-6b). Since it is easier to program an indenter to perform indentations on a grid, the approach is referred to as 'grid–indentation technique' [54].

The grid-indentation technique, here described for a two-phase composite, obviously applies to more phases are well, provided they exhibit sufficient contrast ('mismatch') in their properties. Moreover, the grid-indentation technique can be applied for any property obtained from the indentation tests, i.e., indentation modulus M, indentation hardness H, contact creep compliance $L(t)$ (Chapter 3) or packing densities (Chapter 4). To ensure repeatability of the technique, the analysis of the frequency plot, called the deconvolution technique, needs to be automatized. Such an automatization is presented next.
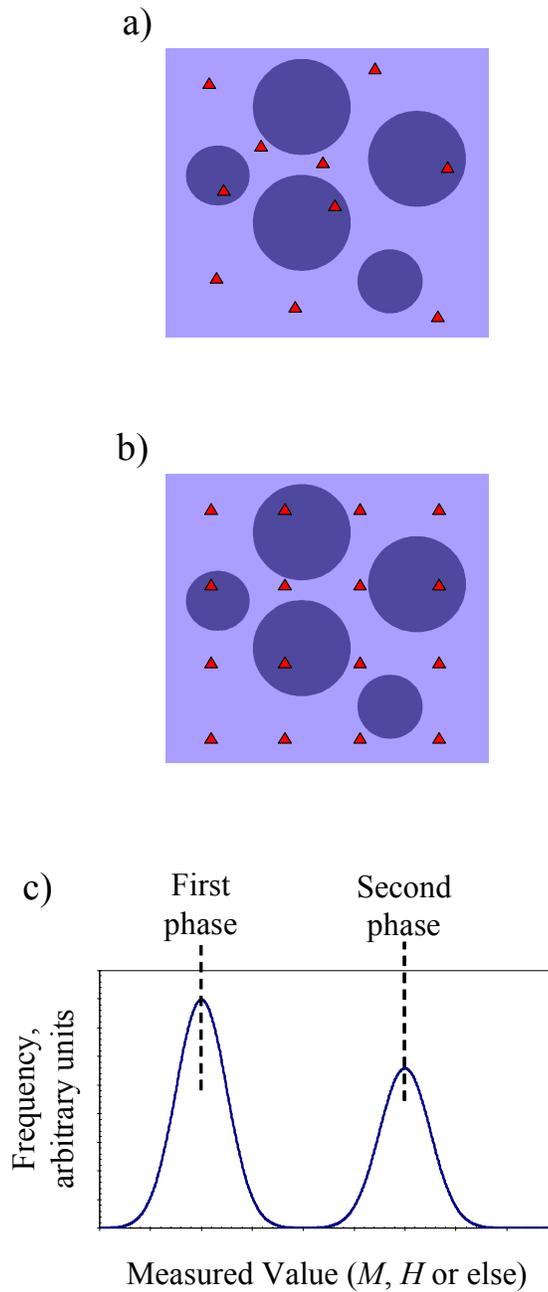
Figure 5-6: Indentations performed on a heterogeneous two-phase material. Each indentation (represented by a red triangle reminiscent of Berkovich indents) provides the mechanical properties of one of the two phases. (a) Indentations are performed at random locations. (b) Indentations are performed on a grid. (c) Resulting histogram (frequency plot).

5.2.3 Deconvolution Technique

The key to the determination of phase properties in the grid-indentation technique is the identification of the statistical distribution of the phases. This requires a deconvolution of the heterogeneous data, hence the name 'deconvolution technique'. In its original development [57] [54], the deconvolution technique was carried out manually by fitting a number of probability density functions (PDF) to the experimental frequency plot (normalized histogram) of the measured quantity; which makes the deconvolution results dependent on the operator. This Section proposes a technique that automatizes this process.

Choice of Phase Distribution Functions

The first point that need to be addressed is the best *a priori* choice of distribution function for each peak in the frequency plot. A distribution function is uniquely defined by its statistical moments [155]:

- The first moment about the origin is the mean.

- The second moment around the mean is the variance and is usually denoted by σ^2, where σ is the standard deviation.

- The third standardized moment, usually written as γ_1, is the skewness and is a measure of the asymmetry of the distribution function (Fig. 5-7). A symmetric distribution function verifies $\gamma_1 = 0$.

- Higher-order moments.

If the measurements and the material were perfect, for infinitely shallow indentations one would expect the peaks to be infinitely sharp (Fig. 5-8a). In this case, each peak would be characterized by its first moment (mean value) only. Practically however, there are several reasons for which the peaks of the histogram are not infinitely sharp, requiring the use of moments of higher order:

- The measurements exhibit some noise. The noise is considered as random and creates a spread of the peaks, but no asymmetry (Fig. 5-8b).
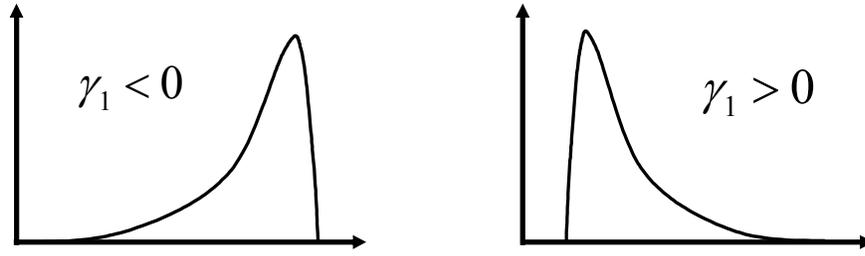
Figure 5-7: Example of distribution functions with negative skewness ($\gamma_1 < 0$) and positive skewness ($\gamma_1 > 0$).

- Each phase has its own intrinsic variability, which also creates a spread of the peaks (Fig. 5-8b). It may well be that, as a result of its processing, the material has a distribution function of its properties within each phase which is asymmetric. Nevertheless, in an *a priori* analysis, with no further information available on processing, it is not possible to justify an asymmetric distribution of the properties in each phase.

- The indentations are not infinitely shallow. Even for an ideal material and ideal measurements, due to their finite depth some indentations will solicit mechanically two (or more) phases simultaneously, and the measured property will be a composite property. Quantifying the composite response is complicated, since it is the result of a three-dimensional interaction between the indenter probe and the phases probed. Nevertheless we can assert that the composite response must be bound by the values of the individual peaks (see Fig. 5-8c). As a result, the finite depth of the indentation introduces some asymmetry: The lowest peak is better characterized by a positive skewness, $\gamma_1 > 0$; and the highest peak with a negative skewness $\gamma_1 < 0$. In order to automatize the deconvolution process, we choose to characterize all peaks with only one distribution. The choice of a distribution with zero skewness $\gamma_1 = 0$ is the most appropriate.

In summary, the distribution sought must have non-zero first and second moments (mean and variance) and a zero skewness $\gamma_1 = 0$. For the sake of simplicity, the distribution is chosen so that all standardized central moments of higher order are zero. This distribution is the Gaussian distribution.
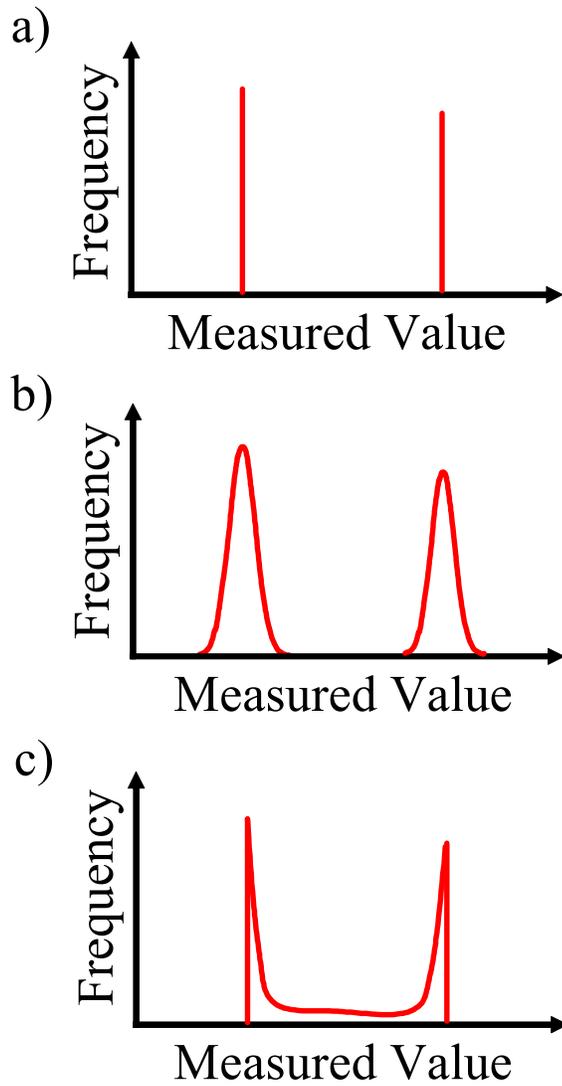
Figure 5-8: Expected frequency plots for a biphasic material. (a) Perfect measurements and materials and infinitely shallow indentations; (b) Imperfect measurements or material and infinitely shallow indentations; (c) Perfect measurements and material and indentations with finite depth.

Implementation of Deconvolution Technique

The deconvolution begins with the generation of the experimental Cumulative Distribution Function (CDF). Let N be the number of indentation tests performed on a specimen and $\{X_i\}_{i=1..N}$ the sorted values of the measured property we want to deconvolute. This parameter can be the indentation modulus M, the indentation hardness H, or any other property obtained from the indentation test (creep properties, packing density, etc). The N points of the experimental CDF of X, denoted by D_X, are obtained from:

$$D_X(X_i) = \frac{i}{N} - \frac{1}{2N}; \text{ for } i \in [1; N] \tag{5.4}$$

Once the experimental CDFs are known, the form of the model CDFs are specified. We consider the heterogeneous material to be composed of n material phases with sufficient contrast in mechanical phase properties. The j-th phase occupies a volume fraction f_j of the indented surface. In an *a priori* analysis (as discussed here above), the best choice for the distribution of the mechanical properties of each phase is a Gaussian distribution, identified by its mean value μ_j^X and its standard deviation s_j^X. The CDF of the j-th Gaussian distributed phase is given by:

$$D(X_i; \mu_j^X, s_j^X) = \frac{1}{s_j^X \sqrt{2\pi}} \int_{-\infty}^{X_i} \exp\left(\frac{-(u - \mu_j^X)^2}{2(s_j^X)^2}\right) du \tag{5.5}$$

The unknowns $\{f_j, \mu_j^X, s_j^X\}$ for $j \in [1, n]$ are determined by minimizing the difference between the experimental CDFs and the weighted model-phase CDFs:

$$\min \sum_{i=1}^{N} \sum_{X} \left(\sum_{j=1}^{n} f_j D(X_i; \mu_j^X, s_j^X) - D_X(X_i)\right)^2$$
$$s.t. \tag{5.6}$$
$$\sum_{j=1}^{n} f_j = 1$$

where the constraint of the minimization problem requires that the volume fractions of the different phases sum to one. To ensure that phases have sufficient contrast in properties, and thus to avoid that two neighboring Gaussians overlap, the optimization problem is additionally
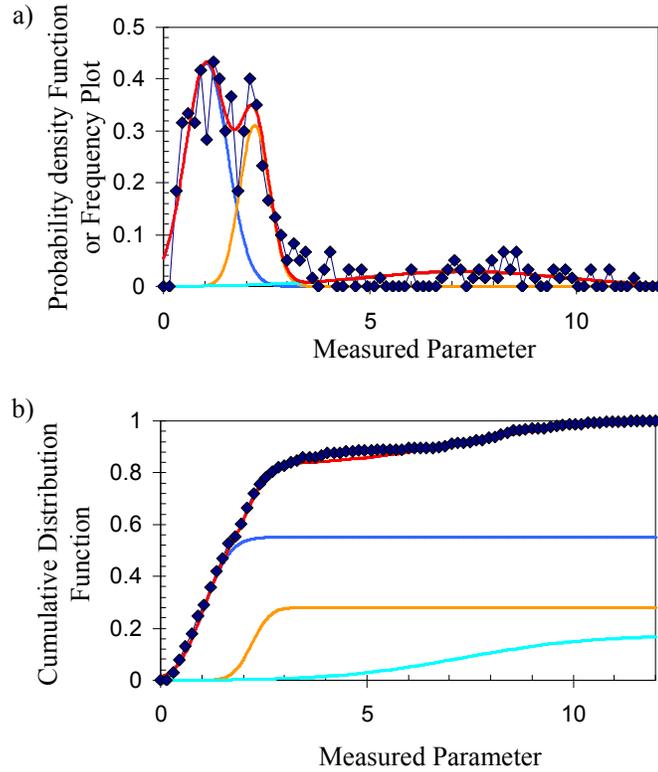
Figure 5-9: Example of a 3-Gaussian deconvolution. The results are displayed in terms of (a) histograms and probability density functions (b) cumulative distributions functions.

constrained by:

$$\mu_j^X + s_j^X \leq \mu_{j+1}^X + s_{j+1}^X \tag{5.7}$$

By way of illustration Figure 5-9 displays the results of a deconvolution by three Gaussians. The results of the deconvolution process will usually be displayed in the form of a histogram (Figure 5-9a). The continuous analog of a discrete histogram is a probability density function (PDF) [155], and the frequency plots will also be referred to as probability density functions. The reason for displaying deconvolution results in terms of probability density functions (PDF) instead of cumulative distribution functions (CDF) becomes apparent when comparing Figures 5-9a and 5-9b: PDFs are more intuitive than CDFs for physical interpretation.

The deconvolution process, here presented for one measured parameter, can easily be extended to several parameters. For instance, indentation modulus, indentation hardness, creep

properties and packing density can all be deconvoluted simultaneously, meaning that the number of phases and their volume fractions are fixed for the sample. For instance, in a simultaneous deconvolution of M and H, the unknowns are $\{f_j, \mu_j^M, s_j^M, \mu_j^H, s_j^H\}_{j=1..n}$, and the process is identical to the process presented earlier in this Section. Instead of (5.6), the function to minimize is:

$$\min \sum_{i=1}^{N} \sum_{X=(M,H)} \left(\sum_{j=1}^{n} f_j D(X_i; \mu_j^X, s_j^X) - D_X(X_i) \right)^2$$

$$s.t. \tag{5.8}$$

$$\sum_{j=1}^{n} f_j = 1$$

In summary, the proposed deconvolution technique, in association with the grid-indentation technique, enables the measurement of phase properties of heterogeneous multiphase materials: Volume fractions, mean values and standard deviations of the mechanical phase properties.

5.3   Self-Consistent Indentation Technique for Multiphase Materials

The previous Section described a method for the identification of phase properties of heterogenous materials obtained by carefully choosing the indentation depth, $h/D < 1/10$. An indentation test operated at $h/D \gg 1$ would sample mechanically the composite response and lead to the experimental determination of homogenized properties. The problem we address in this Section is to link the scale of shallow indentation ($h/D \ll 1$) with the indentation properties at the composite scale ($h/D \gg 1$) — without performing an actual indentation test at the composite scale. In other words, the aim of this Section is to derive estimates of the composite response in the form of homogenized indentation quantities, M^{hom}, H^{hom} and $L^{\mathrm{hom}}(t)$ on the basis of a large heterogeneous data set of indentation properties $\{M_i, H_i, L_i(t)\}_{i=1..N}$ generated at smaller scales, e.g., by the grid indentation technique. The two scales naturally satisfy the scale separability condition in the sense of Eq. (4.1), which makes the use of micromechanics theory most suitable.

5.3.1 Homogenized Indentation Modulus

To illustrate the approach, we start with the indentation modulus.

Consider a large array of indentation tests that satisfy the condition $h/D < 1/10$. In these tests, a heterogeneous data set of indentation moduli $\{M_i\}_{i=1,N}$ is determined which is representative of the heterogeneities of the multiphase material. The question we want to address analytically is: What is the corresponding homogenized indentation modulus M^{hom} that would be measured in indentation tests operated to $h/D \gg 1$? The problem is treated in the framework of linear micromechanics (see Section 4.2.2).

Virtual Composite Material

The fundamental idea of the micromechanics approach developed below is that each test performed at a scale $h/D < 1/10$ is representative of a material phase, so that N indentation tests define a 'virtual' composite material which is composed of N phases characterized by N indentation moduli $\{M_i\}_{i=1,N}$ (Fig. 5-10). From the variational bounds of linear elasticity, it is known that the stiffness of the composite is situated in between the Reuss bound (uniform stress) and the Voigt bound (uniform strain), which for a constant Poisson's ratio for all phases apply equally to the indentation modulus:

$$\left(\frac{1}{N} \sum_{(N)} \frac{1}{M_i} \right)^{-1} \leq M^{\mathrm{hom}} \leq \frac{1}{N} \sum_{(N)} M_i \tag{5.9}$$

The focus of the micromechanics approach is to refine these estimates by considering the interaction between highly heterogeneously distributed phases. In this sense, M^{hom} can be viewed as the homogenized indentation modulus of the virtual composite material composed of N randomly distributed phases in the material.

Self-Consistent Micromechanics Model

The inputs to the micromechanics model are:

- The volume fraction of each phase, $\phi_i = 1/N$,
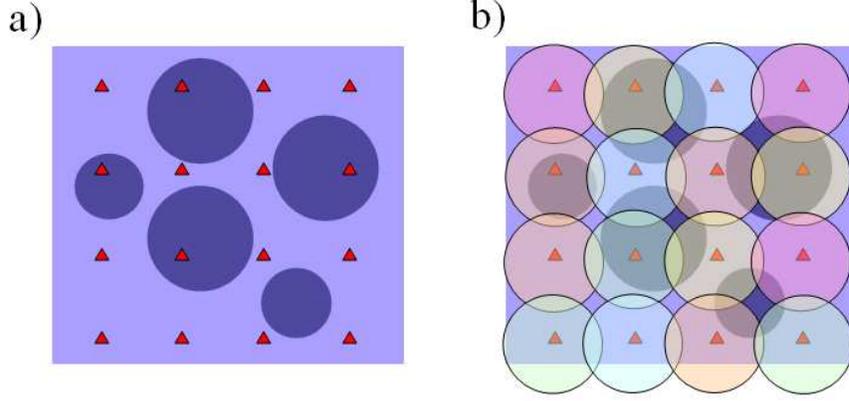
Figure 5-10: (a) Grid of indentations performed on a biphasic material and (b) associated virtual N-phase material. N is the number of indentations performed.

- The elastic properties of each phase, given by the measured indentation modulus M_i and the Poisson's ratio ν_i so that the bulk modulus K_i and shear modulus G_i read:

$$
\begin{aligned}
K_i &= \frac{E_i}{3(1 - 2\nu_i)} = \frac{1 - \nu_i^2}{3(1 - 2\nu_i)} M_i \\
G_i &= \frac{E_i}{2(1 + \nu_i)} = \frac{1 - \nu_i}{2} M_i
\end{aligned}
\tag{5.10}
$$

- The morphology of the virtual composite. Given that each virtual phase only occupies a volume fraction $\phi_i = 1/N$, no phase can reasonably play the role of a matrix. In contrast, a polycrystal morphology seems particularly well-suited. The self-consistent scheme yields particularly good estimates for a polycrystal morphology, for which it was in fact initially developed [89] [107].

Using these elements, an estimate of the homogenized indentation modulus of the virtual composite material is obtained from relation (4.30), which we recall:

$$
\mathbb{C}^{\mathrm{hom}} = \left[\sum_{i=1}^{N} \phi_i \mathbb{C}_i : \left(I + \mathbb{P}^{SC} : \left(\mathbb{C}_i - \mathbb{C}^{\mathrm{hom}} \right) \right)^{-1} \right] : \left[\sum_{i=1}^{N} \phi_i \left(I + \mathbb{P}^{SC} : \left(\mathbb{C}_i - \mathbb{C}^{\mathrm{hom}} \right) \right)^{-1} \right]^{-1}
\tag{5.11}
$$

Considering a spherical morphology for each virtual phase, the Hill tensor $\mathbb{P}^{SC}$ is calculated with Eq. (4.19), and Eq. (5.11) reduces in the isotropic case ($\mathbb{C}_i = 3K_i \mathbb{J} + 2G_i \mathbb{K}$ and $\mathbb{C}^{\mathrm{hom}} =$

$3K^{\text{hom}}\,\mathbb{J}+2G^{\text{hom}}\,\mathbb{K})$ to:

$$K^{\text{hom}}\left[\sum_{i=1}^{N}\frac{1}{K^{\text{hom}}+\alpha^{\text{hom}}(K_i-K^{\text{hom}})}\right]=\sum_{i=1}^{N}\frac{K_i}{K^{\text{hom}}+\alpha^{\text{hom}}(K_i-K^{\text{hom}})}$$
$$G^{\text{hom}}\left[\sum_{i=1}^{N}\frac{1}{G^{\text{hom}}+\beta^{\text{hom}}(G_i-G^{\text{hom}})}\right]=\sum_{i=1}^{N}\frac{G_i}{G^{\text{hom}}+\beta^{\text{hom}}(G_i-G^{\text{hom}})} \tag{5.12}$$

where:

$$\alpha^{\text{hom}}=\frac{3K^{\text{hom}}}{3K^{\text{hom}}+4G^{\text{hom}}}$$
$$\beta^{\text{hom}}=\frac{6}{5}\frac{K^{\text{hom}}+2G^{\text{hom}}}{3K^{\text{hom}}+4G^{\text{hom}}} \tag{5.13}$$

Eqs. (5.12) are non-linear because of the coupling introduced by α^{hom} and β^{hom}. For large N, Eqs. (5.12) cannot be solved analytically, but can easily be solved numerically (e.g., with Matlab). Then, M^{hom} is calculated from Eq. (2.20):

$$M^{\text{hom}}=4G^{\text{hom}}\frac{3K^{\text{hom}}+G^{\text{hom}}}{3K^{\text{hom}}+4G^{\text{hom}}} \tag{5.14}$$

Effect of the Set of Virtual Poisson's Ratios on Estimated Homogenized Indentation Modulus

The sole non-experimental input of the approach is a set of Poisson's ratios $\{\nu_i\}_{i=1,N}$ of the N virtual phases. The effect which this set has on the homogenized indentation modulus M^{hom} is here investigated numerically. A set of $N=400$ values $\{M_i\}_{i=1,N}$, chosen randomly between 0 and 100 GPa, is generated. It is instructive to note that the Reuss-Voigt bounds (5.9) for $N\to\infty$ random realizations between 0 and M_{max} read:

$$0=\lim_{N\to\infty}\left(\frac{1}{N}\sum_{i=1}^{N}\frac{1}{(i/N)}\right)^{-1}\leq\frac{M^{\text{hom}}}{M_{\text{max}}}\leq\lim_{N\to\infty}\left(\frac{1}{N}\sum_{i=1}^{N}(i/N)\right)=\frac{1}{2} \tag{5.15}$$

To study the effect of the Poisson's ratio, the following cases are investigated:

- The Poisson's ratio ν_i is assumed to be the same in all N phases. For each ν_i, Eq. (5.12) is solved numerically with Matlab. Figure 5-11 displays the results of the calculation. The homogenized Poisson's ratio ν^{hom} is roughly equal to the Poisson's ratio ν_i of the virtual phases. In contrast, the homogenized indentation modulus varies little with the
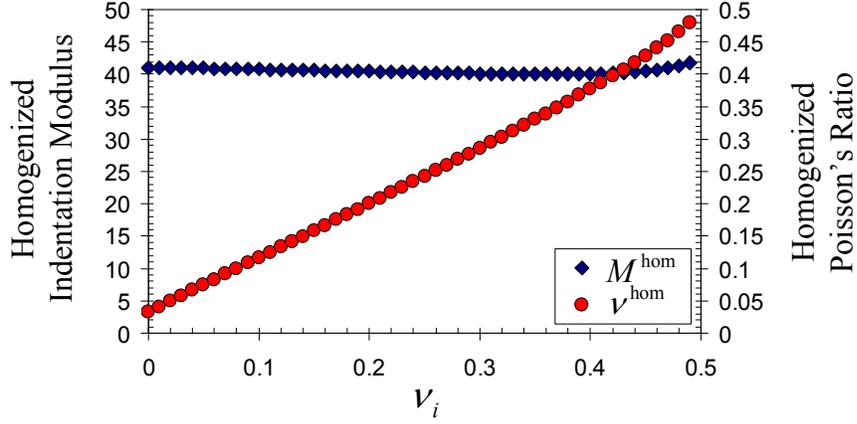
Figure 5-11: Effect of a constant Poisson's ratio ν_i (assigned to 400 virtual phases) on the homogenized indentation modulus M^{hom} (blue diamonds, left axis) and on the homogenized Poisson's ratio ν^{hom} (red circles, right axis).

Poisson's ratio ν_i, $M^{\mathrm{hom}}/M_{\mathrm{max}} = 0.415 \pm 1.5\%$.

- The Poisson's ratios $\{\nu_i\}_{i=1,N}$ are assumed to be uniformly distributed over $[0, 0.5]$. 100 sets are generated, and for each set Eq. (5.12) is solved numerically. The homogenized indentation modulus varies little for the 100 numerical solutions, $M^{\mathrm{hom}}/M_{\mathrm{max}} = 0.415 \pm 0.3\%$.

The case studies show that the Poisson's ratio $\{\nu_i\}_{i=1,N}$ assigned to the phases has little effect on the homogenized indentation modulus M^{hom}, which, however, deviates significantly from the Reuss-Voigt bounds (5.15). The set of a constant Poisson's ratio $\nu_i = 0.2$ is chosen, since it provides a most convenient way to reduce the set of Equations (5.12) to one single equation:

$$\boxed{\sum_{i=1}^{N} \frac{1}{1 + \frac{1}{2}(M_i/M^{\mathrm{hom}} - 1)} = \sum_{i=1}^{N} \frac{M_i/M^{\mathrm{hom}}}{1 + \frac{1}{2}(M_i/M^{\mathrm{hom}} - 1)}} \tag{5.16}$$

This equation can readily be solved numerically and provides a simple way to estimate, from a set of indentation moduli $\{M_i\}_{i=1,N}$ measured with a grid of indentations, the homogenized indentation modulus M^{hom}.

5.3.2 Homogenized Indentation Hardness

We now seek a similar link for the indentation hardness, namely between the set of indentation hardness values $\{H_i\}_{i=1..N}$ determined at a scale $h/D \leq 1/10$ and the homogenized indentation hardness H^{hom} representative of the composite response at a scale $h/D \gg 1$.[2] Similar to the developments in Section 5.3.1, the micromechanical system is a virtual composite material composed of N phases. The strength behavior of each phase is characterized by the indentation hardness H_i.

The homogenization is based on strength homogenization theory (Section 4.3.2). As we shall see below, the strength upscaling of an N-phase material is challenging, both theoretically and numerically. In order to reduce the complexity, we restrict ourselves to purely cohesive materials governed by a Von Mises criterion:

$$f_i(\boldsymbol{\sigma}) = \sqrt{J_2} - c_i \leq 0 \tag{5.17}$$

where $\sigma_d = \sqrt{2J_2} = \sqrt{\mathbf{s}:\mathbf{s}}$ with $\mathbf{s} = \boldsymbol{\sigma} - \frac{1}{3}\text{tr}(\boldsymbol{\sigma})\mathbf{1}$. Herein, c_i is the cohesion of phase i, which relates to the 'phase hardness' H_i by: (Eq. 2.89, $\alpha = 0$):

$$\frac{H_i}{c_i} = 4.76 \tag{5.18}$$

In other words, the strength of the i-th phase of the virtual composite material can be defined either by the hardness H_i or by the cohesion c_i. In this case, the strength homogenization of the hardness of a N-phase composite material is equivalent to the homogenization of the cohesion of an N-phase composite material. As a benchmark, we remind ourselves that the Voigt-Reuss bounds of yield design for a cohesive material [61] equally apply for the hardness:

$$\min_N H_i \leq H^{\text{hom}} \leq \frac{1}{N}\sum_{(N)} H_i \tag{5.19}$$

The non-linear strength homogenization approach aims at improving these bounds.

Following the approach outlined in Section 2.4.2, the strength criterion is approached, for

---

[2]Research in collaboration with B. Gathier during his Master of Science study at MIT [80].

convexity reasons, as the limit case of a more regular elliptical criterion:

$$f_i\left(\boldsymbol{\sigma}\right) = \left(\frac{\sigma_m}{A_i}\right)^2 + \left(\frac{\sigma_d}{\sqrt{2}B_i}\right)^2 \leq 1 \tag{5.20}$$

where the Von-Mises criterion is retrieved by letting $A_i/B_i \rightarrow +\infty$. The corresponding π-function for the elliptical criterion is given by Eq. (4.83) and reads here:

$$\pi_i = \sqrt{\left(A_i d_v\right)^2 + \left(\sqrt{2}B_i d_d\right)^2} \tag{5.21}$$

where $d_v = \operatorname{tr} \mathbf{d} = I_1'$ and $d_d = \sqrt{\boldsymbol{\delta}:\boldsymbol{\delta}} = \sqrt{2J_2'}$. We now apply the methodology of strength upscaling outlined in Section 2.4.2.

Step 1: Strain Rate Energy Function $\mathcal{W}_0\left(\mathbf{D}\right)$ of the Comparison Composite

The first step in solving the strength homogenization problem is to determine the strain rate energy function $\mathcal{W}_0\left(\mathbf{D}\right)$ of the linear comparison composite. For a Drucker-Prager material, the calculation of $\mathcal{W}_0\left(\mathbf{D}\right)$ would have been a challenge due to the necessity of considering a volumetric prestress τ_i. For a Von Mises material, however, no volumetric prestress is needed, and the comparison composite in the i-th phase is:

$$\mathbb{C}^i = 3K^i\mathbb{J} + 2G^i\mathbb{K} \tag{5.22}$$

Since there is no need for a volumetric prestress in the comparison composite, the macroscopic strain energy is readily expressed as:

$$\mathcal{W}_0\left(\mathbf{D}\right) = \frac{1}{2}\mathbf{D}:\mathbb{C}^{\text{hom}}:\mathbf{D} = \frac{1}{2}K^{\text{hom}}D_v^2 + G^{\text{hom}}D_d^2 \tag{5.23}$$

where $\mathbb{C}^{\text{hom}}$ is the macroscopic stiffness tensor, calculated with the linear homogenization method. For the self-consistent (polycrystal) morphology considered, rewriting Eqs. (5.12)

under a slightly different form yields:

$$K^{\text{hom}} = \frac{\sum\limits_i K_i K_{\mathbb{A}_i}}{\sum\limits_i K_{\mathbb{A}_i}} \tag{5.24a}$$

$$G^{\text{hom}} = \frac{\sum\limits_i G_i G_{\mathbb{A}_i}}{\sum\limits_i G_{\mathbb{A}_i}} \tag{5.24b}$$

where:

$$K_{\mathbb{A}_i} = \frac{1}{3} \frac{3K^{\text{hom}} + G^{\text{hom}}}{3K_i + 4G^{\text{hom}}} \tag{5.25}$$

$$G_{\mathbb{A}_i} = \frac{5}{2} \frac{G^{\text{hom}} \left(3K^{\text{hom}} + 4G^{\text{hom}}\right)}{G_i \left(9K^{\text{hom}} + 8G^{\text{hom}}\right) + 6G_i \left(K^{\text{hom}} + 2G^{\text{hom}}\right)} \tag{5.26}$$

so that K^{hom} can be rewritten as:

$$K^{\text{hom}} = \frac{\sum\limits_i \dfrac{K_i}{3K_i + 4G^{\text{hom}}}}{\sum\limits_i \dfrac{1}{3K_i + 4G^{\text{hom}}}} \tag{5.27}$$

Step 2: $\mathcal{V}_i$ Function for an Elliptic Criterion

The derivations performed in Section 2.4.2 remain valid and the calculation of the $\mathcal{V}_i$ function yields:

$$\frac{K^i}{G^i} = \left(\frac{A_i}{B_i}\right)^2 \tag{5.28}$$

and (see Eq. 4.78):

$$\mathcal{V}_i = \frac{c_i^2}{4G} = \frac{B_i^2}{2G} \tag{5.29}$$

Step 3: Stationarity of $\widetilde{\Pi}^{\text{hom}}$

The third step consists in exploring the stationarity of $\widetilde{\Pi}^{\text{hom}}$, defined by Eq. (4.62):

$$\widetilde{\Pi}^{\text{hom}} = \underset{K^i, G^i}{\text{stat}} \left[\mathcal{W}_0 \left(D_v, D_d\right) + \frac{1}{N} \mathcal{V}_i \right] \tag{5.30}$$

so that:

$$\forall i \in \{1..N\}, \quad \frac{\partial \widetilde{\Pi}^{\text{hom}}}{\partial G_i} = \frac{1}{2}\left(\frac{A_i}{B_i}\right)^2 \frac{\partial K^{\text{hom}}}{\partial K_i} D_v^2 + \frac{\partial G^{\text{hom}}}{\partial G_i} D_d^2 - \frac{1}{N}\frac{1}{2}\left(\frac{B_i}{G_i}\right)^2 = 0 \qquad (5.31)$$

in which all occurrences of K^i can be replaced by G^i thanks to Eq. (5.28):

$$\forall i \in \{1..N\}, \quad \frac{\partial \widetilde{\Pi}^{\text{hom}}}{\partial G_i} = \frac{1}{2}\frac{\partial K^{\text{hom}}}{\partial G_i} D_v^2 + \frac{\partial G^{\text{hom}}}{\partial G_i} D_d^2 - \frac{1}{N}\frac{1}{2}\left(\frac{B_i}{G_i}\right)^2 = 0 \qquad (5.32)$$

Step 4 & 5: Strength Criterion

The fourth and fifth steps consist in replacing D_v and D_d in the stationarity conditions (4.80) and in solving the resulting system of equations. The expressions for D_v and D_d are provided by the state equation (4.68) of the linear comparison composite combined with Eq. (4.52):

$$D_v = \frac{\Sigma_m}{K^{\text{hom}}} \qquad (5.33a)$$

$$D_d = \frac{\Sigma_d}{2G^{\text{hom}}} \qquad (5.33b)$$

Once replaced in the N stationarity conditions, Eq. (5.32) becomes:

$$\forall i \in \{1..N\}, \quad \frac{1}{2}\frac{\partial K^{\text{hom}}}{\partial G_i}\left(\frac{\Sigma_m}{K^{\text{hom}}}\right)^2 + \frac{\partial G^{\text{hom}}}{\partial G_i}\left(\frac{\Sigma_d}{2G^{\text{hom}}}\right)^2 - \frac{1}{N}\frac{1}{2}\left(\frac{B_i}{G_i}\right)^2 = 0 \qquad (5.34)$$

which provides N equations. An additional equation is given implicitly for G^{hom} and G^i for $i \in \{1..N\}$ by combining Eqs. (5.24b), (5.25) and (5.27):

$$\mathcal{Q}(G^{\text{hom}}, G^i) = 0 \qquad (5.35)$$

Consequently, a system of $N + 1$ equations is obtained for $N + 2$ unknowns: Σ_m is fixed; G_i, $i \in \{1..N\}$, G^{hom} and Σ_d. The degree of freedom stems from the indeterminate value of the plastic multiplier $\overset{\circ}{\lambda}$ in yield design, which translates here into indeterminacy on a value of G_i. Therefore the system of equations (5.34) and (5.35) can theoretically be solved, providing for each value of Σ_m one value of Σ_d, which thus enables the homogenized strength criterion

172

to be constructed. Nevertheless, implementing this system of equations is a challenge, one reason being that Eq. (5.34) requires the calculation of $\partial G^{\mathrm{hom}}/\partial G_i$ in the case that G^{hom} is defined implicitly only by Eq. (5.35). Moreover, we note that the full solution of the system of equations (5.34) and (5.35) yields the whole strength criterion of a homogenized medium made of N phases with elliptical strength criterion, although we are interested only in the limit case of a Von Mises criterion. Indeed, considering the Von Mises limit case will bring some simplifications to the system of equations.

Simplifications for the Von Mises Limit Case

The cohesion c^{hom} of the homogenized medium is calculated by evaluating Σ_d at $\Sigma_m = 0$. For $\Sigma_m = 0$, Eq. (5.34) simplifies:

$$\forall i \in \{1..N\}, \quad \frac{\partial G^{\mathrm{hom}}}{\partial G_i}\left(\frac{\Sigma_d}{2G^{\mathrm{hom}}}\right)^2 - \frac{1}{N}\frac{1}{2}\left(\frac{B_i}{G_i}\right)^2 = 0 \tag{5.36}$$

Yet an explicit form of $\partial G^{\mathrm{hom}}/\partial G_i$ is still required. This explicit form is obtained in the limit case of Von Mises criteria $A_i/B_i \to +\infty$. Controlling the way in which A_i/B_i tends toward infinity, we impose:

$$\frac{A_1}{B_1} = \frac{A_2}{B_2} = ... = \frac{A_N}{B_N} = \sqrt{r} \tag{5.37}$$

For large r, the combination of Eqs. (5.27) and (5.28) yields:

$$K^{\mathrm{hom}} = r\frac{N}{\sum_i \dfrac{1}{G_i}} \tag{5.38}$$

which, after differentiation, yields:

$$\frac{\partial K^{\mathrm{hom}}}{\partial G_j} = \frac{(K^{\mathrm{hom}})^2}{r}\frac{1}{NG_j^2} = \frac{K^{\mathrm{hom}}}{\sum_i \dfrac{1}{G_i}}\frac{1}{G_j^2} \tag{5.39}$$

As an intermediate step, we calculate:

$$\frac{\partial}{\partial G_j} \left[\frac{1}{G^{\text{hom}}(9K^{\text{hom}} + 8G^{\text{hom}}) + 6G_i(K^{\text{hom}} + 2G^{\text{hom}})} \right] =$$
$$-\frac{1}{3K^{\text{hom}}} \left(\frac{1}{3G^{\text{hom}} + 2G_i} \right)^2 \left[3\frac{\partial G^{\text{hom}}}{\partial G_j} + \frac{1}{\sum_i \frac{1}{G_i}} \frac{1}{G_j^2} (3G^{\text{hom}} + 2G_i) + 2\delta_{ij} \right] \qquad (5.40)$$

where δ_{ij} is the Kronecker symbol. By combining Eqs. (5.27), (5.26) and (5.24b), G^{hom} is now implicitly defined by:

$$G^{\text{hom}} \sum_i \frac{1}{G^{\text{hom}}(9K^{\text{hom}} + 8G^{\text{hom}}) + 6G_i(K^{\text{hom}} + 2G^{\text{hom}})} =$$
$$\sum_i \frac{G_i}{G^{\text{hom}}(9K^{\text{hom}} + 8G^{\text{hom}}) + 6G_i(K^{\text{hom}} + 2G^{\text{hom}})} \qquad (5.41)$$

Differentiating Eq. (5.41) and grouping correctly the terms provides an explicit expression for $\partial G^{\text{hom}}/\partial G_i$:

$$\frac{\partial G^{\text{hom}}}{\partial G_i} = \frac{\dfrac{G^{\text{hom}}}{(3G^{\text{hom}} + 2G_i)^2} + \dfrac{1}{5G_i{}^2 \left(\sum_j \dfrac{1}{G_j} \right)} \sum_i \dfrac{(G^{\text{hom}} - G_j)}{3G^{\text{hom}} + 2G_j}}{\sum_i \dfrac{G_j}{(3G^{\text{hom}} + 2G_j)^2}} \qquad (5.42)$$

In the limit case $A_i/B_i \to +\infty$, for which $K^{\text{hom}}/G^{\text{hom}} \to +\infty$, Eq. (5.41) further simplifies:

$$G^{\text{hom}} \sum_i \frac{1}{3G^{\text{hom}} + 2G_i} - \sum_i \frac{G_i}{3G^{\text{hom}} + 2G_i} = 0 \qquad (5.43)$$

Finally recalling from Eq. (5.18) that $H^{\text{hom}} = 4.76\Sigma_d$ and $B_i = \sqrt{2}c_i = 4.76\sqrt{2}\Sigma_d$, the system of equations (5.34) and (5.35) becomes:

$$\boxed{\begin{array}{l} \forall i \in \{1..N\}, \quad \dfrac{\partial G^{\text{hom}}}{\partial G_i} \left(\dfrac{H^{\text{hom}}}{G^{\text{hom}}} \right)^2 = \dfrac{1}{N} \left(\dfrac{H_i}{G_i} \right)^2 \\[3mm] G^{\text{hom}} \sum_i \dfrac{1}{3G^{\text{hom}} + 2G_i} - \sum_i \dfrac{G_i}{3G^{\text{hom}} + 2G_i} = 0 \end{array}} \qquad (5.44)$$

where $\partial G^{\text{hom}}/ \partial G_i$ is explicitly given by Eq. (5.42).

The system of equations (5.44) can be implemented and provides, from a measured set of indentation hardnesses $\{H_i\}_{i=1..N}$, an estimate of the homogenized indentation hardness H^{hom}.

Validation

The system of Equations (5.44) is validated on two two-phase model materials, for which Gathier [80] obtained analytical solutions. Those two model materials are:

- Solids + voids: The solid has a cohesion $c_s = 1$. For a volume fraction of solid $\eta = 0.7$, Gathier found a homogenized cohesion $c^{\mathrm{hom}} = 0.597$. The numerical solution of Eqs. (5.44) yields exactly the same value $c^{\mathrm{hom}} = 0.597$, which indeed is situated in between the Voigt-Reuss bounds (5.19):

$$0 \le \frac{c^{\mathrm{hom}}}{c_s} = 0.597 \le \eta = 0.7 \tag{5.45}$$

- Solids + hard inclusions: The solid has a cohesion $c_s = 1$. For a volume fraction of solid $\eta = 0.7$, Gathier found a homogenized cohesion $c^{\mathrm{hom}} = 1.577$. For the solution of the system (5.44), we need to input a value for the cohesion of the hard inclusions. A large value $c_{inc} = 4.5$ is chosen and yields exactly the same value $c^{\mathrm{hom}} = 1.577$, which compares to the Voigt-Reuss bounds (5.19) as follows:

$$1 \le \frac{c^{\mathrm{hom}}}{c_s} = 1.577 \le \eta + (1 - \eta)\frac{c_{inc}}{c_s} = 2.05 \tag{5.46}$$

Therefore, the method designed in this Section to assess the homogenized indentation hardness H^{hom} from a set of indentation hardnesses $\{H_i\}_{i=1..N}$ measured with a grid of indentations proves reliable.

5.3.3 Homogenized Indentation Creep Properties

The last Section of this Chapter derives expressions for the homogenized indentation creep properties $L^{\mathrm{hom}}(t)$ or $M^{\mathrm{hom}}(t)$ of the composite material, based on a set of indentation creep properties $\{L_i(t)\}_{i=1..N}$ or $\{M_i(t)\}_{i=1..N}$ measured with a grid of indentations. The derivation is based on the viscoelastic homogenization theory described in Section 2.3.3.

Here, as in Sections 5.3.1 and 5.3.2, the indented material is modeled at a scale $h/D < 1/10$ as a virtual N-phase material, where N is the number of indentation tests. Phase i of volume fraction $\phi_i = 1/N$ is characterized by the contact creep compliance $L_i(t)$ or, equivalently, by the contact relaxation modulus $M_i(t)$. Following the viscoelastic homogenization theory (Section 2.3.3), the solution of the viscoelastic problem is readily obtained from the elastic solution by making use of the s-multiplied Laplace transform. Therefore, $L^{\mathrm{hom}}(t)$ and $M^{\mathrm{hom}}(t)$, which are the solution of the viscoelastic homogenization of the virtual N-phase material, are readily found in the Laplace domain by applying an s-multiplied Laplace transform to Eq. (5.16):

$$\sum_{i=1}^{N} \frac{1}{1 + \frac{1}{2}(\widehat{M_i(s)}/\widehat{M^{\mathrm{hom}}(s)} - 1)} = \sum_{i=1}^{N} \frac{\widehat{M_i(s)}/\widehat{M^{\mathrm{hom}}(s)}}{1 + \frac{1}{2}(\widehat{M_i(s)}/\widehat{M^{\mathrm{hom}}(s)} - 1)}$$

$$\Updownarrow \qquad\qquad (5.47)$$

$$\sum_{i=1}^{N} \frac{1}{1 + \frac{1}{2}(\widehat{L^{\mathrm{hom}}(s)}/\widehat{L_i(s)} - 1)} = \sum_{i=1}^{N} \frac{\widehat{L^{\mathrm{hom}}(s)}/\widehat{L_i(s)}}{1 + \frac{1}{2}(\widehat{L^{\mathrm{hom}}(s)}/\widehat{L_i(s)} - 1)}$$

The determination of $L^{\mathrm{hom}}(t)$ and $M^{\mathrm{hom}}(t)$ requires an inverse Laplace transform of Eqs. (5.47), which, for arbitrary contact creep compliances $\{L_i(t)\}_{i=1..N}$ and relaxation moduli $\{M_i(t)\}_{i=1..N}$, cannot be performed analytically. A possible alternative approach is to invert Eqs. (5.47) numerically, making use of powerful algorithms, which are now available in the literature (e.g., [1]). But such a numerical inversion requires the solution of Eqs. (5.47) at several values of s, some of which for the solution is unstable. Therefore, the estimation of the homogenized creep properties $L^{\mathrm{hom}}(t)$ and $M^{\mathrm{hom}}(t)$ remains problematic in the general case of arbitrary $\{L_i(t)\}_{i=1..N}$ or $\{M_i(t)\}_{i=1..N}$. Two specific creep behaviors for which the homogenized creep properties can be estimated are considered next.

Maxwell Creep

Consider that the contact creep behavior of each phase is governed by a Maxwell unit and characterized by the viscosity ς_i. Following the approach developed in Section 4.4.3, we are interested in the asymptotic behavior of the homogenized creep properties at large times. An

application of the final value theorem [134] to $M_i(t)$ yields:

$$\lim_{s \to 0^+} \widehat{M_i(s)} = \varsigma_i \tag{5.48}$$

Eq. (5.47) is then rewritten in the form:

$$\lim_{s \to 0^+} \sum_{i=1}^{N} \frac{1}{1 + \frac{1}{2}(\varsigma_i / \widehat{M^{\text{hom}}(s)} - 1)} = \lim_{s \to 0^+} \sum_{i=1}^{N} \frac{\varsigma_i / \widehat{M^{\text{hom}}(s)}}{1 + \frac{1}{2}(\varsigma_i / \widehat{M^{\text{hom}}(s)} - 1)} \tag{5.49}$$

and finally:

$$\boxed{\sum_{i=1}^{N} \frac{1}{1 + \frac{1}{2}\left(\varsigma_i / \zeta^{\text{hom}} - 1\right)} = \sum_{i=1}^{N} \frac{\varsigma_i / \varsigma^{\text{hom}}}{1 + \frac{1}{2}\left(\varsigma_i / \varsigma^{\text{hom}} - 1\right)}} \tag{5.50}$$

where:

$$\lim_{s \to 0^+} \widehat{M^{\text{hom}}(s)} = \varsigma^{\text{hom}} \tag{5.51}$$

The above equation enables us to conclude (see Section 4.4.3) that, after a transient phase, the homogenized contact creep behavior is governed by a Maxwell unit of viscosity ς^{hom} which is estimated from the set of measured $\{\varsigma_i\}_{i=1..N}$ by solving Equation (5.50).

Logarithmic Creep

Consider then a logarithmic creep for each indented phase $i = 1, N$, for which the contact creep compliance reads (see Eq. (3.53)):

$$L_i(t) = \frac{1}{M_i} + \frac{\ln(t/\tau_i + 1)}{C_i} \tag{5.52}$$

To simplify the derivation, we assume that $\tau_i = \tau$ and $C_i / M_i = \alpha$ for all indented phases so that the full contact creep behavior of phase $i = 1, N$ is determined by the creep modulus C_i only. Considering these assumptions in (5.52), the Laplace transform of the contact creep compliance of phase i reads:

$$\widehat{L_i(s)} = \frac{\alpha - e^{s\tau} \operatorname{Ei}(-s\tau)}{sC_i} \tag{5.53}$$

where Ei is the exponential integral. Then, a substitution of Eq. (5.53) into Eq. (5.47) yields:

$$\sum_{i=1}^{N} \frac{1}{1 + \frac{1}{2}(\widehat{L^{\mathrm{hom}}(s)}sC_i/(\alpha - e^{S\mathcal{T}}\,\mathrm{Ei}(-s\tau)) - 1)} = \sum_{i=1}^{N} \frac{\widehat{L^{\mathrm{hom}}(s)}sC_i/(\alpha - e^{S\mathcal{T}}\,\mathrm{Ei}(-s\tau))}{1 + \frac{1}{2}(\widehat{L^{\mathrm{hom}}(s)}sC_i/(\alpha - e^{S\mathcal{T}}\,\mathrm{Ei}(-s\tau)) - 1)} \tag{5.54}$$

for which the solution is readily found to be:

$$\widehat{L^{\mathrm{hom}}(s)} = \frac{\alpha - e^{S\mathcal{T}}\,\mathrm{Ei}(-s\tau)}{sC^{\mathrm{hom}}} \tag{5.55}$$

where C^{hom} is given by:

$$\boxed{\sum_{i=1}^{N} \frac{1}{1 + \frac{1}{2}\left(C_i/C^{\mathrm{hom}} - 1\right)} = \sum_{i=1}^{N} \frac{C_i/C^{\mathrm{hom}}}{1 + \frac{1}{2}\left(C_i/C^{\mathrm{hom}} - 1\right)}} \tag{5.56}$$

From a comparison of Eqs. (5.53) and (5.55), we conclude that the contact creep behavior of the composite material is also logarithmic with regard to time. The magnitude of the logarithmic creep C^{hom} is estimated from the set of measured $\{C_i\}_{i=1..N}$ by solving Eq. (5.56).

5.4   Chapter Summary

The aim of indentation analysis is to link indentation data to meaningful mechanical properties of the indented material system. The tools of indentation analysis of multiphase materials presented in this Chapter achieve just this:

1. The statistical indentation technique ('grid indentation', Section 5.2) pioneered by Constantinides et al. and refined in this Chapter allows the extraction of phase properties of multiphase materials by careful monitoring of the indentation depth w.r.t. the characteristic size of the heterogeneity, $h/D < 1/10$. In particular, the proposed automatized deconvolution technique, based on cumulative distribution functions (instead of probability density functions) of the phase properties, enhances the repeatability of the technique.

2. The proposed self-consistent indentation technique (Section 5.3) translates the heterogeneity of the multiphase material from the scale of individual phases, $h/D < 1/10$, to

the composite scale $h/D \gg 1$. The derived self-consistent homogenization relations between grid indentation data and composite indentation properties provide a means to evaluate the influence of the constituent behavior on the composite behavior. Furthermore, a comparison between the analytical predictions and actual indentation test results performed at the composite scale, $h/D \gg 1$, may allow the identification of scale or size effects. In fact, the homogenization approach employed here is based on continuum micromechanics, which, like all continuum theories, does not capture scale effects. Hence, a confrontation of predicted and experimental indentation response at the composite scale allows one either to validate the relevance of the continuum theory (and thus the absence of scale effects) or to assess potential scale effects on stiffness, strength and viscous properties.

The statistical tools developed in this Chapter thus complement the tools of continuum indentation analysis presented in Part II and those of the micromechanics-based indentation analysis of heterogeneous solids presented in Chapter 4. We now have a wealth of methods at our disposal that allow us to characterize by means of indentation a material from the microscale to the macroscale. We are now ready to employ these tools for the indentation analysis of cement pastes, aiming at identifying the link between the multiphase composition, the microstructure and the elastic, strength and creep performance.

Part IV

Indentation Analysis of Cementitious Materials: Principles and Validation

Chapter 6

Multi-Scale Thought-Model of Microstructure

This fourth Part is devoted to the application of the tools of indentation analysis to cementitious materials. This Chapter introduces a multiscale thought-model of the microstructure of cement-based materials, which will form much of the backbone of this experimental investigation. The goal of introducing the multiscale thought-model in this Chapter is to zoom in, top-down, from the macroscale to the atomic scale, on the current state of knowledge about microstructure and properties of Calcium-Silicate-Hydrates (C-S-H), the hydraulic binding phase of all cement-based materials.

6.1 Introduction

Concrete is a fairly complex, heterogeneous and multiphase composite material, with a random microstructure at different length scales ranging from the nanometer scale to the macroscopic decimeter scale. The most prominent heterogeneity of cement-based materials affecting strength and durability properties is the porosity. However the porosity of cement-based materials does not occur at a single scale, but manifests itself at multiple scales from the nanometer to the millimeter level. An analysis of the microstructure, therefore, is suitably done by considering characteristic scales of heterogeneity, and thus the complex microstructure must be broken down to different scales. This division of scales is sketched in Figure 6-1 in the form of a four-level

Level III
Concrete

> -2

Cement paste
+ aggregates

1 cm

Level II
Cement Paste

-5/-4

C-S-H matrix + other
hydration products +
unhydrated clinker

10 μm

Level I
C-S-H Matrix

-7/-6

C-S-H solid + pores

100 nm

Log[m]

Level 0
C-S-H Solid

-9

C-S-H solid phase
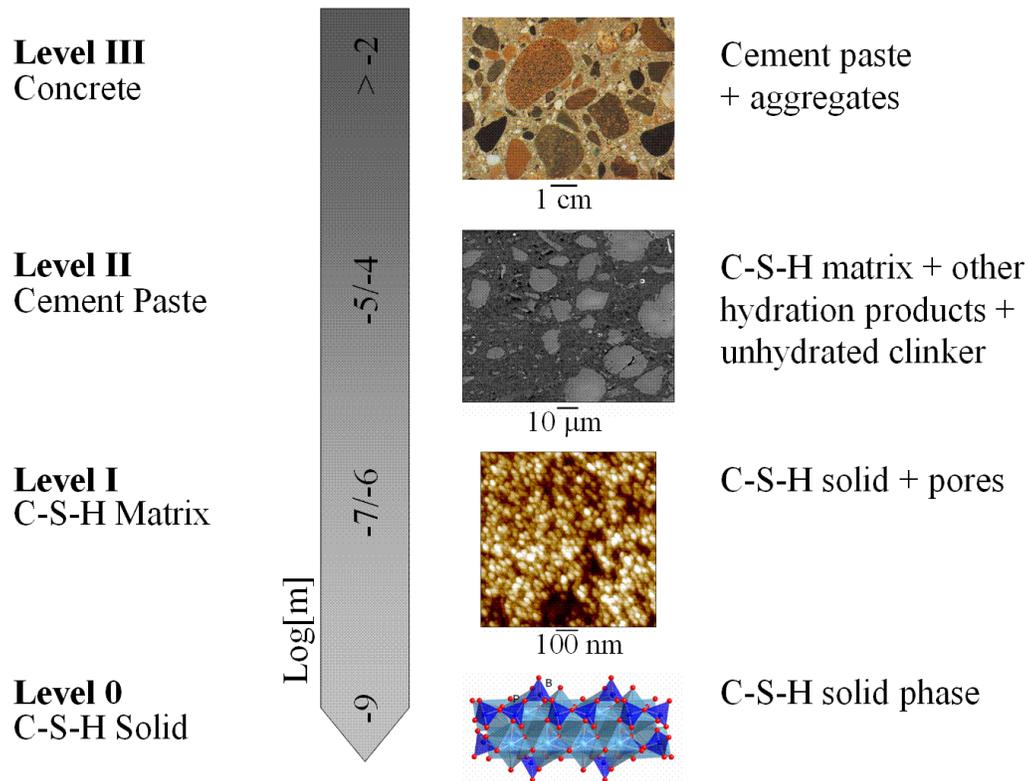
Figure 6-1: Multiscale structure thought model of concrete (adapted from [184]). Image credits: level 0 from [154], level I from [135], level II from [128] and level III from [106] microstructure [56].

6.2   Level III: Macroscale of Concrete

6.2.1   Aggregates

Concrete is a mix of cement paste with aggregates. Aggregates occupy 60% to 75% of the concrete volume, or, equivalently, 70% to 85% by mass [106]. Aggregates are divided into fine aggregates and coarse aggregates. Fine aggregates, mostly sand, have a characteristic size in the millimeter range. Coarse aggregates, mostly gravels and crushed stone, have a characteristic size in the centimeter range. At this macroscale of engineering application, concrete exhibits a distinct matrix-inclusion morphology, wherein the aggregates are the inclusions embedded in
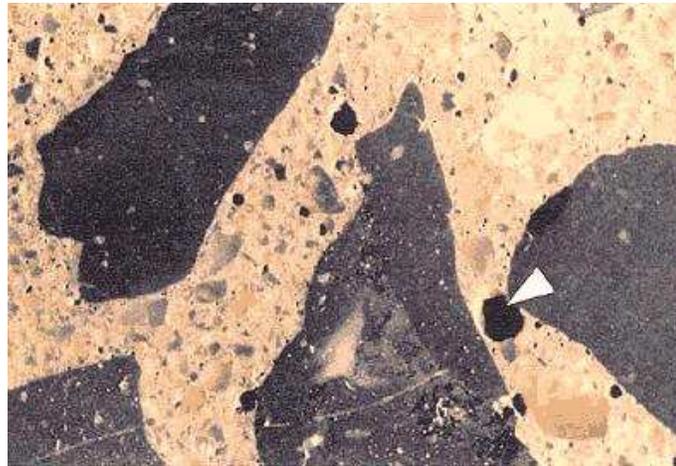
Figure 6-2: Surface of a concrete with macroporosity (from [189]). A macropore with a 2 mm diameter is marked with the arrow.

the cement paste matrix (Fig. 6-1, Level III).

6.2.2 Macroporosity

At the macroscale macropores of a characteristic size in the millimeter range and above may be present. These macropores often result from a lack of fluidity of the fresh material and can be avoided by an appropriate treatment of the fresh material (vibration, fluid admixtures, etc.). Macropores increase the rate of transport phenomena and are therefore detrimental to the durability of concrete.

6.3 Level II: Microscale of Cement Paste

The cement paste is formed by the hydration of cement clinker and water and is composed of hydration phases, residual clinker phases, and, for high water-to-cement ratio (w/c) materials, capillary porosity. The characteristic size of the residual clinker phases due to incomplete hydration is on the order of the micron to dozens of microns, depending on the w/c ratio. The characteristic size of the hydration phases is on the order of a single micron. The hydrated

Usual notation	Cement chemistry convention
CaO	C
SiO_2	S
Al_2O_3	A
Fe_2O_3	F
SO_3	$\underline{S}$
H_2O	H

Table 6.1: Cement chemistry notation.

Name	Notation	Wt%	M/GPa	H/GPa
Alite	C_3S	60-65	135 ± 7	8.7 ± 0.5
Belite	C_2S	20-25	130 ± 20	8 ± 1.0
Tricalcium aluminate	C_3A	8-12	145 ± 10	10.8 ± 0.7
Ferroaluminate	C_4AF	8-10	125 ± 25	9.5 ± 1.4

Table 6.2: Typical composition of a Portland cement (from [38]) and characteristic indentation modulus and hardness values of clinker phases [193]).

cement phase exhibits a distinct matrix-inclusion morphology, in which the unhydrated clinkers are embedded in a matrix of multiple hydration products, namely Calcium Silicate Hydrates (C-S-H), Portlandite (CH), calcium aluminates (AFm) and ettringite (AFt). These multiphase components of the cement paste are reviewed next. In doing so, it is convenient to employ cement chemistry notation as introduced in Table 6.1.

6.3.1 Clinker Phases

Clinker in Portland cement is made up of tricalcium silicate C_3S (also called 'alite'), dicalcium silicate C_2S (also called 'belite'), tricalcium aluminate C_3A, and tetracalcium aluminum ferrite C_4AF (also called 'ferroaluminate'). A typical composition is given in Table 6.2 together with indentation properties obtained by nanoindentation testing of pure clinker phases [193]. The density of the clinker phases is $\rho_{CL} = 3.15$ g/cm^3.

In the presence of water clinker dissolves. From a theoretical point of view, cement chemistry calculations (based on Bogues formula) predict a complete dissolution of clinker phases in pure form for water-to-cement ratios w/c (the usual name for the ratio of the mass of added water to the mass of clinker composing the cement) equal or greater than $w/c \simeq 0.25$. On the other hand, experimental study of the hydration reactions in real cement-based materials suggests

a complete hydration for $w/c \geq 0.38$ [151] if there is adequate supply of water during curing. This critical water-cement ratio required for complete hydration can increase to $w/c = 0.44$ if the paste is cured under sealed conditions [151]. The dissolution is initially fast but slows down dramatically over time, and the total dissolution of clinker may occur over weeks, months or even years, as long as there is water present in the pore space of the hardening material. Motivated by chemistry terminology, we refer to stoichiometric conditions when the water present in the mix is exactly the amount required for a complete dissolution, $w/c \simeq 0.4$. Accordingly, $w/c < 0.4$ will be considered as sub-stoichiometric conditions, for which it can be expected that unhydrated clinker is present at all times in the hydrated cement paste.

6.3.2 Calcium Aluminates and Ettringite

Calcium aluminates (noted 'AFm' by Taylor [177]) and ettringite (noted 'AFt' by Taylor [177]) result from the hydration of tricalcium aluminates C_3A and ferroaluminates C_4AF. AFm form from C_3A according to [177]:[1]

$$2\ C_3A + 27\ H \longrightarrow C_4AH_{19} + C_2AH_8$$
$$2\ C_3A + 21\ H \longrightarrow C_4AH_{13} + C_2AH_8 \qquad (6.1)$$
$$C_3A + CH + 12H \longrightarrow C_4AH_{13}$$
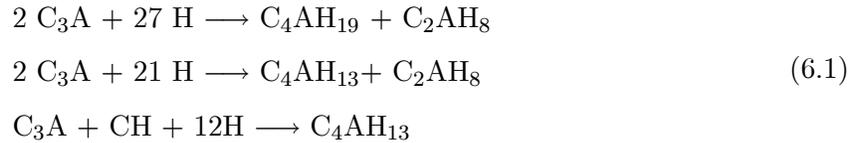
In the presence of sulfates, calcium aluminates also produce ettringite AFm:

$$C_3A + 3\ C\underline{S}H + 26H \longrightarrow C_6A\underline{S}_3H_{32} \qquad (6.2)$$

Once the sulfates are consumed, ettringite becomes an AFm phase:

$$2\ C_3A + C_6AS_3H_{32} + H \longrightarrow 3C_4A\underline{S}_3H_{12} \qquad (6.3)$$

Ettringite and calcium aluminates in the hardened material have a characteristic size on the order of the micrometer and occupy together roughly $15-20\%$ of the volume of hydration products [125]. Ettringite often has a distinctive needle-like shape (Fig. 6-3).

---

[1]The following set of reactions can be rewritten for C_4AF by replacing aluminum by iron.
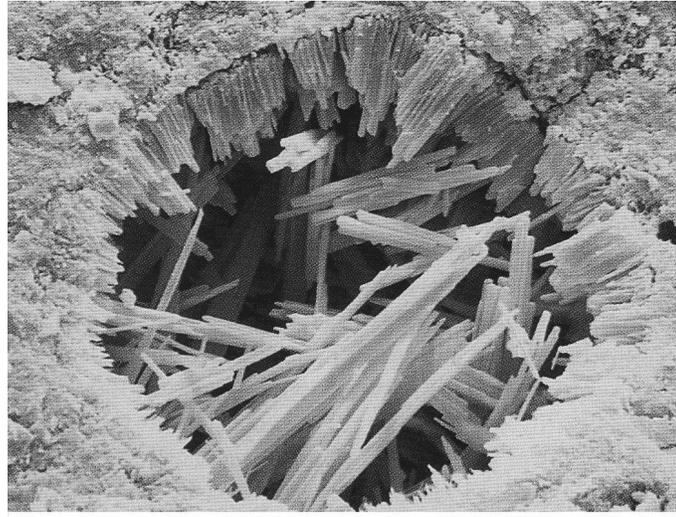
50 μm

Figure 6-3: Ettringite deposit in void (from [106]).

6.3.3 C-S-H Matrix and Portlandite

Calcium silicate hydrates (C-S-H) and Portlandite (CH) are the main products of hydration. C-S-H and CH occupy respectively $50-60\%$ and $20-35\%$ of the volume of hydration products [125]. They result from the hydration of C_3S and C_2S, according to the following reactions:[2]

$$2\ C_3S + 10.6\ H \longrightarrow C_{3.4}S_2H_8 + 2.6\ CH$$
$$2\ C_2S + 8.6\ H \longrightarrow C_{3.4}S_2H_8 + 0.6\ CH$$

(6.4)
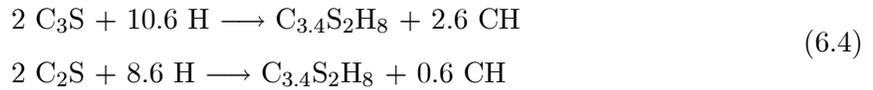
Portlandite (CH) is a crystal with definite stoichiometry and a distinctive hexagonal morphology. Depending on the environment, the characteristic size of the crystal can vary from one micrometer to a hundred micrometers [125]. CH density and mechanical properties are relatively well known [56]:

$$\rho_{CH} = 2.24\ \text{g/cm}^3;\ M_{CH} = 38 \pm 5\ \text{GPa};\ H_{CH} = 1.2 \pm 0.4\ \text{GPa}$$

(6.5)

---

[2]The reaction formulas are approximate, since the stoichiometry of C-S-H is not well-defined. Slightly different formulas are proposed in other references (e.g., in [125]).

In contrast, and in spite of decades of intensive research, many questions regarding the stoichiometry, density and microstructure of C-S-H are still unresolved. This is likely due to the fact that C-S-H at the microscale of the cement paste is not a homogeneous matrix phase, but a composite material composed of different C-S-H phases which are structurally distinct but compositionally similar; this justifies considering the microscale of C-S-H phases as a distinct material scale of cement-based materials.

Capillary Pores

Capillary pores of a characteristic size in the micrometer range are present at the scale of the cement paste due to the so-called Le-Chatelier contraction and/or an excess of water in the mix: The Le-Chatelier contraction in cement-based material is due to the fact that the molar volume of the hydration products is significantly smaller than the molar volume of the initial water and unhydrated clinker. In the hydration of pure clinker phases, the molar volume is reduced by roughly 10% [38] (but it is somewhat smaller for real Portland cements). The resulting voids manifest themselves at the micron scale in the form of capillary pores.

An excess of water beyond the stoichiometric water limit $w/c \simeq 0.4$ required for complete hydration also results in capillary pores saturated by the water not consumed in the hydration reactions. The remaining water prevents the solid hydration products from filling the space, a phenomenon which manifests itself at the micron scale in form of capillary pores.

6.4 Level I: C-S-H Microstructure

C-S-H microstructure refers to the morphology and assembly of C-S-H solid particles, which have been the focus of intensive research for more than sixty years. Most contributions to the C-S-H microstructure can be traced back to the groundbreaking works of Powers and colleagues [151], who by correlating macroscopic strength [194] and stiffness data [88] with physical data of a large range of materials prepared at different w/c-ratios recognized early on the critical role of the C-S-H microstructure, morphology and gel porosity on the macroscopic mechanical behavior (see Fig. 6-4).
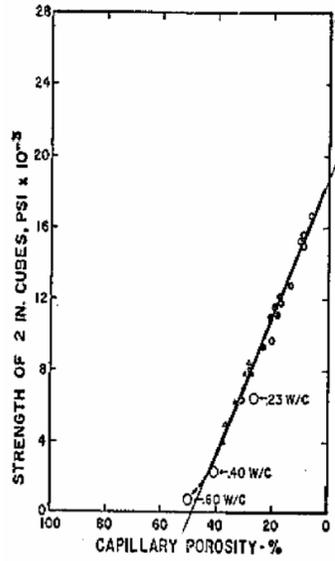
Figure 6-4: Cube strength versus 'capillary' porosity (capillary porosity includes here pores greater than about 1 nm) (from [194]).

6.4.1 C-S-H Morphology

The morphology of C-S-H is not uniform in the cement. In fact, advanced microscopy techniques provide evidence that there is a difference in the texture of the C-S-H close to the clinker grain and further from the grain (see, e.g., Fig. 6-5). Due to their location, those phases with different textures have been coined 'Inner Product C-S-H' and 'Outer Product C-S-H', respectively. But the issue of C-S-H morphology is far from being settled. From atomic force microscope investigations (AFM) [135] (Fig. 6-6) to small angle neutron scattering (SANS) [2] to transmission electron microscopy (TEM) [154][81] (Fig. 6-7), a variety of imaging techniques have provided ample evidence that the C-S-H matrix is composed of elementary C-S-H nanoparticles whose smallest dimension is on the order of 5 nm; however, depending on the type and mode of observation, the opinions differ as regards to other dimensions. To name a few disagreements: Based on AFM measurements, Nonat [135] suggests a brick-type morphology of the nanoparticle (lamellae) of dimension $60 \times 30 \times 5$ nm^3. From density, composition and surface area measurements, Jennings [97][179][98] postulates a globular C-S-H particle morphology of characteristic diameter 5.6 nm. This amorphous morphology is consistent with the

188

absence of any long-range order in C-S-H [177]. These globular particles agglomerate to form a Low Density (LD) and a High Density (HD) C-S-H 'gel', reminiscent of the outer and inner products, respectively. Based on TEM imaging of C_3S and C_2S pastes, Richardson [154] attributes the globular particle morphology to the so-called Inner Product (Ip) C-S-H (which is 4–8 nm in size in pastes hydrated at 20°C but smaller at elevated temperatures, 3–4 nm) which is distinct from the fibrillar morphology he assigns to the Outer Product (Op) C-S-H, which consists of aggregations of long thin particles that are about 3 nm in their smallest dimension and of variable length, ranging from a few nanometers to many tens of nanometers (Fig. 6-5).

6.4.2   Gel Porosity

The space not occupied by solid particles forms the gel porosity, which is fundamental for the understanding of the link between C-S-H microstructure and mechanical properties (see, e.g., Fig. 6-4). Powers considered the C-S-H gel porosity (gel pore volume over total gel volume) to be material invariant and equal to $\varphi_0 = 0.28$ independent of mix proportions, hydration degree, C-S-H morphology, etc. The application of advanced microscopy, X-ray mapping and Neutron scattering techniques to cement-based materials readily revealed that the assumption of a constant gel porosity could not be but an oversimplification of the highly heterogeneous microstructure of cement-based materials, overlooking the particular organizational feature of cement hydration products in highly dense packed 'inner' products (or HD C-S-H), and looser packed 'outer' products (or LD C-S-H). A brief review of microstructural models, in chronological order, is due.

Powers-and-Brownyard 1948 Model

Powers and Brownyard [151] proposed a model to describe the colloidal structure of C-S-H which is a benchmark in the cement community because it provides quantitative estimates while remaining extremely simple. Calibrated with a combination of water sorption and pore volume data, the model predicts a porosity of the C-S-H phase of 28% and an interlayer space (the space between neighboring sheets of C-S-H) of 1.8 nm. The empirical model also provides estimates for the volumetric fractions of different phases present in hardened cement paste [151]:
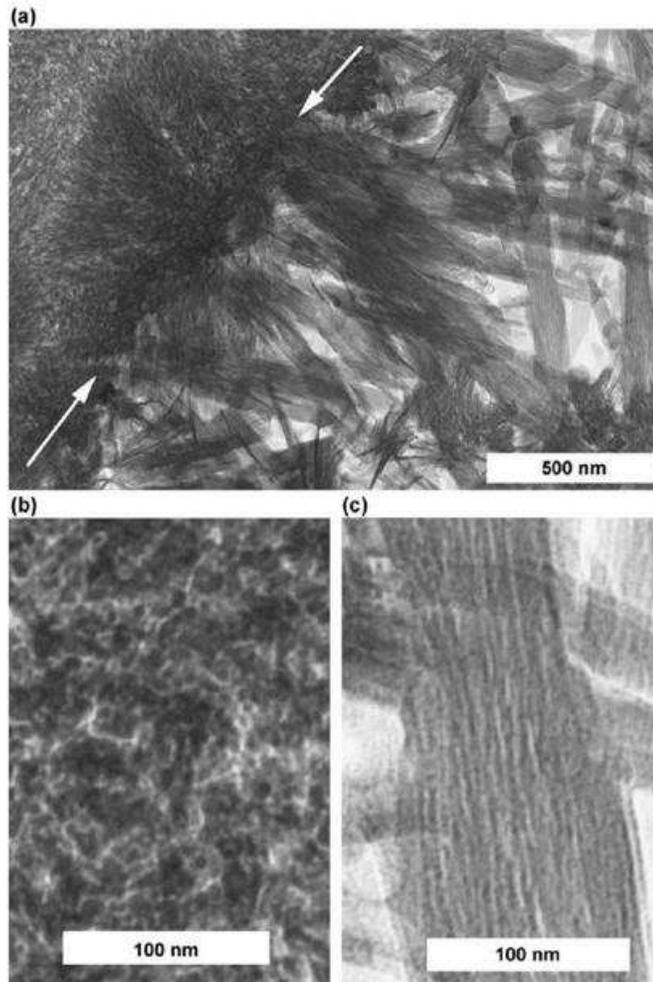
Figure 6-5: Evidence of the existence of two types of C-S-H (from [154]). (a) TEM micrograph showing both inner product C-S-H and outer product C-S-H present in a hardened C_3S paste. The white arrows indicate the boundary between the two types of C-S-H, with the inner product at the top left. (b) Enlargement of a region of inner product C-S-H. (c) Enlargement of a region of outer product C-S-H.

a)
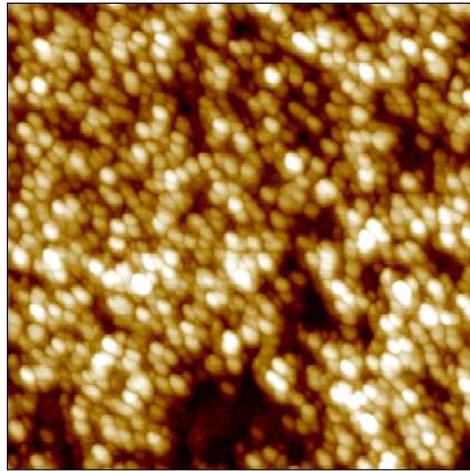
100 nm

b)
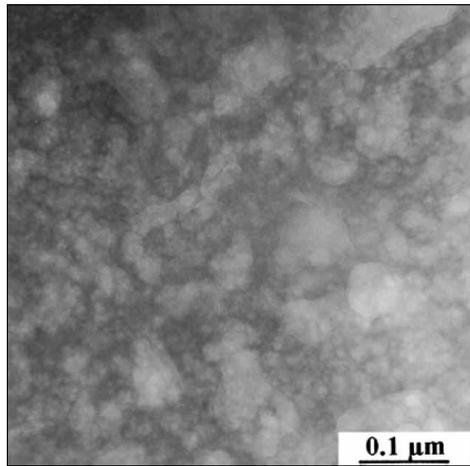
0.1 μm

Figure 6-6: Evidence of the particulate nature of C-S-H. (a) AFM image of the surface of a cement paste cast against a calcite single crystal, revealing particles with a mean size of 30-50 nm (from [135]). (b) TEM image of high performance concrete showing particles ranging in size from 20 to 60 nm (from [81]).

$$\overline{}$$
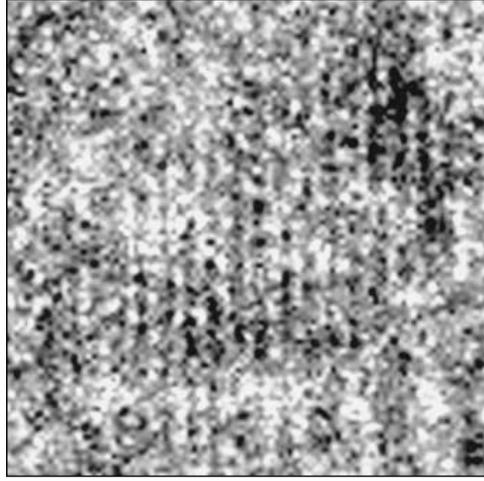
5 nm

Figure 6-7: HRTM picture of a nanocrystalline zone of C-S-H (from [81]).

$$
\begin{aligned}
V_{cs} &= 0.20\,(1-p)\,\xi && \text{Chemical Shrinkage} \\
V_{cw} &= p - 1.32\,(1-p)\,\xi && \text{Capillary Water} \\
V_{gw} &= 0.60\,(1-p)\,\xi && \text{Gel Water} \\
V_{gs} &= 1.52\,(1-p)\,\xi && \text{Gel Solid} \\
V_{cl} &= (1-p)\,(1-\xi) && \text{Unhydrated clinker}
\end{aligned}
\tag{6.6}
$$

where ξ is the hydration degree, defined as the mass fraction (or volume fraction) of clinker which has reacted:

$$
\xi = \frac{(\mathcal{W}_{CL})_{reacted}}{(\mathcal{W}_{CL})_{initial}}
\tag{6.7}
$$

p is the initial porosity, i.e., the volume which water occupies in the fresh mix:

$$
p = \frac{w/c}{w/c + \rho_w/\rho_c}
\tag{6.8}
$$

where $\rho_c = 3.15$ g/cm^3 and $\rho_w = 1.0$ g/cm^3 are the cement and water density, respectively. One verifies that the sum of the volume fractions equals one ($V_{cs} + V_{cw} + V_{gw} + V_{gs} + V_{cl} = 1$),

192

A - Interparticle Bonds
X - Interlayer Hydrate Water
B - Tobermorite Sheets
O - Physically Adsorbed Water
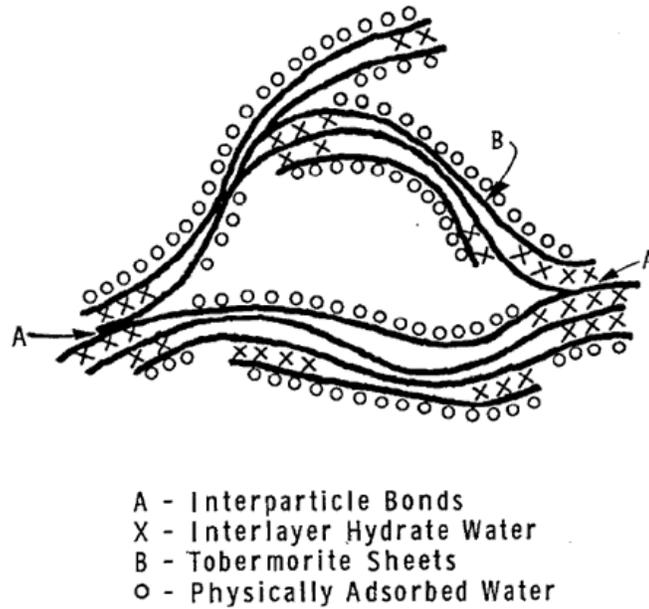
Figure 6-8: Feldman and Sereda model for C-S-H (from [74]).

but should not loose sight of the fact that the actual volume normalized by the initial volume, due to shrinkage, is $1 - V_{cs}$. We thus verify from Eqs. (6.6) that the gel porosity in Powers's model is the same irrespective of the hydration state of the material:

$$\varphi_0 = \frac{V_{gw}}{V_{gs} + V_{gw}} = 0.28 \qquad (6.9)$$

Feldman-Sereda Model

Feldman and Sereda [74] proposed a morphological modification to the Powers-Brownyard model, suggesting that C-S-H sheets stack in groups a few layers thick (Fig. 6-8). These ordered groups organize themselves in a disordered manner. The pore space associated with this model varies locally, the lower bound being the interlayer space. The Feldman-Sereda model assumes an interlayer space varying between 0.5 and 2.5 nm. The model is more qualitative rather than quantitative and may eventually explain why C-S-H, which is amorphous as a whole, can exhibit order at the nanometer scale (see, e.g., Fig. 6-7).

193

The Jennings Model

The quantitative consideration of morphology of the C-S-H phases in the form of a concise microstructural model of the gel microstructure is due to Jennings and coworkers [100] [101] [179] [98] [99], who recognized that outer and inner products are two structurally distinct but compositionally similar C-S-H phases; that is, amorphous nanoparticles of 5 nm characteristic size packed into two characteristic forms, a Low Density (LD) C-S-H phase and a High Density (HD) C-S-H phase, can be associated with outer and inner products, respectively.

The model development was motivated by an experimental inconsistency of surface area measurements: Samples with higher surface areas (measured by nitrogen) exhibit a lower gel porosity (measured by nitrogen as well) [179] (see Fig. 6-9). If C-S-H had a single porosity only, one would expect the opposite. One way to resolve this inconsistency is to consider several C-S-H phases of different densities. In Jennings model, there are two phases [100] [101]: The LD C-S-H phase and the HD C-S-H phase. The compatibility of those phases with the concept of inner and outer products remains an argument in favor of its existential justification, however, a model with more than two C-S-H phases could have equally well resolved the experimental inconsistency.

The original Jennings model is a two-scale porosity model (Fig. 6-10): An elementary C-S-H solid building forms a 'globule' (or a C-S-H particle), reminiscent of the packing of C-S-H sheets in the Feldman-Sereda Model. These globules pack into two different C-S-H phases which differ solely in the packing density of the C-S-H globules. The parameters of the model (density, porosity, size) were fit to an extensive set of density, composition and surface area measurements. The results of this calibration are given in Table 6.3. The globules have a characteristic size of about 5 nm, an intra-globular nanoporosity of $\phi_G = 18\%$, and two inter-globular porosities which can be viewed as the gel porosities: $\phi_{LD} = 37\%$ for the LD C-S-H and $\phi_{HD} = 24\%$ for the HD C-S-H. Constantinides and Ulm [58] noted that the corresponding packing densities ('one minus porosity') of LD C-S-H and HD C-S-H come remarkably close to *limit* packing densities of spheres: Namely the random close-packed limit (RCP [96]) or maximally random jammed state (MRJ [69]) of $\eta \approx 0.64$ for the LD C-S-H phase and the ordered face-centered cubic (fcc) or hexagonal close-packed (hcp) packing of $\eta = \pi/\sqrt{18} \approx 0.74$ [166] for the HD C-S-H phase. In contrast, far from being constant, the gel porosity of the
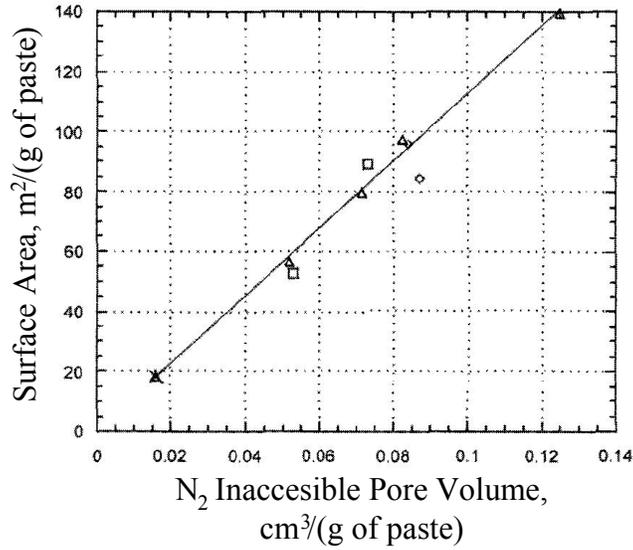
Figure 6-9: Measured surface areas and pore volumes for different cementitious materials (adapted from [98]).

C-S-H phase is recognized to be dependent on the volume proportions, f_{LD} and f_{HD}, which the two phases, LD C-S-H and HD C-S-H, respectively, occupy in the C-S-H matrix:

$$\varphi_0 = 1 - (0.64 \times f_{LD} + 0.74 \times f_{HD}) \tag{6.10}$$

with $f_{LD} + f_{HD} = 1$. Thus considering the existence of two structurally distinct but compositionally similar C-S-H phases introduces a new degree of freedom into the description of the microstructure, which is that of the differing volume fractions of the two phases. Based on multiple linear regression of nitrogen adsorption data on D-dried samples, the Jennings model provides the following empirical relation for the ratio of the mass of LD–C-S-H to the total mass of C-S-H (Fig. 6-11):

$$\mathcal{M}_r = 3.017\frac{w}{c}\xi - 1.347\xi + 0.538 \tag{6.11}$$

LEVEL '0':
C-S-H solid
+ Gel porosity
$d > 16.6$ nm

'Globules':
Basic Bldg. Block
+ Nanoporosity

5.6 nm

LD C-S-H
37% gel porosity

2.2 nm

Basic Building Block

18% nanoporosity
(structural water)

HD C-S-H
24% gel porosity
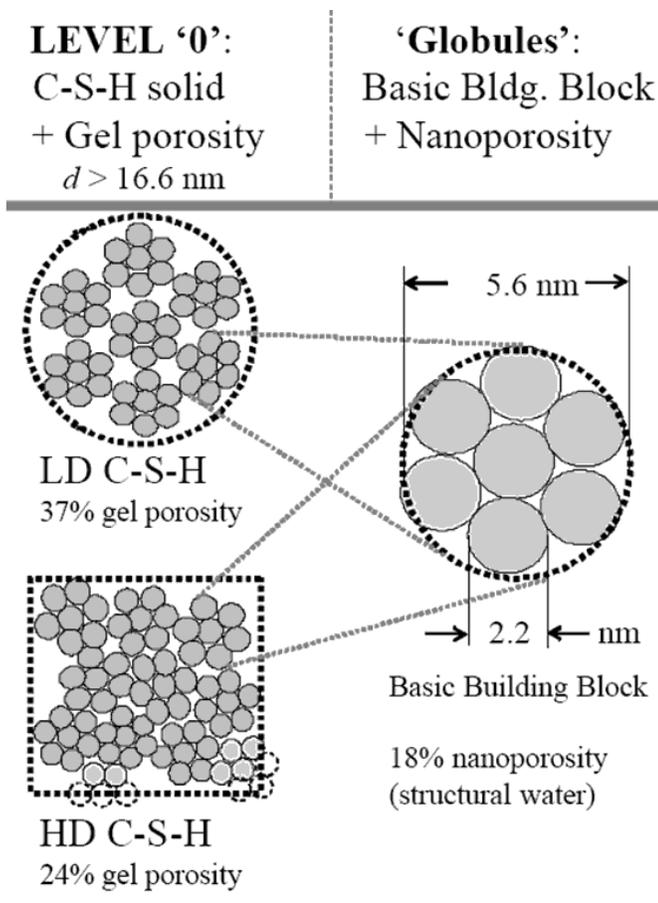
Figure 6-10: Jenning's model of C-S-H (adapted from [57]).
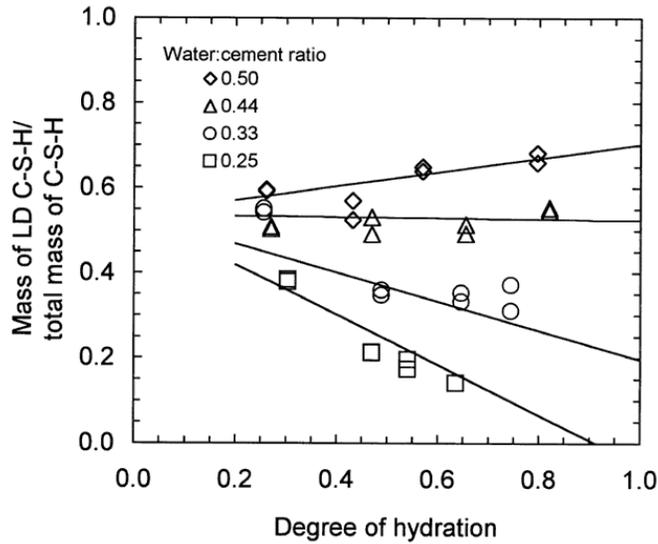
Figure 6-11: Mass ratio of Low Density (LD) C-S-H to total C-S-H (from [179]).

6.4.3 Mechanical Phase Properties and Granular Morphology

The existence and mechanical importance of these phases have been confirmed by statistical nanoindentation [59] [56] [184]: LD C-S-H and HD C-S-H were found to be uniquely characterized by a set of material properties (Tab. 6.3) which do not depend on mix proportions, type of cement, etc. Instead, they are intrinsic phase properties of two structurally distinct but compositionally similar C-S-H phases.

The link between these mechanical C-S-H phase properties and C-S-H packing density has been established, showing that the C-S-H phases exhibit a unique nanogranular morphology [58] [64] [102]. This is shown in Figure 6-12, in which values of indentation modulus and indentation hardness of the Low-Density (or outer products) and the High Density (or inner products) C-S-H structures obtained from statistical nanoindentation technique [58] are plotted versus C-S-H values of packing density obtained from mass density measurements, small-angle neutron scattering (SANS) and X-ray scattering data [98] [102] [3]. The almost linear scaling of the elastic properties with the packing density hints towards a granular morphology of the C-S-H particles with a percolation threshold on the order of $\eta_0 = 1/2$, reminiscent of the self-consistent theory with perfect sphericity (see Section 4.2.4). Although C-S-H particles or stacked layers

197

	Density, g/cm		Porosity, %	Property	
	pores full	pores empty		M, GPa	H, GPa
Basic building block	2.8[a]		N.A.	N.A.	N.A.
Globules	2.48	2.30	17.9[a]	61.2[c]	1.78[c]
LD C-S-H	1.93	1.44	37.4[b]	18.2 ± 4.2	0.45 ± 0.14
HD C-S-H	2.13	1.75	23.9[b]	29.1 ± 4.0	0.83 ± 0.18

Table 6.3: Computed density and porosity of the C-S-H basic building blocks, globules and phases, according to Jennings [97].
(a) The value for the density of the basic building block was recently updated by Allen, Jennings et al. to 2,604 kg.m^{-3} $\pm$ 22% [3], from which value the structural porosity becomes 11.7 %
(b) The calculated porosity is the porosity with respect to the gobule and therefore does not include the structural porosity.
(c) obtained by linear extrapolation to zero porosity [58].

are unlikely to be spherical, given their relatively high packing density any possible asphericity of the C-S-H particle has a negligible effect on the elastic properties of the LD C-S-H and HD C-S-H (see Section 4.2.5).

6.5 Level 0: C-S-H Solid

6.5.1 Atomistic Structure

The stoichiometry of C-S-H is ill-defined and the dashes in 'C-S-H' are here to remind the reader that the main constituents (C, S, and H) are known, but that their stoichiometry is not. To make the comparison between different compositions, the Ca–over–Si mass ratio (called the 'Ca/Si ratio') is a handy parameter, as it varies depending on cement composition [177]. Furthermore, X-ray microanalysis (scanning electron microscopy SEM or electron-probe micro-analysis EPMA) shows that the Ca/Si ratio varies locally within a given sample [178]. Usually, the Ca/Si ratio is comprised between 1.5 and 2 [125] with an average of around 1.75, but values as high 2.3 and as low as 1.2 have been reported (Fig. 6-13).

It is generally agreed that the C-S-H solid phase has a sheet-like molecular structure. The two-dimensional structure of this C-S-H sheet is considered to be a double plane of Ca^{2+} ions 6- or 7- coordinated by central O^{2-} ions [145]. Silica chains are attached on either side. The sheets are stacked separated by water molecules, Ca^{2+} ions and possibly OH^- ions. Still, the exact structure of C-S-H is not known.
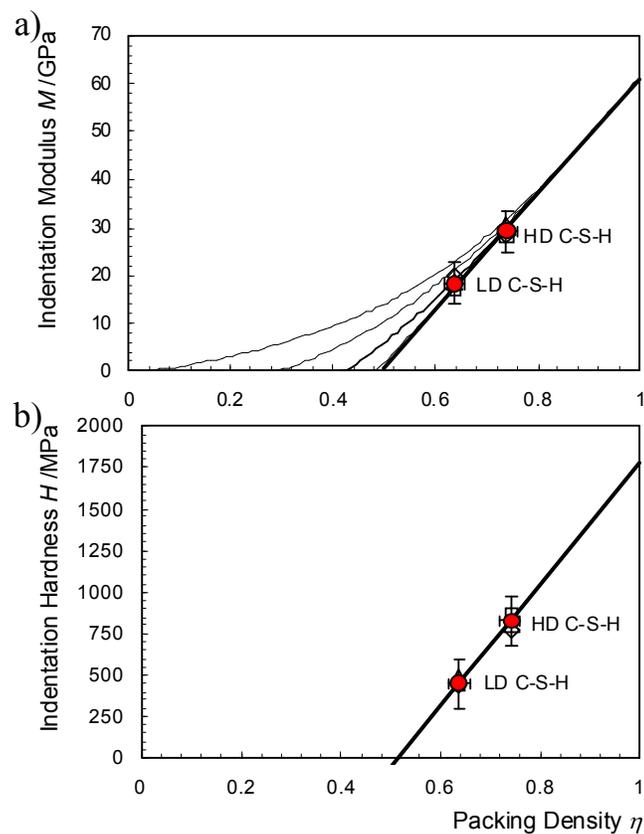
Figure 6-12: Linear extrapolation of (a) measured indentaton moduli and (b) measured indentation hardnesses of LD C-S-H and HD C-S-H to the solid state ($\eta \rightarrow 1$). The packing densities of LD C-S-H and HD C-S-H were obtained separately from specific surface area measurements (adapted from [58]). Figure a) also displays indentation modulus–packing density scaling relations for different particle aspect ratios.
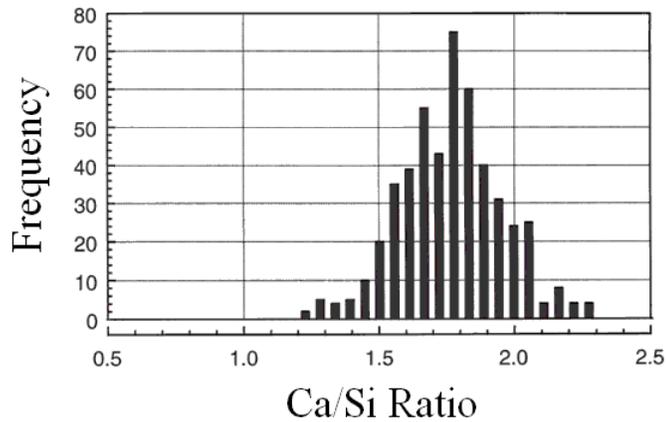
Figure 6-13: Ca/Si ratio frequency histogram in Portland cement pastes, measured by 493 TEM microanalyses of C-S-H free of admixture with other phases (from [153]).

There exists a resemblance in the crystal chemistry and the X-ray diffraction patterns between C-S-H and two naturally occurring minerals, Tobermorite and Jennite [177]; for which reason Tobermorite and Jennite have been proposed as natural analogs of the C-S-H molecular structure. Tobermorite exists in three different forms distinguished by the interlayer spacings: 9 Å, 11 Å and 14 Å. Two structures have been proposed for the 11 Å tobermorite (Fig. 6-14), Hamid's structure and Merlino's structure. In Hamid's structure, the repeating units along the chains are called 'dreierketten', with two pairing tetrahedra linked to the CaO polyhedra layer [84]. The interlayer space is occupied by water molecules only, and no chemical bond exists between two adjacent sheets. In contrast, in Merlino's structure adjacent sheets are linked by bridging covalent Si-O-Si bonds [126].

Making an analogy between real C-S-H and tobermorite should nevertheless be considered with care since the analogy may be incomplete [177]. Indeed, C-S-H in ordinary Portland cement has a Ca/Si ratio of 1.75 on average, whereas tobermorite has a Ca/Si ratio of 0.67, 0.83 or 1 for Hamid's structure and 0.66 or 0.75 for Merlino's structure. At such a large Ca/Si ratio, the structure of C-S-H is controversial. Three main models have been proposed for this structure. These models are either a solid solution with Portlandite, a nanophase mixture of tobermorite- and jennite-related units, or a defective tobermorite further modified by the replacement of SiO_2 units by $Ca(OH)_2$ [145].

200

a)

b)
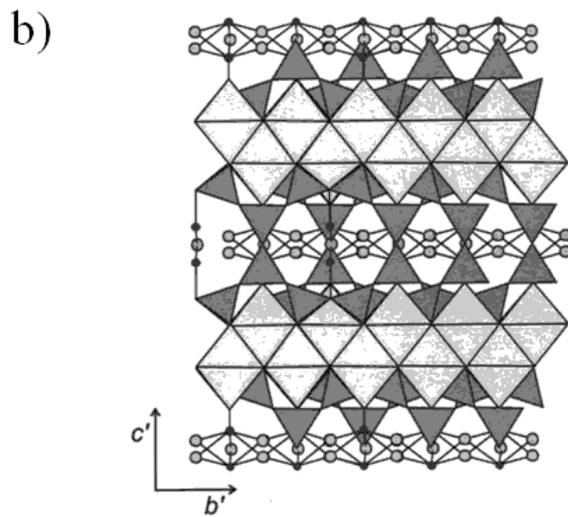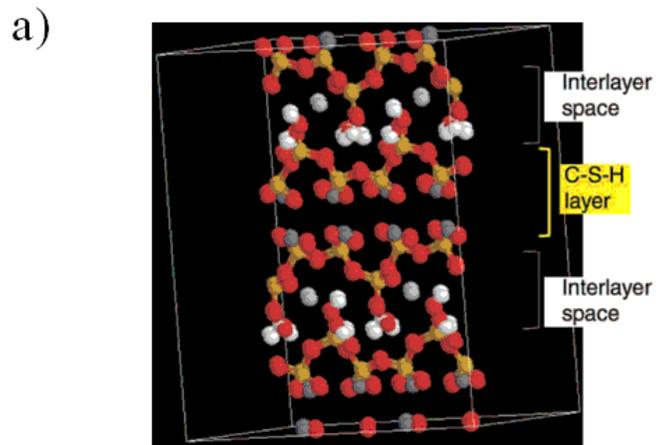
Figure 6-14: Proposed structures for 11 Å tobermorite: (a) Hamid's structure (from [145]) (b) Merlino's structure (from [126]).

The density of the C-S-H solid phase depends on the relative humidity. To enable comparison and remove all evaporable water, C-S-H is often 'D-dried', i.e., heated at 105°C in an atmosphere free of CO_2. By doing so, all water present in the gel pores is removed, although some structural water of the C-S-H solid may also be removed [177]. Density measurements for D-dry C-S-H solid phase range from 2,440 kg/m^3 [151] to 2,860 kg/m^3 [28]. Allen et al. [3] showed recently that D-drying indeed removed part of the structural water. Without D-drying the samples, and from a combination of small-angle neutron and X-ray scattering data, they measured a density $\rho = 2,604$ kg/m^3 of the C-S-H solid phase. They also measured a tentative average composition of C-S-H as:

$$C - S - H = C_{1.7}S_2H_{1.8} \tag{6.12}$$

where we remind ourselves that C, S and H in cement chemistry stand for CaO, SiO_2 and H_2O, respectively (Tab. 6.1).

6.5.2 Mechanical Properties by Molecular Dynamics (MD) Simulations

At present, no direct measurements of the elastic and strength properties of the C-S-H solid phase exist. This is due to the fact that C-S-H solid phase cannot be recapitulated in a bulk solid form suitable for mechanical testing. Most of our knowledge comes from atomistic simulations of tobermorite, the natural analog of C-S-H, and from extrapolation of nanoindentation results of C-S-H phases containing gel porosity to a zero porosity.

From energy minimization at 0 K, Pellenq and Van Damme [145] reported the average Young's modulus of Hamid's structure (Ca/Si = 1) of 11 Å tobermorite to be $E_s = 57.1$ GPa, which translates with an assumed Poisson's ratio of $0.2 - 0.25$ into an equivalent indentation modulus of

$$m_s = \frac{E_s}{1 - \nu_s^2} = 59.5 - 60.9 \text{ GPa} \tag{6.13}$$

This value for the hydration products is significantly lower than the reported stiffness values of the hydration reactants, i.e., clinker phases (see Table 6.2). The order of magnitude of this value was recently confirmed by Shahsavari et al. [163] for Merlino's structure of the 11 Å

tobermorite. From the full elasticity tensor determined from MD-simulations,

$$
\mathbb{C}_s/\text{GPa} = \begin{bmatrix} C_{11}^s = 82.8 & C_{12}^s = 35.5 & C_{13}^s = 25.2 & 0 & 0 & -0.7 \\ & C_{22}^s = 113.4 & C_{23}^s = 22.0 & 0 & 0 & -8.2 \\ & & C_{33}^s = 42.9 & 0 & 0 & 0.9 \\ & & & 2C_{66}^s = 21.0 & -0.1 & 0 \\ & & & & 2C_{44}^s = 16.7 & 0 \\ & & & & & 2C_{44}^s = 36.9 \end{bmatrix}
$$

$$(6.14)$$

one can calculate the quasi-isotropic bulk modulus and shear modulus using the Voigt-Reuss-Hill average[3] and consequently, by means of Eq. (2.20), the quasi-isotropic solid indentation modulus and the Poisson's ratio of the C-S-H solid phase:

$$
\boxed{\begin{aligned} m_s &= 63.5 \text{ GPa} \\ \nu_s &= 0.25 \end{aligned}}
$$

$$(6.20)$$

6.5.3 Asymptotic Nanoindentation Properties

Constantinides and Ulm [58] combined nanoindentation measurements of LD C-S-H and HD C-S-H properties with porosity estimates obtained from specific surface area (SSA) measurements by Jennings [97] (Tab. 6.3) to correct for the effect of porosity of the C-S-H solid phase. The extrapolation shown in Figure 6-12 gives a solid indentation modulus of $m_s = 61.2$ GPa, which compares fairly well with the results obtained from MD-simulations.

---

[3]As a reminder, the Voigt-Reuss-Hill average is the average of the quasi-isotropic bulk modulus and shear modulus of the Voigt and Reuss bounds (see e.g. [4]):

$$K_V = \frac{1}{9}\left(2C_{11}^s + C_{33}^s\right) + \frac{2}{9}\left(C_{12}^s + 2C_{13}^s\right) \tag{6.15}$$

$$G_V = \frac{1}{15}\left(2C_{11}^s + C_{13}^s\right) - \frac{1}{15}\left(C_{12}^s + 2C_{13}^s\right) + \frac{1}{5}\left(2C_{44}^s + C_{66}^s\right) \tag{6.16}$$

$$K_R = \frac{1}{A\left(C_{11}^s + C_{12}^s + 2C_{33}^s - 4C_{13}^s\right)} \tag{6.17}$$

$$G_R = \frac{15}{2A\left(2\left(C_{11}^s + C_{12}^s\right) + 4C_{13}^s + C_{33}^s\right) + 6\left(1/C_{44}^s + 1/C_{66}^s\right)} \tag{6.18}$$

$$K_{VRH} = \frac{1}{2}\left(K_V + K_R\right); \; G_{VRH} = \frac{1}{2}\left(G_V + G_R\right) \tag{6.19}$$

There is thus some strong evidence, supported by both atomistic simulations and nanoindentation tests, that a characteristic value for the C-S-H solid elasticity property is on the order of $m_s = 59 - 65$ GPa.

6.6 Chapter Summary

The goal of introducing the multiscale thought-model in this Chapter was to zoom in, top-down, from the macroscale to the atomic scale on the current state of knowledge about the microstructure and properties of Calcium-Silicate-Hydrates (C-S-H). While it is generally agreed that C-S-H has a layered structure (i.e., is made up of stacked C-S-H sheets) which resembles that of tobermorite and jennite with many imperfections and irregularities [145], the exact atomic structure of C-S-H is still beyond the current knowledge horizon. There is some evidence that the elastic stiffness of the elementary C-S-H particle is on the order of $m_s = 59 - 65$ GPa, but strength properties are still not known. Furthermore, while it is generally agreed that C-S-H exists in different forms, there is no consensus with regard to the number and morphology of these C-S-H phases. The Jennings model postulates the existence of two phases, low and high-density, whose existence and importance have been confirmed by nanoindentation on regular w/c materials [58]. These findings require confirmation in order to solidify this first link between microstructure and properties. In summary, the implementation of the materials science paradigm, which is to link mix proportions and processing to microstructure and mechanical performance, for cementitious materials remains a formidable challenge. The next Chapters will address this challenge by applying the comprehensive tool box of indentation analysis developed in Parts II and III to a large range of cement paste materials of different mix proportions.

Chapter 7

Materials and Methods

The overall goal of the experimental investigation is to make the link between composition –
microstructure – and material performance of cement-based materials. As a prerequisite, this
materials and methods Chapter implements and validates, for cementitious materials, the tools
of indentation analysis developed in Part III. We start by presenting the investigated cement-
based materials and present the specific conditions of use, for cement-based materials, of the
statistical indentation techniques, including experimental indentation issues, sample prepara-
tion, choice of indentation depth; etc. This implementation and validation of the indentation
technique for cement-based materials will be used in the next Part to assess the microstruc-
ture of a large range of cement-based materials and phase properties of C-S-H phases, with a
particular focus on fundamental creep properties of C-S-H.

7.1   Materials

7.1.1   Mix Proportions

Forty-eight (48 *!*) cement paste materials of various mix proportions and processing conditions
were subjected to experimental investigation. All samples were prepared in the central research
laboratory (LCR) of Lafarge[1] and delivered to M.I.T. in sealed conditions. The mix proportions
were chosen in order to generate a sufficiently large range of different compositions which

---

[1]Special thanks to Philippe Fonolossa and Blandine Albert.

CaO	SiO$_2$	Al$_2$O$_3$	Fe$_2$O$_3$	SO$_3$			LOI[a]
67.17	22.14	3.12	2.51	2.13			1.68

alite	belite	ferrite	aluminate	anhydrite	gypsum	calcite
71.1	15.00	7.00	1.2	1.4	1.2	1.8

Table 7.1: Composition of the Portland cement from Le Teil in mass percentage of each component provided by the manufacturer (Lafarge). Components with a mass percentage smaller than one percent are not included. (a) LOI: loss on ignition.

will be linked (by means of statistical indentation methods) to microstructure and mechanical properties. The samples are identified by the following denomination which captures the main compositional parameters varied in the experimental investigation:

$$\boxed{type - w/c - A/c(A) - HT} \tag{7.1}$$

where:

- *type* stands for the type of hydraulic binder employed. The main body of investigated materials was prepared with an alite (C_3S) rich CEM I Portland cement from Le Teil (for the composition, see Tab. 7.1), denoted by 'PC'. But a few samples (8/48) were prepared with pure C_3S clinker phases, denominated by 'C3S'. The rationale for considering both types is to check whether microstructure and phase properties of the hydration phases differ if prepared with pure clinker (C3S) or industrial clinker mixes (PC).

- w/c in mass percentage stands for the water-to-cement (mass) ratio, which was varied in between $w/c = 15\%$ and $w/c = 40\%$. Reminding ourselves that $w/c \simeq 0.4$ corresponds (almost) to stoichiometric conditions ($w/c = 0.38$ according to the Powers model; see Sections 6.3.1 ,6.3.3 and 6.4.2), the focus of the experimental campaign is on cement pastes prepared at sub-stoichiometric conditions. The rationale of investigating sub-stoichiometric conditions is two-fold: (1) To avoid the presence of capillary pores in the hydrated cement paste due to the presence of water in excess of the water required for 'complete' hydration; and thus (2) to focus the experimental investigation on microstructure and properties of the C-S-H phases.

- $A/c(A)$ stands for the admixture-to-cement (mass) ratio (in percent of weight), while (A)

identifies the type of admixture. Two types of admixture are considered in this study:

– Silica Fumes ($A = $ SF), in different mass percentages varying between $SF/c = 8.75\%$ and $SF/c = 32\%$ of the weight of cement. The fineness of the silica fumes, obtained from laser granulometry performed by Lafarge, is 2,550 cm^2/g, yielding an average particle diameter of 7.6 μm (for the granulometric curve, see Figure 7-1). Silica fumes are usually much finer than this (average particle diameter on the order of 10 nm), and it is likely that the laser granulometry sampled silica flocks rather than silica particles. The rationale of considering silica fumes is primarily to consider the pozzolanic effect. Pozzolan contains reactive silica that reacts with Portlandite (CH) to form C-S-H (see, e.g., [125]):

$$\text{pozzolan} + \text{CH} + \text{H} \longrightarrow \text{C-S-H} \tag{7.2}$$

The investigation, therefore, begins by considering whether the hydrates formed by the pozzolanic reaction have a different C-S-H microstructure and C-S-H phase properties than those encountered in normal cement paste materials without pozzolanic additives.

– Calcareous (limestone) filler in amounts of $CF/c = 10\%$ and $CF/c = 25\%$ of the weight of cement. Two types of calcareous filler were considered, $A =$ CF1 and $A =$ CF2, which differ in their fineness only. The fineness of CF1, obtained from laser granulometry, is 12,220 cm^2/g, yielding an average particle diameter of 1.6 μm. The fineness of CF2, also obtained from laser granulometry, is 7,320 cm^2/g, yielding an average particle diameter of 2.6 μm. According to the manufacturer, given the grinding performed, CF2 was expected to be finer than CF1. Therefore, it may well be that the laser granulometry of CF2 sampled flocks rather than particles. The investigation of the effect of calcareous filler on the C-S-H microstructure begins by inquiring whether calcareous fillers are reactive or chemically inert. Indeed, some cement chemistry studies provide evidence that a fraction of calcite present in commercially available cements is 'reactive', altering the mineralogy of hydrated cement pastes without affecting the C-S-H mineralogical compositions [120]. Furthermore
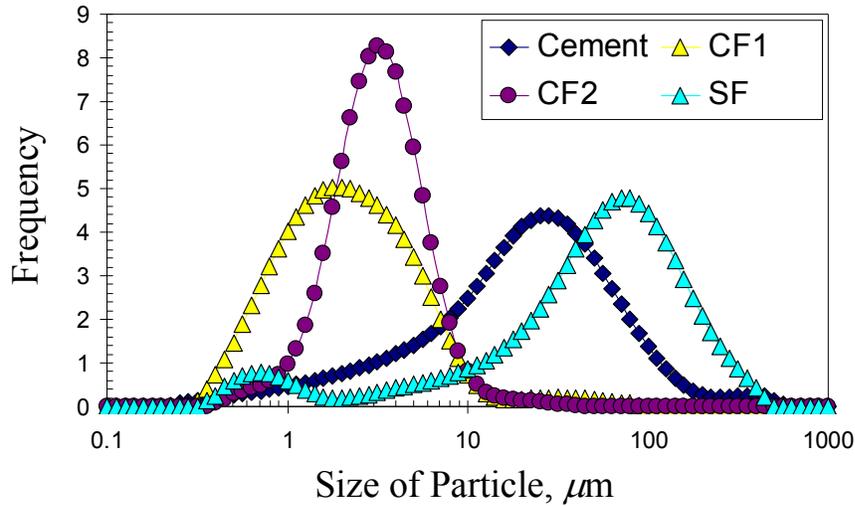
Figure 7-1: Granulometric curves of the cement, calcareous fillers (CF) and silica fumes (SF) used in the nanoindentation experimental campaign [provided by Lafarge]. The curves for CF2 and SF are likely to have yielded the measurement of flocks.

some studies hint towards the provision of nucleation sites for the hydration products [38],[86] that eventually accelerate the early-age hydration of Portland limestone cement. Indeed, during hydration, the hydration products need a support in order to develop. In a cement with no admixture, this support is usually the clinker grain itself. The hydration products then create a layer around the clinker grain, which impedes further hydration. Added (non-reactive) admixtures may provide a new support on which hydration products can precipitate and may therefore decrease the layer of hydrates around the clinker grains and facilitate further hydration. This type of mechanism, if it were to exist, would certainly alter the microstructure.

- $HT = 0$ or $HT = 2$ stands for the duration (in days) of a heat treatment (HT) applied two days after casting of the sample. The HT consists of a 48-hour-long heating of the sample at $90\,^{\circ}$C, representative of an HT protocol employed in the field for advanced concrete solutions. Whether such an HT affects the C-S-H phase properties or the microstructure or both is the focus of the investigation of the effect of HT on the microstructure of C-S-H.

Sample	Sample Name	w/c [%]	SF/c[(1)] [%]	CF/c[(2)] [%]	Heat treatment
1	C3S-20-0-0	20			none
2	C3S-20-0-2	20			at 2 days
3	C3S-20-24(SF)-0	20	24		none
4	C3S-20-24(SF)-2	20	24		at 2 days
5	C3S-25-0-0	25			none
6	C3S-25-0-2	25			at 2 days
7	C3S-30-0-0	30			none
8	C3S-30-0-2	30			none
9	PC-15-0-0	15			none
10	PC-15-0-2	15			at 2 days
11	PC-20-0-0	20			none
12	PC-20-0-2	20			at 2 days
13	PC-20-8(SF)-0	20			none
14	PC-20-8(SF)-2	20	8.75		at 2 days
15	PC-20-10(CF1)-0	20		10	none
16	PC-20-10(CF2)-0	20		10	none
17	PC-20-17(SF)-2	20	17.5		at 2 days
18	PC-20-21(SF)-0	20	21.6		none
19	PC-20-24(SF)-0	20	24		none
20	PC-20-24(SF)-2	20	24		at 2 days
21	PC-20-25(CF1)-0	20		25	none
22	PC-20-25(CF2)-0	20		25	none
23	PC-20-32(SF)-2	20	32		at 2 days
24	PC-25-0-2	25			at 2 days

Table 7.2: List of tested cementitious materials: Part 1.
(1) Weight of silica fumes (SF), in percent of the weight of cement.
(2) Weight of calcareous filler (CF), in percent of the weight of cement.

7.1.2   Subsets of Samples

The 48 samples and their composition are listed in Table 7.2 and 7.3. In addition, Tables 7.4 and 7.5 categorize the samples in subsets that correspond to a specific point of inquiry.

7.2   Methods

The indentation analysis tools rely on the acquisition of the indentation load P and indentation depth h over time. This acquisition, performed by high-precision equipment, can be sensitive to the experimental setup and calibrations. This Section briefly describes indentation equipment, calibration issues and potential sources of error.

Sample	Sample Name	w/c [%]	SF/c[1] [%]	CF/c[2] [%]	Heat treatment
25	PC-30-0-0	30			none
26	PC-30-0-2	30			at 2 days
27	PC-30-8(SF)-0	30	8.75		none
28	PC-30-8(SF)-2	30	8.75		at 2 days
29	PC-30-10(CF1)-0	30		10	none
30	PC-30-10(CF2)-0	30		10	none
31	PC-30-17(SF)-0	30	17.5		none
32	PC-30-17(SF)-2	30	17.5		at 2 days
33	PC-30-21(SF)-0	30	21.6		none
34	PC-30-24(SF)-0	30	24		none
35	PC-30-24(SF)-2	30	24		at 2 days
36	PC-30-25(CF1)-0	30		25	none
37	PC-30-25(CF2)-0	30		25	none
38	PC-30-32(SF)-0	30	32		none
39	PC-30-32(SF)-2	30	32		at 2 days
40	PC-35-0-0	35			none
41	PC-35-0-2	35			at 2 days
42	PC-40-0-0	40			none
43	PC-40-8(SF)-0	40	8.7		none
44	PC-40-10(CF1)-0	40		10	none
45	PC-40-10(CF2)-0	40		10	none
46	PC-40-21(SF)-0	40	21.6		none
47	PC-40-25(CF1)-0	40		25	none
48	PC-40-25(CF2)-0	40		25	none

Table 7.3: List of tested cementitious materials: Part 2.
(1) Weight of silica fumes (SF), in percent of the weight of cement.
(2) Weight of calcareous filler (CF), in percent of the weight of cement.

	C3S	OPC Reference	OPC-HT Reference
1	C3S-20-0-0	PC-15-0-0	PC-15-0-2
2	C3S-20-0-2	PC-20-0-0	PC-20-0-2
3	C3S-20-24(SF)-0	PC-30-0-0	PC-25-0-2
4	C3S-20-24(SF)-2	PC-35-0-0	PC-30-0-2
5	C3S-25-0-0	PC-40-0-0	PC-35-0-2
6	C3S-25-0-2		
7	C3S-30-0-0		
8	C3S-30-0-2		

Table 7.4: Subsets of tested materials. Part 1.

	OPC Silica Fumes	OPC-HT Silica Fumes	OPC Calc.Filler 1	OPC Calc.Filler 2
1	PC-20-8(SF)-0	PC-20-8(SF)-2	PC-20-10(CF1)-0	PC-20-10(CF2)-0
2	PC-20-21(SF)-0	PC-20-17(SF)-2	PC-20-25(CF1)-0	PC-20-25(CF2)-0
3	PC-20-24(SF)-0	PC-20-24(SF)-2	PC-30-10(CF1)-0	PC-30-10(CF2)-0
4	PC-30-8(SF)-0	PC-20-32(SF)-2	PC-30-25(CF1)-0	PC-30-25(CF2)-0
5	PC-30-17(SF)-0	PC-30-8(SF)-2	PC-40-10(CF1)-0	PC-40-10(CF2)-0
6	PC-30-21(SF)-0	PC-30-17(SF)-2	PC-40-25(CF1)-0	PC-40-25(CF2)-0
7	PC-30-24(SF)-0	PC-30-24(SF)-2		
8	PC-30-32(SF)-0	PC-30-32(SF)-2		
9	PC-40-8(SF)-0			
10	PC-40-21(SF)-0			

Table 7.5: Subsets of tested materials. Part 1.

7.2.1 Indentation Equipment

Depending on their depth, indentations are referred to as microindentations (the deeper ones) or as nanoindentations (the shallower ones). Nanoindentations will be performed with a nanohardness tester from CSM Instruments SA (Peseux, Switzerland), while microindentations will be performed with a MicroTest indenter of Micro Materials Ltd. (Wrexham, UK). The CSM Instruments nano-hardness tester applies the load vertically to the specimen (Fig. 7-2b). The Micro Materials MicroTest applies the load horizontally to the specimen, with the tip mounted to a frictionless pivot (Fig. 7-2a). Nevertheless, the measurement heads of both indenters are based on the same functional principle and are load-controlled. By passing a current through a coil mechanically connected to the tip, the coil and a fixed permanent magnet attract each other, which in return sets the indenter into motion and thus enables the application of a load to the specimen, which is firmly clamped to the loading stage. The displacement of the indenter with respect to the surface of the sample is continuously monitored and recorded via the change in the voltage of a parallel plate capacitor. In this way $P(t)$ and $h(t)$ are obtained.

Table 7.6 provides the specifications of the two indenters. For both the load and the depth, the noise is greater than the electronic resolution. Said otherwise, the limitation in the accuracy of the measurement is not due to the electronics, but to mechanical vibrations. To reduce mechanical noise, both devices are mechanically isolated from the surrounding environment by an antivibration table.
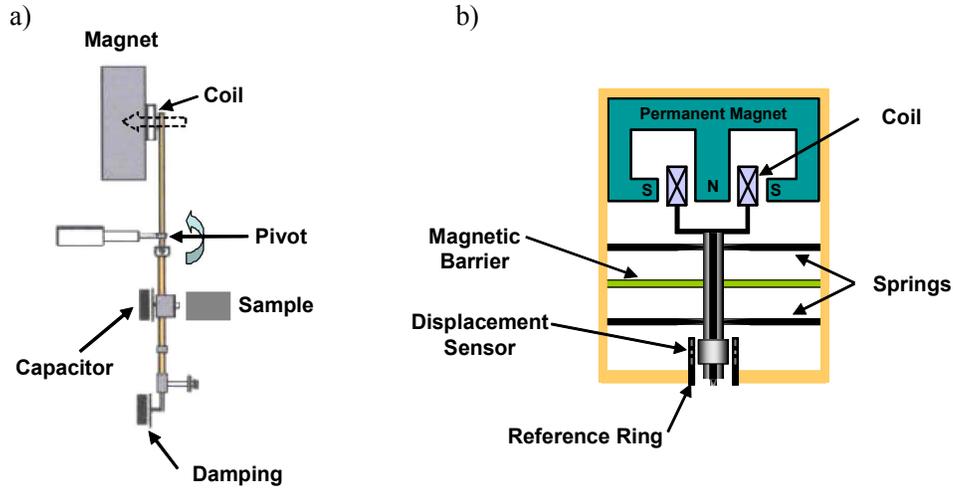
Figure 7-2: Schematics of the measurement head of (a) the Micro Materials Ltd. MicroTest [127] and (b) the CSM Instruments SA Nano-hardness tester (courtesy from Dr. N. Randall).

Manufacturer	Micro Materials Ltd.	CSM Instruments SA
Indenter	MicroTest	Nano-hardness tester
Maximum load[a], mN	20,000	300
Maximum depth[a], μm	30	20
Depth resolution[a], nm	0.2-0.23	0.04
Load resolution[a], nN	15-20	40
Depth noise[b], nm	2.59±0.17	0.154±0.015
Load noise[b], μN	≤100	1.68±0.17

Table 7.6: Specifications of the Micro Materials MicroTest and CSM Instruments nano-hardness tester. (a) Values provided by the manufacturers [127] [62]. (b) Measured values.

7.2.2   Calibration Issues

To ensure that the recorded load and depth data as well as the subsequent indentation analysis provides meaningful results which can be attributed to the indented material only, several calibrations are performed prior to the indentation testing:

- Load versus applied current: The load applied to the specimen is proportional to the current passed into the loading coil (see Section 7.2.1). The proportionality factor should be calibrated, semiannually for the MicroMaterials MicroTest and every two years for the CSM nano-hardness tester. For both indenters, the load calibration is performed by hanging weights of precisely known mass on the indenter and measuring the current necessary to bring the indenter back to its initial position.

- Depth versus change in capacitance: As described in Section 7.2.1, the displacement of the indenter is measured by a change in capacitance in a parallel plate capacitor. The proportionality factor between change in depth and change in capacitance must be calibrated, weekly for the MicroMaterials MicroTest and every two years for the CSM nano-hardness tester. For the MicroMaterials MicroTest, the depth calibration is performed by detecting the surface of a fused silica sample with a spherical indenter, displacing the fused silica sample toward the indenter by a given amount, and detecting the surface of the sample again. For the CSM nano-hardness tester, the depth calibration is performed by indenting a calibrated piezoelectric crystal with a spherical indenter.

- Shape area function of the indenter probe: The projected contact area versus contact depth of the probe $A_c(h_c)$ must be known to ensure that the subsequent data analysis provides meaningful results. An estimate of the projected area of contact A_c, required to calculate indentation properties (see, e.g., the BASh formula (2.13)), is obtained with the Oliver and Pharr method (see Section 2.3.2), which provides an estimate of the contact depth h_c; therefore the function $A_c(h_c)$ must be precisely determined. In the ideal case of a perfectly sharp Berkovich indenter, the shape area function is known (see Section 2.2.1). Practically, however, Berkovich indenters are not infinitely sharp, but somewhat blunt, their radius of curvature usually being greater than 30 nm. Although this imperfection will prove negligible for microindentation testing (for which the depth of the indentations

is much greater than the radius of curvature of the tip), it must be accounted for in nanoindentation testing, and $A_c(h_c)$ must be calibrated. Although the procedure is time-consuming, $A_c(h_c)$ can be found by atomic force microscopy (AFM) or scanning electron microscopy (SEM) imaging [55]; however $A_c(h_c)$ is usually found in an indirect manner by performing indents at various depths on a material of known mechanical properties (e.g., fused silica, which has an indentation modulus $M_{FS} = 72$ GPa [62]). A_c is then calculated with the BASh formula (2.13) and h_c with the Oliver and Pharr method (see Section 2.3.2). To the measured h_c and A_c values is fit a function of the form:

$$A_c(h_c) = C_1 h_c^2 + C_2 h_c + C_3 h_c^{1/2} + C_4 h_c^{1/4} + ... \qquad (7.3)$$

where C_1 is usually fixed to the area-to-depth constant of the perfectly sharp indenter ($C_1 = 24.58$ for a Berkovich indenter, $C_1 = 2.60$ for a Cube-corner indenter) and $\{C_i\}_{i>1}$ capture the bluntness of the tip. For microindentation testing, the tip is considered to be perfectly sharp, no calibration of the shape area function is required, and the ideal shape area function is $A_c(h_c) = C_1 h_c^2$.

- Compliance of the frame: In reaction to the load applied to the sample the frame of the indenter is deformed. Therefore, the measured depth h_{meas} can be divided into two contributions:

$$h_{meas} = h + h_{frame} \qquad (7.4)$$

where h_{frame} captures the deformation of the frame, and h is the true indentation depth. The depth to be reported in indentation testing is h, and therefore h_{frame} must be discarded. Modeling the frame as a spring of compliance C_f, Eq. (7.4) reads:

$$h_{meas} = h + P C_f \qquad (7.5)$$

where P is the applied load. An incorrect frame compliance C_f can have a non-negligible effect on the reported $P - h$ curve (see Figure 7-3). For the CSM nano-hardness tester, due to the specific design of their measurement head the compliance of the frame is fixed, $C_f = 0.1$ nm/mN and requires no calibration. For the MicroMaterials microindenter, C_f
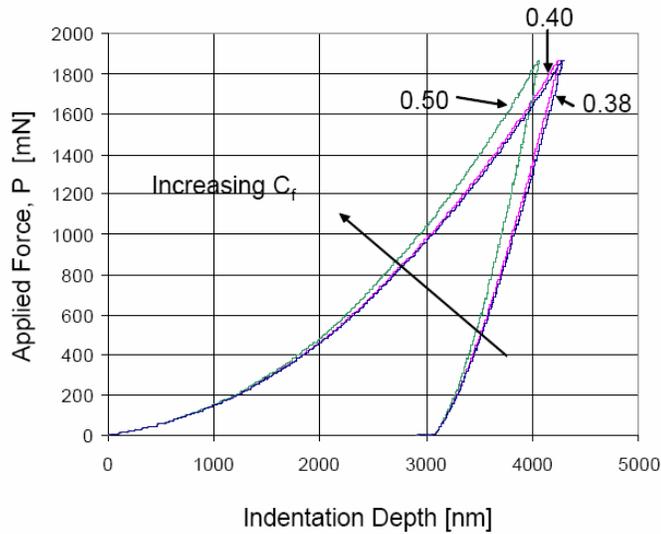
Figure 7-3: Effect of frame compliance on the $P - h$ response (from [57]).

needs to be calibrated. Differentiating Eq. (7.5) at the onset of unloading and making use of the BASh formula (2.13) yields:

$$\frac{1}{S_{meas}} = \frac{\sqrt{\pi}}{2M} \frac{1}{\sqrt{A_c}} + C_f \tag{7.6}$$

where $S_{meas} = dP/dh_{meas}$ is the measured and uncorrected contact stiffness. A graph of the measured $1/S_{meas}$ versus $A_c^{-1/2}$ for a series of indentations performed at different loads yields a straight line with the frame compliance as the intercept with the y-axis.

7.2.3 Ultrashallow Indentations

Once an indenter well calibrated, one can naturally wonder what minimum indentation depths can reliably be measured. This minimum depth is limited by uncontrolled sources of error:

- Mechanical vibrations: As explained in Section 7.2.1 (see Table 7.6) mechanical vibrations are the factor which limits the resolution in depth.

- 'Thermal' drift: Even on non creeping solids a change in depth under constant load is observed due to instabilities of the apparatus. Although usually referred to as 'thermal',

215

the drift of the apparatus may not be due only to thermal changes but also to drift of the electronics themselves. To limit the thermal contribution of the drift indentation instruments usually are equipped with an enclosure which blocks air currents. Even so, a drift on the order of 0.1 nm/s is common. Drift is often accounted for by allowing for hold periods at either the beginning or the end of a test, during which data points are accumulated. A thermal drift correction is calculated and later applied to the whole data set. But this correction, which is first-order in nature, is not fully satisfactory since there is evidence that drift is not constant over the test.

- Inaccuracy of the contact point determination: During an indentation test the indenter probe approaches the surface and, once the surface is detected, the load is increased following a pre-defined load history. But determining when the contact between probe and material surface occurs is not an easy task since for sharp probes, when contact occurs, the area of contact between probe and material surface is theoretically infinitely small! The CSM nano-hardness tester determines the contact point by monitoring the rate of approach of the probe and interpreting a change in this rate as the occurrence of contact. This method is sensitive to mechanical vibrations and, for our apparatus, can yield an uncertainty on the contact point determination up to 2 nm. For us this is the main limiting factor.

Nevertheless, indentations as shallow as a dozen or a few dozens of nanometers are reported in the current literature (e.g., [27] [181]). At those scales, many identify (mostly on crystalline materials, but also on polymers [181]) an indentation size effect. This indentation size effect has been mostly studied for the indentation hardness of crystalline materials, for which a clear increase with shallower depths is observed in the sub-micrometer range (see Figure 7-4). Regarding the indentation modulus of crystalline materials, much fewer data are available, although a slight increase also has been reported (see Figure 7-5). For non-crystalline materials, such as polymers, several identified surface properties differ from the bulk properties (e.g., [181]), but the trends in these differences remain unclear.

We recall that, due to the geometric self-similarity of the Berkovich probe, the indentation depth is the only length scale in the problem, and the measured hardness should be independent
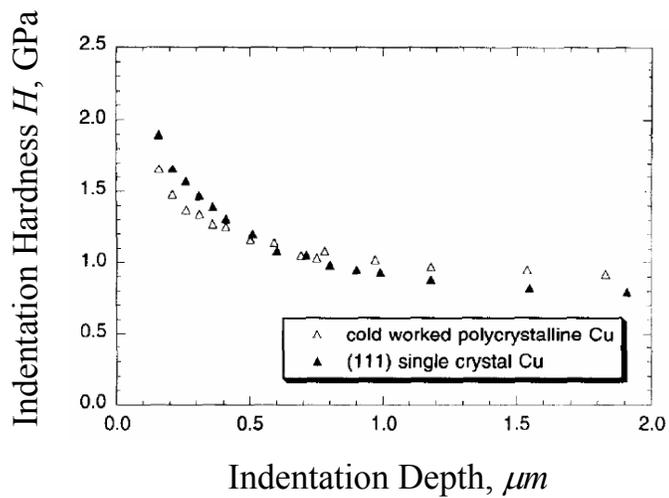
Figure 7-4: Dependence of indentation hardness on indentation depth for copper (from [133] and [123]).
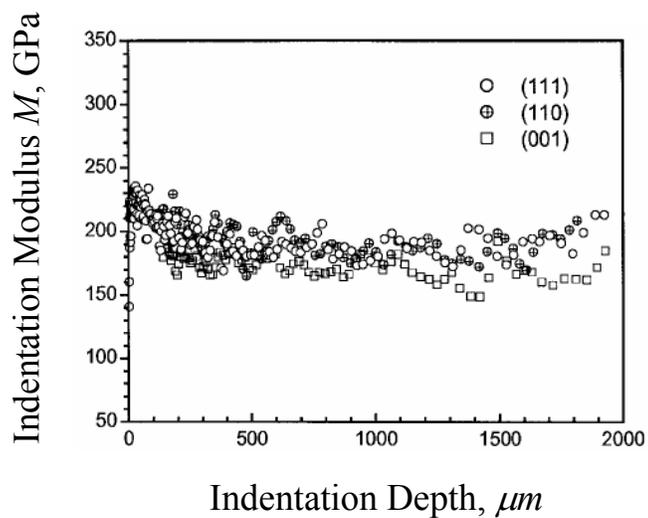
Figure 7-5: Dependence of indentation modulus on indentation depth for Ni$_3$Al single crystals (from [196]).

a)

b)
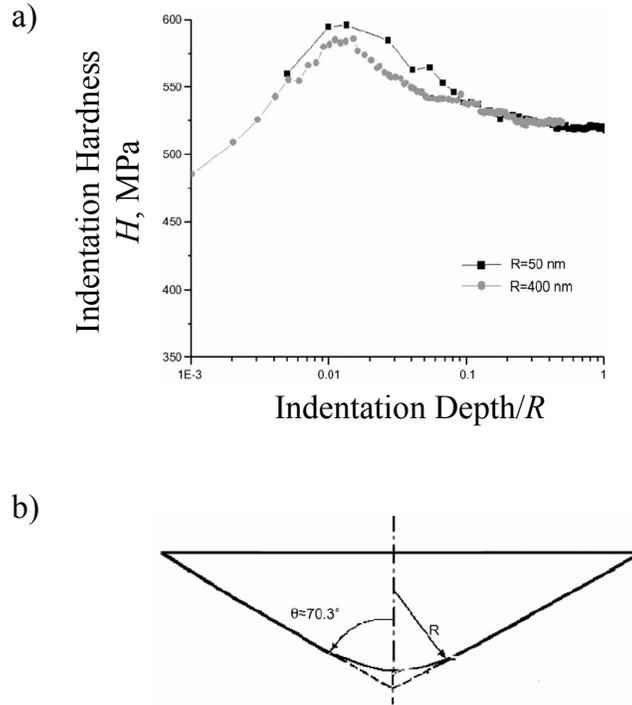
Figure 7-6: Effect of the rounding of the tip on the indentation hardness measurement (Figure a) obtained from numerical simulations on an elastic perfectly plastic material (from [41]). The simulations were performed with a conical tip with radius of curvature R (Figure b).

of the indentation depth (see Section 2.2.3). A change in hardness at low indentation depths implies that another length scale is involved. This length scale may be:

- Material related such as in the model proposed by Nix and Gao [133] and based on geometrically necessary dislocations.

- The radius of curvature of the tip which at shallow depths becomes comparable to the indentation depth. Chen and Li [41] showed that even for elastic perfectly plastic materials the bluntness of the tip yields an increase in hardness at shallower depths (Figure 7-6). For such a material, given that the BASh formula (2.13) is valid for any axisymmetric indenter probe, no change in indentation modulus with the indentation depth is expected.

218

7.3 Surface Preparation

The analytical derivations[2] on which indentation analysis is based were developed by modeling the indented material as an infinite half-space (see Part II). Therefore the surface of the indented cement paste should ideally be flat. From a practical point of view, the samples need to be prepared and polished so that the roughness of their surface is as small as possible. The RMS roughness R_q (homogeneous to a length) of the sample must in fact be much smaller than the maximum indentation depth $h_{\max}$ so that no new length scale is introduced in the indentation problem. Finding out what polishing procedure yields the best surface (the one with the lowest roughness) was referred to as an art [175]! The procedure[3] which yielded the most satisfactory results is the following 3-step procedure:

- The first step is to cut the sample with a diamond saw. The specimen, a cylinder with a 10 mm diameter and a few centimeter length, is cut perpendicular to the length of the cylinder into a disk with a thickness of about 3 mm. The disk is then mounted on a stainless steel AFM plate (Ted Pella) with cyanoacrylate as an adhesive (see Figure 7-7).

- The second step is to grind the sample. The goal of this step is to make the top of the sample as parallel as possible with the bottom of the mounting plate so that there is no tilt of the surface during indentation. The sample is placed in a specially designed jig consisting of a stainless steel outer sleeve with an opening drilled through to match the diameter of the mounting plate. A stainless steel post fits closely inside the opening and rests on the back of the mounting plate to apply a light weight to the sample (see Figure 7-7). The sample, inside the jig, is ground on 120 grit ZirMet (Buehler) abrasive paper until the whole surface is ground. Grinding usually lasts for about 30 s. The sample and the jig are then cleaned separately. The sample is cleaned in a small dish with n-decane in an ultrasonic bath for 5 minutes. The jig and the post are cleaned in a beaker with water in an ultrasonic bath for 5 minutes.

- The third and last step is to polish the sample. A TexMet P (Buehler) pad, a hard,

---

[2]The method and results presented in this section were obtained in collaboration with Chris Bobko during his PhD thesis at MIT, and are presented in a co-authored paper [128].

[3]The procedure is validated later by a comprehensive AFM study.
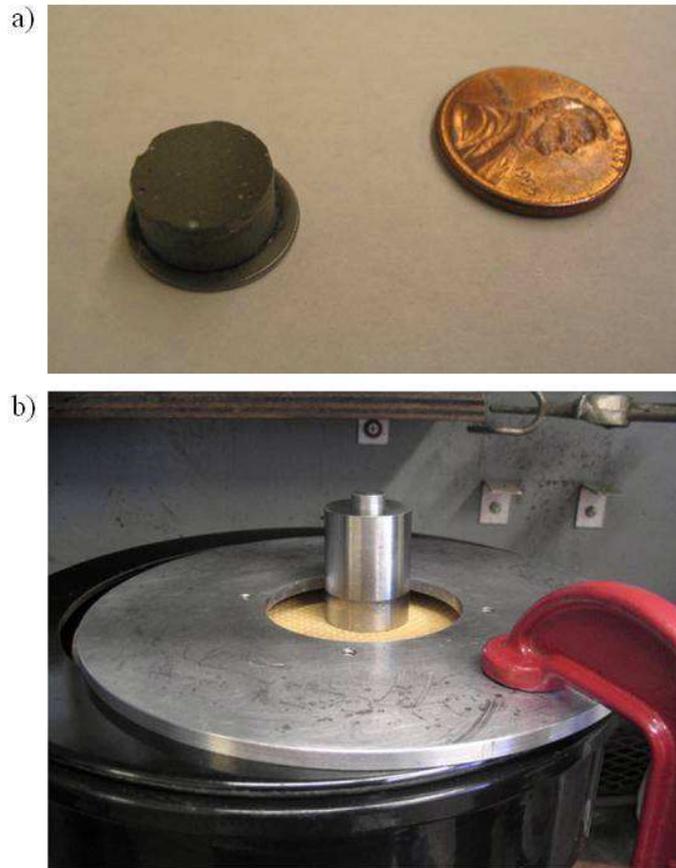
Figure 7-7: (a) Sample on its mounting plate and (b) equipment used to polish the sample.

perforated, non-woven pad is mounted to a lapping wheel. A 1 μm oil-based diamond suspension (Metadi, Buehler) is sprayed on the pad. The sample and the jig are held on the pad. The wheel is spun at about 1 rotation per second, the typical velocity underneath the sample thus being about 20 cm.s^{-1}. The polishing lasts for at least 8 hours. After polishing, the sample is cleaned in the same manner as after the grinding step.

On the samples for which the polishing procedure was designed, we measured the RMS roughness R_q on a 50 μm by 50 μm area, after filtering out of the waviness by cutting the spatial waves with a wavelength greater than 8 μm. The polishing procedure consistently yielded a roughness R_q less than 20 nm, and even less than 10 nm for some of the samples (see Figure 7-8). We observed a correlation between the quality of the polishing, and the reflectivity
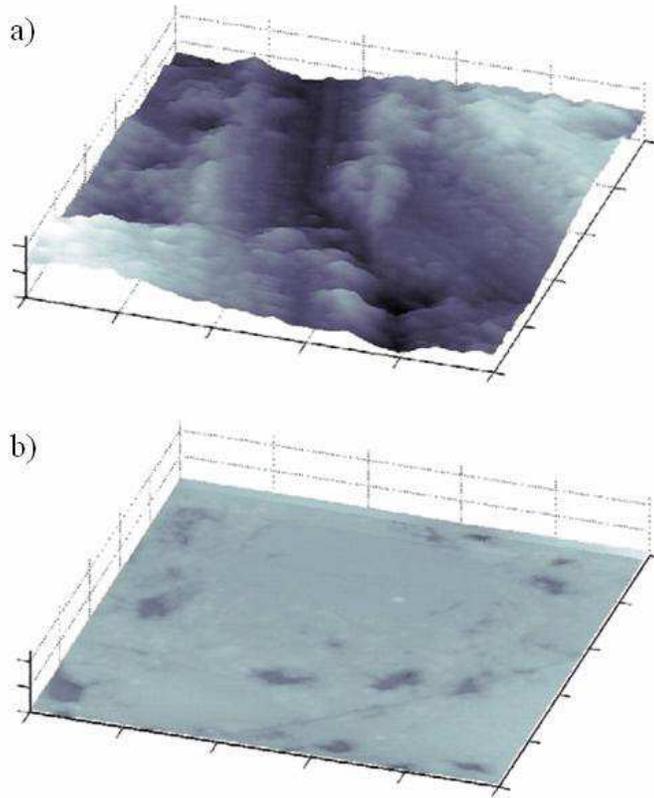
Figure 7-8: AFM picture of a cement sample (a) after grinding and (b) after polishing. The scanned area is 50 μm by 50 μm. The maximum value for the height axis is 5000 nm.
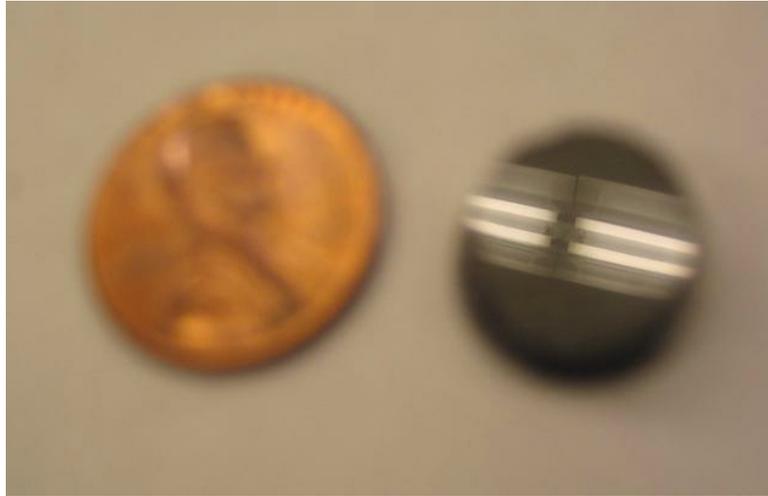
Figure 7-9: Reflectivity of a cement sample after polishing. The reflected image of the ceiling neon lights has a great level of details. The picture was focused on the ceiling lights, which is why the sample appears blurry.

of the surface of the sample. When the surface of the sample became mirror-like (see Figure 7-9), the roughness was below 20 nm.

7.4   *Mode d'Emploi* of Statistical Indentation Technique for Cementitious Materials

Given the technical abilities of today indenters (Section 7.2.1), the four-level structure of cementitious materials (Figure 1-1) can be probed at two levels (Figure 7-10):

- At level I (see Section 6.4): At this level an indentation will probe the individual C-S-H phases and is referred to as a 'nanoindentation'.

- At level II: At this level an indentation will probe the cement paste as a homogeneous composite material and is referred to as a 'microindentation'.

In this investigation mostly nanoindentations will be performed although a few microindentations will also be used for validation purposes. At the scale of nanoindentations the paste is clearly heterogeneous so that we aim to use the grid-indentation technique (Section 5.2.2)

222
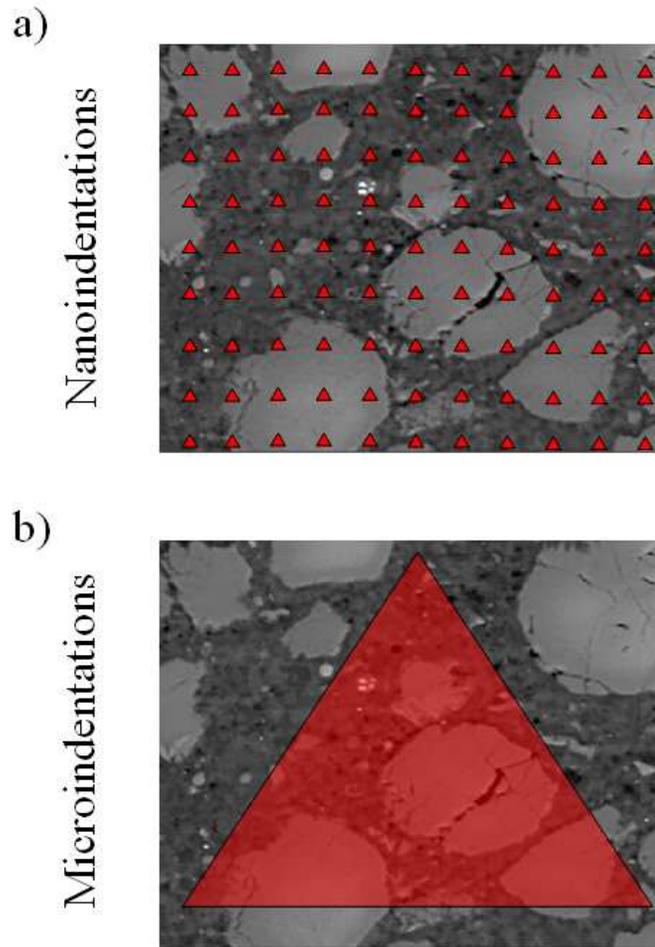
Figure 7-10: Schematics of (a) nanoindentations and (b) microindentations.

and the tools developed in Section 5.3 to measure the C-S-H phase properties and estimate the paste macroproperties, respectively. Moreover, since C-S-H phases are a mix of C-S-H solid and pores, we aim to use the tools introduced in Chapter 4 to characterize the microstructure and the C-S-H solid phase properties. This Section focuses on how to apply these statistical indentation techniques to cementitious materials.

7.4.1 Indentation Parameters

The statistical indentation techniques rely on performing a large number of indentations (see the conclusions of Chapter 4 and Chapter 5). Therefore, first, the parameters defining one

indentation have to be determined.

Indentation Load

In nanoindentation, the maximum indentation depth must be such that the scale separability condition (4.1) and the Buckle rule (5.3) are respected:

$$d_0 \ll h_{\max} \leq d_I/10 \tag{7.7}$$

where d_0 and d_I are characteristic sizes of the heterogeneities at 'Level 0' (see Section 6.5) and 'Level I' (see Section 6.4), respectively. Possible candidates for defining d_0 are the C-S-H particle, for which sizes range from 5 nm (Tennis and Jennings model in Section 6.4.2) up to a few dozen nanometers are proposed (see Section 6.6). On the other hand, d_I is more difficult to estimate, as the structure of the paste can vary from sample to sample or even within a sample. Nevertheless, SEM images available in the literature (e.g., see Figure 6-5 or [73]) suggest $d_I \sim 2$ μm. Therefore Equation (7.7) suggests aiming at:

$$h_{\max}^{nano} \simeq 200 \text{ nm} \tag{7.8}$$

Given that indenters are load-controlled, condition (7.8) can only be satisfied in an average manner. After a few trials and errors the average maximum depth $< h_{\max} > \simeq 200$ nm is obtained with a maximum load:

$$P_{\max}^{nano} = 2 \text{ mN} \tag{7.9}$$

Therefore, such a load will allow us, in a statistical manner, to probe an individual phase of the paste with each nanoindentation.

In contrast the aim of microindentation is to probe the paste at a scale at which it behaves in a homogeneous manner, and the scale separability condition (4.1) now becomes:

$$d_I' \ll h_{\max} \ll D \tag{7.10}$$

where d_I' is the characteristic size of the largest heterogeneities at 'Level I' ($d_I' \simeq 10$ μm, which is the characteristic size of the remaining clinker) and D is the size of the sample (1 cm

224

typically). Given the specifications of the Micro Materials MicroTest (see Section 7.2.1), we aim to maximize the measurement range, which is satisfied for a maximum load $P_{\max} = 8$ N:

$$h_{\max}^{micro} \simeq 20 \ \mu\text{m} \tag{7.11}$$

An interesting observation is that the micro-to-nano indentation parameters scale, on average, according to:

$$\frac{P_{\max}^{micro}}{P_{\max}^{nano}} = \left(\frac{h_{\max}^{micro}}{h_{\max}^{nano}}\right)^{\alpha}$$

where $\alpha = 1.8$ is not far from the theoretical scaling for Berkovich indentation $P \propto h^2$ (see Section 2.2.3, Eq. (2.8)) despite the highly heterogeneous nature of the cement paste at different scales.

Loading Profile

The maximum load $P_{\max}$ is not the only criterion defining the loading profile. Considering a trapezoidal load case, the duration τ_L of the loading phase, τ_H of the holding phase and τ_U of the unloading phase must also be fixed. As explained in Section 2.3.3, the holding phase should be long enough to ensure that the measured stiffness is representative of the elastic properties of the indented material. At the same time, as explained in Section 2.4.3, the holding phase should be as short possible to ensure that the measured hardness is representative of the strength properties of the indented material. Here for fixed $\tau_L = \tau_U = 10$ s, an appropriate duration τ_H of the holding phase is determined experimentally.

8 N

The experimental study of how long the holding phase should be is performed with microindentations ($P_{\max} = 8$ mN, $h_{\max} \sim 20 \ \mu\text{m}$) since at the scale of microindentations the paste is expected to behave in a homogeneous manner, which greatly simplifies the experimental study. The study is performed on samples PC-15-0-0 ($w/c = 0.15$), PC-30-0-0 ($w/c = 0.15$) and PC-40-0-0 ($w/c = 0.4$). On each sample, 50 microindentations are performed with a holding phase of 5 s, and 50 microindentations are performed with a holding phase of 180 s. The indentation modulus M and indentation hardness H are calculated with the Oliver and Pharr method (see Section 2.3.2) and are given in Table 7.7. The coefficient of variation of the 50 tests is on average of 8% for M and of 13% for H, which confirms that at the scale of the microindentations the

	Indentation modulus M, GPa		Indentation hardness H, GPa	
w/c	5 s holding	180 s holding	5 s holding	180 s holding
0.4	30.1±2.3	30.3±2.9	0.47±0.04	0.40±0.06
0.3	33.5±2.0	34.2±2.5	0.55±0.06	0.49±0.04
0.15	59.8±4.0	60.1±5.8	1.12±0.17	1.02±0.19

Table 7.7: Indentation modulus M and indentation hardness H measured with 50 microindentations for different durations of the holding phase on cement pastes with different water-to-cement ratios.

paste behaves in a homogeneous manner.

When increasing the duration of the holding phase from 5 s to 180 s, the measured indentation modulus M changes on average on the three samples by only 1.0%. This observation proves that, for $\tau_L = \tau_U = 10$ s, a duration $\tau_H = 5$ s of the holding phase is long enough to measure elastic properties unbiased by viscous effects. In contrast we observe that, when increasing the duration of the holding phase from 5 s to 180 s, the measured indentation hardness H decreases on average over the three samples by 11.6%. A decrease of the measured indentation hardness with an increase in the duration of the holding phase was expected (see Section 2.4.3).

In summary, to ensure that M and H are representative of the elastic and strength properties of the tested pastes, each nanoindentation will be performed with a loading phase of duration $\tau_L = 10$ s, a holding phase of duration $\tau_H = 5$ s and an unloading phase of duration $\tau_U = 10$ s.

Parameters of Grid of Indentations

On each sample a large number of $N = 400$ nanoindentations will be performed on a grid of 20 by 20. To ensure statistical independence of the measured properties between two neighboring nanoindentations (see Section 5.2.2), the spacing δ between indents must be greater than the characteristic size of the largest heterogeneities at 'Level I'. Those largest heterogeneities are the clinkers which have a characteristic size of about 10 μm (see Figure 1-1). Therefore δ is fixed to $\delta = 20$ μm.

We now have determined all parameters necessary to perform grids of nanoindentations on the surface of the cementitious materials. The application of the statistical indentation techniques presented in Chapters 4 and 5 to the results from grids of nanoindentations is presented next.

7.4.2 Deconvolution Technique

The deconvolution technique presented in Section 5.2.3, when applied to results from a grid of nanoindentations, will provide the mean properties and volume fractions of the mechanically significant phases of the paste. This process is almost fully automatized with Matlab. The deconvolution process does require one important input from the operator, that is the number of phases (or Gaussians) used for the deconvolution. In this Section the number of significant mechanical phases in a hydrated cement paste is determined.

Hydrated cement pastes can be with confidence divided into at least 3 significant mechanical phases [58]: Two hydrated phases and the remaining unhydrated clinker. The two hydrated phases are a low-density (LD) C-S-H phase and a high-density (HD) C-S-H phase. Constantinides and Ulm tentatively identified a third mechanically significant products of hydration (i.e., a fourth mechanically significant phase of the entire paste) which they interpreted as Portlandite [58]. More recently Mondal et al. [129] also identified a third mechanically significant hydration product which they interpreted as a high stiffness C-S-H phase.

A grid of nanoindentations is performed on samples PC-40-0-0 ($w/c = 0.4$) and PC-20-25(CF1)-0 ($w/c = 0.2$, 25% of calcareous filler of first type) with the parameters determined in Section 7.4.1. A coupled (see Section 5.2.3) 4-Gaussian deconvolution of M and H is performed. The results of the deconvolution are displayed in Figure 7-11 and given in Table 7.8. The mean values for the first peak ($M \sim 20$ GPa, $H \sim 0.5$ GPa) and for the second peak ($M \sim 30$ GPa, $H \sim 1$ GPa) compare fairly well with those measured by Constantinides and Ulm [58] (see Tab. 6.3) for LD C-S-H ($M_{LD} = 18.2 \pm 4.2$ GPa, $H_{LD} = 0.45 \pm 0.14$ GPa) and HD C-S-H ($M_{HD} = 29.1 \pm 4.0$ GPa, $H_{HD} = 0.83 \pm 0.18$ GPa) while the fourth peak ($M \sim 120$ GPa, $H \sim 10$ GPa) is identified as unhydrated remaining clinker since its mean properties compare well with those reported for pure clinker phases (for instance, for C$_3$S, $M_{CL} = 135.0 \pm 7.0$ GPa, $H_{CL} = 8.7 \pm 0.5$ GPa, see Tab. 6.2) [193]. Like Constantinides and Ulm [58], we tentatively identify a third mechanically significant hydration product. But this third peak has a low volume fraction and a large standard deviation, and one can reasonably wonder whether this peak characterizes a mechanically significant phase or whether it is rather an artifact of the grid indentation technique, i.e., a composite response. This question is answered by hypothesis testing.
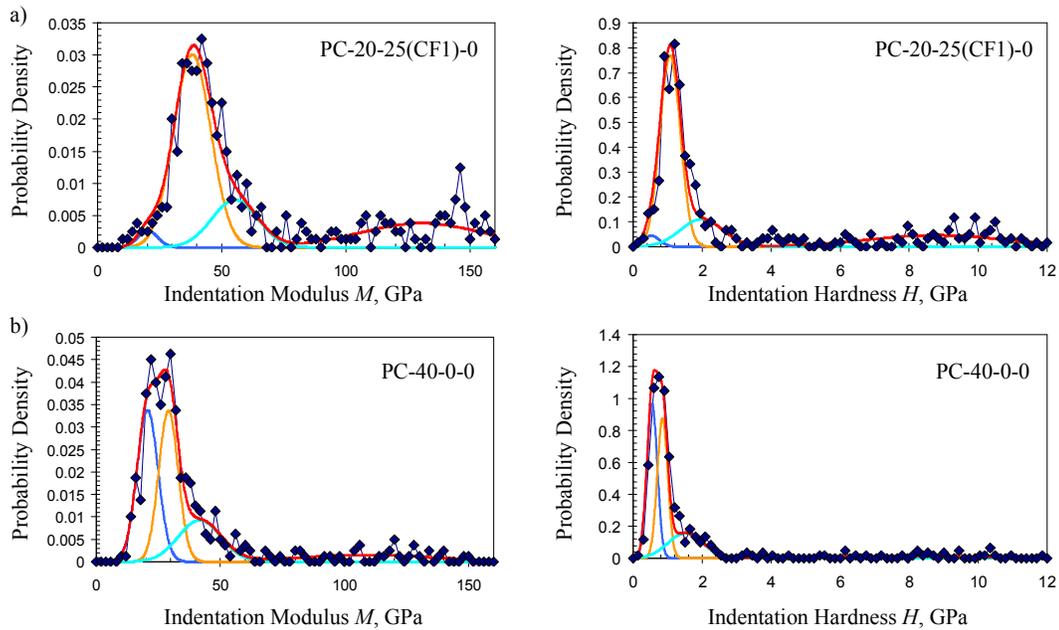
Figure 7-11: 4-Gaussian deconvolution results from a grid of nanoindentations at $P_{max} = 2$ mN for (a) sample PC-20-25(CF1)-0 and (b) sample PC-40-0-0.

If the third peak is a composite response, it should vanish when decreasing the maximum load P_{max} (see Section 5.2.3). Indeed, when decreasing the maximum load, the maximum depth h_{max} decreases as well and hence the volume of material probed. As a consequence, when decreasing P_{max}, the probability of sensing two neighboring phases with one indentation decreases and the composite peak should vanish.

Therefore, on the same two cement samples (PC-40-0-0 and PC-20-25(CF1)-0) a grid of 400 ultrashallow nanoindentations is performed at $P_{max} = 100$ μN. The maximum depth of those ultrashallow indents is $h_{max} = 27 \pm 13$ nm, i.e., one order of magnitude smaller than for nanoindentations. The results of a 4-Gaussian deconvolution of those ultrashallow indentations are displayed in Figure 7-12 and given in Table 7.8. For both samples the volume fraction of the third peak increases with a decreasing P_{max}. Instead of vanishing, the third peak becomes more distinct at low loads. This observation proves that the third peak is not an artifact of the deconvolution technique (a composite response) but a mechanically significant phase. Given that the newly identified phase has mechanical properties greater than those of the already

228

		$P_{\max} = 2$ mN				$P_{\max} = 0.1$ mN			
		PC-20-25(CF1)-0		PC-40–0-0		PC-20-25(CF1)-0		PC-40–0-0	
		M	H	M	H	M	H	M	H
Peak 1	$m^{(1)}$	20.08	0.522	20.67	0.551	29.85	1.267	16.13	0.524
	$s^{(2)}$	4.03	0.236	4.26	0.149	6.95	0.336	5.77	0.337
	$f^{(3)}$	0.026	0.026	0.361	0.361	0.141	0.141	0.268	0.268
Peak 2	$m^{(1)}$	38.08	1.071	29.10	0.852	47.75	2.148	28.57	1.243
	$s^{(2)}$	7.52	0.294	3.93	0.151	8.03	0.542	6.68	0.335
	$f^{(3)}$	0.567	0.567	0.331	0.331	0.370	0.370	0.265	0.265
Peak 3	$m^{(1)}$	55.18	1.982	41.59	1.509	64.60	3.393	46.55	2.135
	$s^{(2)}$	9.27	0.617	8.57	0.507	8.50	0.703	11.20	0.375
	$f^{(3)}$	0.172	0.172	0.199	0.199	0.219	0.219	0.298	0.298
Peak 4	$m^{(1)}$	130.4	8.796	108.4	7.500	144.6	9.540	114.0	6.958
	$s^{(2)}$	24.9	2.023	29.5	3.211	24.1	1.703	56.2	2.674
	$f^{(3)}$	0.235	0.235	0.108	0.108	0.270	0.270	0.169	0.169

Table 7.8: Deconvolution results for a grid of nanoindentations at $P_{max} = 2$ mN and $P_{max} = 100$ μN for samples PC-20-25(CF1)-0 and PC-40-0-0.
(1) Mean value, in GPa
(2) Standard deviation, in GPa
(3) Volume fraction, no units

identified LD C-S-H and HD C-S-H phases, we name it an UHD (Ultra-High Density) C(-S-)H phase, the use of parentheses expressing our inability to determine a priori whether this third peak is made of C-S-H (as postulated by Mondal et al. [129]), of Portlandite CH (as postulated by Constantinides and Ulm [58]), or of a mixture of both.

For both samples the mean indentation modulus of each phase only slightly changes when decreasing $P_{\max}$ from 2 mN to 100 μN. This justifies the choice of the maximum load of $P_{\max} = 2$ mN which appears to be low enough to ensure the scale separability condition: On average each indent probes a volume made of one material phase and not a composite of material phases. In contrast, for both samples the mean indentation hardness H of the first two peaks is significantly greater at $P_{\max} = 100$ μN than at $P_{max} = 2$ mN. A change in hardness at very low depths is not surprising (see Section 7.2.3) and may be due to the bluntness of the tip as well as to an indentation size effect.

In summary, we identified that the cement paste is made of 4 mechanically significant phases, i.e., 3 hydrated phases and the remaining unhydrated clinker. Therefore, a deconvolution of a grid of nanoindentations will be performed with 4 Gaussians (4 phases). Equivalently a
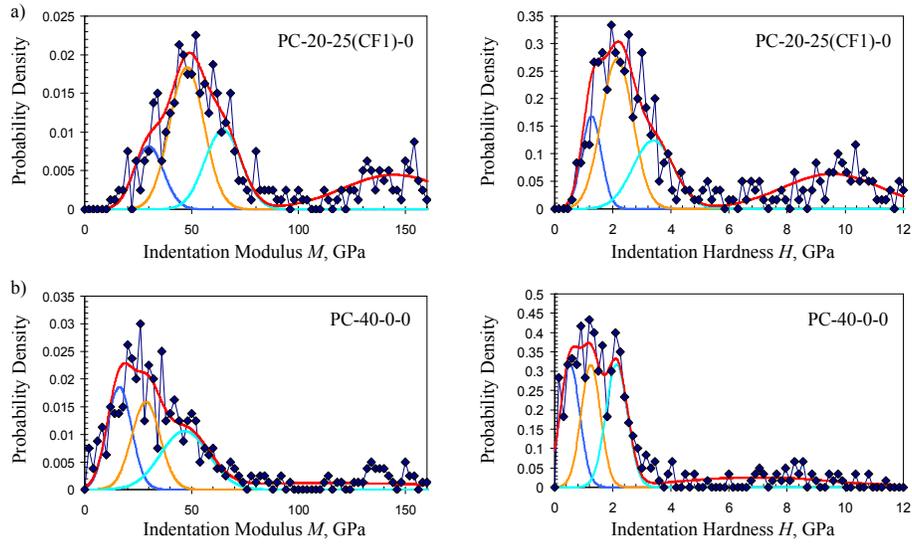
Figure 7-12: 4-Gaussian deconvolution results from a grid of nanoindentations at $P_{\max} = 100$ μN for (a) sample PC-20-25(CF1)-0 and (b) sample PC-40-0-0.

		PC-20-25(CF1)-0		PC-40–0-0	
		M	H	M	H
Peak 1	$m^{(1)}$	29.85	1.267	16.13	0.524
	$s^{(2)}$	6.95	0.336	5.77	0.337
	$f^{(3)}$	0.141	0.141	0.268	0.268
Peak 2	$m^{(1)}$	47.75	2.148	28.57	1.243
	$s^{(2)}$	8.03	0.542	6.68	0.335
	$f^{(3)}$	0.370	0.370	0.265	0.265
Peak 3	$m^{(1)}$	64.60	3.393	46.55	2.135
	$s^{(2)}$	8.50	0.703	11.20	0.375
	$f^{(3)}$	0.219	0.219	0.298	0.298
Peak 4	$m^{(1)}$	144.6	9.540	114.0	6.958
	$s^{(2)}$	24.1	1.703	56.2	2.674
	$f^{(3)}$	0.270	0.270	0.169	0.169

Table 7.9: Deconvolution results for a grid of nanoindentations at $P_{max} = 100$ μN for sample PC-40-0-0 and sample PC-20-25(CF1)-0.
(1) Mean value, in GPa
(2) Standard deviation, in GPa
(3) Volume fraction, no units

deconvolution of nanoindentations performed on the hydrated matter only will be performed with 3 Gaussians (3 phases).

7.4.3 Determination of Microstructure by Indentation

Since a large number N of nanoindentations will be performed with each grid of nanoindentations on the surface of a sample, a large number N' of those nanoindentations will be performed on the C-S-H phases. Therefore, since the C-S-H phases are a mix of C-S-H solid and pores (see Section 6.4), and in accordance with the conclusions of Chapter 4, determining the microstructure of the C-S-H phases, i.e., the C-S-H solid properties and the local packing densities (or porosities) should be possible. Making use of Chapter 4 requires the solid phase to be isotropic, which for C-S-H is unlikely at the scale of a particle (see Section 6.5). Nevertheless, since C-S-H is amorphous as a whole, C-S-H particles are likely to show little order from one to the other and we associate to the C-S-H crystal ('Level 0') an isotropic mechanical equivalent which will be referred to simply as 'the C-S-H solid'.

The assessment of the microstructure is performed by using the dimensionless relations linking indentation modulus to microstructure (Eqs. (4.34) or (4.37), depending on the morphology) and indentation hardness to microstructure (Eqs. (4.99) or (4.100), depending on the morphology). Since the nanoindentations designed and presented here to correctly assess the strength properties are too short in duration to provide a reliable measurement of the creep properties ($\tau_H = 5$ s, see Section 7.4.1), creep properties are not included in the assessment of the microstructure. Making use of the sets of indentation moduli $\{M_i\}_{i=1..N'}$ and indentation hardnesses $\{H_i\}_{i=1..N'}$ measured on the hydration products, the microstructure (indentation modulus m_s, Poisson's ratio ν_s, indentation hardness h_s and friction coefficient α_s of the solid phase, packing density η_0 at percolation, as well as a set $\{\eta_i\}_{i=1..N'}$ of local packing densities) is determined by minimizing the sum of the quadratic error between model predictions and the experiment:

$$\boxed{\min_{\substack{(m_s,\nu_s,h_s,\alpha_s,\eta_0)\\ \eta_{i=1,N'}}} \sum_{i=1}^{N'} \left[\left(1 - \frac{m_s\,\Pi_M\left(\nu_s,\eta_i,\eta_0\right)}{M_i}\right)^2 + \left(1 - \frac{h_s\,\Pi_H\left(\alpha_s,\eta_i,\eta_0\right)}{H_i}\right)^2 \right]} \qquad (7.12)$$

The minimization procedure will gain in stability by fixing some known parameters:

- The percolation threshold at $\eta_0 = 0.5$ (see Figure 6-12) reminiscent of a nanogranular morphology with spherical particles (see Section 6.4.3, Fig. 6-12). Given the relatively high packing densities of C-S-H (on-average greater than $\eta = 0.64$) the particle aspect ratio has a negligible effect on the indentation modulus–packing density scaling relation (see Section 4.2.5.

- The asymptotic indentation modulus of the quasi-isotropic C-S-H solid particle at $m_s = 63.5$ GPa according to Eq. (6.20) determined from MD simulations and confirmed by extrapolation of nanoindentation results (see Section 6.5).

- The Poisson's ratio of the C-S-H solid phase at an arbitrary value $\nu_s = 0.2$, which has a negligible effect on the indentation modulus–packing density scaling relation for any morphology (see Section 4.2.3). The particular value of $\nu_s = 0.2$ simplifies the dimensionless $M - \eta$ scaling relation:

$$\frac{M}{m_s} = \Pi_M \left(\nu_s = 1/5, \eta_i, \eta_0 = 1/2 \right) = 2\eta - 1 \geq 0 \tag{7.13}$$

Assuming that the same holds true for strength properties, the dimensionless relations $\Pi_M \left(\nu_s = 1/5, \eta_i, \eta_0 = 1/2 \right)$ and $\Pi_H \left(\alpha_s, \eta_i, \eta_0 = 1/2 \right)$ given by Eqs. (7.13) and (4.100), respectively, will be used to solve for two solid strength properties (h_s, α_s) and N' packing density values from:

$$\min_{\substack{(h_s, \alpha_s) \\ \eta_{i=1,N'}}} \sum_{i=1}^{N'} \left[\left(1 - \frac{m_s \, \Pi_M \left(\nu_s = 0.2, \eta_i, \eta_0 = 0.5 \right)}{M_i} \right)^2 + \left(1 - \frac{h_s \, \Pi_H \left(\alpha_s, \eta_i, \eta_0 = 0.5 \right)}{H_i} \right)^2 \right] \tag{7.14}$$

where $m_s = 63.5$ GPa.

Finally, a way of filtering the nanoindentations performed on the products of hydration out of a grid of nanoindentations needs to be designed. Since the indentation modulus m_s of the C-S-H solid is expected to be an upper bound of the indentation modulus of all C-S-H phases, all nanoindentations with $M > 63.5$ GPa are discarded when applying the microstructure assessment technique. In addition, to respect a symmetry between indentation modulus and

hardness, a threshold value on the measured indentation hardness is introduced as well. In conclusion, we will consider that all indents with $M \leq 63.5$ GPa and $H \leq 3$ GPa are performed on hydration products. This choice will be validated later on.

7.4.4 Estimation of Indentation Macroproperties

Finally, the derivations performed in Section 5.3 will be used to estimate the composite indentation properties of a cement paste from a grid of nanoindentations. The homogenized indentation modulus of the paste will be calculated with Eq. (5.16) from a set of moduli $\{M_i\}_{i=1..N}$ measured with a grid of nanoindentations while the homogenized indentation hardness of the paste will be calculated by solving Eqs. (5.44) for a set of hardness values $\{H_i\}_{i=1..N}$ measured with a grid of nanoindentations.

We are now ready to validate these tools of indentation analysis for cement-based materials.

7.5 Validation for Cementitious Materials

This Section focuses on validating the techniques here introduced for their use on cementitious materials.

7.5.1 Polishing Procedure

The polishing procedure[4] presented in Section 7.5.1 is here validated on sample PC-20-0-0. To do so, the sample preparation procedure is interrupted to perform both nanoindentation and roughness measurements. Specifically, the sample is tested directly after the grinding and after one hour, two hours, four hours and the full eight hours of polishing.

The primary method of obtaining topographic information about the sample surface is the use of an Atomic Force Microscope (AFM). Topographic images are obtained with a Quesant Q-Scope 250 AFM. The data are acquired using a wavemode or 'tapping' scan. For each scan the resolution is 512x512 pixels and the scan rate is 1.0 Hz. Varying scan sizes are used, from 2 μm by 2 μm to 80 μm by 80 μm.

---

[4]The method and results presented in this section were obtained in cooperation with Chris Bobko during his PhD thesis at MIT, and are presented in a co-authored paper [128].
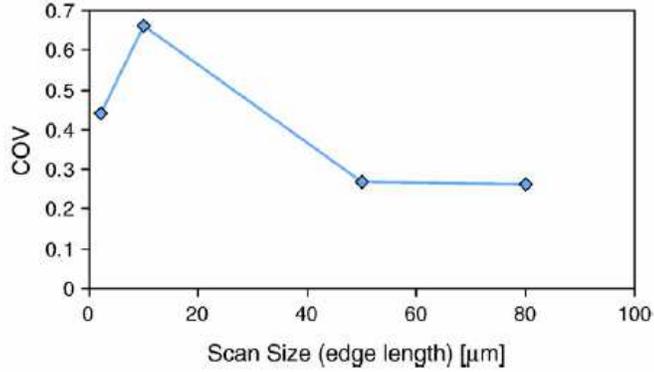
Figure 7-13: Coefficient of variation (COV) of the RMS roughness R_q measured after four hours of polishing versus the scan size (from [128]).

Following the AFM imaging procedure each file is digitally analyzed in order to extract a roughness value. Before calculation of the roughness, a linear slope correction is performed to account for an alignment difference between the reference plane of AFM imaging and the overall slope of the sample surface. The measurement of roughness is a root-mean-squared average (RMS) of the topography of the surface, R_q, defined by:

$$R_q = \sqrt{\frac{1}{N^2} \sum_{i=1}^{N} \sum_{j=1}^{N} z_{ij}^2} \tag{7.15}$$

where N is the number of pixels in each scan edge and z_{ij} is the height at position (i, j) from the mean plane. In addition, a Gaussian filter is applied in order to filter out spatial waves having a larger wavelength than 8 μm, which is out of proportion with regard to the characteristic size of the nanoindentations.

After four hours of polishing, a number of AFM images are obtained at different locations to assess the variability of the roughness measurement for different scanning sizes. As is observed in Figure 7-13, for small scan sizes (2 μm x 2 μm and 10 μm x 10 μm) the measured roughness R_q exhibits significant variability. For larger scan sizes (50 μm x 50 μm and 80 μm x 80 μm) the coefficient of variation of R_q decreases significantly because, for sizes greater than 50 μm, the scanning averages over the characteristic length scale of the cement paste and clinker.
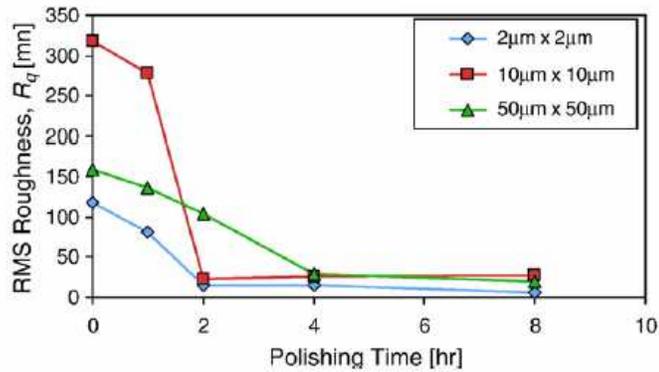
Figure 7-14: RMS roughness R_q for different polishing durations and AFM scan sizes. After two to four hours of polishing, the roughness remains unchanged (from [128]).

The roughness results as a function of polishing time, as displayed in Figure 7-14, show that roughness values, in general, decrease sharply over time. Interestingly however, further polishing after four hours shows little, if any, beneficial effect. Figure 7-14 also highlights the observation that the roughness values at different sampling sizes are drastically different.

The deconvolution of the nanoindentation tests completes the data set linking roughness and nanoindentation results. The deconvolution was carried out with three Gaussians. Figure 7-15 illustrates the relationship between decreasing roughness and the convergence of the mean peak properties and volume fraction results towards unique values. These quantities are graphed versus the roughness values measured over a 50 μm x 50 μm area because of the low coefficient of variation in this sampling size (see Figure 7-13). Figure 7-15 indicates that below a roughness of about 100 nm (corresponding to the roughness achieved after two hours of polishing) the results for the extracted indentation hardness and moduli for the first two peaks are within 5% of the values for the fully (eight hour) polished sample. This result is somewhat surprising, since 100 nm is comparable to the average depth ($h_{\max} \simeq 200$ nm) of the nanoindentations. Those results also show that the 8-hour polishing time used in the procedure described in Section 7.5.1 is a conservative duration.
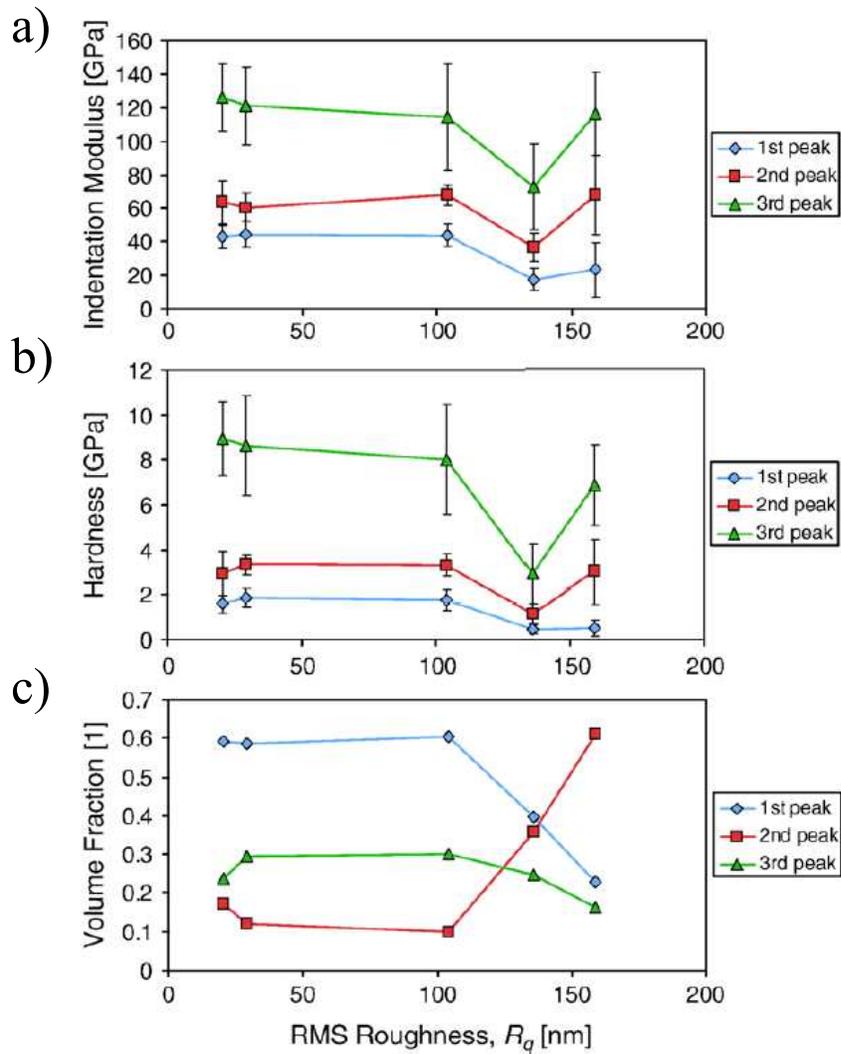
Figure 7-15: Nanoindentation deconvolution results versus RMS Roughness R_q. (a) Mean indentation modulus M of each phase. (b) Mean indentation hardness H of each phase. (c) Volume fraction of each phase. The error bars in indentation modulus and hardness represent plus and minus one standard deviation. The mean properties and volume fractions converge to within about 5% of the final values when the RMS roughness is less than 100 nm.

		Indentation modulus M		Indentation hardness H	
		Grid 1	Grid 2	Grid 1	Grid 2
Peak 1	$m^{(1)}$	N.A.	N.A.	N.A.	N.A.
	$s^{(2)}$	N.A.	N.A.	N.A.	N.A.
	$f^{(3)}$	N.A.	N.A.	N.A.	N.A.
Peak 2	$m^{(1)}$	35.20	39.28	1.106	1.296
	$s^{(2)}$	5.84	5.92	0.251	0.301
	$f^{(3)}$	0.492	0.556	0.492	0.556
Peak 3	$m^{(1)}$	52.43	57.99	1.947	2.187
	$s^{(2)}$	11.39	9.92	0.528	0.590
	$f^{(3)}$	0.252	0.185	0.252	0.185
Peak 4	$m^{(1)}$	117.54	112.79	7.695	7.889
	$s^{(2)}$	28.64	22.88	2.218	1.904
	$f^{(3)}$	0.256	0.259	0.256	0.259

Table 7.10: Results of the 4-Gaussian deconvolution for two grids of 400 nanoindentations on sample PC-20-0-2.
(1) Mean value, in GPa
(2) Standard deviation, in GPa
(3) Volume fraction, no units

7.5.2 Repeatability of Grid-Indentation Technique and Deconvolution Process

This Section focuses on the repeatability of the grid-indentation technique (see Sections 5.2.2) and of the deconvolution process (Sections 5.2.3 and 7.4.2) to measure phase properties. The experimental study is performed on samples PC-30-25(CF1)-0 ($w/c = 0.3$ and 25% of calcareous filler of type 1), PC-40-10(CF1)-0 ($w/c = 0.4$ and 10% of calcareous filler of type 1) and PC-20-0-2 ($w/c = 0.2$ with no additives, heat treated after 2 days of hydration). On each of those samples two grids of nanoindentations are performed with the parameters defined in Section 7.4.1. Each grid is then deconvoluted with four Gaussians. The results of the deconvolution for samples PC-30-25(CF1)-0, PC-40-10(CF1)-0 and PC-20-0-2 are given in Table 7.10, 7.11 and 7.12, respectively, and displayed in Figure 7-16.

For sample PC-20-0-2, the 4-Gaussian deconvolution process converges toward a 3-Gaussian distribution for the two grids performed. On sample PC-40-10(CF1)-0 the two grids yield very different mechanical properties for the peak with the highest mechanical properties, corresponding to the clinker: At a water-cement ratio $w/c = 0.4$, which is close to stoichiometric conditions, clinker almost has disappeared. On average however, the results of the two grids

		Indentation modulus M		Indentation hardness H	
		Grid 1	Grid 2	Grid 1	Grid 2
Peak 1	$m^{(1)}$	21.74	23.38	0.533	0.564
	$s^{(2)}$	3.60	3.39	0.143	0.160
	$f^{(3)}$	0.041	0.086	0.041	0.086
Peak 2	$m^{(1)}$	30.67	31.91	0.921	0.907
	$s^{(2)}$	5.33	4.38	0.228	0.183
	$f^{(3)}$	0.533	0.540	0.533	0.540
Peak 3	$m^{(1)}$	44.52	43.48	1.525	1.477
	$s^{(2)}$	7.16	7.19	0.375	0.327
	$f^{(3)}$	0.264	0.242	0.264	0.242
Peak 4	$m^{(1)}$	104.38	107.65	6.692	7.015
	$s^{(2)}$	39.66	39.83	3.336	2.681
	$f^{(3)}$	0.161	0.133	0.161	0.133

Table 7.11: Results of the 4-Gaussian deconvolution for two grids of 400 nanoindentations on sample PC-30-25(CF1)-0.
(1) Mean value, in GPa
(2) Standard deviation, in GPa
(3) Volume fraction, no units

		Indentation modulus M		Indentation hardness H	
		Grid 1	Grid 2	Grid 1	Grid 2
Peak 1	$m^{(1)}$	17.58	19.63	0.545	0.676
	$s^{(2)}$	4.03	5.42	0.129	0.105
	$f^{(3)}$	0.132	0.055	0.132	0.055
Peak 2	$m^{(1)}$	27.86	30.74	0.888	1.028
	$s^{(2)}$	5.06	5.48	0.214	0.247
	$f^{(3)}$	0.445	0.511	0.445	0.511
Peak 3	$m^{(1)}$	40.84	44.66	1.592	1.685
	$s^{(2)}$	7.91	8.26	0.377	0.410
	$f^{(3)}$	0.273	0.255	0.273	0.255
Peak 4	$m^{(1)}$	90.71	141.39	5.678	8.939
	$s^{(2)}$	41.96	23.69	3.446	1.335
	$f^{(3)}$	0.150	0.179	0.150	0.179

Table 7.12: Results of the 4-Gaussian deconvolution for two grids of 400 nanoindentations on sample PC-40-10(CF1)-0.
(1) Mean value, in GPa
(2) Standard deviation, in GPa
(3) Volume fraction, no units
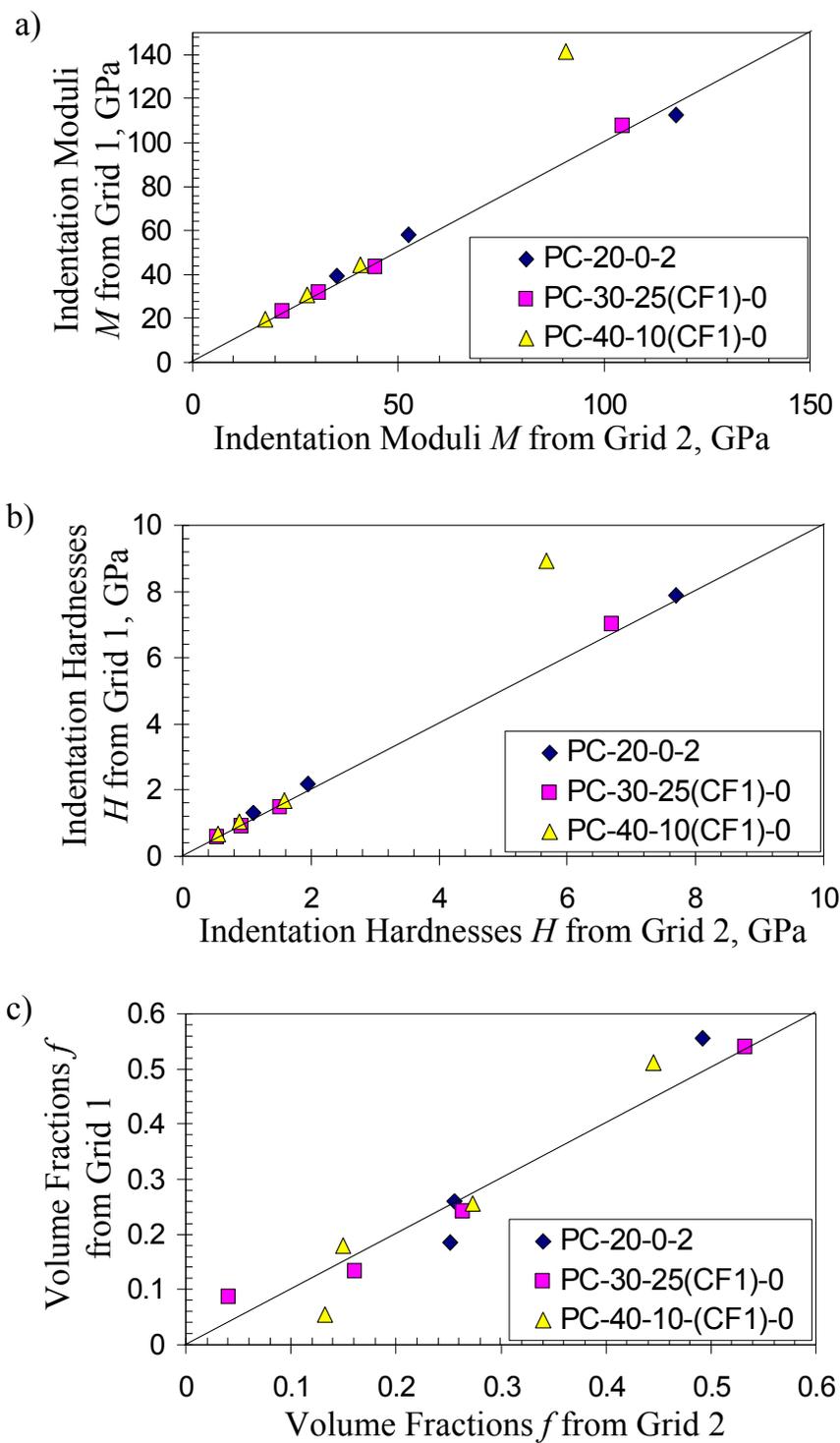
Figure 7-16: Results of the repeatability study of the grid-indentation technique. (a) Deconvoluted indentation moduli M. (b) Deconvoluted indentation hardnesses H. (c) Deconvoluted volume fractions f.

compare very well. For the indentation modulus the two grids yield values which differ on average by 6.9% (3.0 GPa) for the mean value and by 9.6% (1.1 GPa) for the standard deviation. For the indentation hardness those differences are on average of 8.1% (0.14 GPa) for the mean value and of 14.4% (0.13 GPa) for the standard deviation. The deconvoluted volume fractions differ in absolute error by 4.0% on average. Therefore the grid indentation technique associated with the deconvolution process shows a very good repeatability.

7.5.3 Isotropy

The focus of this Section[5] is to verify that at the scale of the nanoindentations cement paste, or more precisely the C-S-H phases, are indeed isotropic, as was assumed to derive the indentation analysis tools in Part II and III. The study is performed with the cement specimens PC-30-0-0 ($w/c = 0.3$, no additives and no heat treatment), PC-25-0-2 ($w/c = 0.25$, heat treatment after two days of hydration) and PC-20-24(SF)-2 ($w/c = 0.2$ and 24% of silica fumes). Within each specimen (a cylinder with a 10 mm diameter and a few centimeters length, see Section 7.3) two samples with two different types of cuts are made. The first sample is cut perpendicular to the length of the cylinder while the second sample is cut along the original length of the cement cylinder. Both samples are then ground and polished according to the surface preparation procedure described in Section 7.3. On both samples a grid of nanoindentations is performed and the nanoindentation results are deconvoluted according to the procedure described in Section 7.4.2.

The results of the deconvolution are displayed in Figure 7-17: Samples with orthogonal cuts yield, at the same scale of nanoindentations monitored by the same indentation force, very similar deconvolution results. The relative difference between orthogonal cuts is on average of 6.6% for the deconvoluted indentation moduli and of 8.9% for the deconvoluted indentation hardnesses. The absolute difference on the deconvoluted volume fractions is on average of 4.6%. Those differences are very close to the accuracy of the deconvolution technique (see Section 7.5.2). This study proves that at the scale of nanoindentations C-S-H indeed behaves mechanically in an isotropic manner.

---

[5]The nanoindentation experiments used in this Section were performed by Mahalia Miller during her Undergraduate Research Opportunity Program in Prof. Ulm's group.
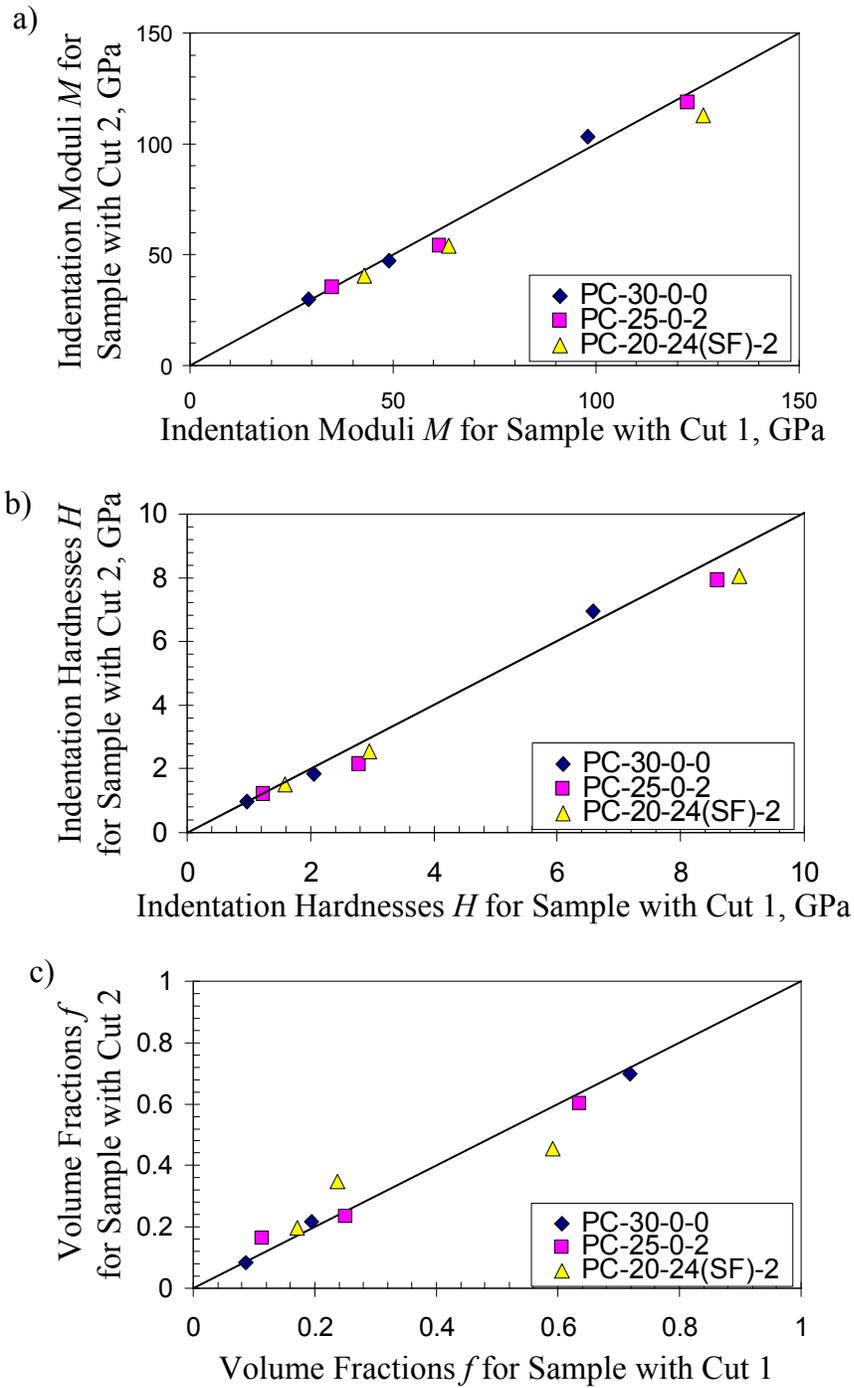
Figure 7-17: Deconvolution results for samples cut perpendicular to the specimen cylinder (cut 1) and along the specimen cylinder (cut 2). (a) Deconvoluted indentation moduli M. (b) Deconvoluted indentation hardnesses H. (c) Deconvoluted volume fractions f.

a)

b)
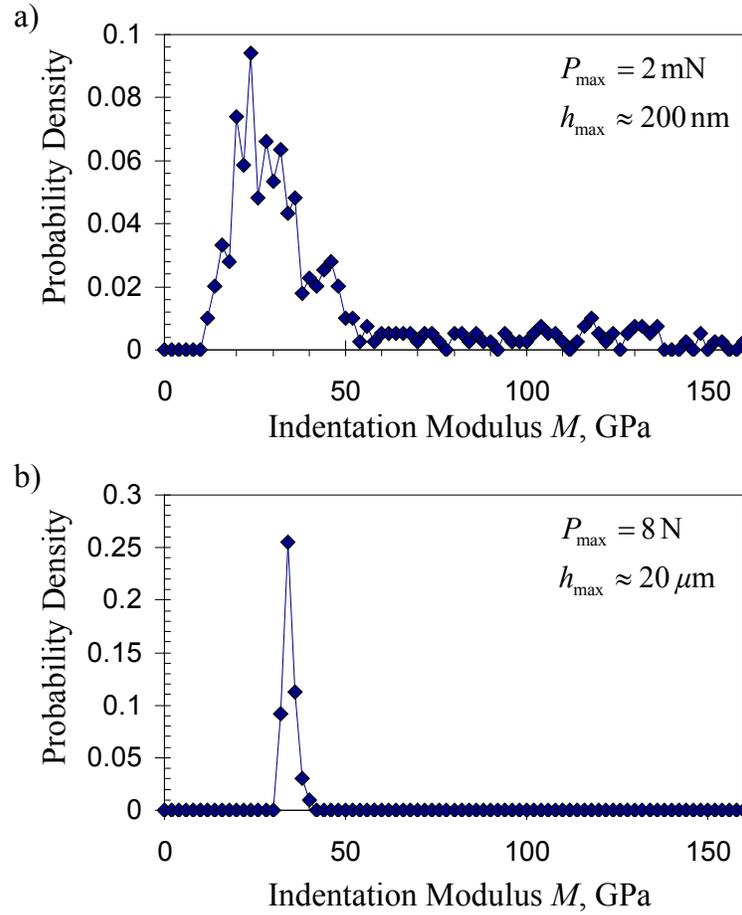
Figure 7-18: Probability density function of the indentation modulus M measured on sample PC-30-0-0 from (a) a grid of nanoindentations and (b) 50 microindentations.

7.5.4 Validation of Self-Consistent Indentation Technique

The focus of this Section is the validation of the technique of self-consistent homogenization of indentation properties developed in Section 5.3 for the indentation modulus and the indentation hardness. The validation is performed on the cement samples PC-15-0-0 ($w/c = 0.15$), PC-30-0-0 ($w/c = 0.3$) and PC-40-0-0 ($w/c = 0.4$). On each paste 50 *micro*indentations ($P_{max} = 8$ N) and a grid of nanoindentations ($P_{max} = 2$ mN) are performed. As can be observed from the frequency plots displayed in Figure 7-18, the nanoindentations yield indeed a heterogeneous response of the paste whereas the microindentations yield a homogeneous response of the paste.

	Indentation modulus		Indentation hardness	
Sample	Homogenized M^{hom}, GPa	Measured M^{micro}, GPa	Homogenized H^{hom}, GPa	Measured H^{micro}, GPa
PC-40-0-0	33.7	30.1±2.3	0.93	0.47±0.04
PC-30-0-0	34.9	33.5±2.0	1.01	0.55±0.06
PC-15-0-0	58.5	59.8±4.0	2.46	1.12±0.17

Table 7.13: Indentation modulus M^{micro} and hardness H^{micro} measured from microindentations; indentation modulus M^{hom} and indentation hardness H^{hom} homogenized from nanoindentations.

Solving Equation (5.16) with Matlab, the homogenized indentation modulus M^{hom} is calculated for each grid of nanoindentations. Table 7.13 gives the homogenized indentation modulus M^{hom} and the indentation modulus M^{micro} measured by microindentations. The difference between M^{micro} and M^{hom} averaged over the three cement samples is only 6.1%, which proves the validity of the homogenization scheme developed in Section 5.3.1 for the indentation modulus.

To calculate the homogenized indentation hardness H^{hom} from a grid of nanoindentations, Maple is used to solve the homogenization scheme described in Section 5.3.2. Table 7.13 gives the homogenized indentation hardness H^{hom} and the indentation hardness H^{micro} measured by microindentations. H^{micro} is significantly lower than the homogenized H^{hom}, by about 50% on average. The observed discrepancy hints towards size effects in the indentation strength response of the material at different scales, induced eventually by microcracking which on a wide range of materials frequently occurs during *micro*indentation.

7.5.5   Validation of Microstructure Assessment Technique

This Section focuses on validating the microstructure assessment technique described in Section 7.4.3. This technique is at the core of this work since it is *the* tool that will enable us to quantify the effect of mix proportions on the microstructure. Consequently, a particular attention is dedicated to its validation.

Filtering Nanoindentations Results

As a prerequisite to the use of the microstructure assessment technique, nanoindentations must be filtered so that only nanoindentations performed on hydration products are kept. This
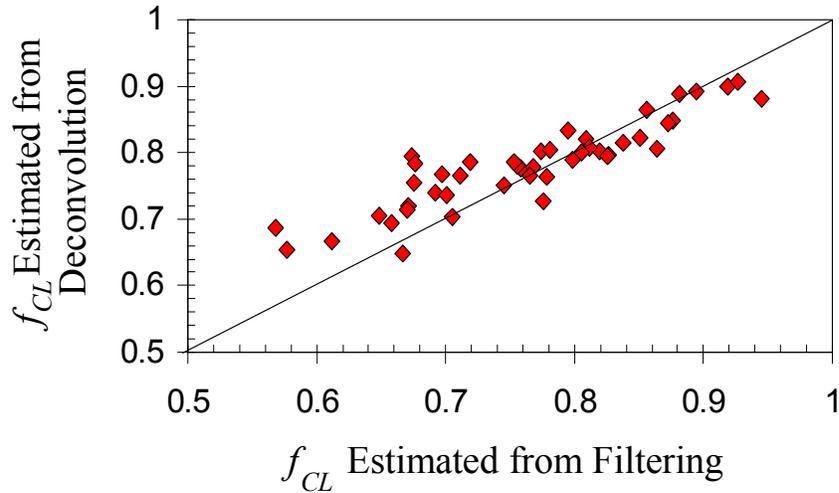
Figure 7-19: Comparison of the volume fraction f_{CL} of clinker as estimated from filtering and from a four-Gaussian deconvolution.

division is done by considering that the sought nanoindentations are those where $M < m_s = 63.5$ GPa and $H < 3$ GPa. Here, the choice of such a criterion is validated.

When filtering the data, discarded nanoindentations are those performed on the remaining unhydrated clinker. Thus the fraction of discarded nanoindentations is an estimate of the volume fraction of remaining unhydrated clinker f_{CL}. An estimate of f_{CL} can be obtained in another manner: By deconvolution. Indeed, when performing a four-Gaussian deconvolution of a whole grid of nanoindentations, the fourth peak is associated with the remaining clinker (see Section 7.4.2) and thus the volume fraction of the fourth peak also provides an estimate of f_{CL}. Recalling that once the number of mechanical phases is fixed the deconvolution process is fully automatized, a comparison of the two estimates of f_{CL} is a good method to validate the filtering.

Figure 7-19 displays for all samples considered in this study the volume fraction f_{CL} of clinker estimated from filtering and that estimated from a four-Gaussian deconvolution. Both estimates yield very similar results, which validates not only the filtering process but also the threshold values used for this filtering.

To further validate the value of $m_s = 63.5$ GPa, Figure 7-20 displays this value on top of
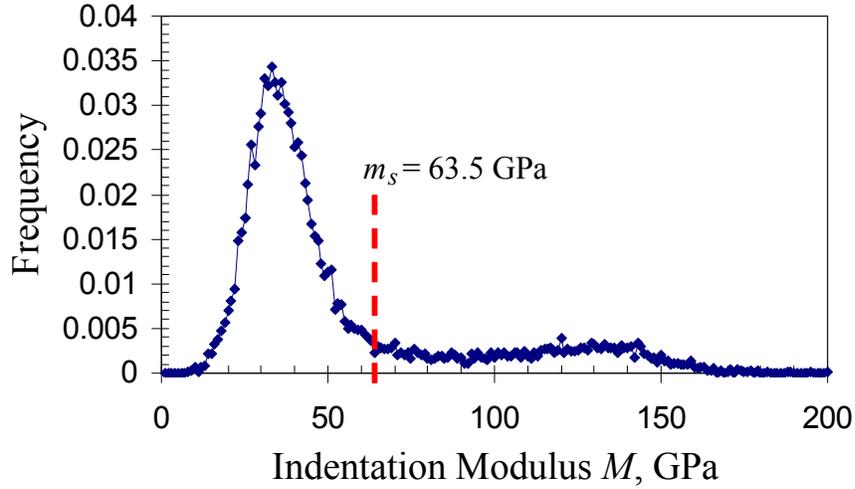
Figure 7-20: Frequency plot of all nanoindentations performed in this work and threshold value $m_s = 63.5$ GPa.

a histogram of all nanoindentations performed in this work. The main peak of this histogram (at $M \sim 35$ GPa) is the hydrated phase of the materials. As expected, $m_s = 63.5$ GPa is an upper bound of this peak.

Choice of Morphology

For each tested sample the C-S-H solid strength properties (h_s, α_s) and local packing densities $\{\eta_i\}_{i=1..N}$ are determined by applying the microstructure assessment technique. Figure 7-21 shows typical results of the $M(\eta)$ and $H(\eta)$ fits. The experimental points are randomly distributed on both sides of the model curves. More precisely Figure 7-22 shows the distribution of the error between the experimental values and the fitted ones. As one can observe, the distribution is close to a normal distribution, which a posteriori justifies the scaling relations $\Pi_M (\nu_s = 0.2, \eta_i, \eta_0 = 0.5)$ and $\Pi_H (\alpha_s, \eta_i, \eta_0 = 0.5)$ used for the fitting. This observation proves the relevance of a granular morphology to capture the mechanical features of C-S-H.

In addition, since the fitting procedure is on all nanoindentations on hydration products, Figure 7-21 also shows that the third hydration product tentatively identified in Section 7.4.2 as ultra-high density (UHD) C(-S-)H is also very well captured by the fitting procedure. Said
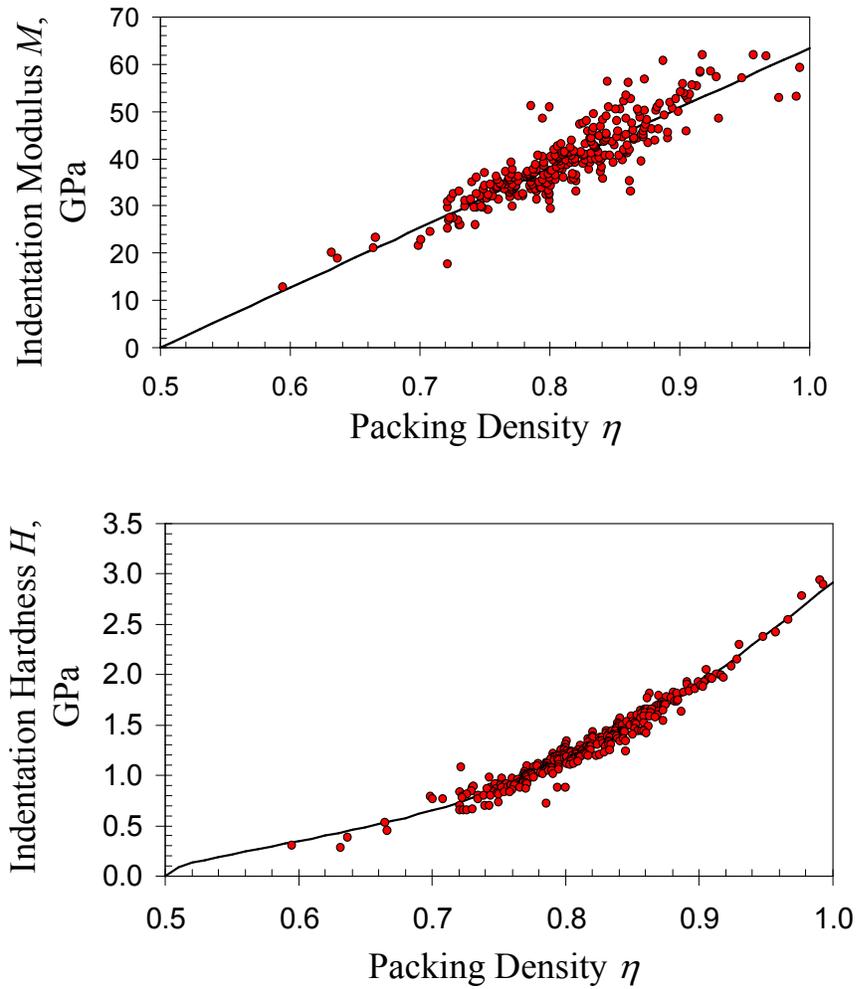
Figure 7-21: Example of assessment of microstructure for sample PC-30-0-0.

otherwise, although the chemical nature of this third hydration product remains unclear, its mechanical behavior as sensed by nanoindentation can perfectly be captured with the same scaling relations as for LD C-S-H and HD C-S-H, which by mechanical analogy justifies the name of ultra-high density (UHD) C(-S-)H.

Packing Density Distribution

The ultimate validation of the microstructure assessment technique must be an independent measurement of the porosity of the sample. Such a measurement, down to pore sizes on the
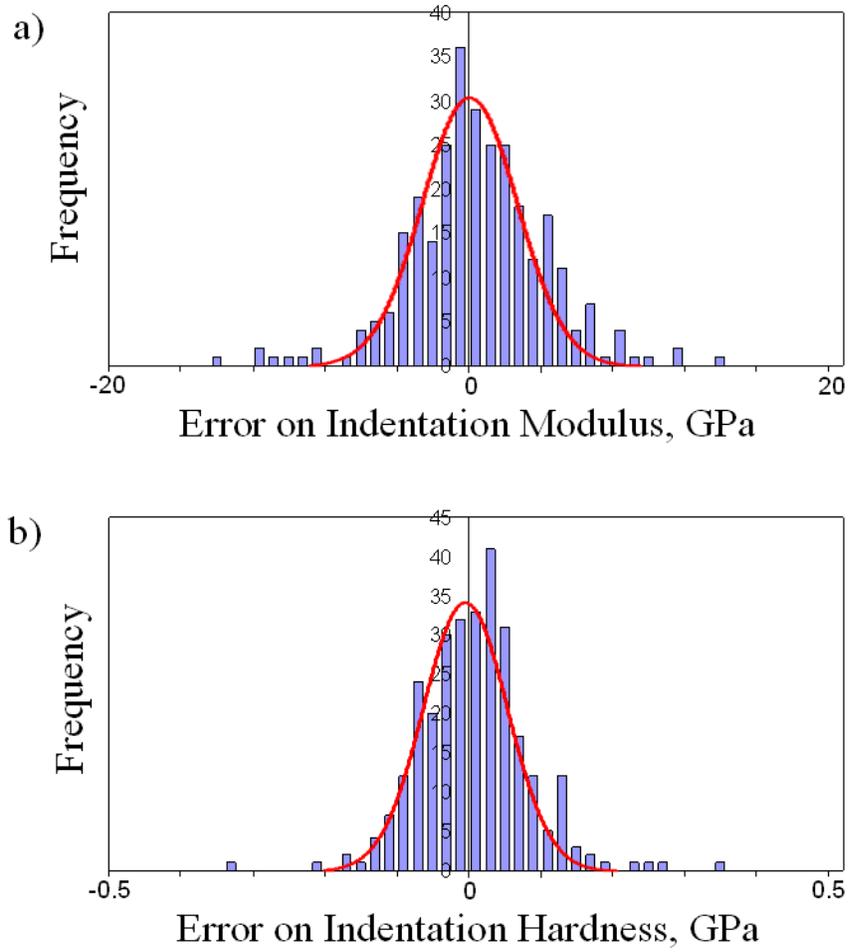
Figure 7-22: Result of the microstructure assessment technique: Distribution of the error (a) on the indentation modulus $M_{\exp} - M_{theo}$ and (b) on the indentation hardness $H_{\exp} - H_{theo}$.

order of a few nanometers, proves particularly complex from an experimental point of view. Nevertheless, a comparison with the benchmark of the Powers-Brownyard model (see Section 6.4.2) can be performed. This comparison is performed on the reference samples with no heat treatment (see Section 7.1.1).

The packing density distribution we obtain for each sample spans a large range of packing densities (see Figure 7-21). In order to compare this packing density distribution with the Powers-Brownyard model, the mean porosity φ is determined from the mean of the set of fitted packing densities $\{\eta_i\}_{i=1..N}$: $\varphi = 1 - <\eta_i>$.

The resulting mean porosity is compared with an estimate of the porosity obtained with the Powers-Brownyard model. Such a comparison requires an adaptation of the Powers-Brownyard model to sub-stoichiometric conditions. Since for cementitious materials in sub-stoichiometric conditions the shrinkage and the volume of capillary pores are both very small, we assume $V_{cs} = 0$ and $V_{cp} = 0$ in Eqs. (6.6). Recalling that the Powers-Brownyard model assumes that C-S-H is a gel made of 28% porosity, the Powers-Brownyard model yields an estimation of the overall porosity of the sample:

$$\varphi = \frac{0.28 V_{gel}}{V_{gel} + V_{cl}} = \frac{0.59\xi}{1 + 1.12\xi} \tag{7.16}$$

where the hydration degree ξ can be calculated from its definition (6.7):

$$\xi = 1 - \frac{f_{CL}}{1 - p} \tag{7.17}$$

In Eq. (7.17) the initial porosity p is given by Eq. (6.8) and the actual volume fraction of clinker f_{CL} can be obtained from a four-Gaussian deconvolution of the results (see Figure 7-19). A comparison of the mean porosities φ as obtained from the packing density distributions and as estimated with the Powers-Brownyard model is reported in Figure 7-23. Except for the most extreme sub-stoichiometric conditions $w/c = 0.15$ (for which the Powers-Brownyard model was not intended), results are in perfect agreement. We conclude that the microstructure assessment technique is a highly reliable means of assessing packing density distributions.

248
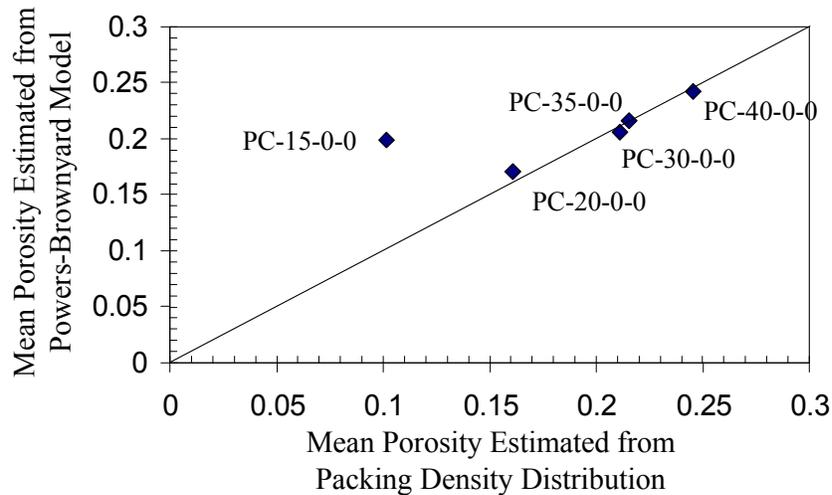
Figure 7-23: Comparison between the mean porosities obtained with the packing density distributions and with the Powers-Brownyard model for reference samples with no heat treatment.

7.6 Chapter Summary

This Chapter introduced and validated experimentally the statistical indentation techniques developed in Part III. The tools of indentation analysis are now in place, both analytically and experimentally. The application of those tools to a grid of nanoindentations performed on cementitious materials will provide a wealth of information on the material:

- The indentation macroproperties, i.e., an estimate of the homogenized properties of the cementitious material.

- The strength properties (h_s, α_s) of the C-S-H solid.

- The porosity (or packing density) distributions and the porosity of the sample.

- The volume fraction of remaining clinker.

- The properties (indentation modulus M, indentation hardness H, packing density η, volume fraction f) of each individual hydration product.

The statistical indentation techniques and their outputs are summarized in Figure 7-24. We are now ready to start the experimental investigation of the effect of mix proportions and
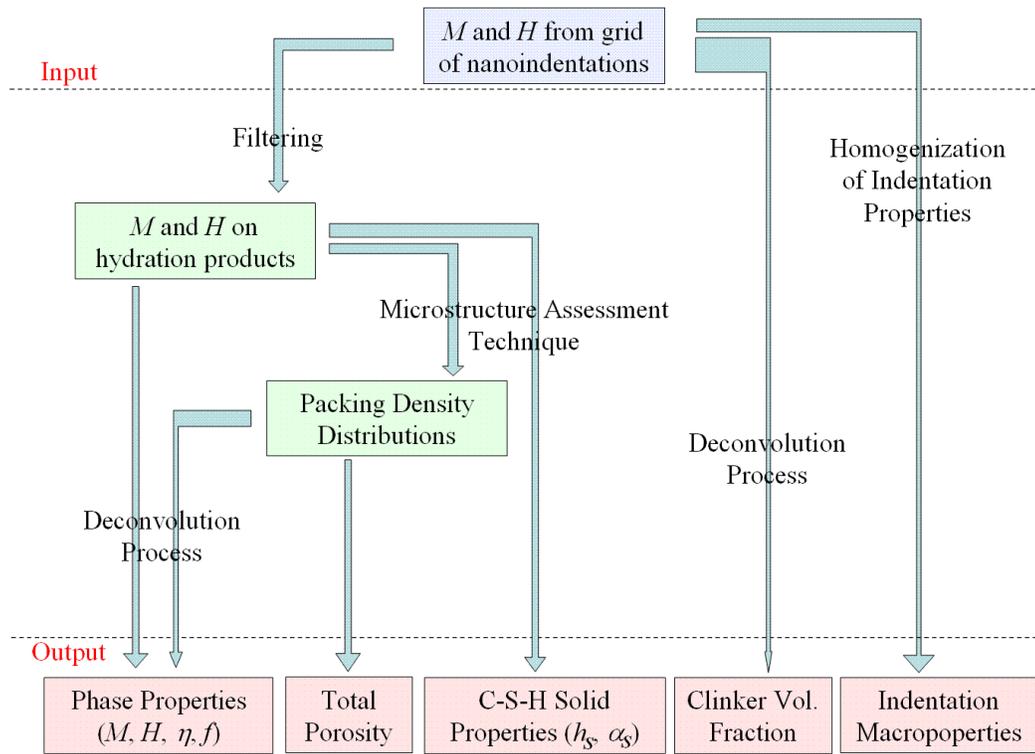
Figure 7-24: Flow chart summarizing the statistical indentation techniques and their outputs for the experimental investigation.

processing on the microstructure and fundamental nanomechanical properties, including creep, of cementitious materials. This investigation is the focus of the next Part.

Part V

Link between Composition–Microstructure–Creep Performance of Sub-stoichiometric Cement-Based Materials

Chapter 8

Influence of Mix Proportions and Processing on Microstructure

Parts II and III of this report developed the statistical indentation techniques necessary to assess microstructure and mechanical performance by indentation means. Chapters 6 and 7 defined the considered cementitious materials and how those techniques were applied. Together, they offer the experimental possibility to implement the Materials Science paradigm for cementitious materials, i.e., to assess the link between mix proportions or processing, microstructure, and performance. This experimental investigation is the focus of this Part, which is composed of two Chapters: This Chapter investigates the link between mix proportions or processing and microstructure for sub-stoichiometric cementitious materials. Chapter 9 investigates the link between creep properties and microstructure.

The experimental investigation presented[1] in this Chapter focuses on elastic and strength indentation properties, which form the basis for the microstructure assessment technique. The influence of water-cement ratio, heat treatment, silica fumes and calcareous filler on the microstructure are considered successively. We aim at determining how each of those parameters modifies the properties of C-S-H particles and the packing density distributions. Then, a predictive tool is developed which provides, for given mix proportions and processing, the volume fractions of remaining clinker, solid C-S-H, and gel porosity.

---

[1]The full results of all deconvolutions, all microstructure assessments and all homogenizations of indentation properties are given in Appendix B.

8.1 Influence of Water-Cement Ratio

This Section presents and discusses the results relative to the effect of the water-to-cement ratio on the microstructure. The question we want to address is whether the water-to-cement ratio modifies the properties of the C-S-H particles and/or the packing density distributions? To answer these questions, here we focus on the non-heat-treated reference samples (PC-15-0-0, PC-20-0-0, PC-30-0-0, PC-35-0-0 and PC-40-0-0, see Section 7.1.1), which cover water-cement ratios ranging from $w/c = 0.15$ to $w/c = 0.4$.

8.1.1 Results

C-S-H Particle Properties

The C-S-H particle properties, back-calculated with the microstructure assessment technique (see Section 7.4.3), are given in Appendix B. The hardness of the C-S-H solid, $h_s = 2.99$ GPa $\pm 6.4\%$ shows very little variability, despite the large span in water-cement ratios considered. Said otherwise, the hardness h_s of the C-S-H solid is independent of the water-cement ratio.

In contrast, the cohesion $c_s = 0.392$ GPa $\pm 27.5\%$ and the friction coefficient $\alpha_s = 0.207 \pm 68.1\%$ show a substantially greater variability, but exhibit no trend with the water-cement ratio: This large variability is most likely due to a high-sensitivity to noise in the reverse analysis of the microstructure assessment.

Properties of C-S-H Phases

The deconvolution process, when applied to the nanoindentations performed on the hydration products, provides the phase properties (indentation modulus M, indentation hardness H and packing density η) of the three identified C-S-H phases (Low-Density C-S-H, High-Density C-S-H and Ultra-High-Density C(-S-)H). The deconvoluted phase properties are displayed in Figure 8-1. Those properties do not depend on the water-cement ratio:

- for Low-Density C-S-H: $M_{LD} = 23.3$ GPa$\pm 8.5\%$, $H_{LD} = 0.60$ GPa$\pm 2.6\%$, $\eta_{LD} = 0.69 \pm 2.5\%$

- for High-Density C-S-H: $M_{HD} = 30.6$ GPa$\pm 5.7\%$, $H_{HD} = 0.86$ GPa$\pm 7.9\%$, $\eta_{HD} = 0.74 \pm 3.5\%$

- for Ultra-High-Density C(-S-)H: $M_{UHD} = 43.2$ GPa$\pm 5.1\%$, $H_{UHD} = 1.5$ GPa$\pm 13.0\%$, $\eta_{UHD} = 0.83 \pm 1.3\%$

Therefore, the phase properties of the three C-S-H phases are material invariant.

Packing Density Distributions and Volume Fractions

The microstructure assessment technique enables to obtain the packing density distributions (see Section 7.4.3). Although the phase properties do not change when modifying the water-to-cement ratio w/c, the packing density distributions change dramatically, as can be observed on Figure 8-2.

Those changes in packing density distributions are a consequence of the changes in volume fractions of the three C-S-H phases within the hydrated matter (see Figure 8-3a). Decreasing the water-cement ratio favors denser phases. Below $w/c = 0.2$, no more LD C-S-H is present. Ultimately, at $w/c = 0.15$, only UHD C(-S-)H is present. When decreasing the water-cement ratio w/c, as a result of the densification of the hydration products with a decreasing water-cement ratio w/c, the gel porosity in the paste decreases as well (see Figure 8-3b). Figure 8-3b also shows that when decreasing the water-cement ratio, the volume fraction of remaining clinker increases.

8.1.2   Discussion

Having quantified the influence of the water-cement ratio on the microstructure, one can reasonably wonder how those changes in microstructure affect the macroproperties. The macroproperties can be estimated from the grid of nanoindentations with the tools presented in Section 7.4.4. Figure 8-4 displays the estimated macroproperties and shows that the water-cement ratio has a dramatic effect on the macroproperties. When decreasing the water-cement ratio from quasi-stoichiometric conditions ($w/c = 0.4$) down to $w/c = 0.15$, both the homogenized indentation modulus M^{hom} and the homogenized indentation hardness H^{hom} increase by more than 100%.
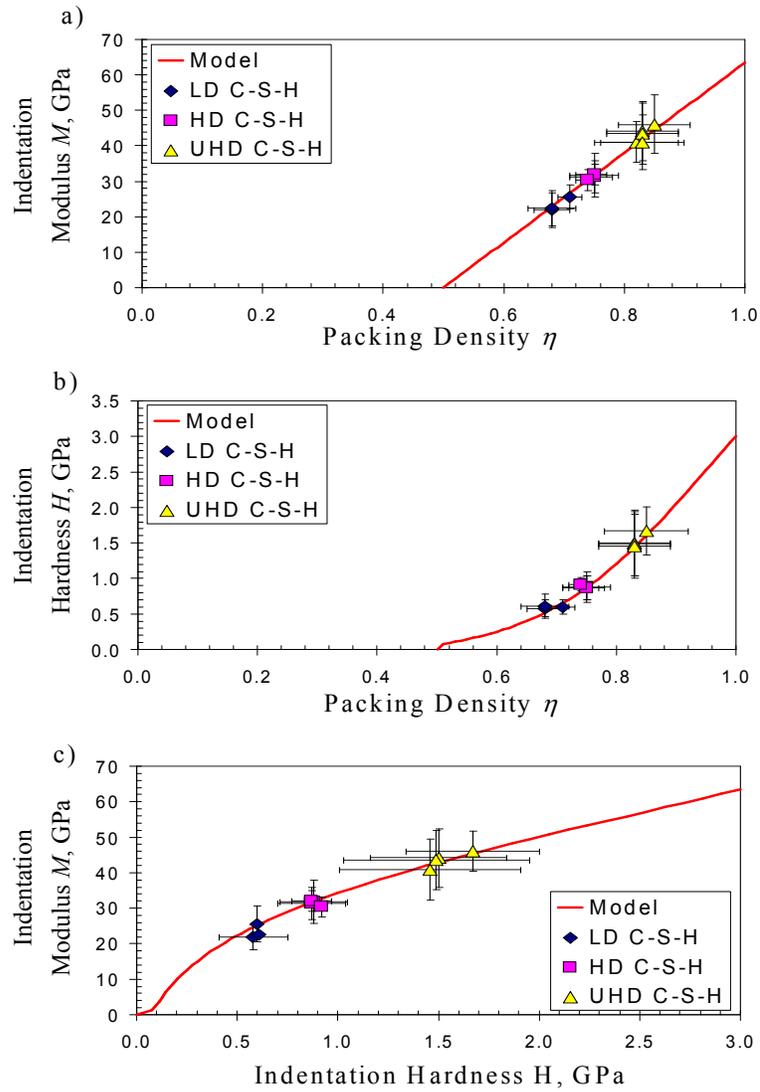
Figure 8-1: Evidence of the invariance of the C-S-H phases properties in samples with various water-cement ratios. (a) $M - \eta$ scaling, (b) $H - \eta$ scaling and (c) $M - H$ scaling.
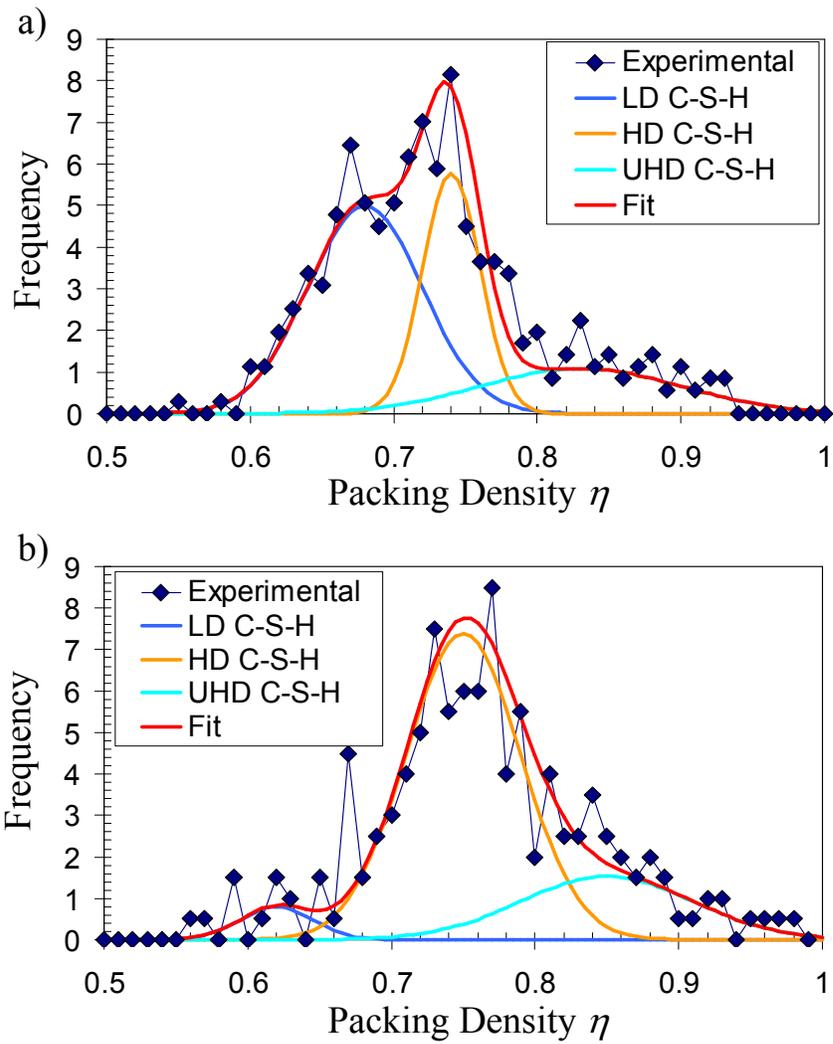
Figure 8-2: Packing density distribution in cement paste with (a) $w/c = 0.4$ and with (b) $w/c = 0.2$.
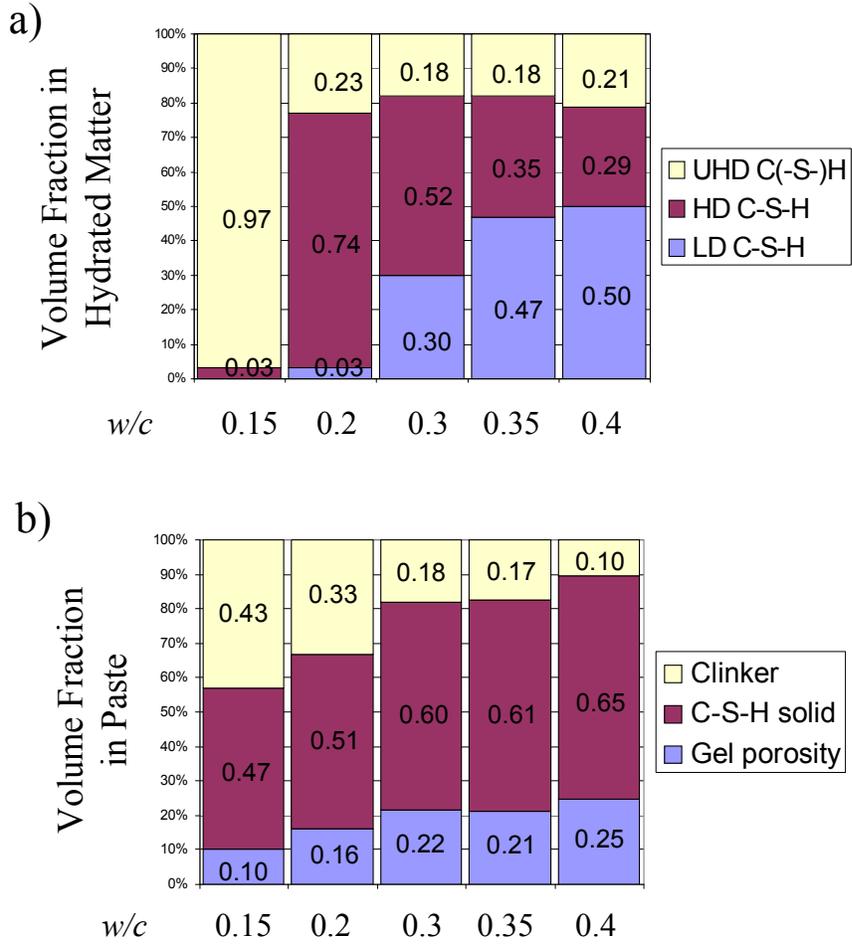
Figure 8-3: Changes in volume fractions with the water-cement ratio. (a) Volume fractions of the three C-S-H phases within the hydrated matter and (b) volume fractions of remaining clinker, C-S-H solid and gel porosity in the paste.
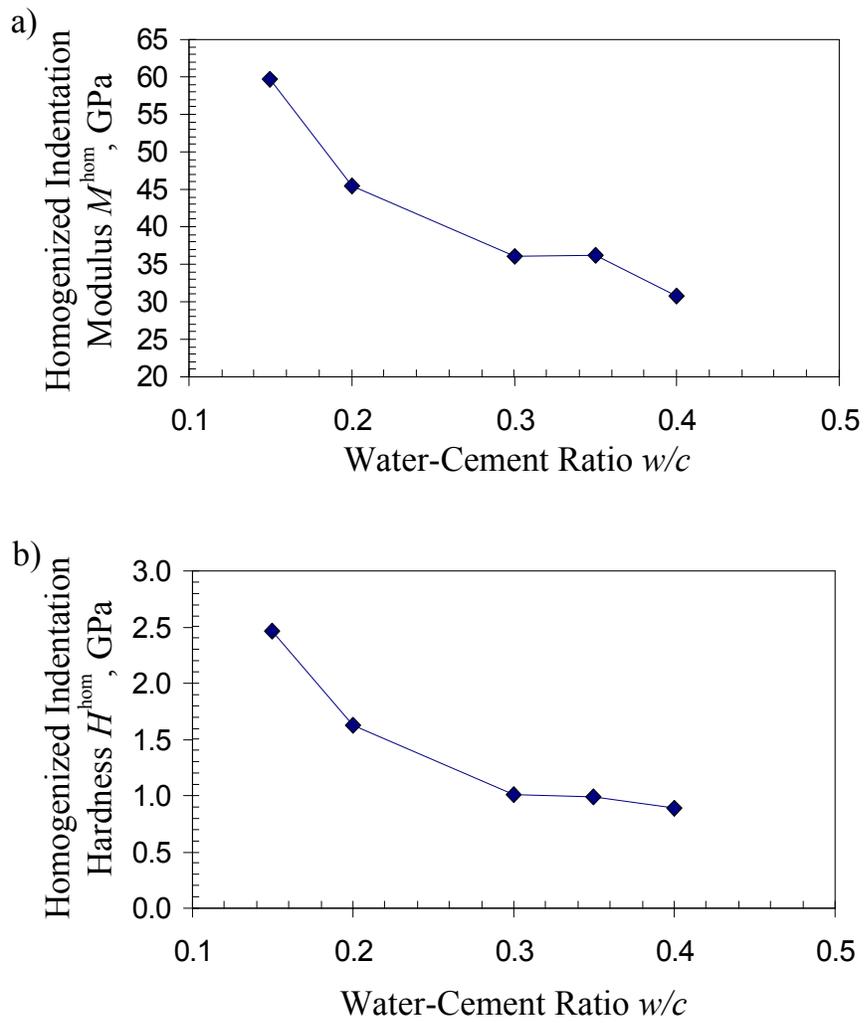
Figure 8-4: Effect of water-cement ratio on the macroproperties. (a) Homogenized indentation modulus M^{hom} and (b) homogenized indentation hardness H^{hom}.
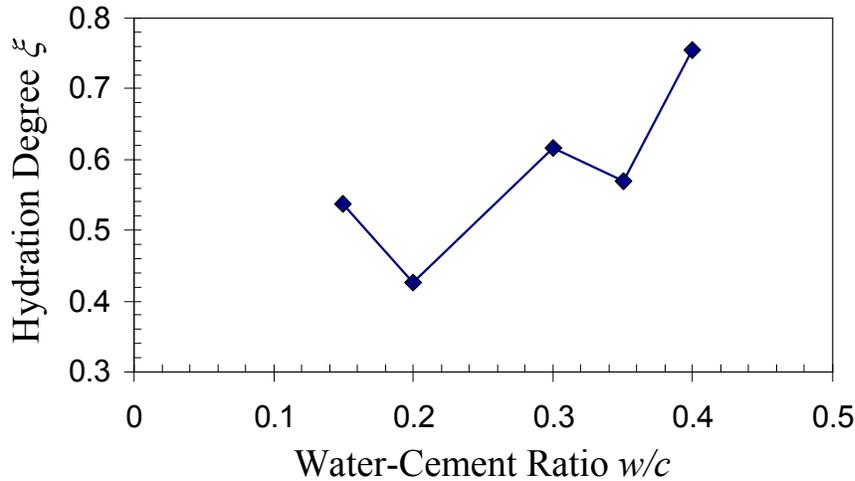
Figure 8-5: Effect of water-cement ratio w/c on hydration degree ξ.

The dramatic effect of the water-cement ratio on the macroproperties is the consequence of two combined effects:

- A decrease in water-cement ratio increases the volume fraction of remaining hydrated clinker. Simply put, when less water is present, less clinker reacts. This observation can be translated in terms of hydration degree ξ. Indeed, the initial volume fraction of clinker is equal by definition to $(1 - p)$, where p is the initial porosity (see Section 6.4.2) and is given by Equation (6.8). In addition, the actual volume fraction f_{CL} of clinker can easily be determined, recalling from Section 7.5.5, as the volume fraction of the fourth peak in a four-Gaussian deconvolution of all the nanoindentations of the grid. The hydration degree $\xi = f_{CL}/(1 - p)$ is displayed in Figure 8-5 and, as expected, decreases with a decreasing water-cement ratio.

- A decrease in water-to-cement ratio decreases the gel porosity in the paste, because it decreases the mean porosity of the hydrates, as becomes evident from Figure 8-6. Close to stoichiometric conditions (i.e., at $w/c = 0.4$), the mean porosity of the hydrates approaches 0.28, which is the porosity of the hydrates in the Powers and Brownyard model (see Section 6.4.2). The decrease in porosity at lower water-to-cement ratios could be
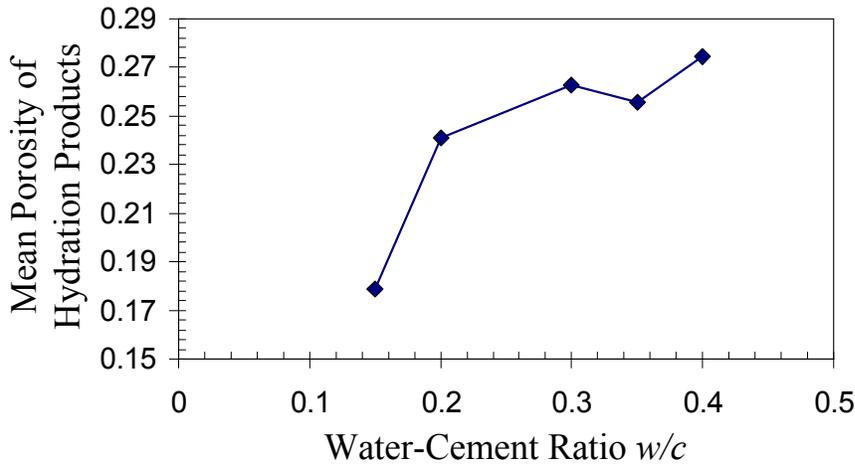
Figure 8-6: Effect of water-cement ratio w/c on mean porosity of hydration products.

due to the confinement imposed by the sub-stoichiometry. Indeed, the lower w/c, the lower the initial porosity p (i.e., the space occupied by water), and consequently, since C-S-H solid has to precipitate somewhere during the hydration process, it will do so in the gel porosity and therefore decrease this gel porosity. Said otherwise, the decrease in gel porosity at low w/c may well be due to geometric reasons.

8.2 Influence of Heat Treatment

This Section presents and discusses the results relative to the effect of a heat treatment on the microstructure. The heat treatment consisted of a 48-hour-long exposure in an oven at $90\,^{\circ}$C at 2 days after casting. The question which is here addressed is whether heat treatment modifies the C-S-H particles properties and/or the packing density distributions? To answer these questions, here we focus on the heat treated reference samples (PC-15-0-2, PC-20-0-2, PC-25-0-2, PC-30-0-2, and PC-35-0-2, see Section 7.1.1), which we compare with the non heat treated reference samples just considered in Section 8.1 (PC-15-0-0, PC-20-0-0, PC-30-0-0, PC-35-0-0 and PC-40-0-0).

8.2.1 Results

C-S-H Particle Properties

The C-S-H particle properties, back-calculated with the microstructure assessment technique (see Section 7.4.3), are given in Appendix B. For the heat treated reference samples, $h_s = 2.96$ GPa $\pm7.7\%$, which is almost identical with the value obtained for the non heat treated samples. Moreover, cohesion $c_s = 0.423$ GPa $\pm28.8\%$ and friction coefficient $\alpha_s = 0.174 \pm 67.7\%$ also are very close to the cohesion and friction coefficient for the non heat treated samples. The heat treatment here considered does not modify the elementary cohesive bonds and pressure dependence of the C-S-H particles.

Properties of C-S-H Phases

The deconvolution process, when applied to the nanoindentations performed on the hydration products, provides the phase properties (indentation modulus M, indentation hardness H and packing density η) of the three identified C-S-H phases (Low-Density C-S-H, High-Density C-S-H and Ultra-High-Density C(-S-)H). The deconvoluted phase properties, displayed in Figure 8-7, are:

- for Low-Density C-S-H: $M_{LD} = 19.9$ GPa$\pm12.3\%$, $H_{LD} = 0.49$ GPa$\pm41.0\%$, $\eta_{LD} = 0.65 \pm 5.9\%$

- for High-Density C-S-H: $M_{HD} = 29.4$ GPa$\pm8.6\%$, $H_{HD} = 0.81$ GPa$\pm17.9\%$, $\eta_{HD} = 0.73 \pm 3.1\%$

- for Ultra-High-Density C(-S-)H: $M_{UHD} = 42.8$ GPa$\pm5.4\%$, $H_{UHD} = 1.42$ GPa$\pm13.6\%$, $\eta_{UHD} = 0.83 \pm 1.9\%$

For the heat treated samples considered, the phase properties of the three C-S-H phases show some more variability than for the non heat treated samples. The most variability is for the first peak, corresponding to LD C-S-H, but as we shall see soon, this peak has a low volume fraction, which could explain why the deconvolution of its mean properties is somewhat noisy. Moreover, on average, the values for the three peaks of the heat treated samples compare

relatively well with the values for the three peaks of the non heat treated samples, from what we conclude that the phase properties are not modified by the application of a heat treatment.

Volume Fractions

Although the phase properties do not change when applying a heat treatment, their volume fractions do, as is observed on Figure 8-8. A comparison of Figures 8-8a and 8-8c shows that the application of a heat treatment favors denser phases. such that, for all water-cement ratios considered, LD C-S-H almost disappears when a heat treatment is applied. A comparison of Figures 8-8b and 8-8d shows that this favoring of denser phases translates into a (rather small) decrease in the total porosity of the sample. For water-cement ratios of 0.3 and 0.35, the decrease in porosity is of about 10%. We note however that, for the lowest water-cement ratio considered ($w/c = 0.15$), application of a heat treatment has no effect on the porosity.

8.2.2   Discussion

Figure 8-9 displays the estimated macroproperties of both heat treated and non heat treated samples. For water-cement ratios $w/c \geq 0.3$, a heat treatment increases the macroproperties, by about 10% for the indentation modulus M, and by about 20% for the indentation hardness H. In contrast, for water-cement ratios $w/c \leq 0.2$, no beneficial effect of a heat treatment is observed. Those observations are consistent with what is observed on the gel porosity (see Figure 8-8).

A vanishing effect of heat treatment at a water-cement ratio $w/c = 0.15$ does make sense. Indeed, even before application of a heat treatment, at such a low water-cement ratio, all C-S-H present is in a Ultra-High-Density form, which already is the densest form of C-S-H identified. Therefore, since the phase properties are invariant, the density of C-S-H in a sample with $w/c = 0.15$ can not increase further.

To determine by what mechanism heat treatment modifies the microstructure, looking at the hydration degree ξ may prove instructive. Figure 8-10 shows that application of a heat treatment, on average, slightly increases the hydration degree. Said otherwise, when applying a heat treatment, more clinker reacts. Such a reaction involves water, which has to come from somewhere. Therefore, it may well be that a heat treatment releases water trapped in the
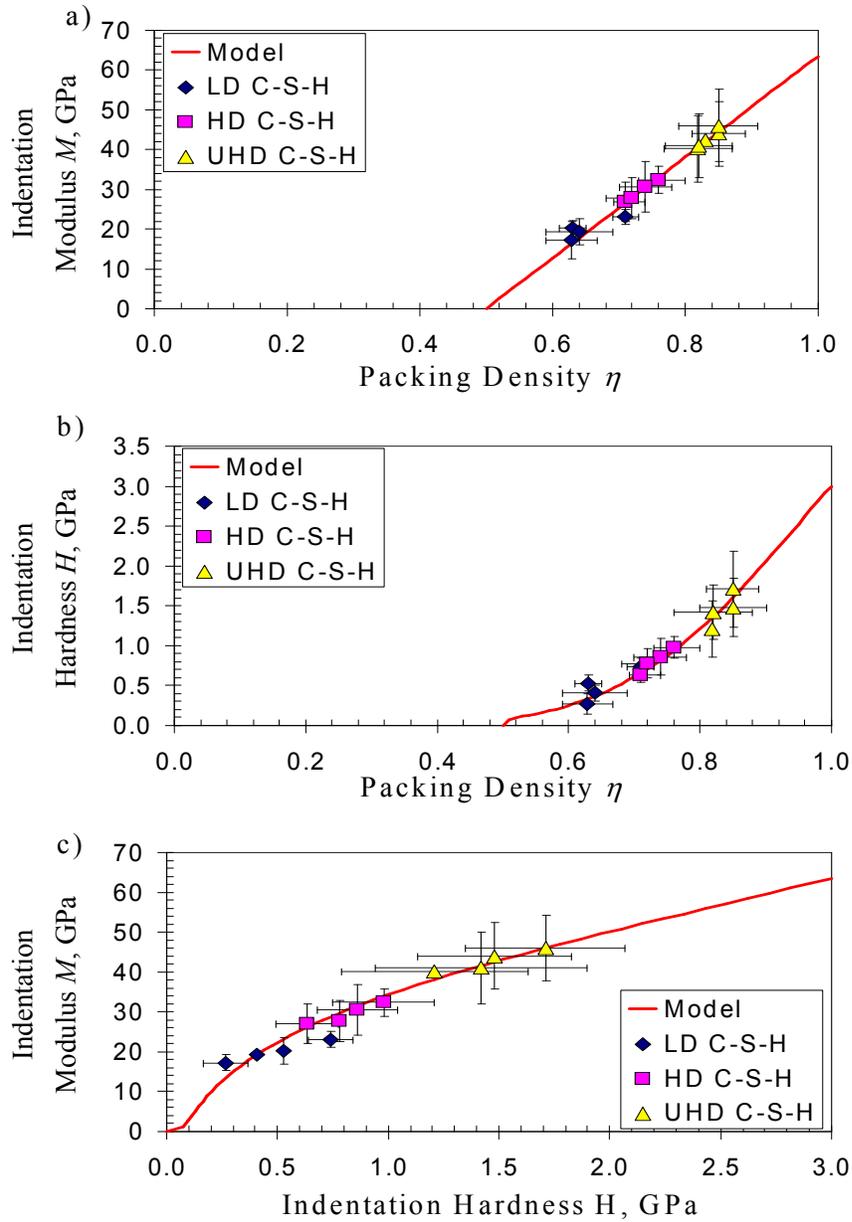
Figure 8-7: Evidence of the invariance of the C-S-H phases properties in heat treated samples with various water-cement ratios. (a) $M - \eta$ scaling, (b) $H - \eta$ scaling and (c) $M - H$ scaling.
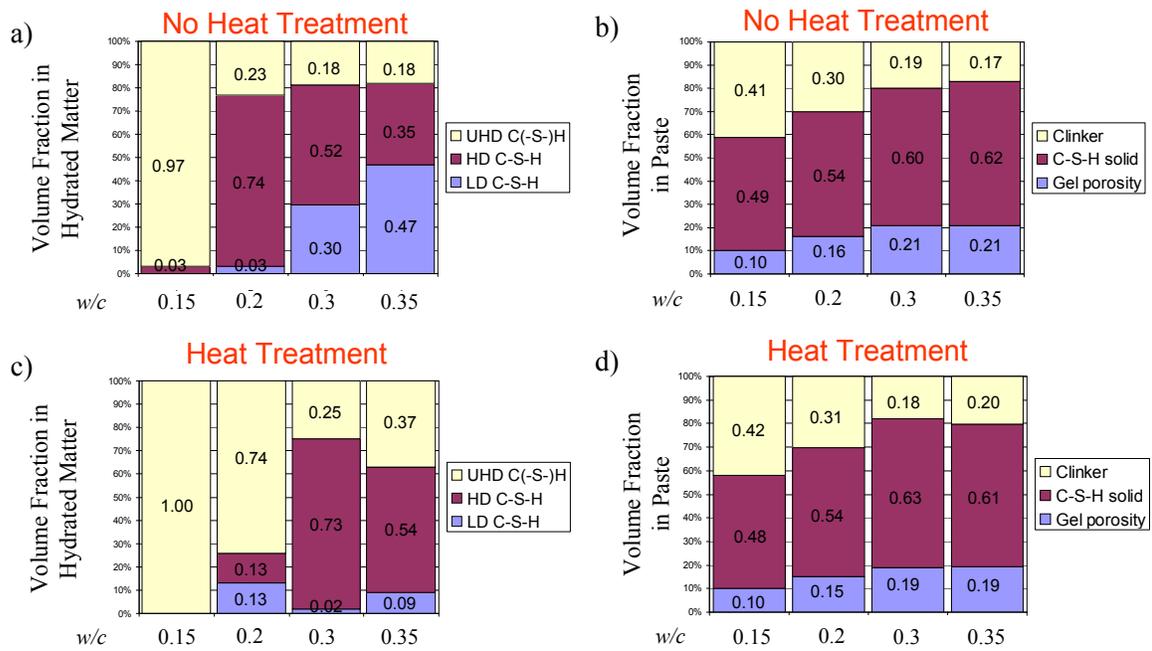
Figure 8-8: Changes in volume fractions with the water-cement ratio for non heat treated samples (a,b) and heat treated samples (c,d). (a,c) Volume fractions of the three C-S-H phases within the hydrated matter. (b,d) Volume fractions of remaining clinker, C-S-H solid and gel porosity in the paste.

a)

b)
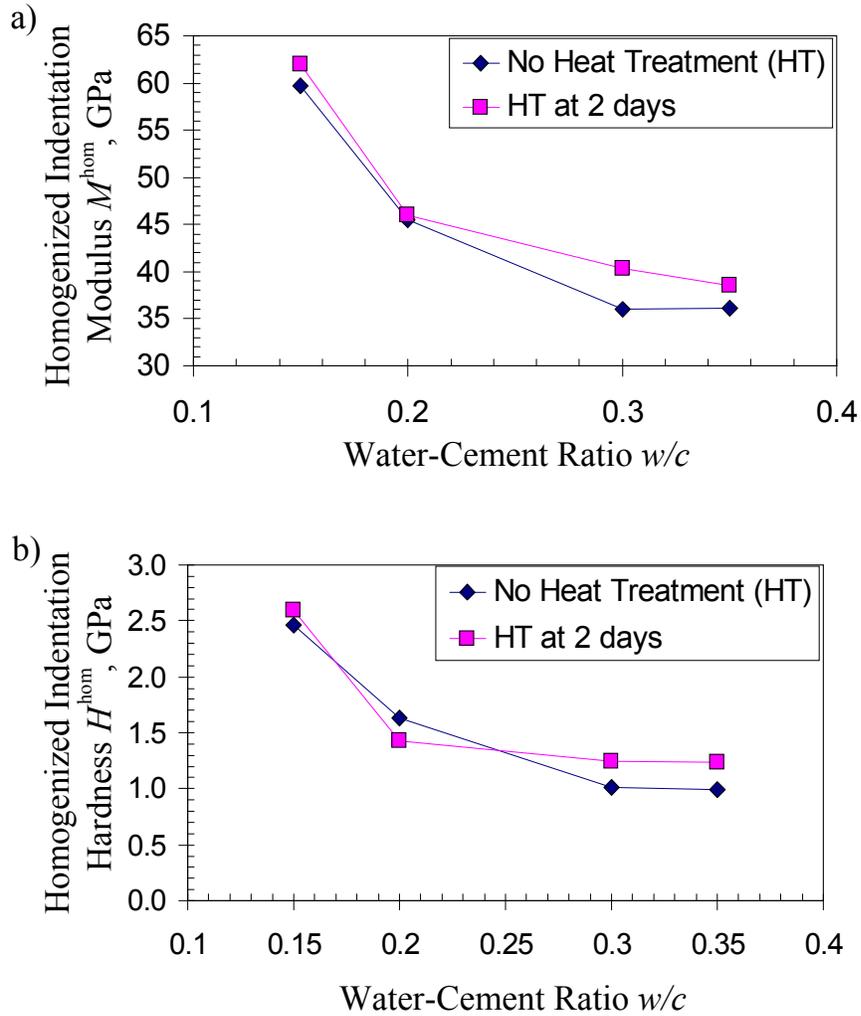
Figure 8-9: Effect of heat treatment on the macroproperties. (a) Homogenized indentation modulus M^{hom} and (b) homogenized indentation hardness H^{hom}.
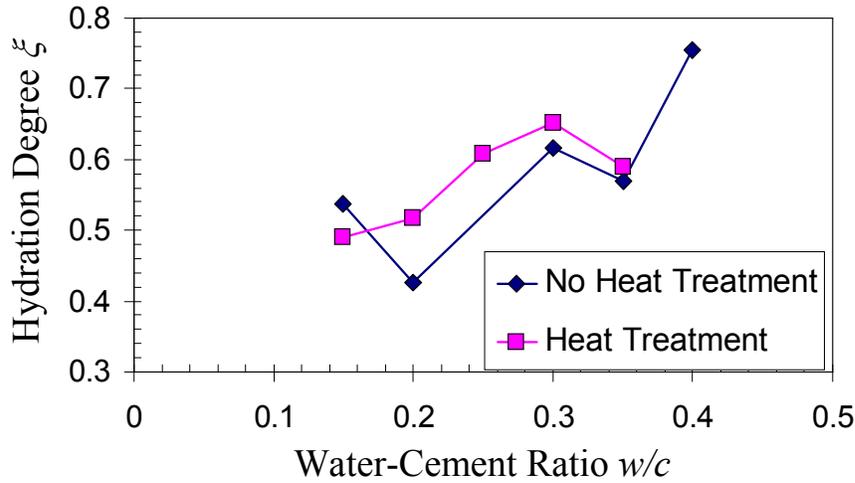
Figure 8-10: Effect of heat treatment on hydration degree ξ.

nanoporosity of the C-S-H nanoparticles, which then becomes available for further hydration of the remaining clinkers.

8.3   Influence of Silica Fumes

This Section presents and discusses the results relative to the effect of an addition of silica fumes with and without heat treatment on the microstructure. Additions of silica fumes up to 32% of the mass of clinker are considered. As before, we seek to answer the question, whether the C-S-H particles properties and/or the packing density distributions are modified by the addition of silica fumes, with or without heat treatment. Here we focus on the non heat treated samples with silica fumes (PC-20-8(SF)-0, PC-20-21(SF)-0, PC-20-24(SF)-0, PC-30-8(SF)-0, PC-30-17(SF)-0, PC-30-21(SF)-0, PC-30-24(SF)-0, PC-30-32(SF)-0, PC-40-8(SF)-0 and PC-40-21(SF)-0, see Section 7.1.1) and on the heat treated samples with silica fumes (PC-20-8(SF)-2, PC-20-17(SF)-2, PC-20-24(SF)-2, PC-20-24(SF)-5, PC-20-32(SF)-2, PC-30-8(SF)-2, PC-30-17(SF)-2, PC-30-24(SF)-2, PC-30-24(SF)-5 and PC-30-32(SF)-2).

8.3.1 Results

C-S-H Particle Properties

The C-S-H particle properties, back-calculated with the microstructure assessment technique (see Section 7.4.3), are given in Appendix B. As can be observed on Figure 8-11a, there is some trend (albeit weakly correlated) that the contact hardness h_s of the C-S-H particles increases with the silica fumes–to–cement ratio. The correlation, however, is pretty weak, as Figure 8-11(b-c) show for the cohesion c_s and the friction coefficient α_s. With some precautions, one may suggest that silica fumes slightly modify the elementary cohesive bonds of the C-S-H particles but not the pressure dependence.

Properties of C-S-H Phases

The deconvolution process, when applied to the nanoindentations performed on the hydration products, provides the phase properties (indentation modulus M, indentation hardness H and packing density η) of the three identified C-S-H phases (Low-Density C-S-H, High-Density C-S-H and Ultra-High-Density C(-S-)H). The deconvoluted phase properties, displayed in Figure 8-12, are:

- for Low-Density C-S-H: $M_{LD} = 22.1$ GPa±9.5%, $H_{LD} = 0.64$ GPa±20.7%, $\eta_{LD} = 0.66 \pm 3.5\%$

- for High-Density C-S-H: $M_{HD} = 31.6$ GPa±8.6%, $H_{HD} = 1.04$ GPa±20.1%, $\eta_{HD} = 0.75 \pm 3.7\%$

- for Ultra-High-Density C(-S-)H: $M_{UHD} = 45.1$ GPa±8.1%, $H_{UHD} = 1.77$ GPa±17.4%, $\eta_{UHD} = 0.84 \pm 3.0\%$

The coefficients of variations of the indentation modulus M and of the packing density η of each phase compare well with those observed on samples without silica fumes in Sections 8.1 and 8.2, and so do their mean values. In contrast, the mean value and coefficient of variation of the indentation hardness of the three hydration products are significantly greater than those of samples without silica fumes. The reason for that is readily understood from an observation of Figure 8-12: An addition of silica fumes increases the hardness of the hydration products, while

a)

$y = 1.70 \, x + 2.92$

$R^2 = 0.41$

Contact Hardness h_s, GPa

Silica Fumes-to-Cement Ratio SF/c, % of mass

- w/c = 0.2, no HT
- w/c = 0.2, HT
- w/c = 0.3, no HT
- w/c = 0.3, HT
- w/c = 0.4, no HT
- Fit

b)

Cohesion c_s, GPa

$y = 0.20 \, x + 0.41$

$R^2 = 0.08$

Silica Fumes-to-Cement Ratio SF/c, % of mass

- w/c = 0.2, no HT
- w/c = 0.2, HT
- w/c = 0.3, no HT
- w/c = 0.3, HT
- w/c = 0.4, no HT
- Fit

c)

Friction Coefficient α_s, GPa

- w/c = 0.2, no HT
- w/c = 0.2, HT
- w/c = 0.3, no HT
- w/c = 0.3, HT
- w/c = 0.4, no HT
- Fit

$y = 0.00 \, x + 0.18$

$R^2 = 0.00$

Silica Fumes-to-Cement Ratio SF/c, % of mass

Figure 8-11: Effect of an addition of silica fumes on the particle properties, i.e., on (a) the contact hardness h_s, (b) the cohesion c_s and (c) the friction coefficient α_s.

letting their indentation moduli and packing densities remain unchanged. Since an addition of silica fumes has no effect on the indentation moduli of the hydration products, it is reasonable to consider that neither does it modify the indentation modulus m_s of the C-S-H particles. This justifies a posteriori the relevance of having fixed $m_s = 63.5$ GPa (see Section 7.4.3).

Porosity and Volume Fractions

Figure 8-13 displays the mean porosity of the hydration products versus the amount of added silica fumes, for samples with or without heat treatment, and various water-cement ratios. The effect of silica fumes on the mean porosity clearly depends on the water-to-cement ratio. The lower the water-to-cement ratio, the more pronounced the beneficial effect of silica fumes. In conditions close to stoichiometry (i.e., at $w/c = 0.4$), silica fumes have no effect. When silica fumes are used, Figure 8-13 shows that a heat treatment does not decrease further the porosity.

For non heat treated samples, the volume fractions of the three hydration products in the hydrated matter are displayed in Figure 8-14a. Surprisingly, when adding silica fumes, even though the hydration products become, on average, denser (see Figure 8-13), the volume fraction of the densest hydration products (UHD C(-S-)H) decreases (see Figure 8-14b). This can be explained by the observed increase in the volume fraction of HD C(-S-)H (see Figure 8-14c), which must overcompensate for the disappearance of UHD C(-S-)H.

For heat treated samples, an interesting behavior also is observed (see Figure 8-15): Once 8% of silica fumes are added, the volume fraction of UHD C(-S-)H drops, and then remains unchanged when adding more silica fumes. We discuss next what those observations tell us about the mechanisms by which silica fumes act, and about the nature of UHD C(-S-)H.

8.3.2   Discussion

To better understand the effect of silica fumes, we need first to understand what silica fumes are. Silica fumes are an industrial by-product, obtained when producing silicon or its alloys [125]. The silica fume particles are very small spheres, with an average diameter of about 100 nm (see Fig. 8-16). They are mostly made of amorphous reactive silica and thus are known to have a pozzolanic effect: They react with Portlandite to produce C-S-H (see Eq. (7.2)).

The decrease in the volume fraction of UHD C(-S-)H when adding silica fumes to non heat

a)

b)

c)
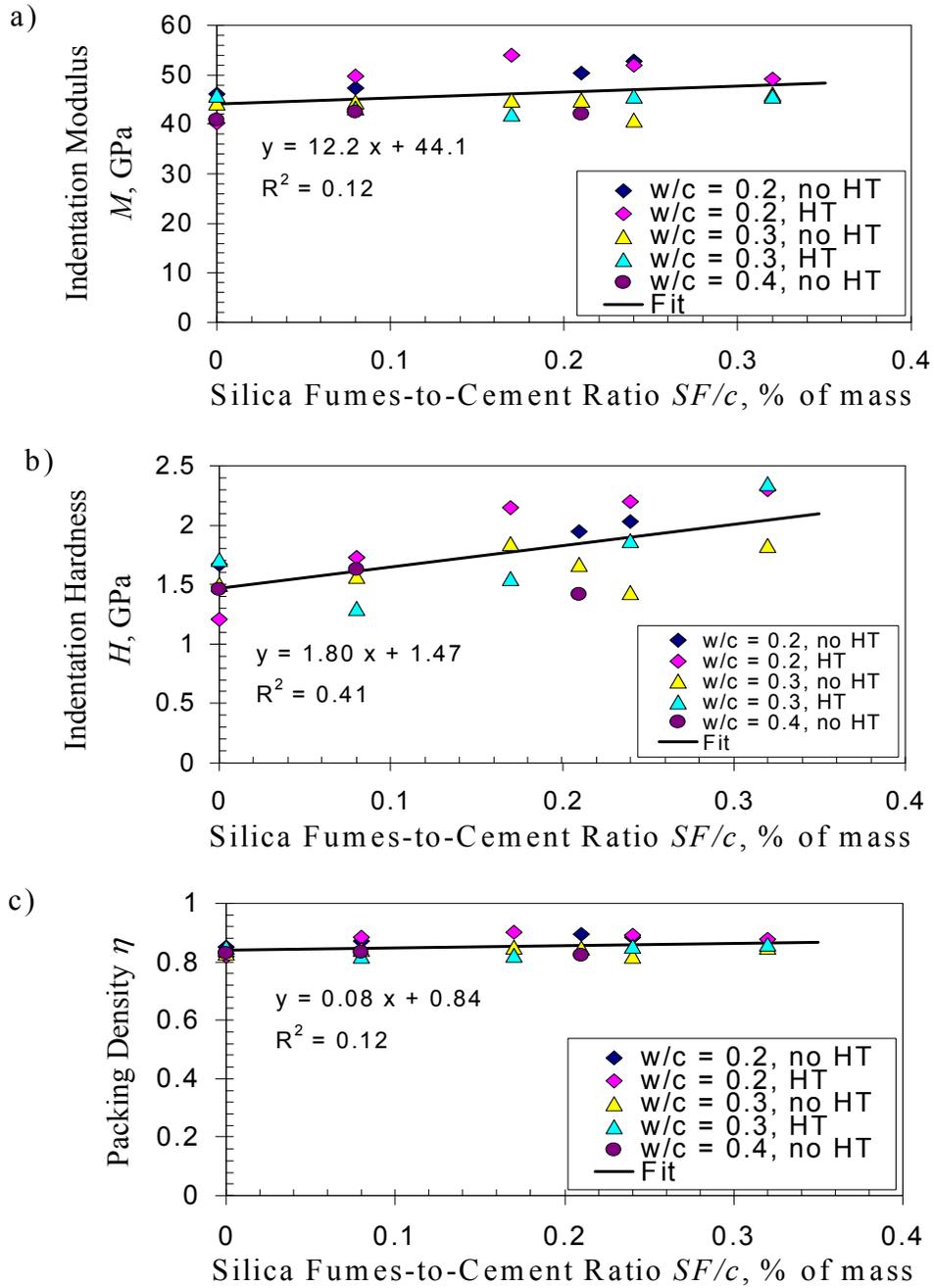
Figure 8-12: Effect of silica fumes on the properties of the UHD C(-S-)H phase. (a) Indentation modulus M, (b) indentation hardness H and (c) packing density η. M and η are unchanged by an addition of silica fumes, while H increases.
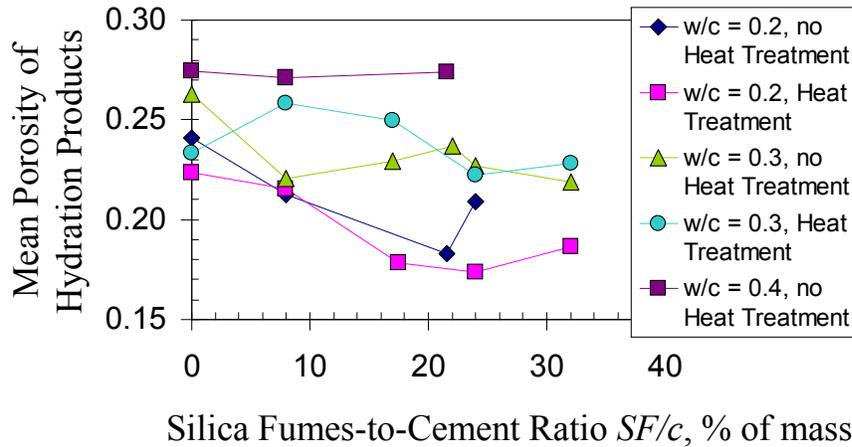
Figure 8-13: Effect of silica fumes on the mean porosity of the hydration products.

treated samples (see Figure 8-14) strongly suggests that UHD C(-S-)H contains C-S-H. At the same time, Figure 8-15 shows that a portion of UHD C(-S-)H (about 20% of the volume of all hydrates) is insensitive to any addition of silica fumes, which strongly suggests that those 20% are not Portlandite. This apparent contradictions between two observations can be resolved, by considering that what we identify as UHD C(-S-)H is in fact a mix of Portlandite (CH) and C-S-H! Those two distinct materials may have close mechanical properties, which prevents from deconvoluting one from the other. Moreover, this also would explain why Constantinides and Ulm [57] identified this phase as Portlandite, while Mondal et al. [129] identified it as C-S-H: They may well be both right!

A comparison of the cement samples with the C3S samples (see Section 7.1.1) also provides valuable information on the UHD C(-S-)H phase. As can be observed in Figure 8-17, the main hydration product in the C3S pastes has the same properties as UHD C(-S-)H in regular cement pastes. Said otherwise, the hydration process of a clinker made of pure C3S provides preferably UHD C(-S-)H: The composition of the clinker plays a role on the packing density distributions and, ultimately, on the microstructure.

On two of the tested samples (PC-20-24(SF)-2 and PC-30-8(SF)-2), we aim to get a better understanding of how UHD C(-S-)H is spatially distributed. To do so, on each of those samples, 900 nanoindentations are performed, with the load profile described in Section 7.4.1, but with a

a)

b)

c)
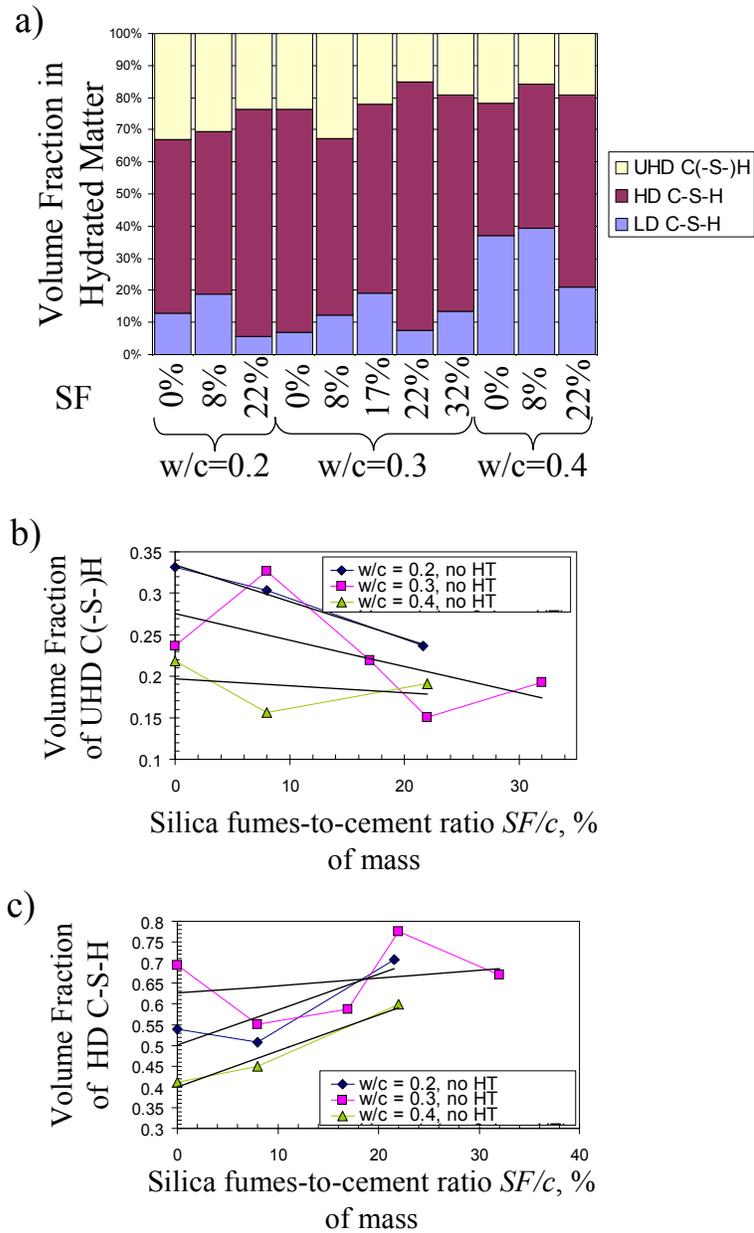
Figure 8-14: Effect of silica fumes on the volumes fractions (a) of all hydration products, (b) of UHD C(-S-)H and (c) of HD C-S-H. The samples are not heat treated.
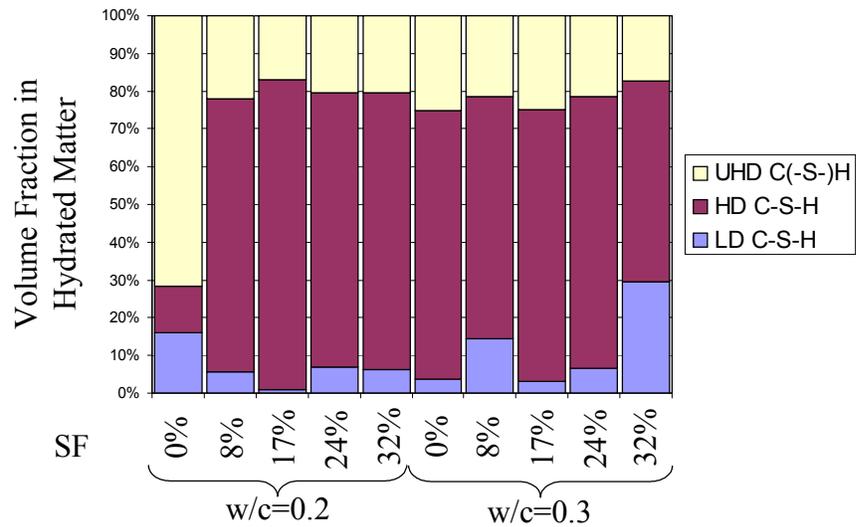
Figure 8-15: Effect of silica fumes on the volume fractions of all hydration products for heat treated samples.
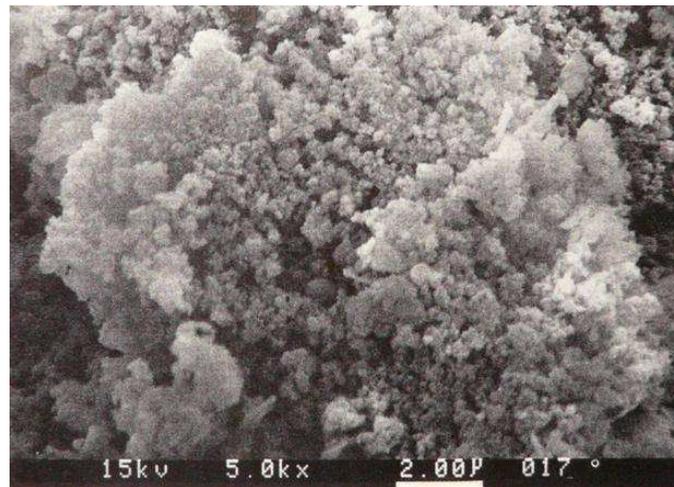
Figure 8-16: Scanning electron microscope micrograph of silica fumes (from [106]).
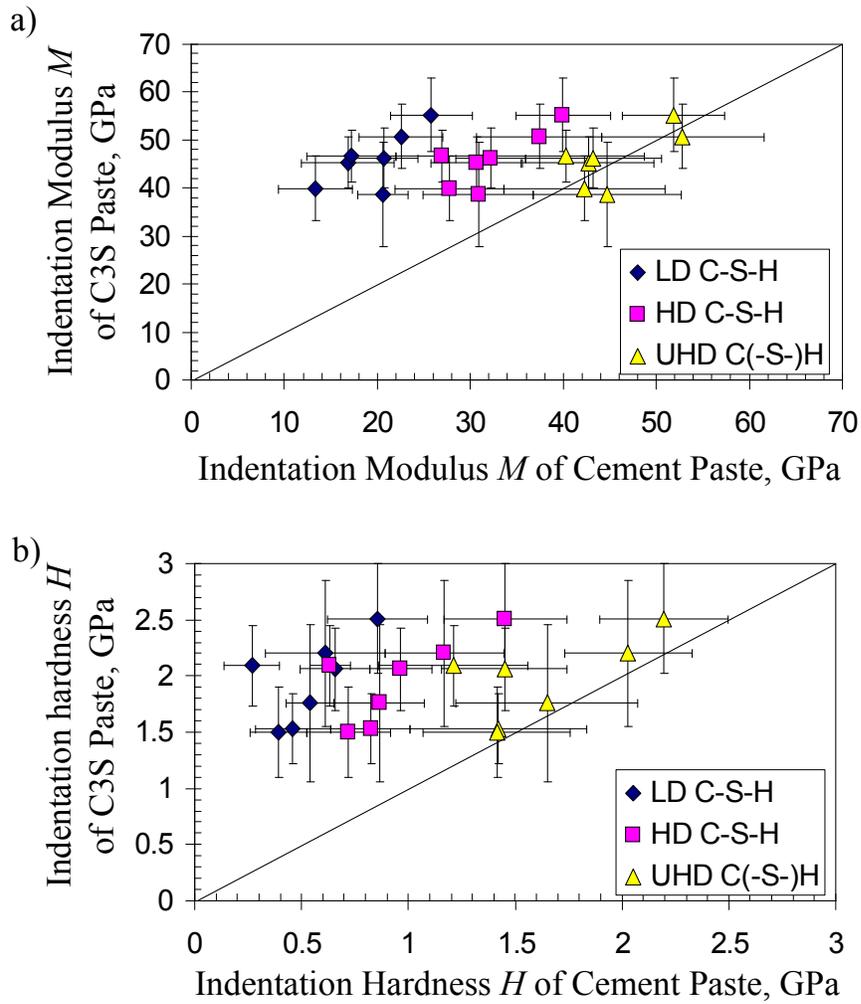
Figure 8-17: Comparison of the phase properties of C3S pastes (dominant hydration product) with phase properties of cement pastes (LD C-S-H, HD C-S-H and UHD C(-S-)H) for identical water-cement ratio, addition of silica fumes and heat treatment.

spacing $\delta = 3 \ \mu$m between nanoindentations. After deconvolution of the 900 nanoindentations, to each phase (LD C-S-H, HD C-S-H, UHD C(-S-)H and clinker) is associated an interval of measured indentation moduli. By doing so, each specific point on the grid of nanoindentations can be associated with the phase on which the nanoindentation was performed. Such a technique provides a mechanical mapping of the indented surface. The results of this mapping for the two samples considered are displayed in Figure 8-18. Both figures 8-18a and 8-18b show that UHD C(-S-)H can be found close to the clinker grain. In addition, Figure 8-18b also shows that some areas of UHD C(-S-)H can tentatively be observed far from the clinker grains. But this observation is not conclusive, since a grain of clinker could nevertheless be close but invisible just below the surface. In conclusion of this short study, it is certain that UHD C(-S-)H can be found close to the clinker grains. But it is not possible to conclude, whether or not it can also be found far from them.

The macroproperties of the pastes, as estimated by the grid of nanoindentations with the tools presented in Section 7.4.4 are displayed in Figure 8-19. The increase in the homogenized indentation hardness H^{hom} is much more pronounced than that of the homogenized indentation modulus M^{hom}, which can be attributed to the effect of silica fumes on the strength properties of the C-S-H particles.

In summary, silica fumes have multiple effects on the cement paste:

- Silica fumes have some tendency to increase the strength properties of the C-S-H particles, but not their elastic properties. A change in mechanical properties could a posteriori be expected, since, by adding silica fumes, i.e., Si, the Ca/Si ratio of C-S-H is decreased, and therefore its chemical composition is modified.

- Silica fumes modify the packing density distributions by two competing effects. On one hand, the pozzolanic reaction consumes Portlandite, mechanically equivalent to the densest of the hydration products, which therefore tends to lower the apparent packing density of the hydrates. On the other hand, the pozzolanic reaction also produces new hydrates, which therefore tends to increase the packing density.
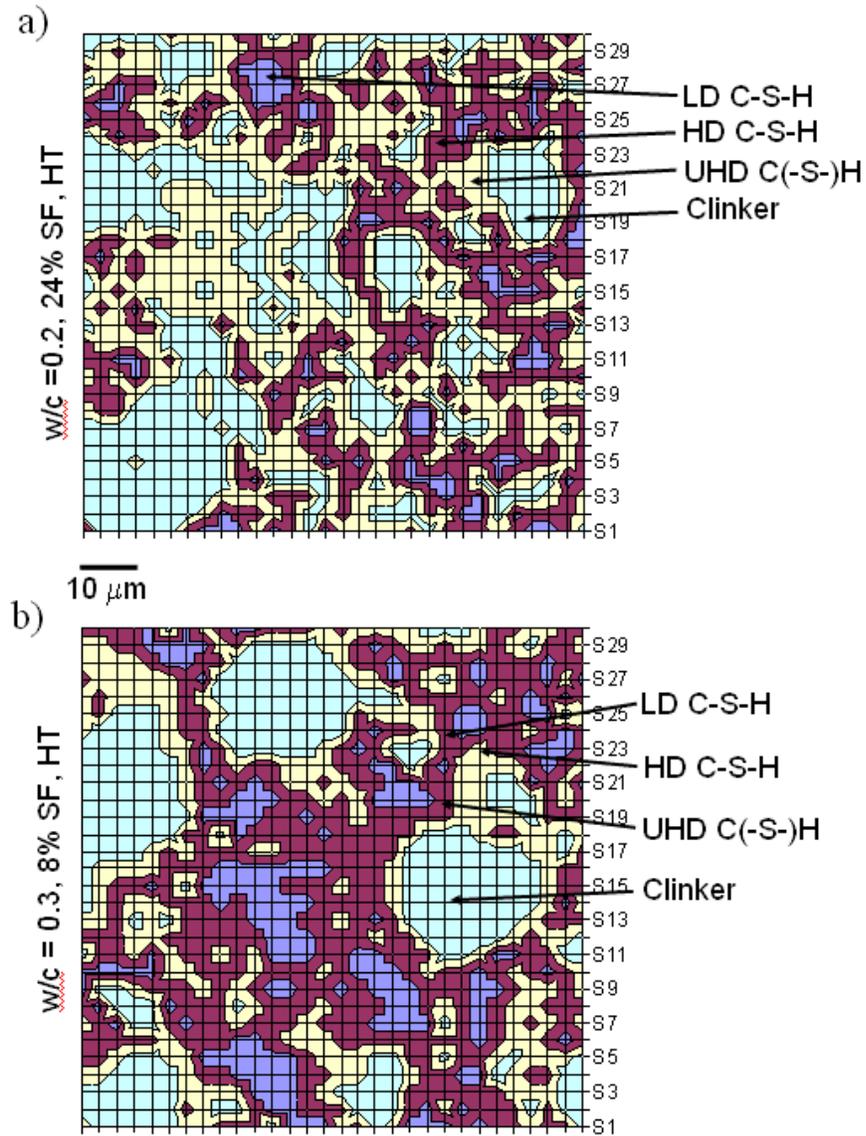
Figure 8-18: Mechanical mapping of (a) PC-20-24(SF)-2 and (b) PC-30-8(SF)-2. UHD C(-S-)H can be found both close to the clinker grains and apparently far from them.

276
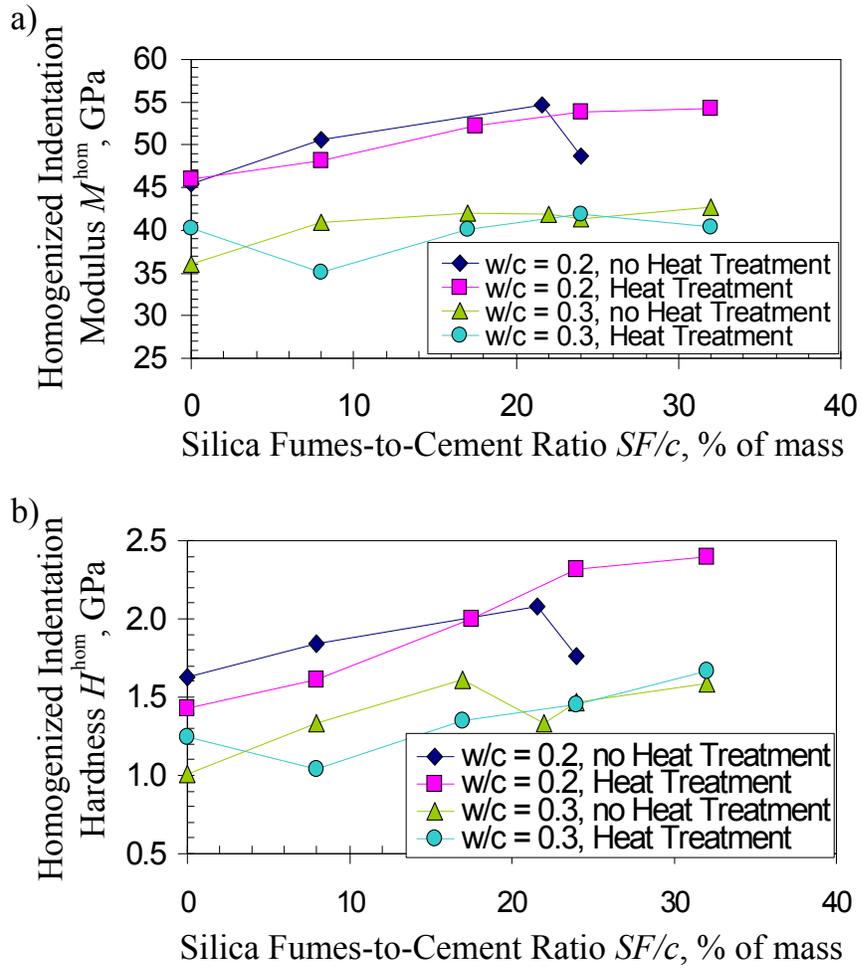
Figure 8-19: Effect of silica fumes on the macroproperties. (a) Homogenized indentation modulus M^{hom} and (b) homogenized indentation hardness H^{hom}.

8.4 Influence of Calcareous Filler

This Section presents and discusses the results relative to the effect of calcareous filler on the microstructure. Additions of a calcareous filler, ground in two different ways, by up to 25% of the mass of clinker are considered. The question we want to address is whether calcareous filler modifies the C-S-H particles properties and/or the packing density distributions. To answer this question, here we focus on the samples with calcareous filler of type 1 (PC-20-10(CF1)-0, PC-20-25(CF1)-0, PC-30-10(CF1)-0, PC-30-25(CF1)-0, PC-40-10(CF1)-0 and PC-40-25(CF1)-0, see Section 7.1.1) and of type 2 (PC-20-10(CF2)-0, PC-20-25(CF2)-0, PC-30-10(CF2)-0, PC-30-25(CF2)-0, PC-40-10(CF2)-0 and PC-40-25(CF2)-0).

8.4.1 Results

C-S-H Particle Properties

The C-S-H particle properties, back-calculated with the microstructure assessment technique (see Section 7.4.3), are given in Appendix B. For both types of filler, the contact hardness shows no trend with the amount of added filler (see Figure 8-20). On average, on all samples with calcareous filler of type 1, we have: $h_s = 3.18$ GPa $\pm 11.7\%$, $c_s = 0.443$ GPa $\pm 17.5\%$ and $\alpha_s = 0.175 \pm 53.8\%$. On average, on all samples with calcareous filler of type 2, we obtain $h_s = 3.13$ GPa $\pm 11.7\%$, $c_s = 0.428$ GPa $\pm 19.2\%$ and $\alpha_s = 0.182 \pm 65.4\%$. Therefore, both fillers have a negligible effect on the strength properties of the C-S-H particles.

Properties of C-S-H Phases

The deconvolution process, when applied to the nanoindentations performed on the hydration products, provides the phase properties (indentation modulus M, indentation hardness H and packing density η) of the three identified C-S-H phases (Low-Density C-S-H, High-Density C-S-H and Ultra-High-Density C(-S-)H). The deconvoluted phase properties of all samples with filler of type 1 are:

- for Low-Density C-S-H: $M_{LD} = 20.6$ GPa$\pm 9.2\%$, $H_{LD} = 0.57$ GPa$\pm 6.0\%$, $\eta_{LD} = 0.66 \pm 2.5\%$
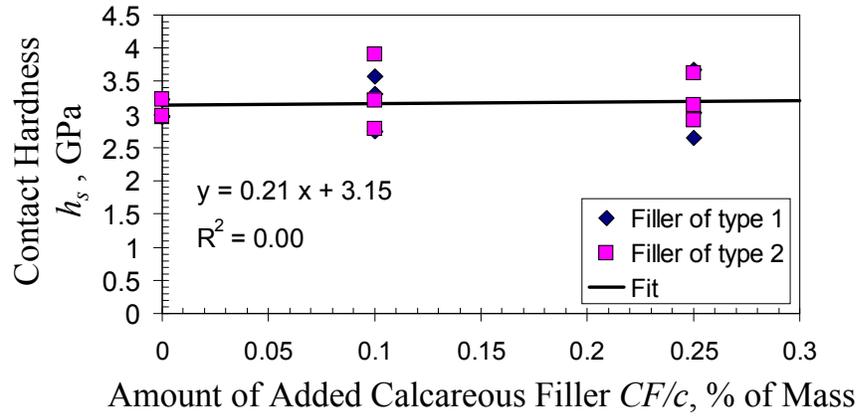
Figure 8-20: Effect of calcareous filler on the contact hardness h_s of the C-S-H particles.

- for High-Density C-S-H: $M_{HD} = 31.5$ GPa$\pm11.8\%$, $H_{HD} = 0.91$ GPa$\pm8.5\%$, $\eta_{HD} = 0.75 \pm 4.1\%$

- for Ultra-High-Density C(-S-)H: $M_{UHD} = 42.9$ GPa$\pm5.1\%$, $H_{UHD} = 1.49$ GPa$\pm8.1\%$, $\eta_{UHD} = 0.83 \pm 4.4\%$

The deconvoluted phase properties of all samples with filler of type 2 are:

- for Low-Density C-S-H: $M_{LD} = 20.5$ GPa$\pm10.6\%$, $H_{LD} = 0.59$ GPa$\pm19.6\%$, $\eta_{LD} = 0.66 \pm 2.8\%$

- for High-Density C-S-H: $M_{HD} = 32.8$ GPa$\pm12.0\%$, $H_{HD} = 1.01$ GPa$\pm16.3\%$, $\eta_{HD} = 0.76 \pm 4.1\%$

- for Ultra-High-Density C(-S-)H: $M_{UHD} = 45.2$ GPa$\pm9.9\%$, $H_{UHD} = 1.64$ GPa$\pm10.8\%$, $\eta_{UHD} = 0.84 \pm 3.9\%$

A comparison clearly shows that the two types of C-S-H yield very similar values of the phase properties. Moreover, those values are in very good agreement with those obtained on the reference non heat treated samples (see Section 8.1.1). In summary, an addition of calcareous filler of either type has no effect on the phase properties of the three hydration products.

279

Volume Fractions

Figure 8-21 displays the volume fraction of the hydration products in the hydrated matter. The two types of filler yield very similar results and tend to decrease the volume fraction of LD C-S-H, while increasing that of UHD C(-S-)H. This densification translates into a decrease in the mean porosity of the hydration products (see Figure 8-22). The two types of filler have an identical effect on the microstructure.

8.4.2   Discussion

Calcareous filler results from the grinding of calcareous stones, such as limestone, and contains mostly calcite $CaCO_3$. Calcareous filler is used for economic reasons, since a substitution of calcareous filler to cement proves to be energy- and money-saving [95]. The question of the reactivity of the filler has been addressed by several researchers, but there is no agreement as to what extent calcite participates in the hydration process. Although it was noted that calcite may react with the tricalcium aluminate C_3A in the clinker [95], there is also experimental evidence that calcite is mostly non reactive [169], such that the Portland Cement Association recommends limestone in practice to be considered as an inert material [86]. Nevertheless, Matschei and Lohtenbach showed very recently that calcite does indeed participate in the hydration process and that the amount of reactive calcite depends on the amount of initial solid Al_2O_3 and SO_3 in the cement [120] (see Figure 8-23). From an initial solid $SO_3 = 2.13$ content, and a sulfate/alumina ratio $S0_3/Al_2O_3 = 0.68$ from Table 7.1, their results suggest that, of the added calcareous filler, only about 1% to 2% of the weight of the cement is reactive. Since we here consider additions of calcareous filler in amounts of 10% and 25% of the weight of cement, most of this calcite is likely to be non reactive. The non-reactivity of the filler could explain why the two types of filler, although ground differently, and therefore possess different specific surface areas, yield the same effect.

But if the filler is non-reactive, why do not we identify it, by nanoindentation, as one the phases in the paste? One reason may be the size of the filler. As explained in Section 7.1.1, the fillers used in this study have a sub-micrometric size. By comparison with the depth of the nanoindentations ($h_{\max} \simeq 200$ nm), it may well be that the scale separability condition (4.1) is not satisfied. If it were indeed the case, each nanoindentation performed on a filler would
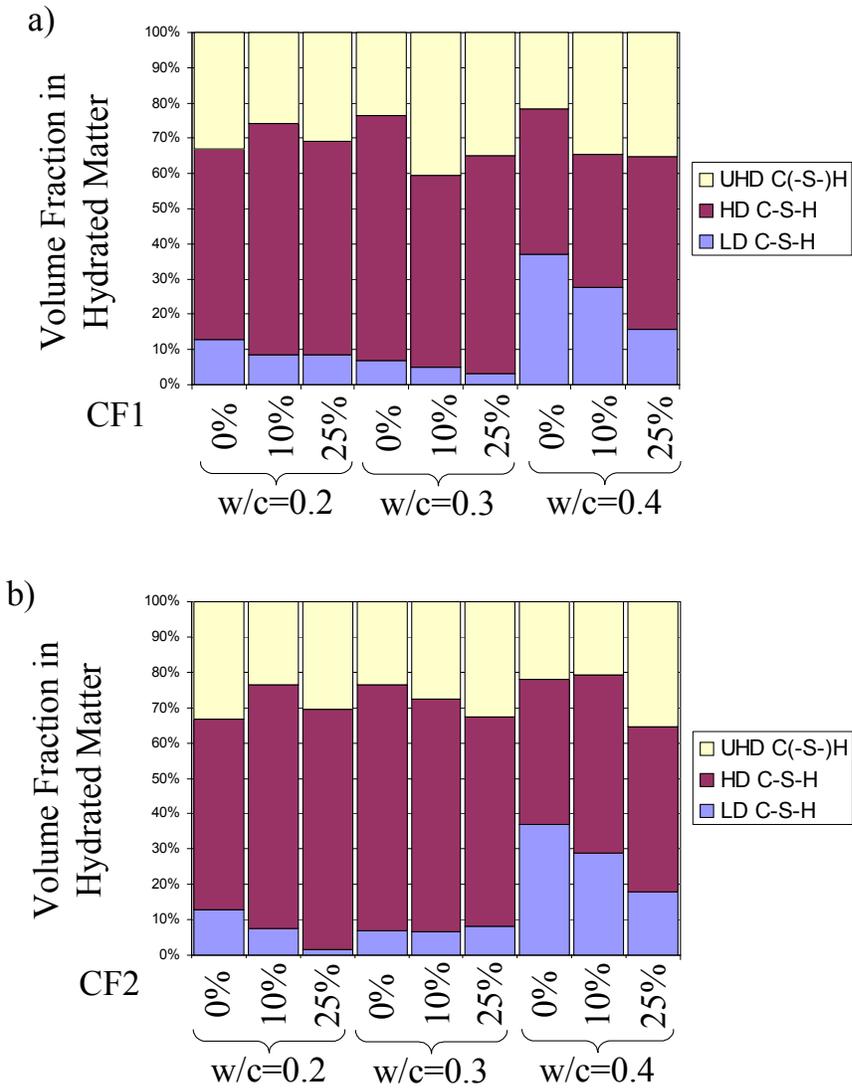
Figure 8-21: Effect of calcareous filler on the volume fractions of the hydration products. (a) Calcareous filler of type 1 and (b) calcareous filler of type 2.
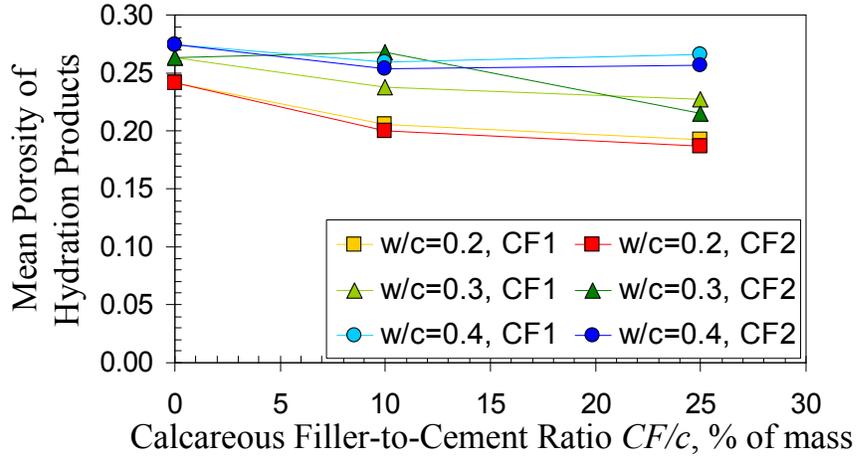
Figure 8-22: Effect of an addition of calcareous filler on the mean porosity of the hydration products.

provide not the mechanical property of the filler itself, but a composite response of the filler and of what is around it, i.e., hydrated matter. Here this hypothesis is tested.

The filler, of indentation modulus M_{CF}, is assumed to be embedded in the hydrated matter (of average indentation modulus M_h). The nanoindentations are assumed to 'sense' only the composite response M^{comp} of those two materials. Here we estimate M^{comp} and compare it with experimental nanoindentation results

A cement is prepared by mixing a mass $\mathcal{M}_{CL}$ of clinker with water, at a water-cement ratio w/c. After hydration, the volume fraction of remaining clinker is f_{CL}. The volume V_h of hydrated matter is therefore given by:

$$V_h = (1 - f_{CL}) \left(\frac{1}{\rho_{CL}} + w/c \right) \mathcal{M}_{CL} \qquad (8.1)$$

where $\rho_{CL} = 3,150$ kg/m^3 is the density of the clinker [38]. To this cement paste is added an amount x of calcareous filler, where x is the calcareous filler-to-cement mass ratio. This addition corresponds to a volume V_{CL} of clinker:

$$V_{CF} = \frac{x}{\rho_{CF}} \mathcal{M}_{CL} \qquad (8.2)$$

282

a)

Amount of Al$_2$O$_3$, weight-%

b)

Amount of SO$_3$, weight-%
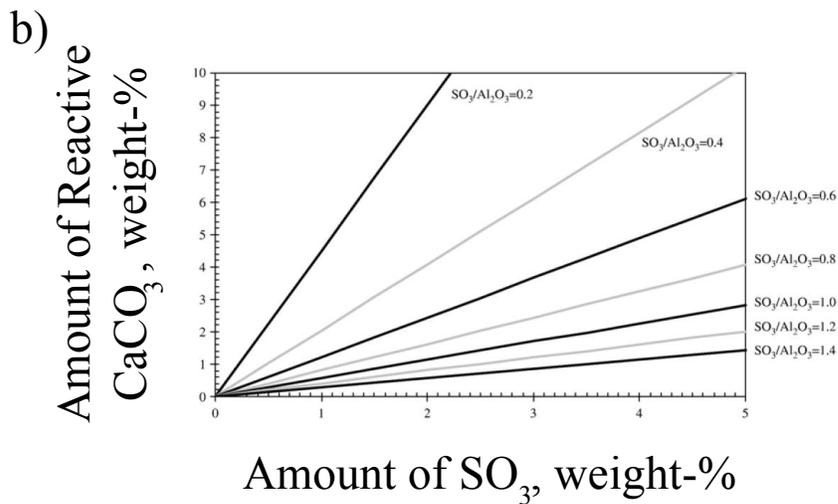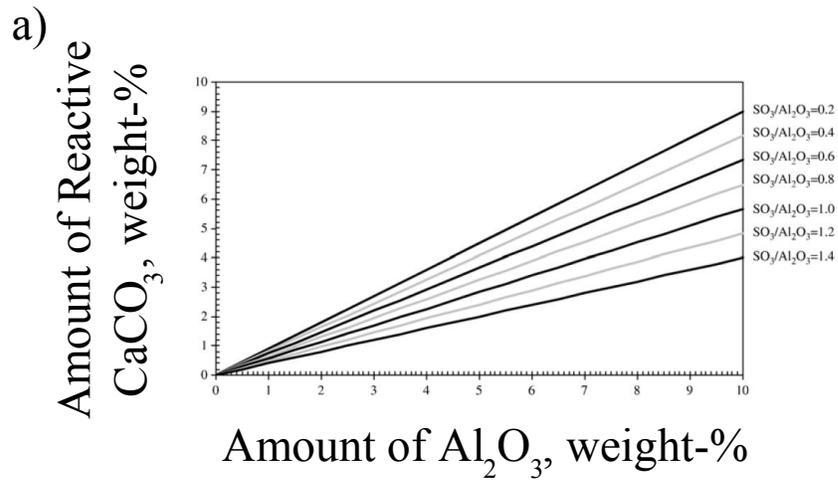
Figure 8-23: Amount of reactive CaCo$_3$ for different initial solid ratios SO$_3$/Al$_2$O$_3$ and different amounts of (a) initial solid Al$_2$O$_3$ and (b) initial solid SO$_3$. Data are expressed in weight units.

where $\rho_{CF} = 2,700$ kg/m^3 is the density of calcite [52]. From Equations (8.1) and (8.2), the volume fractions of filler and hydrated matter in the filler-hydrated matter composite can easily be calculated, and depend on x, w/c and f_{CL}. Knowing those respective volumes fractions, the homogenized response of the filler-hydrated matter composite can be estimated, with the homogenization techniques introduced in Section 4.2.2. More specifically, with the filler being embedded in the hydrated matter, the homogenized indentation modulus M^{comp} of the filler-hydrated matter composite can be estimated with a Mori-Tanaka scheme (Equation (4.29)):

$$M^{comp} = \frac{V_h M_h + \dfrac{V_{CF} M_{CF}}{1 + \dfrac{1}{2}\left(\dfrac{M_{CF}}{M_h} - 1\right)}}{V_h + \dfrac{V_{CF}}{1 + \dfrac{1}{2}\left(\dfrac{M_{CF}}{M_h} - 1\right)}} \tag{8.3}$$

where M_h is the mean indentation modulus of the hydrated matter with no filler embedded, and M_{CF} is the indentation modulus of the filler. The hypothesis of a non-reactive filler embedded in the hydration products is tested by comparing M^{comp} with the experimental results. The mean indentation modulus of the hydrated matter is obtained as the mean value of the first peak of a two-Gaussian deconvolution of a grid of nanoindentations. The results of the comparison are displayed in Figure 8-24 for an indentation modulus $M_{CF} = 100$ GPa of the filler. For this stiffness of the filler, the hypothesis of a non reactive filler embedded in the hydration products captures remarkably well the experimental data.

A value $M_{CF} = 100$ GPa proves to be very close to the measured value for calcite ($M_{CF} = 95.3$ GPa [40]), which validates the hypothesis. Said otherwise, the effect of calcareous fillers can be explained by a simple mechanical reinforcement of the hydrated matter.

8.5 Predictive Composition-Microstructure Model

This Section aims to develop a predictive model to capture the effect of mix proportions and processing on the microstructure for sub-stoichiometric cement pastes. Since the effect of calcareous filler is mainly not on the microstructure, but a mere mechanical reinforcement, calcareous filler is not included in this model. Therefore, we aim to develop a model which captures
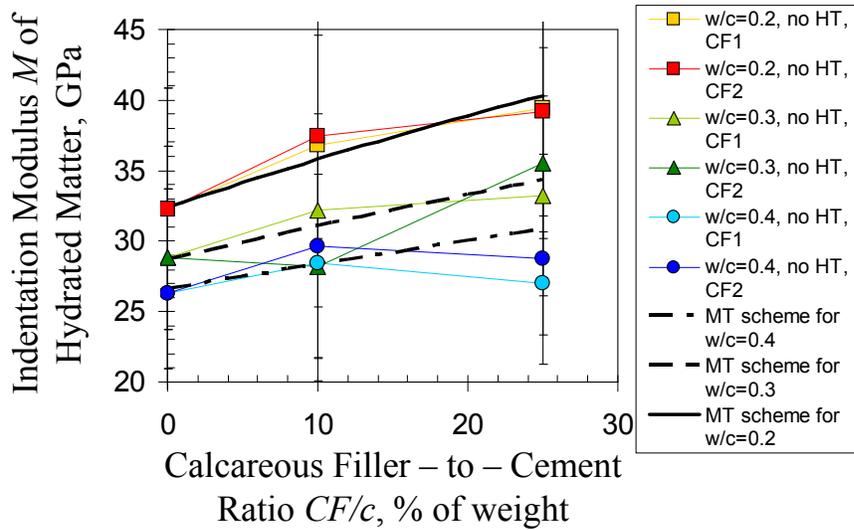
Figure 8-24: Indentation modulus M of the hydrated matter versus the amount of added calcareous filler for samples with different water-cement ratios, and results of the hypothesis testing (thick black lines) of a non-reactive calcareous filler embedded in the hydration products.

the influence of sub-stoichiometry, silica fumes and heat treatment.

8.5.1 Model Development and Calibration

The model is constructed very similarly to Powers' model (see Section 6.4.2). Here we neglect chemical shrinkage and capillary porosity, so that the paste is considered to be made only of clinker and a porous C-S-H matrix:

$$
\begin{aligned}
V_{cl} &= (1-p)(1-\xi) \\
V_{CSH} &= 1 - (1-p)(1-\xi)
\end{aligned}
\tag{8.4}
$$

where V_{cl} is the volume fraction of clinker, V_{CSH} is the volume fraction of the porous C-S-H matrix, ξ is the hydration degree (see Equation 6.7) and p is the initial porosity, i.e., the space initially occupied by water (see Equation 6.8). We note φ_0 as the average porosity of the C-S-H; that is:

$$
\varphi_0 = 1 - \overline{\eta}^{V_{CSH}}
\tag{8.5}
$$

The hydration degree ξ depends on the water-cement ratio w/c. Although heat treatment

285

has a slight effect on the hydration degree (see Figure 8-10), this effect is rather small and here neglected. Moreover, since the pozzolanic reaction which characterizes the effect of silica fumes (see Section 8.3.2) does not involve clinker, we consider that the hydration degree is a function of the water-cement ratio w/c only and is sought for in the simple form:

$$\xi = \xi(w/c) = x_1 \times (w/c) + x_2 \tag{8.6}$$

In contrast, the mean porosity of C-S-H, φ_0, depends on the water-cement ratio w/c, the amount of added silica fumes (SF/c), and the heat treatment. Noting that, in stoichiometric conditions, the mean porosity $\varphi_0 = 0.28$ of Powers model is retrieved (see Figure 8-6), and noting that the effect of silica fumes depends on the stoichiometry (see Figure 8-13), the mean porosity φ_0 is sought for in the form:

$$\varphi_0 = 0.28 - x_3(x_4 - (w/c)) - x_5(SF/c)(x_6 - w/c) \tag{8.7}$$

Since the effect of a heat treatment depends on the stoichiometry, x_3 will be different for heat treated and non heat treated samples. Likewise, since the effect of silica fumes depends on the heat treatment, x_5 will be different for heat treated and non heat treated samples.

The model is fit on all samples heat treated or not, with or without added silica fumes. The equation for the hydration degree (8.6) is fit to the hydration degrees estimated from the grid of nanoindentations with Equation (7.17). The result of the fit is:

$$\xi = 0.582 \times (w/c) + 0.434 \tag{8.8}$$

where the quality of this fit can be observed on Figure 8-25 for the samples with no additions of silica fumes.

The equation for the mean porosity of C-S-H (8.7) is fit to the mean porosity estimated from the packing density distributions obtained with the microstructure assessment technique (see Section 7.4.3). The coefficients x_3 and x_5 are allowed to differ for heat treated and non

286
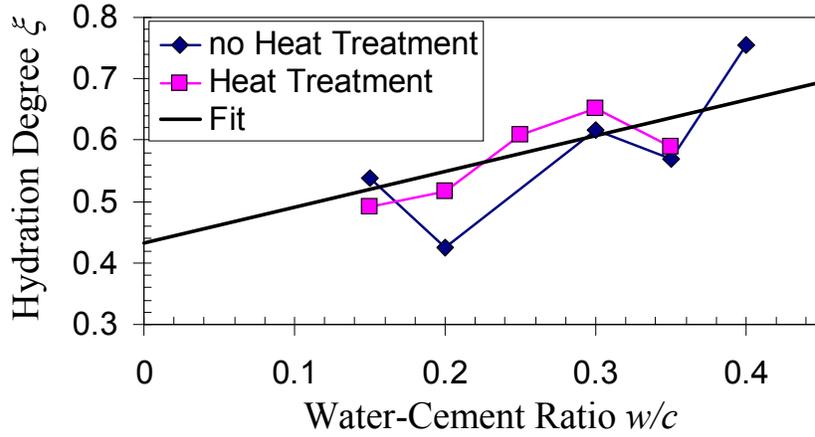
Figure 8-25: Results of the fit of the hydration degree ξ for samples without silica fumes.

heat treated samples. The result of this fit is:

$$\varphi_0 = 0.28 - a(0.442 - (w/c)) - b(SF/c)(0.400 - w/c) \tag{8.9}$$

where:

$$a = \begin{cases} 0.197 \text{ if no heat treatment} \\ 0.246 \text{ if heat treatment} \end{cases} \tag{8.10}$$

$$b = \begin{cases} 0.905 \text{ if no heat treatment} \\ 0.701 \text{ if heat treatment} \end{cases}$$

The quality of this fit can be observed on Figure 8-26.

8.5.2 Model Validation

The developed model enables to estimate, for given mix proportions (w/c, SF/c) and processing (heat treatment or no heat treatment), the volume fractions of clinker V_{CL}, of C-S-H solid $(1 - \varphi_0)V_{CSH}$, and the gel porosity $\varphi_0 V_{CSH}$. Therefore, the model can be used to estimate macroproperties. Here the model is validated by comparing the homogenized indentation modulus M^{hom} it provides with the one obtained from a grid of nanoindentations.
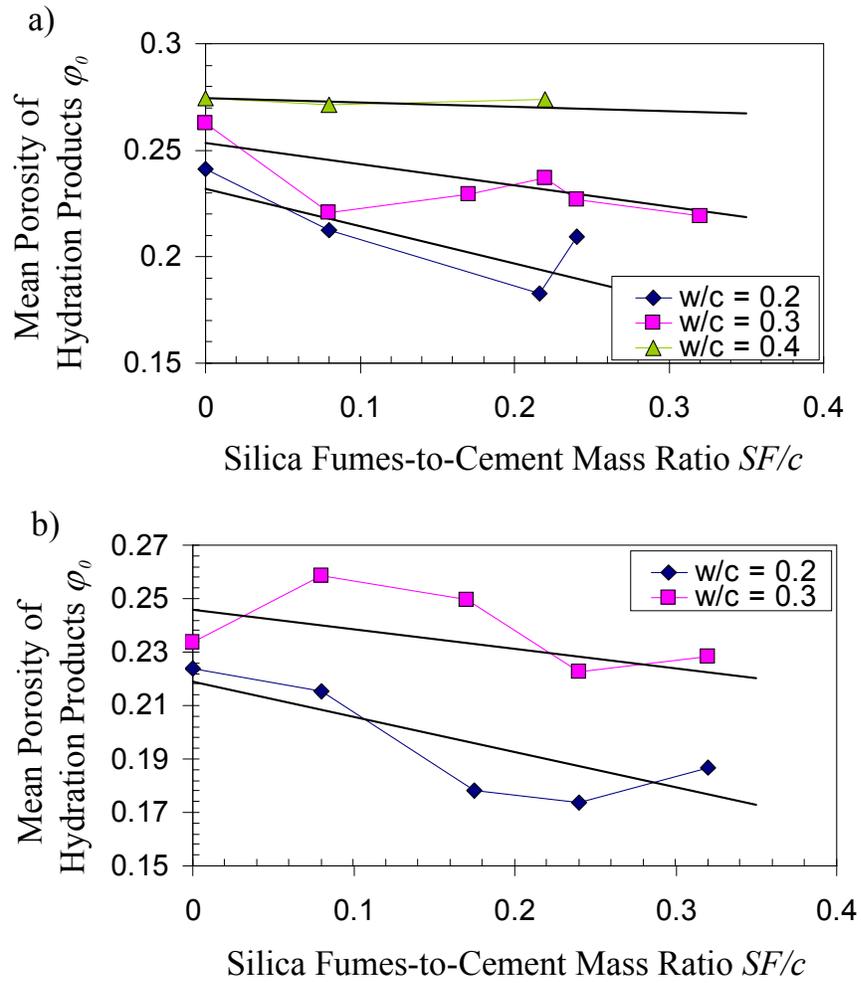
Figure 8-26: Results of the fit of the mean porosity of the hydration products ϕ_{CSH} for (a) non heat treated samples and (b) heat treated samples.

The indentation modulus m_s of the C-S-H solid being known ($m_s = 63.5$ GPa, see Section 7.4.3), the indentation modulus M_{CSH} of the C-S-H phase can be estimated with Equation (4.37):

$$M_{CSH} = m_s(1 - 2\varphi_0) \tag{8.11}$$

The clinker (of indentation modulus $M_{CL} = 135$ GPa [193]) being embedded in the hydrated matter, the homogenized indentation modulus can be estimated with a Mori-Tanaka scheme (4.29):

$$M^{\text{hom}} = \frac{V_{CSH}M_{CSH} + \dfrac{V_{CL}M_{CL}}{1 + \dfrac{1}{2}\left(\dfrac{M_{CL}}{M_{CSH}} - 1\right)}}{V_{CSH} + \dfrac{V_{CSH}}{1 + \dfrac{1}{2}\left(\dfrac{M_{CL}}{M_{CSH}} - 1\right)}} \tag{8.12}$$

A comparison of the homogenized indentation modulus M^{hom} estimated by the model developed in Section 8.5.1, with the homogenized indentation modulus M^{hom} obtained from grids of nanoindentations, for all samples with or without heat treatment and with or without silica fumes, is displayed in Figure 8-27. But for the lowest water-cement ratio considered ($w/c = 0.15$), the model developed is in excellent an agreement with experimental values, the average error on M^{hom} being only of 7.7%.

8.6   Chapter Summary

This Chapter focused on the experimental investigation of the influence of mix proportions and processing on the microstructure. Sub-stoichiometry, heat treatment, additions of silica fumes and calcareous filler were considered successively. The following mechanisms by which mix proportions and processing affect the microstructure are suggested:

- Heat treatment releases water trapped in the nanoporosity of the C-S-H nanoparticles, which then becomes available for further hydration of the remaining clinkers.

- Silica fumes do not modify the pressure dependence of the C-S-H particles but may modify their elementary cohesive bonds, thus increasing their contact hardness. In addition, silica
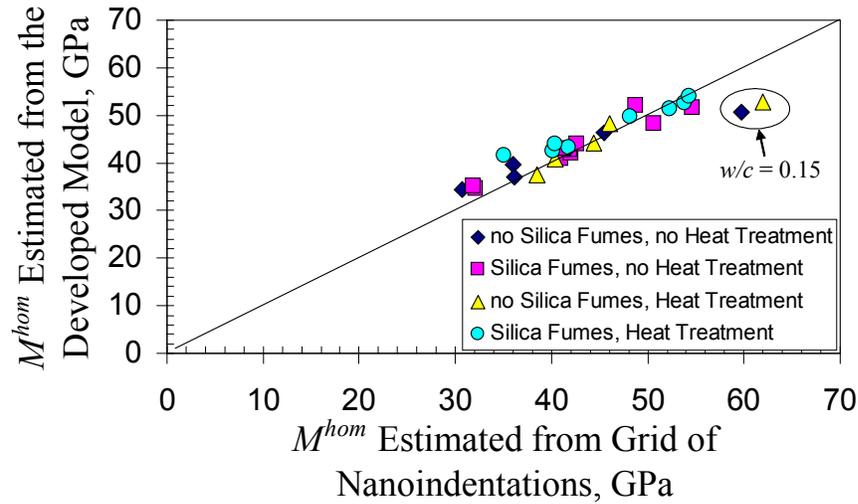
Figure 8-27: Homogenized indentation modulus predicted by the model versus homogenized indentation modulus obtained from grids of nanoindentations.

fumes produce more C-S-H by reacting with Portlandite (pozzolanic reaction).

- Calcareous filler is mostly non reactive (for the type of clinker and the amounts of filler here considered) and acts by mere mechanical reinforcement of the hydrated matter.

In addition, the experimental investigation allowed us to identify the UHD C(-S-)H phase as a mix of Portlandite (CH) and C-S-H. Finally, a predictive model was developed which enables, for given mix proportions and processing, to calculate the volume fractions of clinker and C-S-H solid, as well as the gel porosity in the paste. This model was calibrated and validated for water-cement ratios $0.2 \leq w/c \leq 0.4$, for additions of silica fumes up to 32% (in mass of clinker) and for application of a heat treatment (48-hour-long placement in an oven at $90\,^{\circ}$C at 2 days after casting).

The characterization of the microstructure was performed by assessing the elastic and strength indentation properties of the paste. Next, the investigation is extended to other mechanical properties of the paste, namely the creep properties, and the link between creep properties and microstructure is assessed.

Chapter 9

Link Between Microstructure and Creep Properties for Cementitious Materials

This Chapter carries the implementation of the Materials Science paradigm for cementitious materials further still. In contrast to Chapter 8 in which the emphasis was on the link between mix proportions and microstructure, here the emphasis is on the link between microstructure and mechanical performance. More specifically the focus of this Chapter is the experimental investigation of the link between microstructure and creep properties. The indentation analysis tools developed in Chapter 3 for the assessment of viscous properties and the statistical indentation techniques developed to probe the microstructure of cementitious materials (see Chapters 4, 5 and 7) provide a convenient framework for such an investigation.

The experimental investigation requires the statistical indentation techniques developed in Chapter 7 to be slightly modified to allow for the assessment of creep properties. Once the methods are defined the experimental results are presented. A comparison with other creep data on cementitious materials is then drawn to gain a better understanding of the significance of our results. The last Section discusses mechanisms at the origin of creep of C-S-H in the context of results from nanoindentation and macroscopic experiments on concrete and other geomaterials.

Sample Name	w/c [%]	SF/c[1] [%]	CF/c[2] [%]	Heat treatment
PC-15-0-0	15			none
PC-20-0-2	20			at 2 days
PC-20-24(SF)-0	20	24		none
PC-20-32(SF)-2	20	32		at 2 days
PC-30-0-0	30			none
PC-30-0-5	30			at 5 days
PC-30-22(SF)-0	30	22		none
PC-30-25(CF1)-0	30		25	none
PC-40-0-0	40			none

Table 9.1: List of cement pastes tested for the experimental investigation of creep properties of C-S-H.
(1) Weight of silica fumes (SF), in percent of the weight of cement.
(2) Weight of calcareous filler (CF), in percent of the weight of cement.

9.1 Materials and Methods

This Section focuses on defining the materials and methods for the experimental investigation of the creep properties of C-S-H and their link with the microstructure.

9.1.1 Materials

The experimental investigation of the creep properties will be performed on a subset of the set of samples tested for the assessment of the influence of mix proportions and processing on the microstructure (see Chapter 8). Those samples were presented in Section 7.1.1. The subset is chosen such to be representative of all possible mix proportions (w/c ratio, additions of silica fumes and calcareous filler) and processings (heat treatment). Following the denomination introduced in Section 7.1.1, the samples tested for the experimental investigation of creep properties are given in Table 9.1.

9.1.2 Methods

So that statistical indentation techniques can be used, a 20 by 20 grid of 400 Berkovich nanoindentations will be performed on each sample with the Nano-hardness tester of CSM Instruments. To ensure that, on average, each nanoindentation provides the properties of an individual phase of the paste, the maximum load $P_{\max}$ of the trapezoidal load case is fixed to $P_{\max} = 2$ mN (see Section 7.4.1).

Now the loading profile must be defined to allow the measurement of creep properties as well as the assessment of the microstructure for the nanoindentations performed on the hydration products. For creep properties to be measured, the holding phase should be reasonably long (at least a few minutes, see the conclusions of Chapter 3). In contrast, the assessment of the microstructure is based on the measurement of the indentation modulus M and the indentation hardness H (see Section 7.4.3). For the indentation hardness to be representative of the strength properties, the holding phase should be as short as possible (see Section 2.4.3). An experimental study performed in Section 7.4.1 showed that, for equal durations τ_L of the loading phase and τ_U of the unloading phase $\tau_L = \tau_U = 10$ s, the measured indentation hardness decreases by about 10% over a creep phase of 180 s, which is acceptable. Therefore the duration τ_H of the creep (holding) phase is fixed to $\tau_H = 180$ s.

From the very definition of the indentation hardness (2.57) the increase in contact radius $a(t)$ over the 180-s holding phase is estimated to about 5%, which is negligible. Therefore, for each nanoindentation the rate expression $\dot{L}(t)$ of the contact creep compliance is calculated with Equation (3.69):

$$\dot{L}(t) = \frac{2a_U \dot{h}(t)}{P_{\max}} \tag{9.1}$$

where a_U is the contact radius at the onset of unloading. a_U is calculated with the Oliver and Pharr method (see Section 2.3.2) and thus the indentation modulus M and the indentation hardness H. After integration Equation (9.1) can be rewritten as:

$$L(t) = \frac{2a_U \Delta h(t)}{P_{\max}} + c_1 \tag{9.2}$$

where $\Delta h(t)$ is the change in depth during the creep phase and c_1 is a constant.

9.2   Experimental Results

This Section presents the results of the experimental investigation of the creep behavior of C-S-H by nanoindentations and of the creep behavior's link with the microstructure.

9.2.1 Logarithmic Creep of C-S-H and Contact Creep Modulus

On average over all samples the noise in the depth measurement during the 3-minute creep phase is 0.39 nm ± 0.09 nm. The change in depth $\Delta h(t)$ over the creep phase is fit with a function of the form:

$$\Delta h(t) = x_1 \ln(x_2 t + 1) + x_3 t + x_4 \tag{9.3}$$

The fit is performed with a non linear least-squares solver in Matlab. The average error of this fit is 0.48 nm ± 0.09 nm, which is slightly above (but very close to) the noise level. Said otherwise, within the noise of the measurement, the fitted function is in almost perfect agreement with the experimental data (see Figure 9-1). The coefficient $x_4 = 1.27$ nm ±1.92 nm captures any inaccuracy in the determination of the beginning of the creep phase. The coefficient x_3 of the linear term has a correlation $R^2 = 0.0006$ with M and $R^2 = 0.0050$ with H (see Figure 9-2). From those very low coefficients of correlation we conclude that x_3 is random from one nanoindentation to the other and is not material-related. The linear term of the fitting function is thus interpreted as drift of the indentation apparatus. The only material-related term in the fitting function is the logarithmic one, from what we infer that the creep of C-S-H is logarithmic with regard to time.

The characteristic viscous time $1/x_2$ of the creep phenomenon is displayed in Figure 9-3. This characteristic time shows a weak correlation with the indentation modulus ($R^2 = 0.042$) and with the indentation hardness ($R^2 = 0.064$). The characteristic viscous time is $1/x_2 = 1.66$ s±4.76 s on average.

We also attempt a power fit of the form $\Delta h(t) = x_1 t^{x_2} + x_3 t + x_4$. Such a fit also provides very satisfactory results (see Figure 9-1), the average error 0.59 nm ± 0.25 nm being only slightly greater than that obtained with the logarithmic fit. The power exponent is $x_2 = 0.298 \pm 21.2\%$.

For a power-like time dependence of the creep phenomenon the long-term creep compliance is given by $\dot{L}(t) = bt^{x_2-1}$ and requires thus the knowledge of two parameters. In contrast, for a logarithmic time-dependence of the creep phenomenon the long-term creep compliance rate is given by

$$\dot{L}(t) = \frac{1}{Ct}; \quad \text{where: } C = \frac{M}{2a_U x_1} \tag{9.4}$$

Pmax

and requires thus the knowledge of one parameter only. By working with the logarithmic ex-
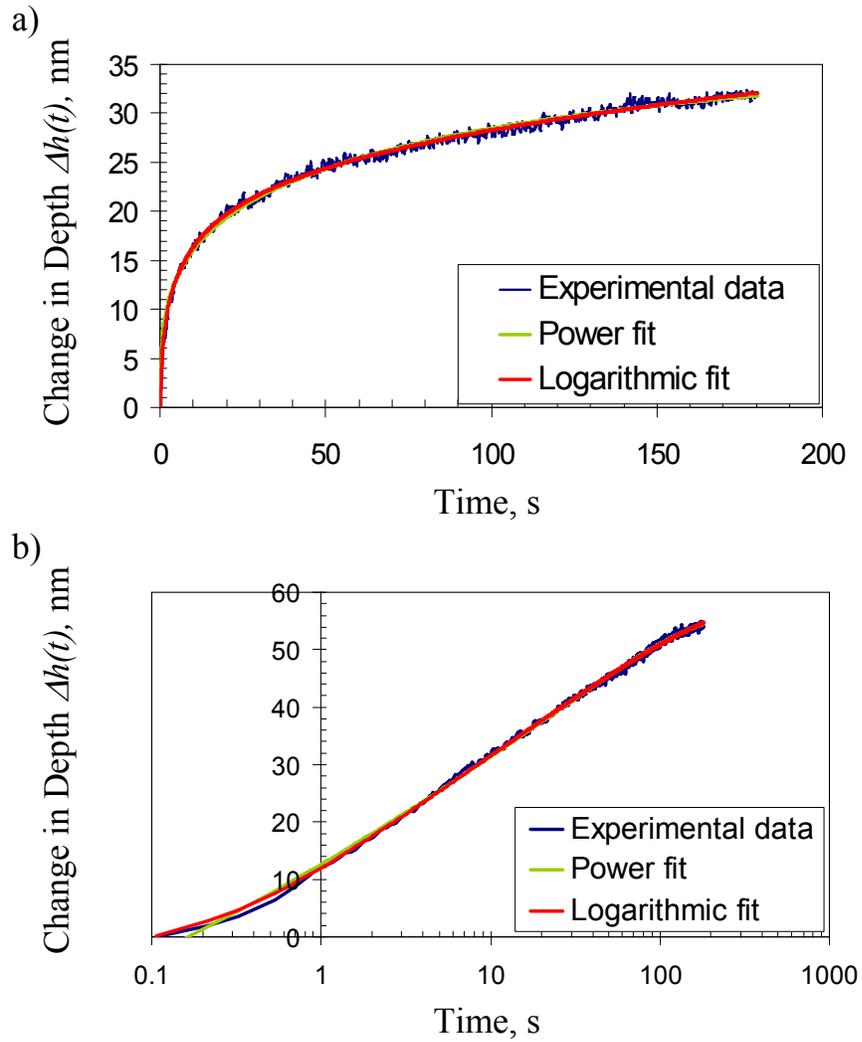
Figure 9-1: Examples of change in depth $\Delta h(t)$ versus time curve during the creep phase and corresponding logarithmic and power fits (a) on a linear scale and (b) on a logarithmic scale.
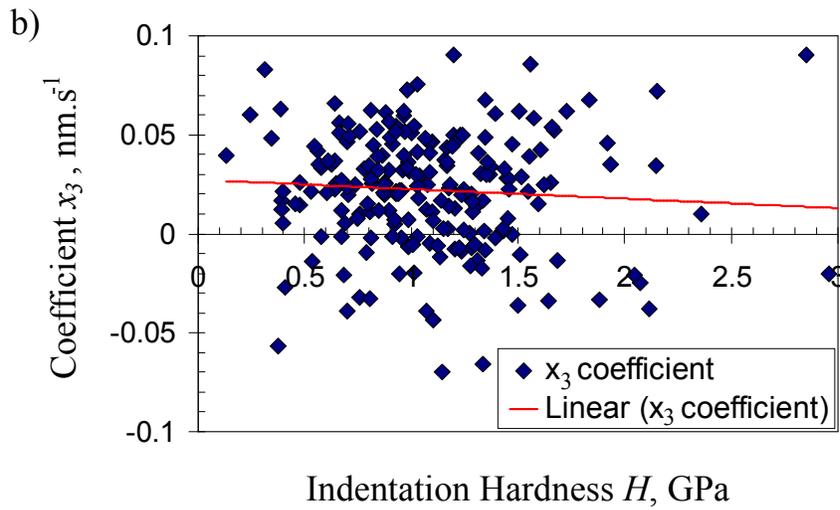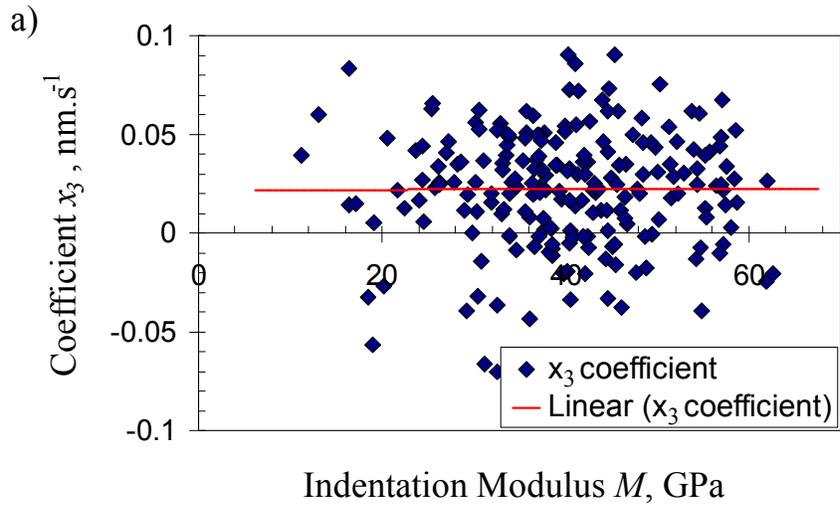
Figure 9-2: Coefficient x_3 versus (a) the indentation modulus M and (b) the indentation hardness H for sample PC-15-0-0.

a)

b)
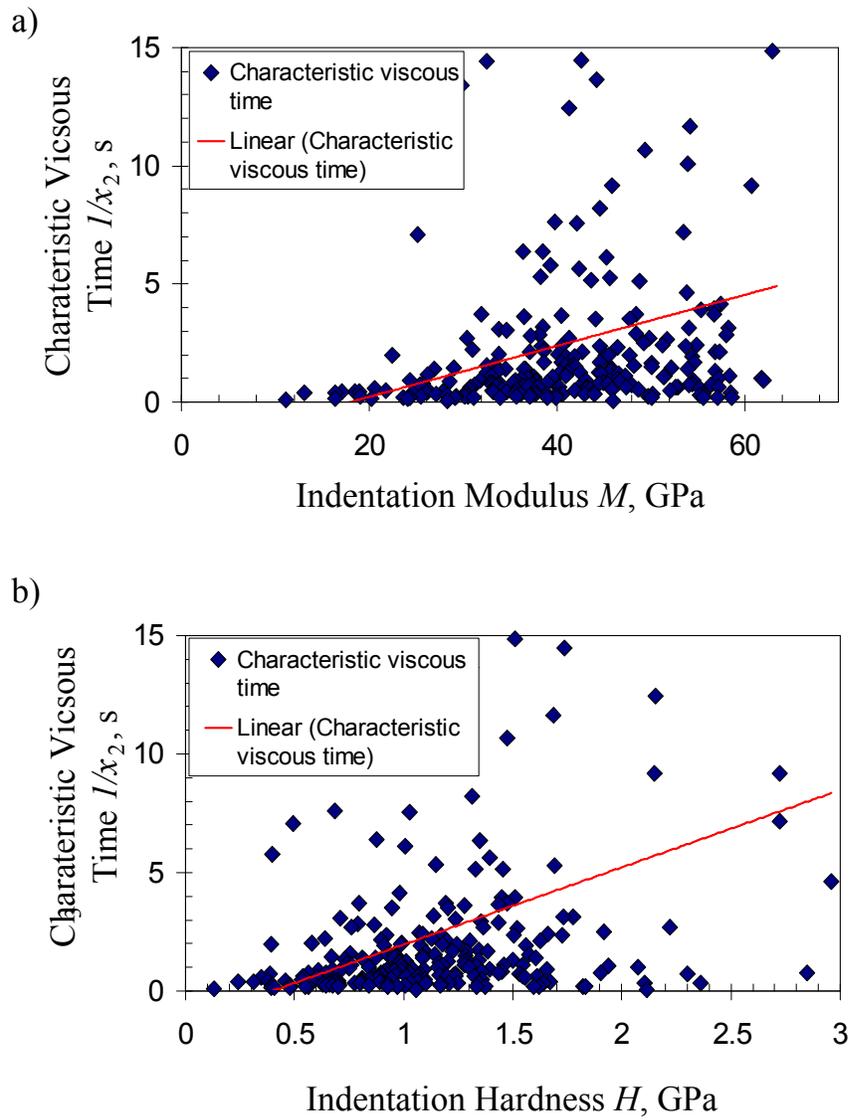
Figure 9-3: Characteristic viscous time $1/x_2$ versus (a) the indentation modulus M and (b) the indentation hardness H.

pression of the contact creep compliance, all information regarding the long-term creep behavior is therefore condensed in the parameter C only. This parameter is homogeneous to a modulus and is named the *contact creep modulus*.

9.2.2 Link Between Creep and Microstructure

This Section focuses on assessing the link between microstructure (packing density) and creep properties. In addition to the indentation modulus M and indentation hardness H each nanoindentation also provides the contact creep modulus C. Making use of the microstructure assessment technique (see Section 7.4.3) the packing density distribution in the hydration products is determined. Therefore, each nanoindentation performed on the hydration products now provides four parameters: M, H, C and η. Out of those four parameters the first three are mechanical properties of the material and one describes the microstructure.

For each tested sample, for all nanoindentations performed on the hydrated matter M, H, C and η are deconvoluted in a coupled manner (see Section 5.2.3) using a three-Gaussian deconvolution. The results of the deconvolution are given in Tables 9.2, 9.3 and 9.4. As expected the indentation moduli M, indentation hardnesses H and packing densities η of the three peaks are in good agreement with those found previously for LD C-S-H, HD C-S-H and UHD C(-S-)H. But, in addition this deconvolution now provides the contact creep modulus of each phase. LD C-S-H, HD C-S-H and UHD C-S-H have for contact creep modulus:

$$C_{LD} = 112.2 \pm 23.3 \text{ GPa} \tag{9.5}$$

$$C_{HD} = 182.5 \pm 43.7 \text{ GPa} \tag{9.6}$$

$$C_{UHD} = 342.6 \pm 85.0 \text{ GPa} \tag{9.7}$$

With a coefficient of variation less than 25% the creep modulus of the three C-S-H phases does not vary much from sample to sample.

Figure 9-4 displays the deconvoluted contact creep modulus C versus the deconvoluted indentation modulus M and hardness H. In both the $C - M$ plane and the $C - H$ plane data points align nicely along a master curve. The scaling relation between the contact creep modulus C on one hand and M and H on the other hand does not depend on the water-to-

Sample	M		H		C		η		
	m[1]	sd[2]	m[1]	sd[2]	m[1]	sd[2]	m[1]	sd[2]	$f^{[3]}$
PC-15-0-0	25.30	6.22	0.594	0.193	110.22	22.10	0.698	0.046	0.148
PC-20-0-2	N.A.	N.A.	N.A.	N.A.	N.A.	N.A.	N.A.	N.A.	0.000
PC-20-24(SF)-0	24.68	5.58	0.867	0.044	112.03	31.63	0.640	0.099	0.032
PC-20-32(SF)-2	24.81	3.68	0.678	0.250	148.61	24.89	0.709	0.021	0.110
PC-30-0-0	19.47	3.78	0.454	0.161	91.60	27.62	0.654	0.036	0.319
PC-30-0-5	21.52	3.45	0.586	0.168	134.04	26.80	0.666	0.028	0.104
PC-30-22(SF)-0	21.56	3.81	0.498	0.148	97.28	3.27	0.681	0.033	0.019
PC-30-25(CF1)-0	18.74	7.75	0.620	0.157	103.62	25.96	0.648	0.072	0.056
PC-40-0-0	23.03	4.48	0.561	0.121	100.38	24.37	0.685	0.033	0.510
average	22.39	4.84	0.607	0.155	112.22	23.33	0.673	0.046	0.162

Table 9.2: Results of the 3-peak deconvolution of the indentation modulus M, the indentation hardness H, the contact creep modulus C and the packing density η: first peak, representing the low density (LD) C-S-H phase.
(1) Mean value, in GPa.
(2) Standard deviation, in GPa.
(3) Volume fraction, no units.

Sample	M		H		C		η		
	m[1]	sd[2]	m[1]	sd[2]	m[1]	sd[2]	m[1]	sd[2]	$f^{[3]}$
PC-15-0-0	39.21	6.00	1.042	0.255	176.11	43.78	0.810	0.043	0.583
PC-20-0-2	37.15	5.40	1.067	0.219	197.32	48.15	0.798	0.041	0.688
PC-20-24(SF)-0	39.17	5.91	1.169	0.258	210.04	60.51	0.808	0.038	0.721
PC-20-32(SF)-2	37.77	5.00	1.271	0.299	225.74	52.24	0.801	0.035	0.693
PC-30-0-0	28.72	5.47	0.834	0.201	165.84	38.69	0.732	0.041	0.451
PC-30-22(SF)-0	33.65	5.73	1.035	0.223	207.32	46.49	0.769	0.041	0.652
PC-30-25(CF1)-0	31.48	5.18	0.794	0.148	132.11	31.55	0.748	0.035	0.770
PC-30-0-5	34.86	4.67	0.966	0.189	166.55	35.77	0.773	0.032	0.514
PC-40-0-0	31.35	3.84	0.812	0.131	161.26	36.52	0.744	0.026	0.299
average	34.82	5.25	0.999	0.214	182.48	43.74	0.776	0.037	0.597

Table 9.3: Results of the 3-peak deconvolution of the indentation modulus M, the indentation hardness H, the contact creep modulus C and the packing density η : second peak, representing the high density (HD) C-S-H phase.
(1) Mean value, in GPa.
(2) Standard deviation, in GPa.
(3) Volume fraction, no units.

Sample	M		H		C		η		
	m[1]	sd[2]	m[1]	sd[2]	m[1]	sd[2]	m[1]	sd[2]	f[3]
PC-15-0-0	53.84	5.48	1.667	0.370	341.55	92.00	0.898	0.045	0.269
PC-20-0-2	50.87	5.66	1.643	0.357	344.55	91.25	0.886	0.047	0.311
PC-20-24(SF)-0	50.48	5.40	1.944	0.455	416.50	80.20	0.893	0.047	0.247
PC-20-32(SF)-2	49.79	7.02	2.014	0.445	414.37	70.23	0.876	0.041	0.197
PC-30-0-0	43.13	8.31	1.393	0.334	318.69	81.37	0.816	0.043	0.230
PC-30-22(SF)-0	46.97	7.60	1.696	0.439	359.57	55.55	0.860	0.050	0.245
PC-30-25(CF1)-0	44.39	7.73	1.354	0.391	258.98	65.62	0.841	0.058	0.210
PC-30-0-5	45.57	6.04	1.533	0.325	286.19	83.87	0.861	0.040	0.430
PC-40-0-0	42.77	6.45	1.379	0.257	343.14	145.36	0.834	0.040	0.191
average	47.53	6.63	1.625	0.375	342.61	85.05	0.863	0.046	0.259

Table 9.4: Results of the 3-peak deconvolution of the indentation modulus M, the indentation hardness H, the contact creep modulus C and the packing density η: third peak, representing the ultra-high density (UHD) C-(S-)H phase.
(1) Mean value, in GPa.
(2) Standard deviation, in GPa.
(3) Volume fraction, no units.

cement ratio, w/c, heat treatment or admixtures. Fitting a power function to the C versus M relation yields $C = 1.355M^{1.410}$ (where both C and M are expressed in GPa) with a correlation $R^2 = 0.889$. Fitting a power function to the M versus C relation yields a slightly different relation $C = 0.7302M^{1.5858}$ (where both C and M are expressed in GPa) with the same correlation $R^2 = 0.889$. Interestingly, a linear scaling is found between the contact creep compliance and the indentation hardness: $C = 200.8H$ with a correlation $R^2 = 0.936$.

Reworking the data in the $C - \eta$ plane yields Figure 9-5. The contact creep modulus C scales in a unique manner with the packing density η. A power function fit to the data yields $C = 1128.5(\eta - 0.5)^{1.378}$ where C is expressed in GPa. Fitting a power function to the $\eta - 0.5$ versus C relation yields a slightly different relation $C = 1588.9(\eta - 0.5)^{1.597}$. The unique scaling between contact creep modulus and packing density proves that the creep behavior the hydrated phase of cementitious materials is fully determined by its packing density. Mix design has an influence on the packing density distribution but has no influence on the scaling between contact creep modulus and packing density.
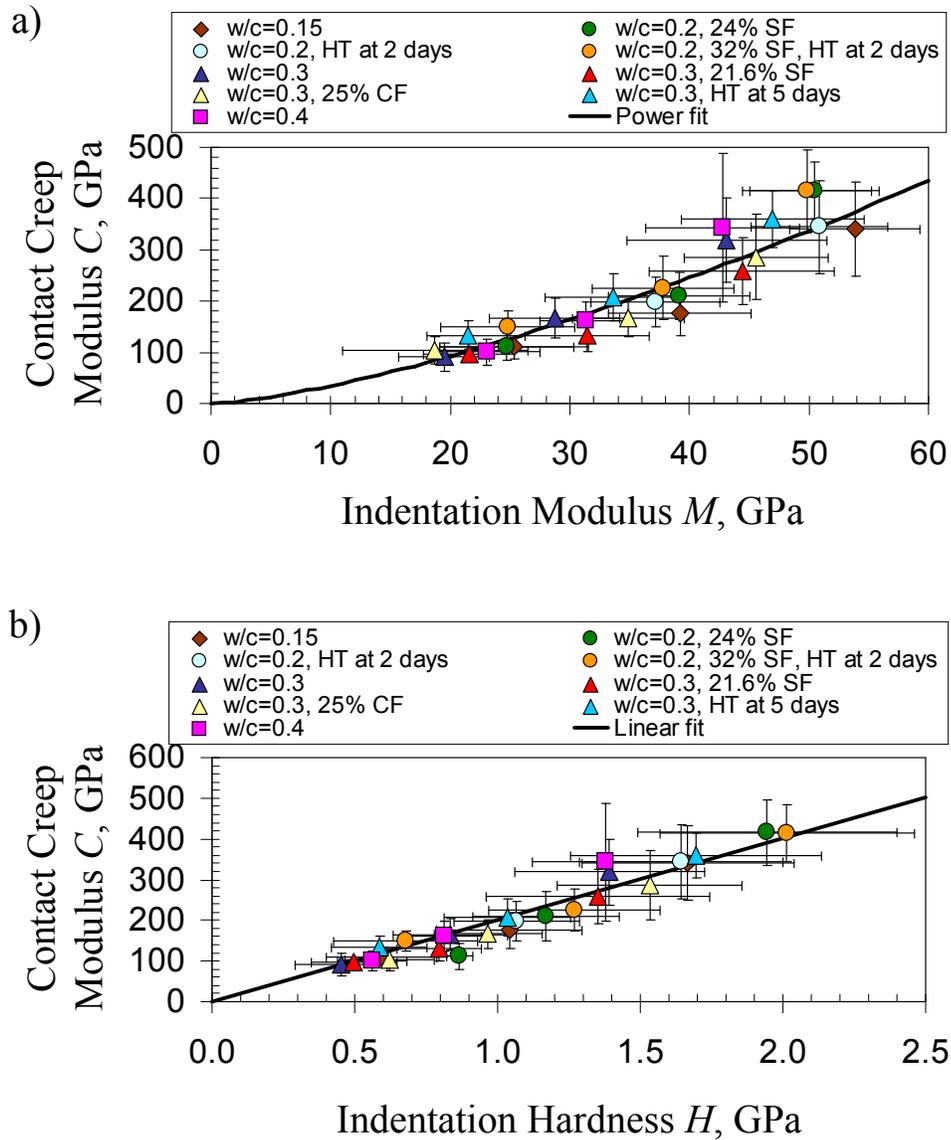
Figure 9-4: Deconvoluted indentation creep modulus C (a) versus the deconvoluted indentation modulus M and (b) versus the deconvoluted indentation hardness H for indents performed on the products of hydration.
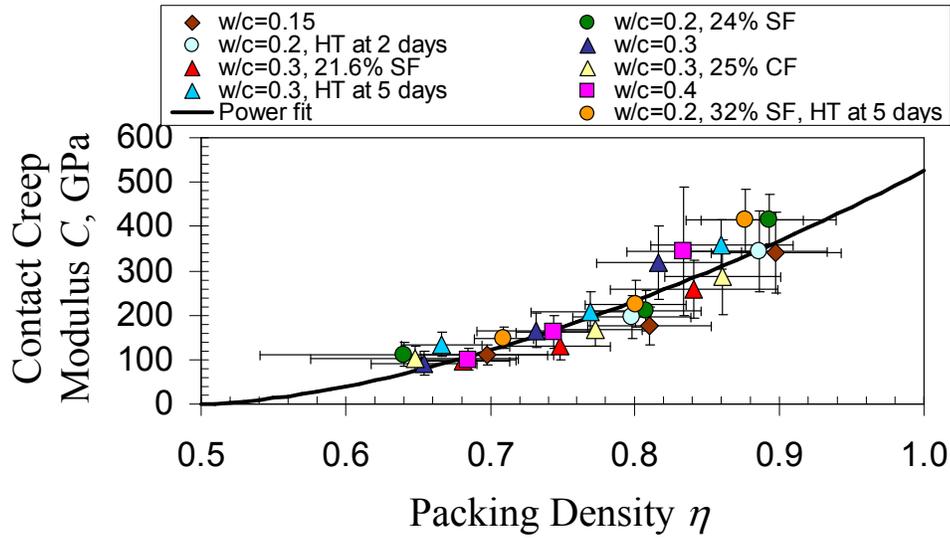
Figure 9-5: Deconvoluted contact creep modulus C versus deconvoluted packing density η.

9.3 Discussion: Comparison with Other Creep Data

This Section discusses the results of the experimental investigation with respect to results gathered with another geometry of indenter, at another indentation load, or at another scale.

9.3.1 Creep Data from Cube Corner Indentation

In this Section we verify whether the creep behavior of C-S-H is linear with regard to the applied stress by using an indenter probe of different geometry. If the creep behavior is linear with regard to stresses (which was indeed assumed for all derivations in Chapter 3) the measured creep properties should not depend on the shape of the indenter (see Chapter 3). A Cube Corner indenter (equivalent half-cone angle $\theta = 42.24^o$) is much sharper than a Berkovich indenter. Although the stresses below a conical indenter are not homogeneous, Tabor [174] showed that it is possible to introduce a 'representative strain' characterizing the strain distributions in the indented material. Whereas the representative strain below a Berkovich indenter is of 10%, the representative strain below a Cube Corner indenter is of 25% [6]. Therefore, below a Berkovich and a Cube Corner probe the material is solicited at two very different strain levels.

Grids of nanoindentations are performed on samples PC-20-24(SF)-2, PC-20-32(SF)-2 and

PC-30-0-5 with a Cube Corner indenter. The maximum load is $P_{\max} = 0.5$ mN so that the maximum depths $h_{\max} \simeq 260$ nm ± 90 nm are close to those obtained with $P_{\max} = 2$ mN for Berkovich indentation. The issue with an indenter as sharp as a Cube Corner is that the material 'piles-up', which leads to an erroneous estimation of the projected area of contact by the Oliver and Pharr method (see Section 2.3.2). Consequently, a direct application of the Oliver and Pharr method yields an erroneous contact radius a^{meas}, which leads to an erroneous determination of indentation modulus M^{meas}, indentation hardness H^{meas} and contact creep modulus C^{meas}. For geomaterials, however, Constantinides and Ulm [57] showed that if the contact radius is correctly measured (e.g., optically for deep indents) the indentation modulus measured by Berkovich and Cube Corner indentation are identical. Since the indentation moduli M^{Berk} obtained by Berkovich indentation are known for the individual hydration products from Tables 9.2, 9.3 and 9.4, the correct contact radius a^{CC} for Cube Corner indentation can be estimated:

$$a^{CC} = a^{meas} \frac{M^{meas}}{M^{Berk}} \tag{9.8}$$

from which the correct indentation modulus M^{CC}, indentation hardness H^{CC} and contact creep modulus C^{CC} for Cube Corner indentation can be obtained:

$$M^{CC} = M^{Berk} \tag{9.9}$$

$$H^{CC} = H^{Berk} \left(\frac{M^{Berk}}{M^{CC}} \right)^2 \tag{9.10}$$

$$C^{CC} = C^{Berk} \frac{M^{Berk}}{M^{CC}} \tag{9.11}$$

The deconvoluted mechanical properties, corrected for the wrongly estimated projected area of contact with the two equations above, are given in Table 9.5 and displayed in Figure 9-6 together with the scaling relations obtained in Section 9.2.2 for grids performed with a Berkovich indenter at $P_{\max} = 2$ mN. The best power fit of the C versus M relation is $C = 0.841 M^{1.380}$ (where C and M are expressed in GPa) with a correlation $R^2 = 0.736$. The best linear fit of the C versus H relation is $C = 91.4H$ with a correlation $R^2 = 0.897$.

From a qualitative point of view creep data gathered with a Cube Corner probe and with a Berkovich probe are in perfect agreement. For both indenter probes C scales linearly with

303

a)

b)
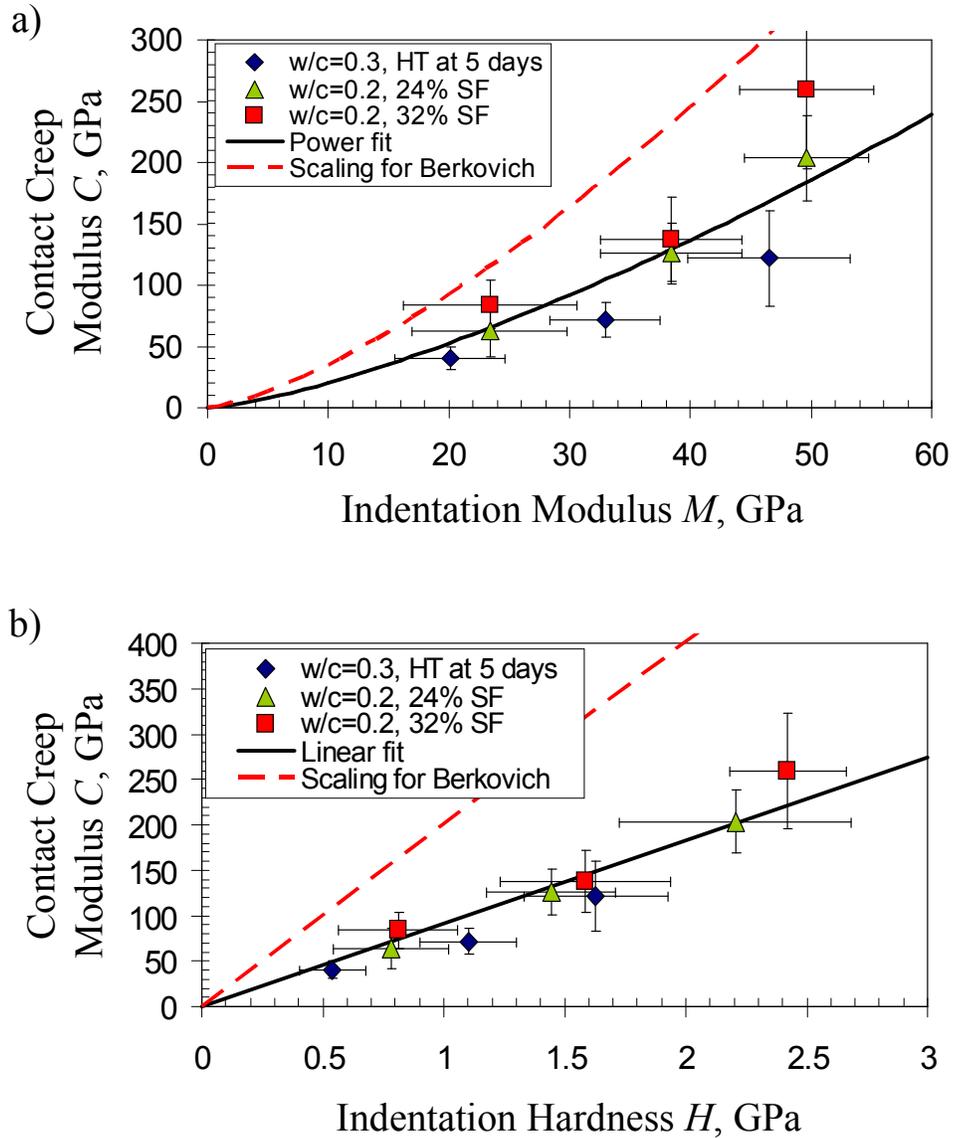
Figure 9-6: Deconvoluted contact creep modulus C (a) versus the deconvoluted indentation modulus M and (b) versus the deconvoluted indentation hardness H obtained from indents performed on the products of hydration with a Cube Corner indenter. The scalings obtained with a Berkovich indenter at $P_{\max} = 2$ mN also are displayed on the figure (dashed red lines).

		PC-20-24(SF)-2			PC-20-32(SF)-2			PC-30-0-5		
		Peak 1	Peak 2	Peak 3	Peak 1	Peak 2	Peak 3	Peak 1	Peak 2	Peak 3
M	m[1]	23.41	38.45	49.65	23.41	38.45	49.65	20.09	32.96	46.51
	sd[2]	7.21	5.83	5.55	6.41	5.84	5.14	4.56	4.59	6.74
H	m[1]	0.812	1.586	2.421	0.784	1.443	2.205	0.541	1.102	1.629
	sd[2]	0.245	0.353	0.242	0.238	0.265	0.480	0.139	0.201	0.297
C	m[1]	84.24	137.6	259.3	63.13	125.8	203.6	40.62	71.28	121.80
	sd[2]	19.85	34.59	64.20	22.18	24.69	35.07	9.06	14.10	38.56
	f	0.120	0.685	0.195	0.076	0.613	0.310	0.347	0.429	0.224

Table 9.5: Results of the 3-peak deconvolution obtained for grids performed at $P_{max} = 0.5$ mN with a Cube Corner indenter.
(1) Mean value, in GPa.
(2) Standard deviation, in GPa.
(3) Volume fraction, no units.

H and the exponent of the power $C - M$ relation is the same. From a quantitative point of view the creep data gathered at the two maximum loads differ from each other. For a given indentation hardness H the measured contact creep modulus C is about 55% smaller with a Cube Corner indenter than with a Berkovich indenter. For a given indentation modulus M the measured contact creep modulus C is about 40% smaller with a Cube Corner indenter than with a Berkovich indenter. In the case of an indentation exhibiting a lot of plasticity (which is the case with Cube Corner indentation) instantaneous plasticity may occur during the creep phase and lead to an overestimation of the creep behavior and to an underestimation of the contact creep modulus (see Section 3.3.3). As noted in Section 3.3.3, this underestimation is more pronounced with a Cube Corner probe than with a Berkovich probe, which may explain the discrepancy observed between creep data gathered with the two different probes. Therefore the comparison with Cube Corner indentation is rather inconclusive with regard to the linearity (with respect to stresses) of the creep behavior.

9.3.2 Creep Data from Berkovich Indentation at $P_{\max} = 100$ mN

In contrast, the linearity of the creep behavior with regard to the applied stress may be checked by changing not the indenter probe but the indentation load. This check is the focus of this Section. Here the creep properties are measured with a grid of Berkovich indentations performed at $P_{\max} = 100$ mN on samples PC-15-0-0, PC-20-0-2 and PC-30-0-0. For a maximum load

		PC-15-0-0		PC-20-0-2		PC-30-0-0	
		Peak 1	Peak 2	Peak 1	Peak 2	Peak 1	Peak 2
M	m$^{(1)}$	44.95	52.79	41.61	49.40	24.47	30.22
	sd$^{(2)}$	3.51	2.96	4.03	3.76	2.38	2.93
H	m$^{(1)}$	1.178	1.598	1.172	1.741	0.541	0.843
	sd$^{(2)}$	0.221	0.199	0.239	0.261	0.119	0.183
C	m$^{(1)}$	365.91	499.62	326.20	506.49	162.11	255.30
	sd$^{(2)}$	57.08	75.30	65.22	89.37	32.30	41.11
	f	0.462	0.372	0.664	0.301	0.467	0.341

Table 9.6: Results of the 3-peak deconvolution obtained for grids performed at $P_{max} = 100$ mN.
(1) Mean value, in GPa.
(2) Standard deviation, in GPa.
(3) Volume fraction, no units.

$P_{\max} = 100$ mN the maximum indentation depth ($h_{\max} \sim 2020$ nm ± 440 nm) no longer satisfies the scale separability conditions (4.1). The deconvoluted properties are not representative of an individual product of hydration but are instead a composite response of the products of hydration. The deconvoluted properties of the first two peaks are given in Table 9.6 and displayed in Figure 9-7 together with the scaling relations obtained in Section 9.2.2 for grids performed at $P_{\max} = 2$ mN. The best power fit of the C versus M relation is $C = 1.901 M^{1.404}$ (where C and M are expressed in GPa) with a correlation $R^2 = 0.955$. The best linear fit of the C versus H relation is $C = 299.1 H$ with a correlation $R^2 = 0.984$.

From a qualitative point of view creep data gathered at $P_{\max} = 2$ mN and at $P_{\max} = 100$ mN are in perfect agreement. For both maximum loads C scales linearly with H and the exponent of the power $C - M$ relation is the same. From a quantitative point of view the creep data gathered at the two maximum loads differ from each other slightly. For a given indentation hardness H the measured contact creep modulus C is about 30% smaller at $P_{\max} = 2$ mN than at $P_{\max} = 100$ mN. For a given indentation modulus M the measured contact creep modulus C is about 20% smaller at $P_{\max} = 2$ mN than at $P_{\max} = 100$ mN. Although the agreement is not perfect it remains quite remarkable given that the maximum load $P_{\max}$ was multiplied by 50! Therefore the assumption of linearity of the creep behavior with regard to the applied stresses is reasonable.

Further increasing the maximum load, up to the microindentation level, will provide the
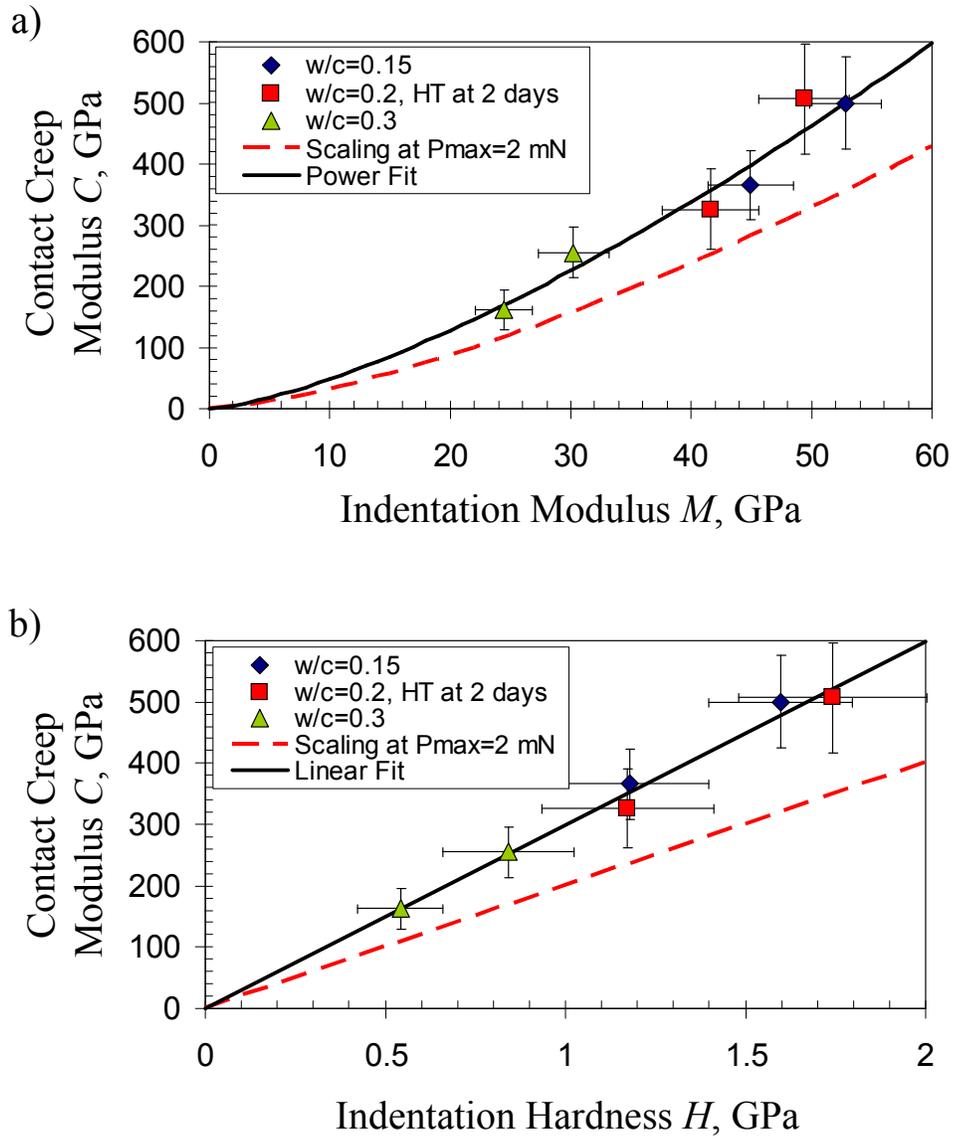
Figure 9-7: Deconvoluted contact creep modulus C (a) versus the deconvoluted indentation modulus M and (b) versus the deconvoluted indentation hardness H obtained from indents performed on the products of hydration at $P_{\max} = 100$ mN. The scalings obtained at $P_{\max} = 2$ mN also are displayed on the figure (dashed red lines).

		PC-15-0-0	PC-30-0-0	PC-40-0-0	Error[4], %
Contact	Measured from microindentations	404.0±38.6	177.9±11.5	126.4±10.6	N.A.
Creep	Homogenized from nano $C^{(1)}$	282.2	199.9	165.1	24.4
Modulus	Homogenized from nano $H^{(2)}$	371.3	207.6	164.9	18.4
C^{micro}, GPa	Homogenized from nano $M^{(3)}$	420.6	192.3	157.0	12.1

Table 9.7: Microscopic indentation creep modulus C (in GPa) measured by microindentations and homogenized from grids of nanoindentations.
(1) The homogenized C is calculated from the indentation creep moduli measured by nanoindentations.
(2) The homogenized C is calculated from the indentation hardnesses H measured by nanoindentations and converted into indentation creep moduli.
(3) The homogenized C is calculated from the indentation moduli M measured by nanoindentations and converted into indentation creep moduli.
(4) The error is the relative error with respect to the creep modulus measured from microindentations, averaged over the three samples.

homogeneous creep response of the paste.

9.3.3 Microindentations on Cement Paste

This Section aims to validate the homogenization procedure developed in Section 5.3.3 for heterogeneous solids with logarithmic creep by comparing estimates of homogenized contact creep moduli with experimental data from microindentation. On three samples (PC-15-0-0, PC-30-0-0 and PC-40-0-0) 50 microindentations are performed (at $P_{\max} = 8$ N) with a creep phase of duration $\tau_H = 180$ s. The microindentations probe the material at a homogeneous level, as can be observed from the low coefficient of variations (less than 10% for all samples) of the measured contact creep moduli C^{micro} (see Table 9.7).

Following the homogenization procedure described in Section 5.3.3 the homogenized contact creep modulus C^{micro} can be estimated from the 400 contact creep moduli $\{C_i\}_{i=1..400}$ measured by a grid of nanoindentations with Equation (5.56):

$$\sum_{i=1}^{N} \frac{1}{1 + \frac{1}{2}(C_i/C^{micro} - 1)} = \sum_{i=1}^{N} \frac{C_i/C^{micro}}{1 + \frac{1}{2}(C_i/C^{micro} - 1)} \qquad (9.12)$$

The results of this calculation are given in Table 9.7. On average for the three samples the difference between the contact creep modulus measured by microindentation and that homog-

enized from a grid of nanoindentations is of 24.4%. Although not perfect, the agreement is reasonable.

A candidate for the discrepancy could simply be noise in the measured $\{C_i\}_{i=1..400}$ at the scale of the nanoindentations. We test this hypothesis by making use of the correlation between contact creep modulus and indentation modulus or hardness. Instead of homogenizing $\{C_i\}_{i=1..400}$ directly we aim to convert the measured $\{M_i\}_{i=1..400}$ and $\{H_i\}_{i=1..400}$ into contact creep moduli and then homogenize them. To do so, the C versus M and C versus H relations, which are known for the products of hydration only (see Section 9.2.2), need to be extended. From a 4-Gaussian deconvolution of all nanoindentations of a grid of nanoindentations Figure 9-8 shows that even for non hydrated matter the contact creep modulus is strongly correlated with indentation modulus and indentation hardness. The scaling relations derived for hydration products in Section 9.2.2 are extended above $M = 63.5$ GPa and $H = 3$ GPa. The contact creep modulus C_i can be calculated from the indentation modulus M_i with:

$$\begin{cases} C_i = 0.730 M_i^{1.586} \text{ if } M_i < 63.5 \text{ GPa} \\ C_i = 8.790 M_i - 30.54 \text{ if } M_i > 63.5 \text{ GPa} \end{cases} \qquad (9.13)$$

and from the indentation hardness H_i with:

$$\begin{cases} C_i = 200.8 H_i \text{ if } H_i < 3 \text{ GPa} \\ C_i = 99.50 H_i + 304.0 \text{ if } H_i > 3 \text{ GPa} \end{cases} \qquad (9.14)$$

For the three samples of interest in this Section (PC-15-0-0, PC-30-0-0 and PC-40-0-0), from the measured indentation hardnesses $\{H_i\}_{i=1..400}$ and Equation (9.14) the indentation creep moduli $\{C_i\}_{i=1..400}$ are calculated and then homogenized (see Table 9.7). The same process is repeated with the indentation moduli $\{M_i\}_{i=1..400}$ and Equation (9.13) (see Table 9.7). The so obtained homogenized contact creep moduli C^{micro} compare much better with the indentation creep moduli measured by microindentations. When basing the study on the indentation modulus especially, on average over the three samples the relative difference is of only 12.1%, which is very satisfactory. This observation suggests that the discrepancy observed when homogenizing directly the measured contact creep moduli $\{C_i\}_{i=1..400}$ may mostly be due to noise in the measurement of $\{C_i\}_{i=1..400}$. In addition it validates the homogenization
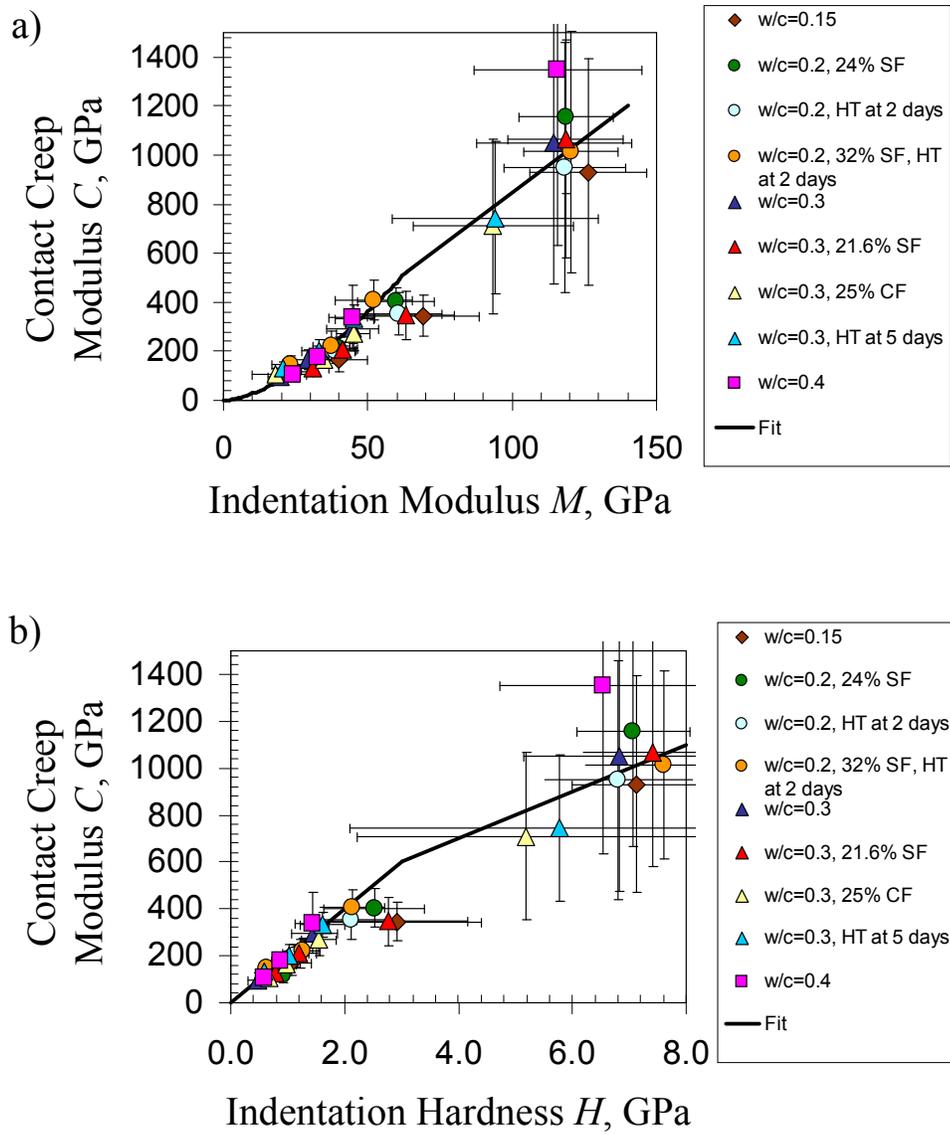
Figure 9-8: Deconvoluted contact creep modulus C (a) versus the deconvoluted indentation modulus M and (b) versus the deconvoluted indentation hardness H obtained from indentation grids performed with a Berkovich indenter at $P_{\max} = 2$ mN. The fits up to $M = 63.5$ GPa and $H = 3$ GPa are the fits obtained on the products of hydration in Section 9.2.2.

procedure developed in Section 5.3.3 for creep properties.

9.3.4 Comparison with Macroscopic Creep of Concrete

Cementitious materials in general and concrete in particular have been the subject of extensive macroscopic testing of their creep behavior. Therefore a discussion of our nanoindentation results with respect to the macroscopic creep of concrete may prove instructive.

Qualitative Comparison

Creep experiments on concrete are often performed for several months to several years. The total creep deformation is usually divided among two contributions which are termed the basic creep and drying creep. Basic creep occurs under conditions of no moisture exchange with the ambient medium, i.e., at hygral equilibrium [132]. Any additional deformation to basic creep is said to be drying creep. Given the characteristic size (on the order of the micron) of the volume of material probed by each nanoindentation, this volume is at hygral equilibrium and we expect nanoindentation testing to provide the basic creep of the indented phase.

Relative humidity has an influence on the basic creep [132]. Different relative humidities imply different moisture contents within the paste, with different continued hydration kinetics as a consequence. Since the creep behavior depends on the structure of the cement and therefore on the hydration degree, the relative humidity has an influence through the differences in aging of the paste. In the long term the rate of the basic creep does not depend on the relative humidity, as can be observed in Figure 9-9. In indentation testing the duration of the creep tests is on the order of the minute, i.e., much shorter than the characteristic time of the process of hydration. Therefore the aging of the paste during an indentation creep experiment is negligible.

The kinetics of the creep of concrete can be divided among a short-term and a long-term regime. Since a long-term creep behavior has been identified the question of its dependence with respect to time has been asked. There is no experimental evidence that the creep behavior reaches an asymptote over time [132], and it is generally believed that concrete creeps with no limiting value. Two functions (and many variations of them) which capture an asymptote-free behavior are usually proposed for concrete:

- The first proposed function is a power function of time, in which the creep deformation
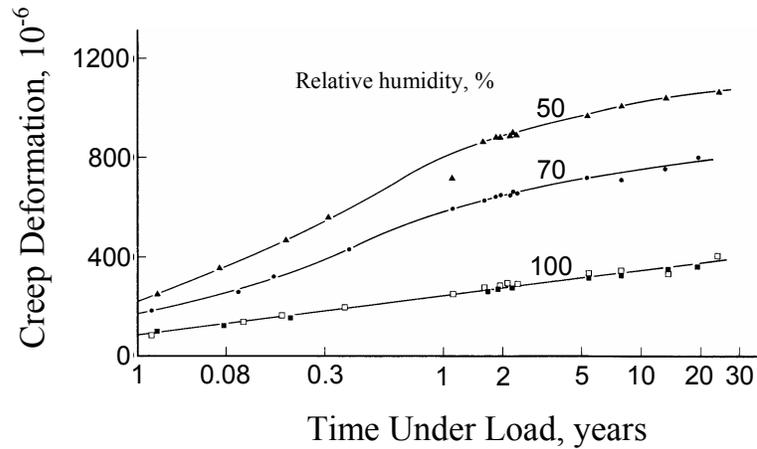
Figure 9-9: Influence of relative humidity of storage on creep of concrete cylinders (100 x 150 mm) moist-cured for 28 days and then loaded at the humidity indicated (adapted from [132]). We note that from the age of about one year the curves are parallel to each other.

$c(t)$ is proportional to t^α [171]. The power function appears to be the best equation to fit many sets of data although it generally overestimates the creep deformations at large times.

- The second proposed function is a logarithmic function of time, in which the creep deformation $c(t)$ is proportional to $\ln(t/\tau)$ [188] [11]. Although the logarithmic function does not capture well the short-term creep behavior it captures well the long-term behavior, as can be observed in Figure 9-10. This observation suggests the surprising result that creep testing by nanoindentation may give access in a minute-long test to the long-term creep behavior of concrete. This suggestion is verified in a more quantitative manner in the next Section.

Quantitative Comparison

The creep experiments performed on concrete by Le Roy [113], which are displayed in Figure 9-10, are here considered. Those experiments exhibit a clear logarithmic dependence. The tested concrete was made up of 71.5% of granulates (in volume of concrete) and of a cement with water-cement ratio $w/c = 0.33$ and 10% of silica fumes added [113]. The creep experiments

312
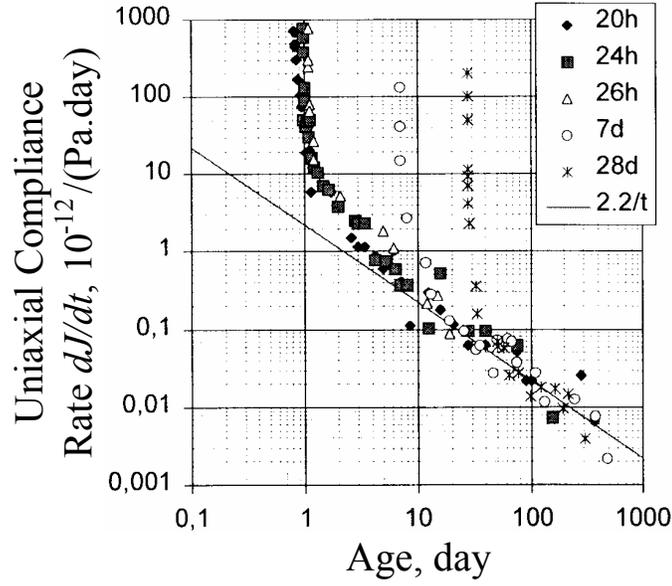
Figure 9-10: Logarithmic time-dependence of the creep behavior of concrete samples loaded at different ages (adapted from [186]). The experiments were performed by Le Roy [113].

were run for up to a few years. The samples were cylinders of 16 cm in diameter and 1 meter in length, protected from hygral exchanges with the surrounding environment and tested in uniaxial compression. The uniaxial creep modulus $C^{uni} = tdJ/dt$ of the creep experiment performed on the concrete can easily be calculated from Figure 9-10: $C^{uni} = 455$ GPa.

We perform a grid of nanoindentations on sample PC-30-8(SF)-0 which has mix proportions close to those of the cement paste of the concrete tested by Le Roy. For sample PC-30-8(SF)-0, from the measured indentation moduli $\{M_i\}_{i=1..400}$ and by using Equations (9.13) and (5.56) we calculate a homogenized contact creep modulus C^{micro} of the paste $C^{micro} = 240$ GPa.

At the scale above the concrete has a clear matrix-inclusion morphology (see Section 6.2). The granulates do not creep. The granulates (volume fraction $f_2 = 0.715$ and contact creep modulus $C_2 = +\infty$) being embedded in the cement paste (volume fraction $f_1 = 0.285$ and contact creep modulus $C_1 = C^{micro}$) the macroscopic contact creep modulus C^{macro} can be estimated by a Mori-Tanaka scheme (see Section 5.3.3):

$$C^{macro} = \frac{\displaystyle\sum_{i=1}^{2} \frac{f_i C_i}{1 + \frac{1}{2}(\frac{C_i}{C_1} - 1)}}{\displaystyle\sum_{i=1}^{2} \frac{f_i}{1 + \frac{1}{2}(\frac{C_i}{C_1} - 1)}} = C^{micro} \left(1 + 2\frac{f_2}{f_1}\right) \qquad (9.15)$$

from which expression is found $C^{macro} = 1445$ GPa$\simeq 3C^{uni}$. Said otherwise, we estimate a contact creep modulus about 3 times as great as the measured uniaxial creep modulus of the concrete. This proportionality factor of 3 may not be a coincidence. Indeed, contact creep modulus and indentation hardness are strongly correlated (see Section 9.2.2). Therefore, by analogy with Tabor's law (2.58) which stipulates that the indentation hardness is about three times as great as the uniaxial compressive strength, it is not that surprising for the contact creep modulus to be about three times as great as the uniaxial creep modulus.

Nanoindentation creep experiments yield results which compare well with macroscopic creep experiments. The observed logarithmic dependence of macroscopic creep tests (see Section 9.3.4) proves that the creep assessed by nanoindentation is indeed the long-term creep of concrete. Each nanoindentation probes a micrometer-sized volume of material, the creep phase being on the order of a minute. In comparison, meter-sized concrete samples are tested for up to three years. In length as in time, measuring the long-term creep behavior of cementitious materials by nanoindentation instead of macroscopically enables to gain not less than 6 orders of magnitude!

9.4   Speculations on Origin of Creep of C-S-H

Numerous mechanisms were proposed to explain the creep behavior of cementitious materials. To explain the short-term creep various models involve migration of water (seepage theory [150]), densification and ordering due to gradual crystallization (interlayer theory [74]), increase in the rate of hydration under stress [82], stress redistribution consecutive to the formation of new hydrates (solidification theory [13] [14]) or thermally activated processes (thermal activation theory [197]). Regarding the long-term creep behavior the proposed mechanisms are mostly mechanical and involve the shear of C-S-H layers [156] or the relaxation of micro-prestresses

[12].

In Section 9.2 we identified a logarithmic creep of C-S-H as well as scaling relations of the contact creep modulus C with the indentation modulus M or the indentation hardness H. Do those results provide or confirm information regarding the C-S-H microstructure?

9.4.1 Does C-S-H Solid Creep?

In this Section the question addressed is whether the C-S-H solid creeps. The question is addressed by hypothesis testing by assuming that the C-S-H solid does indeed creep. Such a hypothesis (a composite C-S-H phase made of a creeping C-S-H solid and pores) was in fact considered in Section 4.4, in which the link between the C-S-H solid creep properties and those of the solid-pore composite was derived. We recall that for any morphology the parameter which governs the amplitude of the creep scales almost linearly with the indentation modulus of the C-S-H phase. A time-dependent Poisson's ratio (case of a deviatoric creep in Section 4.4) may create a slight non-linearity of this scaling but this non-linearity is almost negligible.

Therefore the pronounced non-linearity of the contact creep modulus C versus indentation modulus M scaling relation, which we observe experimentally (see Section 9.2.2), implies that the mechanism of creep deformation of the C-S-H phases is not the deformation of the C-S-H solid particles in their bulk.

9.4.2 Comparison with Geomaterials

Here we compare the creep behavior of C-S-H with the creep behavior of geomaterials such as clay, sandstone, and sand. The reason for attempting such a comparison is that C-S-H and geomaterials are all natural composites with a (more or less) disordered heterogeneous assembly.

In geotechnical engineering the creep of geomaterials is measured by oedometer testing (see Figure 9-11). It is widely admitted in the geotechnical community that all geomaterials creep logarithmically with respect to time [108]. In oedometer testing the tested sample is cylindrical, of horizontal circular cross-section A. The sample is surrounded by a ring which prevents any lateral deformation (see Figure 9-11). A vertical load F is applied to the loading cap. The displacement h of the loading cap (and thus the vertical strain ε_v of the sample) is measured over time. Although the boundary conditions on the side of the sample are different,
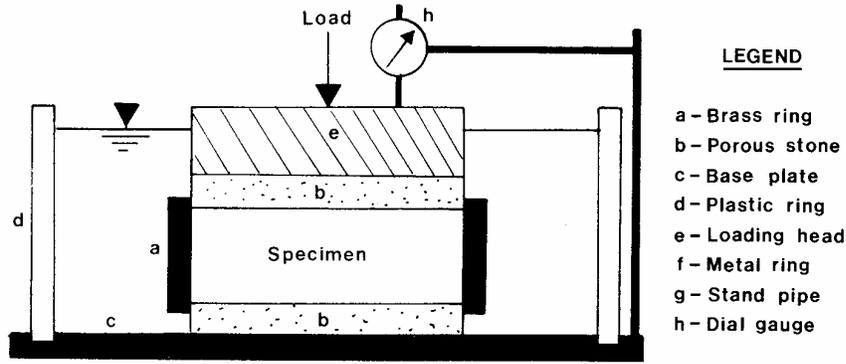
Figure 9-11: Apparatus for oedometer testing (courtesy from J. Germaine).

an oedometer test looks a lot like a flat punch indentation test, the hardness being the (ideally) uniform vertical stress $\sigma_v = F/A$ in the sample!

In geotechnical engineering creep is quantified by the coefficient of secondary compression $C_{\alpha\varepsilon}$ defined as $C_{\alpha\varepsilon} = d\varepsilon_v/d(\log t)$ [108]:

$$C_{\alpha\varepsilon} = \frac{d\varepsilon_v}{d(\log t)} = t\dot{\varepsilon}_v \tag{9.16}$$

For geomaterials as different as clays, sands or peat, $C_{\alpha\varepsilon}$ exhibits a very specific behavior, as it remains nearly constant over wide ranges of applied vertical stresses σ_v (see Figure 9-12) and thus of packing densities η.

We now apply the formalism of indentation analysis to oedometer testing. For flat punch indentation the displacement rate $\dot{h}(t)$ of the loading cap relates by definition to the contact creep compliance $L(t)$ of the the tested material by (see Equation 3.43):

$$\dot{h}(t) = \dot{L}(t)P_{\max}$$

Noting that $P_{\max}$ is proportional to the indentation hardness H and that by definition $\dot{L}(t) = 1/(Ct)$ (see Equation 3.53), we have:

$$\dot{h}(t) = \dot{L}(t)P_{\max} \propto \dot{L}(t)H = \frac{H}{Ct} \tag{9.17}$$

316
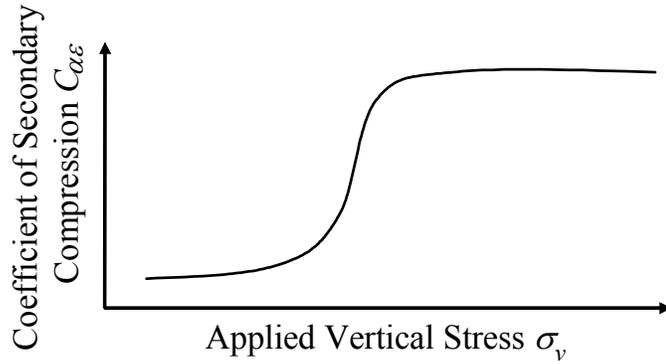
Figure 9-12: Schematic of the coefficient of secondary compression $C_{\alpha\varepsilon}$ versus applied vertical stress σ_v curve. $C_{\alpha\varepsilon}$ varies little with σ_v but around the preconsolidation pressure.

Combining Equations (9.16) and (9.17) yields:

$$C_{\alpha\varepsilon} \propto \frac{H}{C} \tag{9.18}$$

Therefore the coefficient of secondary compression $C_{\alpha\varepsilon}$ used in geotechnical engineering is inversely proportional to the C-to-H ratio obtained in indentation analysis. The linear scaling between the contact creep modulus C and the indentation hardness H for C-S-H over a wide range of packing densities in indentation testing is equivalent to the invariability of the coefficient of secondary compression $C_{\alpha\varepsilon}$ for geomaterials over a wide range of vertical stresses in oedometer testing. This observation suggests that C-S-H behaves very much like geomaterials. All geomaterials have in common that they are made of particles. At least for sands, for which the grains do not creep, creep deformations are the result of intergranular sliding. This suggests that creep deformations in C-S-H are not distributed in the bulk of the C-S-H solid particles but are localized on surfaces. Therefore the creep of C-S-H may well be due to sliding between neighboring C-S-H particles.

9.4.3 Can a Logarithmic Creep be Explained by a Granular Behavior?

If a granular behavior can explain the linear scaling between contact creep compliance C and indentation hardness, can it also explain the logarithmic time-dependence of the creep behavior?

Answering this question is the focus of this Section.

The physics community started studying the creep behavior of granular media after it was experimentally shown that the compaction of vibrated granular media is logarithmic with respect to time [105]. Several models were then proposed to explain this feature, among which the diffusing void model [93] and a model involving a combination of independent-particle movements and collective excitations [8]. But the most popular and plausible explanation is now based on free volume dynamics [136] [25] [114], although the free volume kinetics are often assumed by lack of understanding. This explanation, presented next for C-S-H and inspired from the work of Nowak and Knight [136], relies on the idea that the rate of increase in the volume fraction of solid decreases exponentially with the excluded volume.

The derivation is based on the idea that, when a load is applied to the system, the basic creep event, i.e., the displacement of a C-S-H particle with regard to the others can only occur if there is a pore large enough for the particle. The C-S-H particles are assumed to have a unique volume ω. Let n be the number of particles per unit volume, $\eta_{\max}$ be the limit packing density of the particles and $n_{\max}$ be the limit number of particles per unit volume. The free volume per grain v is:

$$v = \frac{1}{n} - \frac{1}{n_{\max}} = \omega \left(\frac{1}{\eta} - \frac{1}{\eta_{\max}} \right) \tag{9.19}$$

Considering that the variations in packing density during the creep process are small yields:

$$v \simeq \omega \frac{\eta_{\max} - \eta}{\eta_{\max}^2} \tag{9.20}$$

The pore volume distribution is assumed to follow a Poisson's distribution with the free volume v as a mean value so that the probability for a pore to have a volume Ω larger than ω is given by $P(\Omega > \omega) = \exp(-\omega/v)$. We expect the kinetics of the creep process to be governed by this factor:

$$\frac{d\eta}{dt} \propto \exp\left(-\frac{\omega}{v} \right) = \exp\left(-\frac{\eta_{\max}^2}{\eta_{\max} - \eta} \right) \tag{9.21}$$

The same type of kinetics can also be obtained by considering that rearrangements of particles become less frequent with time passing by, such that $t \sim e^n$ [136]. The interpretation for such kinetics is that when the packing density increases each rearrangement involves a larger amount

318

of particles (this interpretation is supported experimentally [85]). Equation (9.21) is rewritten:

$$dt \propto d\eta \exp\left(\frac{\eta_{\max}^2}{\eta_{\max} - \eta}\right) \qquad (9.22)$$

After integration between the initial and the current states the dominating exponential term is kept:

$$t \propto \frac{(\eta_{\max} - \eta)^2}{\eta_{\max}^2} \exp\left(\frac{\eta_{\max}^2}{\eta_{\max} - \eta}\right) \qquad (9.23)$$

Since the term in front of the exponential varies slowly we have:

$$t \propto \exp\left(\frac{\eta_{\max}^2}{\eta_{\max} - \eta}\right) \qquad (9.24)$$

and finally, combining Equations (9.22) and (9.20), we find:

$$\frac{d\eta}{dt} \propto \frac{1}{t} \qquad (9.25)$$

which translates into a logarithmic dependence of the creep behavior of C-S-H with regard to time. Free volume dynamics justify the observed kinetics of the creep of C-S-H but are not limited to volumetric deformations. Although free volume dynamics lead to volumetric deformations in oedometer testing or compaction of vibrated granular media, they can also be applied to explain the kinetics of shear deformations [114].

In conclusion, the observed logarithmic dependence of the time-dependent behavior and the C versus H scaling (see Section 9.4.2) can be explained by a rearrangement of the C-S-H particles. The creep of cementitious materials may then well be due to the sliding of C-S-H particles with respect to each other, leading to a rearrangement of collections of C-S-H particles and of the force network within the products of hydration.

9.5   Chapter Summary

In this Chapter we focused on assessing the creep behavior of C-S-H. We showed that the creep behavior is well described over time by a logarithmic function. Thus the long-term creep behavior can be characterized by a unique parameter, namely the contact creep modulus C.

The scaling between the contact creep modulus C and the microstructure (packing density η) of C-S-H is independent of the mix proportions and processing.

The non-linear scaling of the contact creep modulus with the packing density leads to discarding the hypothesis that the C-S-H solid particle creeps in its bulk. The linear scaling of the contact creep modulus C with the indentation hardness H is reminiscent of the creep behavior of geomaterials which also exhibit a creep behavior which is logarithmic with regard to time. A free volume dynamics theory can explain the logarithmic creep behavior of granular materials, which strongly suggests that the creep behavior of C-S-H is due to sliding of C-S-H particles with respect to each other and consequently that creep deformations in the C-S-H solid are localized on surfaces of contact between C-S-H particles.

The creep properties measured by nanoindentation can well explain, qualitatively as well as quantitatively, the long-term creep behavior of concrete. Indentation creep experiments, compared to macroscopic creep experiments, are faster by about 6 orders of magnitude and performed on samples smaller by about 6 orders of magnitude. Therefore indentation creep experiments may prove to be of high interest for the assessment of the long-term creep behavior of cementitious materials.

Part VI

Conclusions

Chapter 10

Summary of Results and Perspectives

At the outset of this thesis we defined as the ultimate goal of this study the implementation of the Materials Science paradigm for cementitious materials, that is, the assessment of the link between mix proportions, microstructure and mechanical performances. This Chapter presents a summary of this implementation for sub-stoichiometric cement pastes. Based on the findings and contributions some future research is proposed.

10.1   Summary of Main Findings

The study revealed the following scientific findings about the microstructure of sub-stoichiometric cement pastes and its link with mix proportions and mechanical performance:

- The C-S-H solid (i.e., the C-S-H particle) is a cohesive frictional material. Its mechanical properties ($m_s = 63.5$ GPa, $h_s = 3.0$ GPa, $c_s = 0.40$ GPa and $\alpha_s = 0.19$) do not depend on the water-cement ratio, on the application of a heat treatment or on an addition of calcareous filler. In contrast, an addition of silica fumes may eventually increase the contact hardness h_s of the C-S-H solid by modifying the elementary cohesive bonds of the C-S-H particles without modifying their pressure dependence. This modification may be due to the decrease in Ca/Si ratio of the C-S-H solid consecutive to the addition of silica.

- The C-S-H phases are a mix of C-S-H solid and pores as a result of the packing of the C-S-H particles. The C-S-H phases present a nanogranular morphology. Although the particles may be elongated, shape does not matter at the levels of packing typically encountered in mature cement pastes ($\eta > 0.64$). Consequently the mechanical properties of the C-S-H phases are a sole function of their packing density η.

- Three preferential packing patterns have been observed in sub-stoichiometric cement pastes: In addition to the Low-Density (LD) C-S-H and High-Density (HD) C-S-H phases, an Ultra-High-Density (UHD) C(-S-)H phase has been identified. Its properties ($M_{UHD} = 43$ GPa, $H_{UHD} = 1.5$ GPa and $\eta_{UHD} = 0.83$) vary little with mix proportions (except when adding silica fumes) and processing. UHD C(-S-)H may well contain some Portlandite (CH) and not be made of C-S-H only. Nevertheless its mechanical behavior is perfectly captured by the formalism here developed (C-S-H solid and pores).

- The mechanisms by which mix proportions and processing modify the microstructure have been identified. Heat treatment releases water trapped in the nanoporosity of the C-S-H nanoparticles, which then becomes available for further hydration of the remaining clinkers. In addition to modifying the C-S-H particle cohesive bonds, silica fumes produce more C-S-H by reacting with Portlandite (pozzolanic reaction). Calcareous filler is mostly non reactive and does not, strictly speaking, modify the microstructure but acts by mere mechanical reinforcement of the hydrated matter.

- A predictive model has been proposed which enables estimation of the volume fractions of clinker and C-S-H solid as well as the gel porosity in the paste, for water-cement ratios $0.2 \leq w/c \leq 0.4$, for additions of silica fumes up to 32% (in mass of clinker) and for application of a heat treatment (48-hour long placement in an oven at $90\,°C$ at 2 days after casting) or not.

- The creep of the C-S-H phases is perfectly captured by a logarithmic function. The magnitude of this creep is a sole function of their packing density η and is thus an intrinsic property of each C-S-H phase ($C_{LD} = 110$ GPa, $C_{HD} = 180$ GPa and $C_{UHD} = 340$ GPa). The creep identified by indentation testing is the long-term creep behavior of cementitious

materials. The contact creep compliance scales inversely with the indentation hardness $(C = 200H)$.

10.2 Research Contributions

The implementation of the Materials Science paradigm for sub-stoichiometric cement pastes required the development of new indentation analysis techniques, which are listed below:

- The existing indentation analysis tools which assess the elastic and strength properties of cohesive-frictional materials have been extended to linear-viscoelastic cohesive-frictional materials. Viscosity can have a non-negligible effect on the measured indentation modulus and hardness. By carefully designing the loading profile however, those effects can be limited.

- The analysis tools which allow the extraction of the viscous properties of a solid by sharp indentation have been developed. For indentation creep and relaxation tests simple formulas (Eqs. (3.30) and (3.69)) have been derived which enable a reliable measurement of those viscous properties even when plasticity occurs during loading.

- The implementation of hardness-packing density and modulus-packing density scaling relations in a reverse analysis algorithm provides a versatile means to probe the microstructure of any cohesive-frictional porous material and to separate constituent strength properties (c_s, α_s) from microstructure (η, η_0) in indentation analysis of porous materials. Given the difficulty of estimating the porosity of porous materials with classical methods, the reverse algorithm provides a new, nondestructive means to determine the porosity of nanogranular materials from their nanomechanical response.

- Techniques have been developed which enable the macroscopic indentation properties of a highly heterogeneous material to be estimated from a grid of nanoindentations. Those techniques apply to elastic, strength and creep properties.

10.3 Industrial Benefit

Associated with the scientific contributions is an industrial benefit. The experimental study showed that indentation creep experiments on cement pastes provide results comparable to macroscopic creep experiments but faster by about six orders of magnitude and on samples smaller by about six orders of magnitude. It can be used by the cement and concrete industry to obtain long term creep properties in a quick and inexpensive manner.

10.4 Limitations and Suggestions for Future Research

The homogenization scheme designed to estimate a macroscopic indentation hardness from a grid of nanoindentations could not be directly validated through microindentation testing. The observed discrepancy was attributed to microcracking during microindentation. A deeper scrutiny of the reasons for this discrepancy is necessary: If it is confirmed that cracking is a governing mechanism of failure at the macroscopic scale, an extension of the strength description which incorporates the fracture parameters needs to be developed.

UHD C(-S-)H was tentatively identified as a mix of C-S-H and Portlandite. A definitive proof is unlikely to be obtained by indentation means only since, by definition, the indentation technique is a mechanical test. A combination of the indentation technique with other sophisticated materials science analysis techniques such as Scanning Electron Microscopy (SEM), X-Ray Diffraction (XRD), X-Ray Fluorescence (XRF), Small Angle Neutron Scattering (SANS) and Nuclear Magnetic Resonance (NMR) would undoubtedly provide valuable information which would complement and help to interpret the indentation results.

Modeling of the C-S-H phases has been performed within the framework of continuum mechanics. The analogy of the mechanical behavior of C-S-H with that of granular materials suggests however that the use of granular mechanics could be well-suited to model C-S-H. Such an analysis might, for instance, help to explain the linear scaling between contact creep modulus and indentation hardness, which for now remains unexplained.

10.5   Perspectives

Civil infrastructures are usually built at least for decades, sometimes for much longer. Nuclear waste storage sites, for instance, are intended to retain structural integrity for hundreds of years. For such critical structures, the knowledge of the material behavior on time scales comparable to that of the structure is required. Obviously, this is not an easy task!

This study suggests that, to identify determinants of the creep behavior, probing the nanoscale enables an assessment of the long term macroscopic behavior that is orders of magnitude faster than can be found by macroscopic analysis. Given the potential impact of such an approach we hope this study will incite consideration of "length-time equivalence" (large time scales can be accessed by looking at small length scales) for other natural composites.

Appendix A

Proof of Relevance of Method of Functional Equations for Calculating the Initial Unloading Slope

We show in this appendix that the method of functional equations used to calculate the response during the loading and holding phases still remains valid to calculate the initial unloading slope of the load-displacement curve. The proof is based on the results of T.C.T. Ting [180], who succeeded in solving analytically, in 1966, in an implicit form, the problem of the indentation of a linear viscoelastic half-space by a rigid axisymmetric indenter for a load case with any number of extrema.

A.1   Presentation of Ting's solution

We consider the case of a contact area monotonically increasing and then decreasing. Ting introduces in his solution several auxiliary functions and parameters:

- $a(t)$ is the radius of the contact area

- t_m is the time at which $a(t)$ reaches its maximum

- $t_1(t)$ is an auxiliary time, introduced for $t > t_m$. $t_1(t)$ is defined by: $a(t_1) = a(t)$ and $t_1(t) < t_m$.

- $\Psi(t)$ and $\Phi(t)$ are two material functions, defined from the relaxation functions of the material according to the following equations in the Laplace domain:

$$s\widehat{\Phi(s)} = \frac{\widehat{\lambda(s)} + 2\widehat{G(s)}}{2s\widehat{G(s)}(\widehat{\lambda(s)} + \widehat{G(s)})} \quad \text{and} \quad s\widehat{\Psi(s)} = \frac{1}{s\widehat{\Phi(s)}}$$

where $\widehat{\Psi(s)}$, $\widehat{\Phi(s)}$, $\widehat{\lambda(s)}$ and $\widehat{G(s)}$ are the Laplace transforms of $\Psi(t)$, $\Phi(t)$, $\lambda(t)$ and $G(t)$. $\lambda(t)$ and $G(t)$ are the relaxations functions of the Lame's coefficients.

- $h_e(t)$ is the penetration depth solution for an elastic material. For a circular conical indenter $h_e(t)$ can be expressed as follows: $h_e(t) = \dfrac{\pi}{2\tan(\alpha)}a(t)$

- $P_e(t)$ is the solution for the load applied on the indenter for an elastic material. For a circular indenter $P_e(t)$ can be expressed as $cP_e(t) = \dfrac{\pi a^2(t)}{\tan(\alpha)} = \dfrac{4\tan(\alpha)}{\pi}h_e^2(t)$, where $c = \dfrac{1-\nu}{G}$.

With the above notations, Ting's solution of the considered viscoelastic problem has the following implicit form:

$$\begin{cases} h(t) = h_e(t) \\ P(t) = \int_{0^-}^{t} \Psi(t-\tau)\dfrac{\partial}{\partial\tau}(cP_e(\tau))\,d\tau \end{cases} \quad \text{for } 0 \leq t \leq t_m \qquad (A.1)$$

$$\begin{cases} h(t) = h_e(t) - \int_{t_m}^{t} \Phi(t-\tau)\dfrac{\partial}{\partial\tau}\int_{t_1(\tau)}^{\tau} \Psi(\tau-\eta)\dfrac{\partial}{\partial\eta}h_e(\eta)\,d\eta\,d\tau \\ P(t) = \int_{0^-}^{t_1(t)} \Psi(t-\tau)\dfrac{\partial}{\partial\tau}(cP_e(\tau))\,d\tau \end{cases} \quad \text{for } t_m \leq t \qquad (A.2)$$

A.2 Equivalence of Ting's Solution and the Method of Functional Equations

First of all, we have to check that the solution developed by Ting for $0 \leq t \leq t_m$ gives the same results as the method of functional equations. The problem of the circular conical indentation of an elastic material is governed by the equation:

$$h_e^2(t) = \frac{\pi}{2\tan(\alpha)}\frac{1-\nu^2}{E}P_e(t) \qquad (A.3)$$

328

Therefore, the use of the method of functional equations allows us to assert that the problem of the circular indentation of a linear viscoelastic material, for $0 \leq t \leq t_m$, is governed in the Laplace domain by:

$$\widehat{h^2(s)} = \frac{\pi}{2\tan(\alpha)} \frac{1 - \left(\widehat{\nu(s)}\right)^2}{\widehat{E(s)}} \widehat{P(s)} = \frac{\pi}{2\tan(\alpha)} \frac{\widehat{P(s)}}{\widehat{M(s)}} \tag{A.4}$$

where $\widehat{h^2(s)}$ and $\widehat{P(s)}$ are the Laplace transforms of respectively $h^2(t)$ and $P(t)$. $\widehat{\nu(s)}$ and $\widehat{E(s)}$ are the Laplace transforms of the differential operators associated with the viscoelastic Poisson's ratio and Young's modulus.

Ting's solution for the circular conical indentation of a linear viscoelastic material, for $0 \leq t \leq t_m$, can be rewritten as:

$$
\begin{aligned}
P(t) &= \int_{0^-}^t \Psi(t-\tau) \frac{\partial}{\partial\tau}\left(cP_e(\tau)\right) d\tau = \int_{0^-}^t \Psi(t-\tau)\frac{\partial}{\partial\tau}\left(\frac{4\tan(\alpha)}{\pi} h_e^2(\tau)\right) d\tau \quad \text{(A.5)} \\
&= \frac{4\tan(\alpha)}{\pi} \int_{0^-}^t \Psi(t-\tau)\frac{\partial}{\partial\tau}\left(h^2(\tau)\right) d\tau
\end{aligned}
$$

A derivation in the time domain is equivalent to a multiplication by s in the Laplace domain. A convolution product between two functions in the time domain is equivalent, in the Laplace domain, to a multiplication between their Laplace transforms. Therefore, Ting's solution can be rewritten in the Laplace domain as:

$$\widehat{P(s)} = \frac{4\tan(\alpha)}{\pi} \widehat{\Psi(s)} s \widehat{h^2(s)} \tag{A.6}$$

which yields:

$$\widehat{h^2(s)} = \frac{\pi}{4\tan(\alpha)} \frac{1}{s\widehat{\Psi(s)}} = \frac{\pi}{4\tan(\alpha)} s\widehat{\Phi(s)} \tag{A.7a}$$

$$= \frac{\pi}{8\tan(\alpha)} \frac{\widehat{\lambda(s)} + 2\widehat{G(s)}}{\widehat{G(s)}(\widehat{\lambda(s)} + \widehat{G(s)})} \tag{A.7b}$$

Finally, if we employ the elastic relations,

$$\lambda = E\frac{\nu}{(1+\nu)(1-2\nu)}; \ G = \frac{E}{2(1+\nu)} \tag{A.8}$$

329

we have for a viscoelastic material:

$$\widehat{\lambda(s)} \;\; = \;\; \widehat{E(s)} \frac{\widehat{\nu(s)}}{\left(1 + \widehat{\nu(s)}\right)\left(1 - 2\widehat{\nu(s)}\right)} \tag{A.9a}$$

$$\widehat{G(s)} \;\; = \;\; \frac{\widehat{E(s)}}{2\left(1 + \widehat{\nu(s)}\right)} \tag{A.9b}$$

Then, equation (A.7) yields:

$$\widehat{h^2(s)} = \frac{\pi}{2\tan(\alpha)} \frac{\widehat{P(s)}}{\widehat{M(s)}}; \;\; \widehat{M(s)} = \frac{\widehat{E(s)}}{1 - \left(\widehat{\nu(s)}\right)^2} \tag{A.10}$$

which is the same equation as (A.4). Therefore, for $0 \leq t \leq t_m$, Ting's solution and the method of functional equations are equivalent.

A.3   Calculation of the Initial Unloading Slope

The initial slope of the unloading part of the load-displacement curve is given by $\left(\dfrac{dP}{dh}\right)_{t=t_m^+} = \dfrac{\dot{P}(t_m^+)}{\dot{h}(t_m^+)}$. We want to check if Ting's solution for $0 \leq t \leq t_m$, extended to $t = t_m^+$, gives the same results as Ting's solution for $t_m \leq t$. We assume that $\Psi(t)$ and $\Phi(t)$ are continuous and derivable on $[0, t]$, and that $P(t)$, $P_e(t)$, $h(t)$ and $h_e(t)$ are continuous on $[0, t]$ and derivable on $[0, t_m[$ and $]t_m, t]$. The proof will require the use of the following relationship, valid for any continuous and derivable function $f(x, y)$:

$$\frac{d}{dx} \int_0^x f(x, y) dy = f(x, x) + \int_0^x \frac{\partial}{\partial x} f(x, y) dy \tag{A.11}$$

Since we consider a load-controlled test, whatever the set of equation considered, $\dot{P}(t_m^+)$ is a prescribed data. Therefore, $\dot{h}(t_m^+)$ can be calculated from the set of equations (A.1) as well as from the set of equations (A.2). The calculation of the initial unloading slope from the set of equations (A.1) yields:

$$\dot{h}(t_m^+) = \lim_{t \to t_m^+} \dot{h}(t) = \dot{h}_e(t_m^+) \tag{A.12}$$

330

The use of the set of equations (A.2) leads to:

$$\dot{h}(t_m^+) = \lim_{t \to t_m^+} \left[\dot{h}_e(t) - \frac{d}{dt} \left(\int_{t_m^+}^t \Phi(t-\tau) \frac{d}{d\tau} \left(\int_{t_1(\tau)}^\tau \Psi(\tau-\eta) \frac{d}{d\eta} h_e(\eta) d\eta \right) d\tau \right) \right] \qquad \text{(A.13)}$$

Furthermore, by applying (A.11), we have:

$$\frac{d}{dt} \left(\int_{t_m^+}^t \Phi(t-\tau) \frac{d}{d\tau} \left(\int_{t_1(\tau)}^\tau \Psi(\tau-\eta) \dot{h}_e(\eta) d\eta \right) d\tau \right) \qquad \text{(A.14)}$$

$$= \Phi(0) \frac{d}{dt} \left(\int_{t_1(t)}^t \Psi(t-\eta) \dot{h}_e(\eta) d\eta \right) + \int_{t_m^+}^t \dot{\Phi}(t-\tau) \frac{d}{d\tau} \left(\int_{t_1(\tau)}^\tau \Psi(\tau-\eta) \dot{h}_e(\eta) d\eta \right) d\tau$$

Since,

$$\lim_{t \to t_m^+} \int_{t_m^+}^t \dot{\Phi}(t-\tau) \frac{d}{d\tau} \left(\int_{t_1(\tau)}^\tau \Psi(\tau-\eta) \dot{h}_e(\eta) d\eta \right) d\tau \qquad \text{(A.15)}$$

we have:

$$\dot{h}(t_m^+) = \dot{h}_e(t_m^+) - \Phi(0) \frac{d}{dt} \left(\int_{t_1(t)}^t \Psi(t-\eta) \dot{h}_e(\eta) d\eta \right)_{t=t_m^+} \qquad \text{(A.16)}$$

which can be decomposed into:

$$\dot{h}(t_m^+) = \dot{h}_e(t_m^+) - \Phi(0) \frac{d}{dt} \left(\int_{t_m^+}^t \Psi(t-\eta) \dot{h}_e(\eta) d\eta \right)_{t=t_m^+} + \Phi(0) \frac{d}{dt} \left(\int_{t_m^-}^{t_1(t)} \Psi(t-\eta) \dot{h}_e(\eta) d\eta \right)_{t=t_m^+} \qquad (A.17)$$

The application of (A.11) to the first integral term in (A.17) leads to:

$$\frac{d}{dt} \left(\int_{t_m^+}^t \Psi(t-\eta) \dot{h}_e(\eta) d\eta \right)_{t=t_m^+} = \lim_{t \to t_m^+} \left[\Psi(0) \dot{h}_e(t) + \left(\int_{t_m^+}^t \dot{\Psi}(t-\eta) \dot{h}_e(\eta) d\eta \right) \right] \qquad \text{(A.18)}$$

$$= \Psi(0) \dot{h}_e(t_m^+)$$

The application of (A.11) to the second integral term in (A.17) leads to:

$$\frac{d}{dt}\left(\int_{t_m^-}^{t_1(t)}\Psi(t-\eta)\dot{h}_e(\eta)d\eta\right)_{t=t_m^+} = \lim_{t\to t_m^+}\frac{d}{dt}\left(\int_{t_m^-}^{t_1(t)}\Psi(t-\eta)\dot{h}_e(\eta)d\eta\right) \tag{A.19}$$

$$= \lim_{t\to t_m^+}\left[\dot{t}_1(t)\frac{d}{dt_1}\left(\int_{t_m^-}^{t_1(t)}\Psi(t-\eta)\dot{h}_e(\eta)d\eta\right)\right]$$

$$= \dot{t}_1(t_m^+)\lim_{t\to t_m^+}\left[\frac{d}{dt_1}\left(\int_{t_m^-}^{t_1(t)}\Psi(t-\eta)\dot{h}_e(\eta)d\eta\right)\right]$$

$$= \dot{t}_1(t_m^+)\lim_{t\to t_m^+}\left[\begin{array}{c}\Psi(t(t_1)-t_1)\dot{h}_e(t_1)+\\ \int_{t_m^-}^{t_1(t)}\left(\dot{\Psi}(t-\eta)\dot{h}_e(\eta)/\dot{t}_1(t)\right)d\eta\end{array}\right]$$

Since $\lim_{t\to t_m^+}t_1(t)=t_m^-$, we eventually have:

$$\frac{d}{dt}\left(\int_{t_m^-}^{t_1(t)}\Psi(t-\eta)\dot{h}_e(\eta)d\eta\right)_{t=t_m^+} = \dot{t}_1(t_m^+)\lim_{t_1\to t_m^-}\left[\begin{array}{c}\Psi(t(t_1)-t_1)\dot{h}_e(t_1)+\\ \int_{t_m^-}^{t_1(t)}\left(\dot{\Psi}(t-\eta)\dot{h}_e(\eta)/\dot{t}_1(t)\right)d\eta\end{array}\right] \tag{A.20}$$

$$= \dot{t}_1(t_m^+)\Psi(0)\dot{h}_e(t_m^-)$$

Finally, by using the set of equations (A.2), $\dot{h}(t_m^+)$ can be expressed as follows:

$$\dot{h}(t_m^+) = \dot{h}_e(t_m^+) - \Phi(0)\Psi(0)\left[\dot{h}_e(t_m^+) - \dot{t}_1(t_m^+)\dot{h}_e(t_m^-)\right] \tag{A.21}$$

We now come back to the definition of $t_1(t)$:

$$a(t) = a(t_1(t)) \tag{A.22}$$

which after derivation with respect to t can be rewritten as

$$\dot{a}(t) = \dot{a}(t_1)\dot{t}_1(t) \tag{A.23}$$

which leads to:

$$\lim_{t\to t_m^+}\dot{a}(t) = \lim_{t\to t_m^+}\dot{a}(t_1)\dot{t}_1(t) \tag{A.24}$$

and

$$\dot{a}(t_m^+) = \dot{a}(t_m^-)\dot{t}_1(t_m^+) \tag{A.25}$$

Since $h_e(t) = g(a(t))$ where g is a derivable function, we have:

$$\dot{h}_e(t) = \dot{g}(a(t))\dot{a}(t) \tag{A.26}$$

and:

$$\frac{\dot{h}_e(t_m^+)}{\dot{h}_e(t_m^-)} = \frac{\dot{g}(a(t_m^+))\dot{a}(t_m^+)}{\dot{g}(a(t_m^-))\dot{a}(t_m^-)} \tag{A.27}$$

Since $a(t)$ is a continuous function, we eventually find that:

$$\frac{\dot{h}_e(t_m^+)}{\dot{h}_e(t_m^-)} = \frac{\dot{a}(t_m^+)}{\dot{a}(t_m^-)} = \dot{t}_1(t_m^+) \tag{A.28}$$

Therefore, the calculation of the initial unloading slope by the use of the valid set of equations (A.2) leads to:

$$\dot{h}(t_m^+) = \dot{h}_e(t_m^+) \tag{A.29}$$

which is equal to the result given by the set of equations (A.1). This proves that the method of functional equations can be applied to the calculation of the initial unloading slope.

Appendix B

Results of Statistical Indentation Techniques

B.1 3-Gaussian Deconvolution of Hydration Products

Sample	M m[1]	M sd[2]	H m[1]	H sd[2]	η m[1]	η sd[2]	f[3]
PC-15-0-0	N.A.	N.A.	N.A.	N.A.	N.A.	N.A	0.000
PC-15-0-2	N.A.	N.A.	N.A.	N.A.	N.A.	N.A.	0.000
PC-20-0-0	19.40	4.80	0.440	0.230	0.620	0.020	0.030
PC-20-0-2	17.19	4.80	0.268	0.132	0.629	0.039	0.160
PC-20-8(SF)-0	24.63	4.74	0.724	0.271	0.701	0.036	0.188
PC-20-8(SF)-2	20.03	4.75	0.608	0.059	0.662	0.054	0.058
PC-20-10(CF1)-0	22.36	4.94	0.530	0.149	0.669	0.032	0.084
PC-20-10(CF2)-0	21.48	3.27	0.676	0.103	0.675	0.059	0.074
PC-20-17(SF)-2	23.26	4.92	0.659	0.218	0.675	0.062	0.011
PC-20-21(SF)-0	22.45	3.35	0.679	0.245	0.681	0.070	0.056
PC-20-24(SF)-0	22.57	4.51	0.610	0.281	0.689	0.050	0.146
PC-20-24(SF)-2	25.79	4.41	0.854	0.234	0.710	0.050	0.071
PC-20-25(CF1)-0	20.99	3.59	0.526	0.202	0.663	0.068	0.084
PC-20-25(CF2)-0	21.16	3.12	0.549	0.212	0.658	0.071	0.016
PC-20-32(SF)-2	23.95	4.14	0.806	0.226	0.699	0.053	0.062
PC-25-0-2	23.10	2.00	0.740	0.100	0.710	0.020	0.090

Table B.1: Results of the 3-peak deconvolution of the hydration products: first peak, representing Low Density (LD) C-S-H. First Part.
(1) Mean value, in GPa.
(2) Standard deviation, in GPa.
(3) Volume fraction, no units.

Sample	M		H		η		
	m[1]	sd[2]	m[1]	sd[2]	m[1]	sd[2]	f[3]
PC-30-0-0	21.90	4.90	0.580	0.120	0.680	0.030	0.300
PC-30-0-2	20.20	2.00	0.530	0.100	0.630	0.020	0.020
PC-30-8(SF)-0	21.35	3.91	0.620	0.162	0.674	0.047	0.122
PC-30-8(SF)-2	20.93	3.13	0.566	0.089	0.665	0.028	0.146
PC-30-10(CF1)-0	18.53	1.66	0.592	0.082	0.640	0.056	0.051
PC-30-10(CF2)-0	16.28	3.80	0.396	0.155	0.627	0.041	0.065
PC-30-17(SF)-0	24.45	4.18	0.748	0.129	0.699	0.018	0.193
PC-30-17(SF)-2	18.79	3.98	0.608	0.012	0.654	0.034	0.031
PC-30-21(SF)-0	21.67	1.80	0.626	0.128	0.661	0.053	0.075
PC-30-24(SF)-0	20.70	4.63	0.662	0.183	0.670	0.048	0.116
PC-30-24(SF)-2	23.81	3.39	0.611	0.134	0.678	0.022	0.065
PC-30-25(CF1)-0	18.99	1.51	0.556	0.148	0.646	0.054	0.032
PC-30-25(CF2)-0	21.28	3.15	0.593	0.206	0.666	0.044	0.083
PC-30-32(SF)-0	22.87	3.36	0.771	0.236	0.697	0.039	0.137
PC-30-32(SF)-2	24.30	4.32	0.878	0.277	0.703	0.039	0.297
PC-35-0-0	25.60	3.50	0.600	0.100	0.710	0.020	0.470
PC-35-0-2	19.30	3.30	0.410	0.100	0.640	0.050	0.090
PC-40-0-0	22.50	5.00	0.610	0.170	0.680	0.040	0.500
PC-40-8(SF)-0	22.49	3.53	0.568	0.103	0.682	0.024	0.394
PC-40-10(CF1)-0	19.76	5.03	0.592	0.167	0.662	0.039	0.277
PC-40-10(CF2)-0	22.11	4.31	0.730	0.181	0.679	0.036	0.289
PC-40-21(SF)-0	23.64	4.07	0.621	0.133	0.689	0.033	0.599
PC-40-25(CF1)-0	23.26	1.56	0.603	0.087	0.687	0.014	0.158
PC-40-25(CF2)-0	19.27	4.81	0.570	0.188	0.653	0.042	0.177

Table B.2: Results of the 3-peak deconvolution of the hydration products: first peak, representing Low Density (LD) C-S-H. Second Part.
(1) Mean value, in GPa.
(2) Standard deviation, in GPa.
(3) Volume fraction, no units.

| | M | | H | | η | | |
Sample	$m^{(1)}$	$sd^{(2)}$	$m^{(1)}$	$sd^{(2)}$	$m^{(1)}$	$sd^{(2)}$	$f^{(3)}$
PC-15-0-0	27.70	5.70	0.740	0.110	0.690	0.070	0.030
PC-15-0-2	N.A.	N.A.	N.A.	N.A.	N.A.	N.A.	0.000
PC-20-0-0	31.80	6.10	0.880	0.210	0.750	0.040	0.740
PC-20-0-2	26.93	4.94	0.634	0.092	0.709	0.017	0.123
PC-20-8(SF)-0	37.05	4.60	1.138	0.143	0.792	0.022	0.508
PC-20-8(SF)-2	33.69	6.50	0.876	0.209	0.766	0.043	0.722
PC-20-10(CF1)-0	35.05	6.32	0.972	0.196	0.781	0.043	0.657
PC-20-10(CF2)-0	36.20	5.02	1.002	0.221	0.784	0.037	0.692
PC-20-17(SF)-2	38.37	7.14	1.237	0.298	0.808	0.050	0.820
PC-20-21(SF)-0	38.76	5.45	1.130	0.207	0.802	0.035	0.707
PC-20-24(SF)-0	37.42	6.72	1.169	0.278	0.796	0.044	0.736
PC-20-24(SF)-2	39.97	5.12	1.453	0.289	0.819	0.034	0.726
PC-20-25(CF1)-0	36.99	5.78	1.022	0.223	0.794	0.042	0.607
PC-20-25(CF2)-0	36.50	5.03	1.120	0.253	0.792	0.040	0.681
PC-20-32(SF)-2	38.41	6.07	1.371	0.339	0.804	0.038	0.733
PC-25-0-2	32.40	3.40	0.980	0.140	0.760	0.030	0.610

Table B.3: Results of the 3-peak deconvolution of the hydration products: second peak, representing High Density (HD) C-S-H. First Part.
(1) Mean value, in GPa.
(2) Standard deviation, in GPa.
(3) Volume fraction, no units.

	M		H		η		
Sample	m[1]	sd[2]	m[1]	sd[2]	m[1]	sd[2]	f[3]
PC-30-0-0	31.30	4.50	0.870	0.170	0.750	0.040	0.520
PC-30-0-2	30.60	6.30	0.860	0.230	0.740	0.040	0.730
PC-30-8(SF)-0	33.29	4.37	0.975	0.131	0.762	0.027	0.551
PC-30-8(SF)-2	28.87	4.81	0.844	0.189	0.731	0.038	0.640
PC-30-10(CF1)-0	29.58	3.98	0.865	0.190	0.733	0.033	0.542
PC-30-10(CF2)-0	27.06	4.74	0.723	0.173	0.714	0.034	0.660
PC-30-17(SF)-0	33.68	4.17	1.130	0.178	0.766	0.027	0.588
PC-30-17(SF)-2	28.78	5.03	0.849	0.229	0.729	0.040	0.721
PC-30-21(SF)-0	32.60	4.85	0.945	0.190	0.757	0.034	0.774
PC-30-24(SF)-0	32.10	2.87	1.004	0.138	0.755	0.023	0.475
PC-30-24(SF)-2	33.05	5.85	1.048	0.272	0.764	0.040	0.721
PC-30-25(CF1)-0	30.71	4.77	0.879	0.175	0.744	0.037	0.619
PC-30-25(CF2)-0	33.45	4.97	1.031	0.232	0.766	0.037	0.591
PC-30-32(SF)-0	35.66	4.48	1.187	0.180	0.779	0.026	0.671
PC-30-32(SF)-2	36.52	4.52	1.414	0.260	0.782	0.032	0.531
PC-35-0-0	32.00	2.90	0.870	0.170	0.750	0.030	0.350
PC-35-0-2	27.80	5.20	0.780	0.180	0.720	0.040	0.540
PC-40-0-0	30.40	2.90	0.920	0.100	0.740	0.020	0.290
PC-40-8(SF)-0	30.26	4.24	0.856	0.184	0.734	0.028	0.450
PC-40-10(CF1)-0	28.92	4.12	0.941	0.182	0.729	0.028	0.377
PC-40-10(CF2)-0	30.84	4.42	1.194	0.273	0.751	0.035	0.503
PC-40-21(SF)-0	30.59	2.87	0.905	0.109	0.745	0.023	0.211
PC-40-25(CF1)-0	27.51	2.70	0.809	0.119	0.718	0.018	0.491
PC-40-25(CF2)-0	28.50	4.43	0.944	0.185	0.728	0.032	0.467

Table B.4: Results of the 3-peak deconvolution of the hydration products: second peak, representing High Density (HD) C-S-H. Second Part.
(1) Mean value, in GPa.
(2) Standard deviation, in GPa.
(3) Volume fraction, no units.

Sample	M		H		η		
	m[1]	sd[2]	m[1]	sd[2]	m[1]	sd[2]	f[3]
PC-15-0-0	41.10	8.10	1.150	0.330	0.820	0.060	0.970
PC-15-0-2	42.50	9.50	1.290	0.420	0.830	0.070	1.000
PC-20-0-0	46.10	8.30	1.670	0.340	0.850	0.060	0.230
PC-20-0-2	40.26	8.39	1.210	0.347	0.819	0.051	0.716
PC-20-8(SF)-0	47.33	5.68	1.728	0.326	0.869	0.038	0.304
PC-20-8(SF)-2	49.74	9.56	1.730	0.515	0.882	0.074	0.220
PC-20-10(CF1)-0	48.70	7.34	1.610	0.252	0.870	0.046	0.259
PC-20-10(CF2)-0	49.74	7.03	1.770	0.546	0.886	0.065	0.234
PC-20-17(SF)-2	54.03	5.96	2.150	0.316	0.902	0.045	0.169
PC-20-21(SF)-0	50.36	6.16	1.946	0.354	0.895	0.045	0.236
PC-20-24(SF)-0	52.83	8.69	2.029	0.297	0.882	0.043	0.118
PC-20-24(SF)-2	51.85	5.50	2.196	0.300	0.890	0.037	0.203
PC-20-25(CF1)-0	48.93	6.15	1.553	0.308	0.874	0.039	0.309
PC-20-25(CF2)-0	48.65	6.13	1.671	0.299	0.868	0.035	0.303
PC-20-32(SF)-2	49.18	4.70	2.295	0.352	0.877	0.035	0.205
PC-25-0-2	44.00	8.20	1.480	0.360	0.850	0.040	0.300

Table B.5: Results of the 3-peak deconvolution of the hydration products: third peak, representing Ultra-High Density (UHD) C(-S-)H. First Part.
(1) Mean value, in GPa.
(2) Standard deviation, in GPa.
(3) Volume fraction, no units.

Sample	M		H		η		
	m[1]	sd[2]	m[1]	sd[2]	m[1]	sd[2]	f[3]
PC-30-0-0	44.20	8.40	1.500	0.460	0.830	0.060	0.190
PC-30-0-2	46.00	9.10	1.710	0.480	0.850	0.060	0.250
PC-30-8(SF)-0	44.44	6.79	1.572	0.331	0.844	0.047	0.327
PC-30-8(SF)-2	43.30	9.61	1.303	0.184	0.818	0.039	0.214
PC-30-10(CF1)-0	40.31	6.74	1.483	0.425	0.817	0.051	0.407
PC-30-10(CF2)-0	38.77	6.97	1.330	0.349	0.801	0.053	0.275
PC-30-17(SF)-0	44.93	6.05	1.843	0.535	0.849	0.055	0.219
PC-30-17(SF)-2	42.12	8.32	1.553	0.311	0.823	0.051	0.247
PC-30-21(SF)-0	44.98	7.52	1.667	0.288	0.845	0.054	0.151
PC-30-24(SF)-0	40.87	5.90	1.434	0.292	0.818	0.040	0.409
PC-30-24(SF)-2	45.73	6.72	1.867	0.369	0.854	0.051	0.215
PC-30-25(CF1)-0	42.97	6.79	1.475	0.405	0.835	0.054	0.349
PC-30-25(CF2)-0	44.74	6.32	1.624	0.239	0.848	0.032	0.326
PC-30-32(SF)-0	46.04	5.90	1.831	0.339	0.850	0.029	0.193
PC-30-32(SF)-2	45.78	4.75	2.352	0.288	0.861	0.034	0.172
PC-35-0-0	43.60	8.60	1.490	0.450	0.830	0.060	0.190
PC-35-0-2	41.00	8.00	1.420	0.340	0.820	0.050	0.370
PC-40-0-0	40.90	7.70	1.460	0.450	0.830	0.070	0.210
PC-40-8(SF)-0	42.41	7.91	1.629	0.389	0.834	0.044	0.156
PC-40-10(CF1)-0	40.88	7.84	1.574	0.403	0.816	0.049	0.346
PC-40-10(CF2)-0	44.22	6.05	1.830	0.363	0.829	0.040	0.208
PC-40-21(SF)-0	42.18	5.87	1.415	0.401	0.822	0.053	0.191
PC-40-25(CF1)-0	35.74	5.53	1.272	0.344	0.778	0.041	0.351
PC-40-25(CF2)-0	39.60	6.67	1.544	0.354	0.809	0.043	0.355

Table B.6: Results of the 3-peak deconvolution of the hydration products: third peak, representing Ultra-High Density (UHD) C(-S-)H. Second Part.
(1) Mean value, in GPa.
(2) Standard deviation, in GPa.
(3) Volume fraction, no units.

B.2   2-Gaussian Deconvolution of All Nanoindentations of a Grid

Sample	M		H		
	$m^{(1)}$	$sd^{(2)}$	$m^{(1)}$	$sd^{(2)}$	$f^{(3)}$
C3S-20-0-0	47.37	7.12	1.749	0.343	0.574
C3S-20-0-2	48.19	6.88	2.176	0.402	0.607
C3S-20-24(SF)-0	53.42	8.62	2.372	0.759	0.630
C3S-20-24(SF)-2	55.61	7.06	2.587	0.466	0.649
C3S-25-0-0	41.89	7.44	1.544	0.377	0.628
C3S-25-0-2	46.18	8.27	2.038	0.442	0.649
C3S-30-0-0	39.13	8.87	1.587	0.504	0.566
C3S-30-0-2	39.36	10.57	1.847	0.674	0.670
PC-15-0-0	41.06	8.52	1.158	0.332	0.559
PC-15-0-2	42.53	9.52	1.292	0.417	0.591
PC-20-0-0	32.29	8.55	0.883	0.313	0.582
PC-20-0-2	36.46	13.51	1.045	0.558	0.743
PC-20-8(SF)-0	38.05	8.60	1.189	0.320	0.645
PC-20-8(SF)-2	34.66	7.61	0.913	0.241	0.542
PC-20-10(CF1)-0	36.83	9.05	1.044	0.325	0.705
PC-20-10(CF2)-0	37.41	7.22	1.046	0.291	0.642
PC-20-17(SF)-2	40.33	8.54	1.316	0.375	0.661
PC-20-21(SF)-0	40.52	7.00	1.195	0.288	0.596
PC-20-24(SF)-0	37.13	9.22	1.181	0.372	0.632
PC-20-24(SF)-2	41.53	7.25	1.548	0.423	0.651
PC-20-25(CF1)-0	39.44	9.22	1.121	0.364	0.690
PC-20-25(CF2)-0	39.18	7.36	1.254	0.340	0.704
PC-20-32(SF)-2	39.96	8.20	1.491	0.512	0.658
PC-25-0-2	33.31	5.23	1.017	0.204	0.667

Table B.7: Results of the 2-peak deconvolution: first peak, representing hydration products. First Part.
(1) Mean value, in GPa.
(2) Standard deviation, in GPa.
(3) Volume fraction, no units.

	M		H		
Sample	$m^{(1)}$	$sd^{(2)}$	$m^{(1)}$	$sd^{(2)}$	$f^{(3)}$
PC-30-0-0	28.85	7.86	0.767	0.274	0.735
PC-30-0-2	32.39	7.46	0.927	0.286	0.718
PC-30-8(SF)-0	34.57	7.25	1.023	0.258	0.723
PC-30-8(SF)-2	28.77	6.79	0.856	0.267	0.786
PC-30-10(CF1)-0	32.16	6.85	0.985	0.334	0.776
PC-30-10(CF2)-0	28.22	6.52	0.773	0.253	0.695
PC-30-17(SF)-0	33.71	6.42	1.110	0.282	0.666
PC-30-17(SF)-2	30.04	6.35	0.921	0.305	0.690
PC-30-21(SF)-0	32.98	5.93	0.962	0.231	0.703
PC-30-24(SF)-0	33.76	6.03	1.091	0.276	0.695
PC-30-24(SF)-2	34.23	7.28	1.108	0.369	0.725
PC-30-25(CF1)-0	33.24	7.10	0.965	0.275	0.749
PC-30-25(CF2)-0	35.56	8.17	1.166	0.400	0.781
PC-30-32(SF)-0	35.92	6.67	1.198	0.259	0.705
PC-30-32(SF)-2	34.79	8.70	1.330	0.462	0.761
PC-35-0-0	29.34	5.19	0.725	0.204	0.702
PC-35-0-2	30.25	8.42	0.895	0.361	0.703
PC-40-0-0	26.33	7.33	0.744	0.262	0.792
PC-40-8(SF)-0	27.40	6.41	0.735	0.243	0.789
PC-40-10(CF1)-0	28.43	8.32	0.911	0.358	0.744
PC-40-10(CF2)-0	29.60	7.82	1.115	0.427	0.853
PC-40-21(SF)-0	26.44	5.92	0.723	0.211	0.763
PC-40-25(CF1)-0	27.08	3.68	0.788	0.167	0.677
PC-40-25(CF2)-0	28.72	7.42	0.940	0.314	0.771

Table B.8: Results of the 2-peak deconvolution: first peak, representing hydration products. Second Part.

(1) Mean value, in GPa.
(2) Standard deviation, in GPa.
(3) Volume fraction, no units.

B.3 Particle Properties

Sample	c_s [1], GPa	α_s [2]	h_s [3], GPa
C3S-20-0-0	0.636	0.000	3.03
C3S-20-0-2	0.317	0.335	3.42
C3S-20-24(SF)-0	0.676	0.000	3.22
C3S-20-24(SF)-2	0.281	0.359	3.25
C3S-25-0-0	0.664	0.016	3.29
C3S-25-0-2	0.374	0.281	3.50
C3S-30-0-0	0.456	0.224	3.69
C3S-30-0-2	0.645	0.122	4.10
PC-15-0-0	0.486	0.063	2.70
PC-15-0-2	0.494	0.067	2.77
PC-20-0-0	0.414	0.174	2.97
PC-20-0-2	0.257	0.322	2.67
PC-20-8(SF)-0	0.521	0.085	3.05
PC-20-8(SF)-2	0.429	0.118	2.71
PC-20-10(CF1)-0	0.483	0.074	2.75
PC-20-10(CF2)-0	0.434	0.126	2.79
PC-20-17(SF)-2	0.511	0.089	3.01
PC-20-21(SF)-0	0.467	0.111	2.90
PC-20-24(SF)-0	0.403	0.193	3.03
PC-20-24(SF)-2	0.377	0.255	3.30
PC-20-25(CF1)-0	0.460	0.079	2.65
PC-20-25(CF2)-0	0.489	0.094	2.92
PC-20-32(SF)-2	0.171	0.544	3.66
PC-25-0-2	0.579	0.044	3.07

Table B.9: Particle properties. First Part. (1) Cohesion.(2) Friction coefficient.(3) Contact hardness.

Sample	c_s [1], GPa	α_s [2]	h_s [3], GPa
PC-30-0-0	0.418	0.170	2.97
PC-30-0-2	0.412	0.193	3.09
PC-30-8(SF)-0	0.504	0.108	3.11
PC-30-8(SF)-2	0.519	0.092	3.08
PC-30-10(CF1)-0	0.398	0.234	3.30
PC-30-10(CF2)-0	0.328	0.299	3.21
PC-30-17(SF)-0	0.501	0.160	3.48
PC-30-17(SF)-2	0.425	0.212	3.34
PC-30-21(SF)-0	0.416	0.192	3.12
PC-30-24(SF)-0	0.556	0.090	3.29
PC-30-24(SF)-2	0.311	0.328	3.29
PC-30-25(CF1)-0	0.493	0.106	3.02
PC-30-25(CF2)-0	0.463	0.150	3.14
PC-30-32(SF)-0	0.533	0.126	3.42
PC-30-32(SF)-2	0.483	0.236	4.02
PC-35-0-0	0.206	0.444	3.07
PC-35-0-2	0.375	0.246	3.20
PC-40-0-0	0.437	0.186	3.23
PC-40-8(SF)-0	0.319	0.317	3.28
PC-40-10(CF1)-0	0.504	0.169	3.57
PC-40-10(CF2)-0	0.555	0.166	3.91
PC-40-21(SF)-0	0.426	0.181	3.11
PC-40-25(CF1)-0	0.249	0.442	3.68
PC-40-25(CF2)-0	0.521	0.161	3.63

Table B.10: Particle properties. Second Part.
(1) Cohesion.
(2) Friction coefficient.
(3) Contact hardness.

B.4 Mean Packing Density of Hydrates

Sample	$< \eta >$	Sample	$< \eta >$
C3S-20-0-0	0.872	PC-30-0-0	0.737
C3S-20-0-2	0.873	PC-30-0-2	0.766
C3S-20-24(SF)-0	0.893	PC-30-8(SF)-0	0.779
C3S-20-24(SF)-2	0.916	PC-30-8(SF)-2	0.742
C3S-25-0-0	0.828	PC-30-10(CF1)-0	0.762
C3S-25-0-2	0.853	PC-30-10(CF2)-0	0.732
C3S-30-0-0	0.795	PC-30-17(SF)-0	0.771
C3S-30-0-2	0.805	PC-30-17(SF)-2	0.750
PC-15-0-0	0.821	PC-30-21(SF)-0	0.763
PC-15-0-2	0.830	PC-30-24(SF)-0	0.773
PC-20-0-0	0.759	PC-30-24(SF)-2	0.777
PC-20-0-2	0.776	PC-30-25(CF1)-0	0.773
PC-20-8(SF)-0	0.787	PC-30-25(CF2)-0	0.785
PC-20-8(SF)-2	0.785	PC-30-32(SF)-0	0.781
PC-20-10(CF1)-0	0.795	PC-30-32(SF)-2	0.772
PC-20-10(CF2)-0	0.800	PC-35-0-0	0.744
PC-20-17(SF)-2	0.822	PC-35-0-2	0.750
PC-20-21(SF)-0	0.817	PC-40-0-0	0.726
PC-20-24(SF)-0	0.791	PC-40-8(SF)-0	0.729
PC-20-24(SF)-2	0.826	PC-40-10(CF1)-0	0.741
PC-20-25(CF1)-0	0.808	PC-40-10(CF2)-0	0.746
PC-20-25(CF2)-0	0.813	PC-40-21(SF)-0	0.726
PC-20-32(SF)-2	0.813	PC-40-25(CF1)-0	0.734
PC-25-0-2	0.775	PC-40-25(CF2)-0	0.744

Table B.11: Mean packing density $< \eta >$ of hydrates.

B.5 Volume Fraction of Remaining Clinker

Sample	f_{CL}^{dec}	f_{CL}^{cut}	Sample	f_{CL}^{dec}	f_{CL}^{cut}
C3S-20-0-0	0.249	0.410	PC-30-0-0	0.198	0.181
C3S-20-0-2	0.257	0.407	PC-30-0-2	0.179	0.191
C3S-20-24(SF)-0	0.277	0.523	PC-30-8(SF)-0	0.204	0.173
C3S-20-24(SF)-2	0.252	0.507	PC-30-8(SF)-2	0.178	0.149
C3S-25-0-0	0.184	0.327	PC-30-10(CF1)-0	0.194	0.136
C3S-25-0-2	0.223	0.377	PC-30-10(CF2)-0	0.222	0.232
C3S-30-0-0	0.126	0.335	PC-30-17(SF)-0	0.215	0.247
C3S-30-0-2	0.353	0.360	PC-30-17(SF)-2	0.234	0.235
PC-15-0-0	0.314	0.432	PC-30-21(SF)-0	0.198	0.226
PC-15-0-2	0.346	0.423	PC-30-24(SF)-0	0.273	0.224
PC-20-0-0	0.352	0.333	PC-30-24(SF)-2	0.168	0.205
PC-20-0-2	0.297	0.295	PC-30-25(CF1)-0	0.185	0.162
PC-20-8(SF)-0	0.260	0.308	PC-30-25(CF2)-0	0.199	0.195
PC-20-8(SF)-2	0.280	0.329	PC-30-32(SF)-0	0.236	0.222
PC-20-10(CF1)-0	0.224	0.242	PC-30-32(SF)-2	0.210	0.201
PC-20-10(CF2)-0	0.214	0.281	PC-35-0-0	0.205	0.175
PC-20-17(SF)-2	0.232	0.302	PC-35-0-2	0.196	0.219
PC-20-21(SF)-0	0.286	0.330	PC-40-0-0	0.108	0.106
PC-20-24(SF)-0	0.206	0.327	PC-40-8(SF)-0	0.112	0.119
PC-20-24(SF)-2	0.217	0.324	PC-40-10(CF1)-0	0.151	0.124
PC-20-25(CF1)-0	0.235	0.289	PC-40-10(CF2)-0	0.100	0.081
PC-20-25(CF2)-0	0.249	0.255	PC-40-21(SF)-0	0.157	0.127
PC-20-32(SF)-2	0.295	0.352	PC-40-25(CF1)-0	0.120	0.055
PC-25-0-2	0.219	0.245	PC-40-25(CF2)-0	0.093	0.073

Table B.12: Volume fraction of remaining clinker. f_{CL}^{dec} is the volume fraction estimated as the volume fraction of the fourth peak in a 4-Gaussian deconvolution of all nanoindentations of the grid. f_{CL}^{cut} is the volume fraction estimated by filtering out the data with a threshold at $M = 63.5$ GPa and $H = 3$ GPa.

B.6 Homogenized Properties

Sample	M^{hom}, GPa	H^{hom}, GPa	Sample	M^{hom}, GPa	H^{hom}, GPa
C3S-20-0-0	61.7	2.71	PC-30-0-0	36.0	1.01
C3S-20-0-2	60.9	3.15	PC-30-0-2	40.3	1.25
C3S-20-24(SF)-0	65.5	3.31	PC-30-8(SF)-0	41.0	1.33
C3S-20-24(SF)-2	63.8	3.49	PC-30-8(SF)-2	35.0	1.04
C3S-25-0-0	52.0	2.20	PC-30-10(CF1)-0	37.6	1.22
C3S-25-0-2	58.7	2.93	PC-30-10(CF2)-0	38.9	1.15
C3S-30-0-0	47.4	2.07	PC-30-17(SF)-0	42.1	1.61
C3S-30-0-2	53.4	2.74	PC-30-17(SF)-2	40.2	1.35
PC-15-0-0	59.7	2.46	PC-30-21(SF)-0	41.9	1.33
PC-15-0-2	62.0	2.59	PC-30-24(SF)-0	41.4	1.47
PC-20-0-0	45.5	1.63	PC-30-24(SF)-2	41.8	1.45
PC-20-0-2	46.0	1.43	PC-30-25(CF1)-0	40.2	1.25
PC-20-8(SF)-0	50.6	1.84	PC-30-25(CF2)-0	43.3	1.43
PC-20-8(SF)-2	48.2	1.61	PC-30-32(SF)-0	42.7	1.59
PC-20-10(CF1)-0	46.8	1.44	PC-30-32(SF)-2	40.3	1.67
PC-20-10(CF2)-0	49.3	1.61	PC-35-0-0	36.2	0.99
PC-20-17(SF)-2	52.3	2.00	PC-35-0-2	38.5	1.24
PC-20-21(SF)-0	54.7	2.08	PC-40-0-0	30.7	0.89
PC-20-24(SF)-0	48.7	1.76	PC-40-8(SF)-0	32.1	0.92
PC-20-24(SF)-2	53.8	2.32	PC-40-10(CF1)-0	33.2	1.14
PC-20-25(CF1)-0	51.5	1.68	PC-40-10(CF2)-0	32.6	1.22
PC-20-25(CF2)-0	49.9	1.67	PC-40-21(SF)-0	31.8	0.89
PC-20-32(SF)-2	54.3	2.40	PC-40-25(CF1)-0	31.1	0.95
PC-25-0-2	44.4	1.46	PC-40-25(CF2)-0	32.0	1.10

Table B.13: Estimated homogenized indentation modulus M^{hom} and indentation hardness H^{hom}.

Bibliography

[1] Abate J. and Valko P. P. (2004). "Multi-precision laplace transform inversion." *International Journal for Numerical Methods in Engineering* 60(5): 979-993.

[2] Allen A. J. and Thomas J. J. (2007). "Analysis of C-S-H gel and cement paste by small-angle neutron scattering." *Cement and Concrete Research* 37(3): 319-324.

[3] Allen A. J., Thomas J. J. and Jennings H. M. (2007). "Composition and density of nanoscale calcium-silicate-hydrate in cement." *Nature Materials* 6(4): 311-316.

[4] Antonangeli D., Krisch M., Fiquet G., Badro J., Farber D. L., Bossak A. and Merkel S. (2005). "Aggregate and single-crystalline elasticity of hcp cobalt at high pressure." *Physical Review B* 72.

[5] Ashby M. (2004). *Materials selection in mechanical design*, Elsevier Butterworth Heinemann.

[6] Atkins A.G. and Tabor D. (1965). "Plastic indentation in metals with cones." *Journal of the Mechanics and Physics of Solids* 13(3): 149-164.

[7] Barenblatt G. I. (1996). *Scaling, self-similarity, and intermediate asymptotics.* Cambridge, Cambridge University Press.

[8] Barker G. C. and Mehta A. (1993). "Transient phenomena, self-diffusion, and orientational effects in vibrated powders." *Physical Review E* 47(1): 184-188.

[9] Barthélémy J.-F. (2005). *Approche micromécanique de la rupture et de la fissuration dans les géomatériaux.* Champs-sur-Marne, France, Ecole Nationale des Ponts et Chaussées. PhD thesis.

[10] Barthelemy J. F. and Dormieux L. (2003). "Determination of the macroscopic strength criterion of a porous medium by nonlinear homogenization." *Comptes Rendus Mécanique* 331(4): 271-276.

[11] Bazant Z. P. and Chern J. C. (1984). "Double-power logarithmic law for concrete creep." *Cement and Concrete Research* 14(6): 793-806.

[12] Bazant Z. P., Hauggaard A. B., Baweja S. and Ulm F. J. (1997). "Microprestress-solidification theory for concrete creep .1. Aging and drying effects." *Journal of Engineering Mechanics* 123(11): 1188-1194.

[13] Bazant Z. P. and Prasannan S. (1989). "Solidification theory for concrete creep .1. formulation." *Journal of Engineering Mechanics* 115(8): 1691-1703.

[14] Bazant Z. P. and Prasannan S. (1989). "Solidification theory for concrete creep .2. verification and application." *Journal of Engineering Mechanics* 115(8): 1704-1725.

[15] Benboudjema F. (2002). *Modélisation des déformations différées du béton sous sollicitations biaxiales. Application aux enceintes de confinement de bâtiment réacteurs des centrales nucléaires.* Marne-La-Vallée, France, Université de Marne-La-Vallée. PhD thesis.

[16] Ben-Naim E., Knight J. B., Nowak E. R., Jaeger H. M. and Nagel S. R. (1998). "Slow relaxation in granular compaction." *Physica D* 123(1-4): 380-385.

[17] Bentur A., Berger R. L., Lawrence F. V., Milestone N. B., Mindess S. and Young J. F. (1979). "Creep and drying shrinkage of calcium silicate pastes .3. Hypothesis of irreversible strains." *Cement and Concrete Research* 9(1): 83-95.

[18] Bentur A., Milestone N. B. and Young J. F. (1978). "Creep and drying shrinkage of calcium silicate pastes .2. Induced microstructural and chemical changes." *Cement and Concrete Research* 8(6): 721-732.

[19] Bolshakov A. and Pharr G. M. (1998). "Influences of pileup on the measurement of mechanical properties by load and depth sensing indentation techniques." *Journal of Materials Research* 13(4): 1049-1058.

[20] Borges L. A., Zouain N. and Huespe A. E. (1996). "A nonlinear optimization procedure for limit analysis." *European Journal of Mechanics A-Solids* 15(3): 487-512.

[21] Borodich F. M. (1989). "Hertz contact problems for an anisotropic physically nonlinear elastic medium." *Problemy Prochnosti* 12: 47-53 (in Russian, English translation in Strength of Materials 21: 1668-1676).

[22] Borodich F. M. (1998). *Similarity methods in Hertz contact problems and their relations with the Meyer hardness test.* Glasgow, Glasgow Caledonian University: 1-45.

[23] Borodich F. M. and Galanov B. A. (2002). "Self-similar problems of elastic contact for non-convex punches." *Journal of the Mechanics and Physics of Solids* 50(11): 2441-2461.

[24] Borodich F. M., Keer L. M. and Korach C. S. (2003). "Analytical study of fundamental nanoindentation test relations for indenters of non-ideal shapes." *Nanotechnology* 14(7): 803-808.

[25] Boutreux T. and de Gennes P. G. (1997). "Compaction of granular mixtures: a free volume model." *Physica A* 244(1-4): 59-67.

[26] Brinell J. A. (1901). *Mémoire sur les épreuves à bille en acier.* Congrès International des Méthodes d'Essai des Matériaux de Construction, Paris.

[27] Bruet B. J. F., Qi H. J., Boyce M. C., Panas R., Tai K., Frick L. and Ortiz C. (2005). "Nanoscale morphology and indentation of individual nacre tablets from the gastropod mollusc Trochus niloticus." *Journal of Materials Research* 20(9): 2400-2419.

[28] Brunauer S. and Greenberg S. A. (1962). *The hydration of tricalcium silicate and β-dicalcium silicate at room temperature.* 4th ISCC, Washington, D.C., National Bureau of Standards.

[29] Buchalter B. J. and Bradley R. M. (1994). "Orientational order in amorphous packings of ellipsoids." *Europhysics Letters* 26(3): 159-164.

[30] Buckingham E. (1914). "On physically similar systems; illustrations of the use of dimensional equations." *Physical Reviews* 4: 345-376.

[31] Buckle H. (1973). *The science of hardness testing and its applications.* J. W. Westbrook and H. Conrad. Metal Park, OH, American Society for Metals: 453-491.

[32] Bulychev S. I., Alekhin V. P., Shorshorov M. K., Ternovskii A. P. and Shnyrev G. D. (1975). "Determination of Young's modulus according to indentation diagram." *Zavodskaya Laboratoria* (Transl: Industrial Laboratory) 41: 1137.

[33] Cariou S. and Ulm F.-J. (2006). *The effect of the packing density on the indentation hardness of cohesive-frictional porous materials.* Cambridge, MA, Civil and Environmental Engineering Department, Massachusetts Institute of Technology. MS thesis.

[34] Cariou S., Ulm F. J. and Dormieux L. (2008). "Hardness-packing density scaling relations for cohesive-frictional porous materials." *Journal of the Mechanics and Physics of Solids* 56(3): 924-952.

[35] Castaneda P. P. (1992). "New variational-principles in plasticity and their application to composite-materials." *Journal of the Mechanics and Physics of Solids* 40(8): 1757-1788.

[36] Castaneda P. P. (1996). "Exact second-order estimates for the effective mechanical properties of nonlinear composite materials." *Journal of the Mechanics and Physics of Solids* 44(6): 827-862.

[37] Castaneda P. P. (2002). "Second-order homogenization estimates for nonlinear composites incorporating field fluctuations: I - theory." *Journal of the Mechanics and Physics of Solids* 50(4): 737-757.

[38] Chanvillard G. (1999). *Le matériau béton: connaissances générales.* Vaulx-en-Velin, ENTPE-Aléas.

[39] Chatterji S. and Jeffery J. W. (1966). "Three-dimensional arrangement of hydration products in set cement paste." *Nature* 209: 1233.

[40] Chen C. C., Lin C. C., Liu L. G., Sinogeikin S. V. and Bass J. D. (2001). "Elasticity of single-crystal calcite and rhodochrosite by Brillouin spectroscopy." *American Mineralogist* 86(11-12): 1525-1529.

[41] Chen W. M., Li M., Zhang T., Cheng Y. T. and Cheng C. M. (2007). "Influence of indenter tip roundness on hardness behavior in nanoindentation." *Materials Science and Engineering A-Structural Materials Properties Microstructure and Processing* 445: 323-327.

[42] Chen X., Ogasawara N., Zhao M. H. and Chiba N. (2007). "On the uniqueness of measuring elastoplastic properties from indentation: The indistinguishable mystical materials." *Journal of the Mechanics and Physics of Solids* 55(8): 1618-1660.

[43] Cheng L., Xia X., Scriven L. E. and Gerberich W. W. (2005). "Spherical-tip indentation of viscoelastic material." *Mechanics of Materials* 37(1): 213-226.

[44] Cheng L., Xia X., Yu W., Scriven L. E. and Gerberich W. W. (2000). "Flat-punch indentation of viscoelastic material." *Journal of Polymer Science Part B-Polymer Physics* 38(1): 10-22.

[45] Cheng Y. T. and Cheng C. M. (1998). "Scaling approach to conical indentation in elastic-plastic solids with work hardening." *Journal of Applied Physics* 84(3): 1284-1291.

[46] Cheng Y. T. and Cheng C. M. (1999). "Scaling relationships in conical indentation of elastic perfectly plastic solids." *International Journal of Solids and Structures* 36(8): 1231-1243.

[47] Cheng Y. T. and Cheng C. M. (2000). "What is indentation hardness?" *Surface & Coatings Technology* 133: 417-424.

[48] Cheng Y. T. and Cheng C. M. (2004). "Scaling, dimensional analysis, and indentation measurements." *Materials Science & Engineering R-Reports* 44(4-5): 91-149.

[49] Chitkara N. R. and Butt M. A. (1992). "Numerical construction of axisymmetrical slip-line fields for indentation of thick blocks by rigid conical indenters and friction at the tool metal interface." *International Journal of Mechanical Sciences* 34(11): 849-862.

[50] Christensen R. M. (1982). *Theory of viscoelasticity: An introduction.* New York, Academic Press.

[51] Chudoba T. and Richter F. (2001). "Investigation of creep behaviour under load during indentation experiments and its influence on hardness and modulus results." *Surface & Coatings Technology* 148(2-3): 191-198.

[52] Clarke F. W. (1911). *The data of geochemistry.* Washington, D.C., Government printing office.

[53] Coelho D., Thovert J. F. and Adler P. M. (1997). "Geometrical and transport properties of random packings of spheres and aspherical particles." *Physical Review E* 55(2): 1959-1978.

[54] Constantinides G., Chandran K. S. R., Ulm F.-J. and Van Vliet K. J. (2006). "Grid indentation analysis of composite microstructure and mechanics: Principles and validation." *Materials Science and Engineering A-Structural Materials Properties Microstructure and Processing* 430(1-2): 189-202.

[55] Constantinides G., Silva E., Blackman G. S. and Van Vliet K. J. (2007). "Dealing with imperfection: quantifying potential length scale artefacts from nominally spherical indenter probes." *Nanotechnology* 18(30).

[56] Constantinides G. and Ulm F.-J. (2004). "The effect of two types of C-S-H on the elasticity of cement-based materials: Results from nanoindentation and micromechanical modeling." *Cement and Concrete Research* 34(1): 67-80.

[57] Constantinides G. and Ulm F.-J. (2006). *Invariant mechanical properties of calcium-silicat-hydrates (C-S-H) in cement-based materials: Instrumented nanoindentation and microporomechanical modeling.* Cambridge, MA, Civil and Environmental Engineering Department, Massachusetts Institute of Technology. PhD thesis.

[58] Constantinides G. and Ulm F.-J. (2007). "The nanogranular nature of C-S-H." *Journal of the Mechanics and Physics of Solids* 55(1): 64-90.

[59] Constantinides G., Ulm F.-J. and Van Vliet K. (2003). "On the use of nanoindentation for cementitious materials." *Materials and Structures* 36(257): 191-196.

[60] Cook R. F. and Oyen M. L. (2007). "Nanoindentation behavior and mechanical properties measurement of polymeric materials." *International Journal of Materials Research* 98(5): 370-378.

[61] Coussy O. and Ulm F.-J. (2004). *Mechanics and durability of solids.* Upper Saddle Liver, NJ, Prentice Hall.

[62] CSM Instruments SA (2004). *Nanohardness test users manual.* Peseux, Switzerland

[63] Degennes P. G. (1976). "Relation between percolation theory and elasticity of gels." *Journal De Physique Lettres* 37(1): L1-L2.

[64] DeJong M. J. and Ulm F. J. (2007). "The nanogranular behavior of C-S-H at elevated temperatures (up to 700 degrees C)." *Cement and Concrete Research* 37(1): 1-12.

[65] Delafargue A. Ulm F.-J. (2004). Material invariant properties of shales: Nanoindentation and microporoelastic analysis. Cambridge, MA, Civil and Environmental Engineering Department, Massachusetts Institute of Technology. MS thesis.

[66] Delesse M. (1847). "Procédé mécanique pour déterminer la composition des roches." *Comptes Rendus de l'Académie des Sciences* 25: 544-547.

[67] Desrues J. (2002). "Limitations du choix de l'angle de frottement pour le critère de plasticité de Drucker-Prager." *Revue Française de Génie Civil* 6: 853-862.

[68] Diamond S. (1976). *Hydraulic cement pastes; their structure and properties.* Slough, UK, Cement and Concrete Association: 2-30.

[69] Donev A., Cisse I., Sachs D., Variano E., Stillinger F. H., Connelly R., Torquato S. and Chaikin P. M. (2004). "Improving the density of jammed disordered packings using ellipsoids." *Science* 303(5660): 990-993.

[70] Dormieux L., Kondo D. and Ulm F.-J. (2006). *Microporomechanics*, Wiley.

[71] Durst K., Goken M. and Vehoff H. (2004). "Finite element study for nanoindentation measurements on two-phase materials." *Journal of Materials Research* 19(1): 85-93.

[72] Eshelby J. D. (1957). "The determination of the elastic field of an ellipsoidal inclusion, and related problems." *Proceedings of the Royal Society of London. Series A, Mathematical and Physical Sciences* A241: 376-396.

[73] Famy C., Scrivener K. L., Atkinson A. and Brough A. R. (2002). "Effects of an early or a late heat treatment on the microstructure and composition of inner C-S-H products of Portland cement mortars." *Cement and Concrete Research* 32(2): 269-278.

[74] Feldman R. F. and Sereda P. J. (1968). "A model for hydrated portland cement paste as deduced from sorption-length change and mechanical properties." *Materials and Structures* 1(6): 509-520.

[75] Feng G. and Ngan A. H. W. (2002). "Effects of creep and thermal drift on modulus measurement using depth-sensing indentation." *Journal of Materials Research* 17(3): 660-668.

[76] Galin L. A. (1953). *Contact problems in the theory of elasticity.* Moscow, Gostekhizdat.

[77] Ganneau F. P., Constantinides G. and Ulm F. J. (2006). "Dual-indentation technique for the assessment of strength properties of cohesive-frictional materials." *International Journal of Solids and Structures* 43(6): 1727-1745.

[78] Ganneau F. P. and Ulm F.-J. (2004). *From nanohardness to strength properties of cohesive-frictional materials - Application to shale materials.* Cambridge, MA, Department of Civil and Environmental Engineering, Massachusetts Institute of Technology. SM thesis.

[79] Gao H. J., Chiu C. H. and Lee J. (1992). "Elastic contact versus indentation modeling of multilayered materials." *International Journal of Solids and Structures* 29(20): 2471-2492.

[80] Gathier B. and Ulm F.-J. (2008). *Multiscale strength homogenization - application to shale nanoindentation.* Cambridge, MA, Civil and Environmental Engineering Department, Massachusetts Institute of Technology. SM thesis.

[81] Gatty L., Bonnamy S., Feylessoufi A., Clinard C., Richard P. and Van Damme H. (2001). "A transmission electron microscopy study of interfaces and matrix homogeneity in ultra-high-performance cement-based materials." *Journal of Materials Science* 36(16): 4013-4026.

[82] Ghosh R. S. (1973). "A hypothesis on mechanism of maturing creep of concrete." *Materials and Structures* 6(31): 37-43.

[83] Guénot-Delahaie I. (1996). *Contribution à l'analyse physique et à la modélisation du fluage propre du béton*. Paris, France, Ecole Nationale des Ponts et Chaussées. PhD thesis.

[84] Hamid S. A. (1981). "The crystal-structure of the 11 Å natural tobermorite $Ca_{2.25}[Si_3O_{7.5}(OH)_{1.5}].1H_2O$." Zeitschrift fur Kristallographie 154(3-4): 189-198.

[85] Hartley R. R. and Behringer R. P. (2003). "Logarithmic rate dependence of force networks in sheared granular materials." *Nature* 421(6926): 928-931.

[86] Hawkins P., Tennis P. and Detwiler R. (2003). *The use of limestone in Portland cement: A state-of-the-art review*. Skokie, Illinois.

[87] Hay J. C., Bolshakov A. and Pharr G. M. (1999). "A critical examination of the fundamental relations used in the analysis of nanoindentation data." *Journal of Materials Research* 14(6): 2296-2305.

[88] Helmuth R. A. and Turk D. A. (1966). Symposium on structure of Portland cement paste and concrete, Washington. 90: 135-144.

[89] Hershey A. V. (1954). "The elasticity of an isotropic aggregate of anisotropic cubic crystals." *Journal of Applied Mechanics* 21: 236-240.

[90] Hertz H. (1896). *Miscellaneous papers*. London, Macmillan.

[91] Hill R. (1967). "The essential structure of constitutive laws for metal composites and polycrystals." *Journal of the Mechanics and Physics of Solids* 15: 79-95.

[92] Hockey B. J. and Lawn B. R. (1975). "Electron-microscopy of microcracking about indentations in aluminum-oxide and silicon-carbide." *Journal of Materials Science* 10(8): 1275-1284.

[93] Hong D. C., Yue S., Rudra J. K., Choi M. Y. and Kim Y. W. (1994). "Granular relaxation under tapping and the traffic problem." *Physical Review E* 50(5): 4123-4135.

[94] Hunter S. C. (1960). "The Hertz problem for a rigid spherical indenter and a viscoelastic half-space." *Journal of the Mechanics and Physics of Solids* 8: 219-234.

[95] Ingram K. D. and Daugherty K. E. (1991). "A review of limestone additions to Portland cement and concrete." *Cement and Concrete Composites* 13: 165-170.

[96] Jaeger H. M. and Nagel S. R. (1992). "Physics of the Granular State." *Science* 255(5051): 1523-1531.

[97] Jennings H. M. (2000). "A model for the microstructure of calcium silicate hydrate in cement paste." *Cement and Concrete Research* 30(1): 101-116.

[98] Jennings H. M. (2004). "Colloid model of C-S-H and implications to the problem of creep and shrinkage." *Materials and Structures* 37(265): 59-70.

[99] Jennings H. M. (2008). "Refinements to colloid model of C-S-H in cement: CM-II." *Cement and Concrete Research* 38(3): 275-289.

[100] Jennings H. M. and Tennis P. D. (1994). "Model for the developing microstructure in Portland-cement pastes." *Journal of the American Ceramic Society* 77(12): 3161-3172.

[101] Jennings H. M. and Tennis P. D. (1995). "Model for the developing microstructure in Portland-cement pastes (Vol 77, Pg 3161, 1994)." *Journal of the American Ceramic Society* 78(9): 2575-2575.

[102] Jennings H. M., Thomas J. J., Gevrenov J. S., Constantinides G. and Ulm F.-J. (2007). "A multi-technique investigation of the nanoporosity of cement paste." *Cement and Concrete Research* 37(3): 329-336.

[103] Johnson K. L. (1985). *Contact mechanics.* Cambridge University Press.

[104] Joshi R. C. and Lohtia R. P. (1997). *Fly ash in concrete: production, properties and uses.* Talyor & Francis.

[105] Knight J. B., Fandrich C. G., Lau C. N., Jaeger H. M. and Nagel S. R. (1995). "Density relaxation in a vibrated granular material." *Physical Review E* 51(5): 3957-3963.

[106] Kosmatka S. H., Kerkhoff B. and Panarese W. C. (2002). *Design and control of concrete mixtures.* Skokie, Illinois.

[107] Kröner E. (1958). "Berechnung der elastischen konstanten des vielkristalls aus den konstanten des einkristalls." *Zeitschrift für Physik.*

[108] Lambe T. W. and Whitman R. V. (1969). *Soil mechanics.* New York, Wiley.

[109] Larsson P. L., Giannakopoulos A. E., Soderlund E., Rowcliffe D. J. and Vestergaard R. (1996). "Analysis of Berkovich indentation." *International Journal of Solids and Structures* 33(2): 221-248.

[110] Laws N. (1985). "A note of penny-shaped cracks in transversely isotropic materials." *Mechanics of Materials* 4: 209-212.

[111] Lee E. H. (1955). "Stress analysis in visco-elastic bodies." *Quarterly of applied mathematics* 13: 183-190.

[112] Lee E. H. and Radok J. R. M. (1960). "The contact problem for viscoelastic bodies." *Journal of applied mechanics* 27: 438-444.

[113] Le Roy R. (1996). *Déformations instantanées et différées des bétons à hautes performances.* Série ouvrages d'art. Paris, Laboratoire Central des Ponts et Chaussées.

[114] Lemaitre A. (2002). "Rearrangements and dilatancy for sheared dense materials." *Physical Review Letters* 89(19).

[115] Leung C. F., Lee F. H. and Yet N. S. (1996). "The role of particle breakage in pile creep in sand." *Canadian Geotechnical Journal* 33(6): 888-898.

[116] Lockett F. (1963). "Indentation of a rigid plastic material by a conical indenter." *Journal of the Mechanics and Physics of Solids* 11(345-355).

[117] Love A. E. H. (1929). "The stress produced in a semi-infinite solid by pressure on part of the boundary." *Philosophical Transactions of the Royal Society of London. Series A, Mathematical and Physical Sciences.* 228: 377-420.

[118] Love A. E. H. (1939). "Boussinesq's problem for a rigid cone." *The Quarterly Journal of Mathematics* 10: 161-175.

[119] Mandel J. (1994). *Cours de mécanique des milieux continus.* Paris, Editions Jacques Gabay.

[120] Matschei T., Lothenbach B. and Glasser F. P. (2007). "The role of calcium carbonate in cement hydration." *Cement and Concrete Research* 37(4): 551-558.

[121] Mayo M. J. and Nix W. D. (1988). "A micro-indentation study of superplasticity in Pb, Sn, and Sn-38 Wt-Percent-Pb." *Acta Metallurgica* 36(8): 2183-2192.

[122] McDowell G. R. and Khan J. J. (2003). "Creep of granular materials." *Granular Matter* 5(3): 115-120.

[123] McElhaney K. W., Vlassak J. J. and Nix W. D. (1998). "Determination of indenter tip geometry and indentation contact area for depth-sensing indentation experiments." *Journal of Materials Research* 13(5): 1300-1306.

[124] Mehta P. K. (1981). "Studies on blended Portland cements containing Santorin earth." *Cement and Concrete Research* 11(4): 507-518..

[125] Mehta P. K. and Monteiro P. J. M. (2006). *Concrete: microstructure, properties and materials.* McGraw-Hill.

[126] Merlino S., Bonaccorsi E. and Armbruster T. (2001). "The real structure of tobermorite 11 angstrom: normal and anomalous forms, OD character and polytypic modifications." *European Journal of Mineralogy* 13(3): 577-590.

[127] Micromaterials Ltd. (2002). *Micromaterials nanotest user manual.* Wrexham, UK

[128] Miller M., Bobko C., Vandamme M. and Ulm F.-J. (2008). "Surface roughness criteria for cement paste nanoindentation." *Cement and Concrete Research* 38(4): 467-476.

[129] Mondal P., Shah S. P. and Marks L. (2007). "A reliable technique to determine the local mechanical properties at the nanoscale for cementitious materials." *Cement and Concrete Research* 37: 1440-1444.

[130] Mori T. and Tanaka K. (1973). "Average stress in matrix and average elastic energy of materials with misfitting inclusions." *Acta Metallurgica* 21(5): 571-574.

[131] Nawy E. G. (2001). *Fundamentals of high-performance concrete.* John Wiley and Sons.

[132] Neville A. M., Dilger W. H. and Brooks J. J. (1983). *Creep of plain and structural concrete.* Construction Press.

[133] Nix W. D. and Gao H. J. (1998). "Indentation size effects in crystalline materials: A law for strain gradient plasticity." *Journal of the Mechanics and Physics of Solids* 46(3): 411-425.

[134] Nixon F. E. (1965). *Handbook of Laplace transformation.* Prentice Hall.

[135] Nonat A. (2004). "The structure and stoichiometry of C-S-H." *Cement and Concrete Research* 34(9): 1521-1528.

[136] Nowak E. R., Knight J. B., Ben-Naim E., Jaeger H. M. and Nagel S. R. (1998). "Density fluctuations in vibrated granular materials." *Physical Review E* 57(2): 1971-1982.

[137] Oliver W. C. and Pharr G. M. (1992). "An improved technique for determining hardness and elastic-modulus using load and displacement sensing indentation experiments." *Journal of Materials Research* 7(6): 1564-1583.

[138] Oliver W. C. and Pharr G. M. (2004). "Measurement of hardness and elastic modulus by instrumented indentation: Advances in understanding and refinements to methodology." *Journal of Materials Research* 19(1): 3-20.

[139] Onoda G. Y. and Liniger E. G. (1990). "Random loose packings of uniform spheres and the dilatancy onset." *Physical Review Letters* 64(22): 2727-2730.

[140] Oyen M. L. (2005). "Spherical indentation creep following ramp loading." *Journal of Materials Research* 20(8): 2094-2100.

[141] Oyen M. L. (2006). "Analytical techniques for indentation of viscoelastic materials." *Philosophical Magazine* 86(33-35): 5625-5641.

[142] Oyen M. L. (2007). "Sensitivity of polymer nanoindentation creep measurements to experimental variables." *Acta Materialia* 55(11): 3633-3639.

[143] Oyen M. L. and Cook R. F. (2003). "Load-displacement behavior during sharp indentation of viscous-elastic-plastic materials." *Journal of Materials Research* 18(1): 139-150.

[144] Oyen M. L., Cook R. F., Emerson J. A. and Moody N. R. (2004). "Indentation responses of time-dependent films on stiff substrates." *Journal of Materials Research* 19(8): 2487-2497.

[145] Pellenq R. J. M. and Van Damme H. (2004). "Why does concrete set?: The nature of cohesion forces in hardened cement-based materials." *Mrs Bulletin* 29(5): 319-323.

[146] Perriot A. and Barthel E. (2004). "Elastic contact to a coated half-space: Effective elastic modulus and real penetration." *Journal of Materials Research* 19(2): 600-608.

[147] Pharr G. M. and Bolshakov A. (2002). "Understanding nanoindentation unloading curves." *Journal of Materials Research* 17(10): 2660-2671.

[148] Pontes I. D. S., Borges L. A., Zouain N. and Lopes F. R. (1997). "An approach to limit analysis with cone-shaped yield surfaces." *International Journal for Numerical Methods in Engineering* 40(21): 4011-4032.

[149] Powers T. C. (1958). "Structure and physical properties of hardened Portland cement paste." *Journal of the American Ceramic Society* 41(1): 1-6.

[150] Powers T. C. (1968). *Mechanisms of shrinkage and reversible creep of hardened portland cement paste.* International Conference on the Structure of Concrete, London, England.

[151] Powers T. C. and Brownyard T. L. (1948). "Studies of the physical properties of hardened portland cement paste." *PCA Bulletin*, Portland Cement Association 22: 22.

[152] Radok J. R. M. (1957). "Visco-elastic stress analysis." *Quarterly of applied mathematics* 15: 198-202.

[153] Richardson I. G. (1999). "The nature of C-S-H in hardened cements." *Cement and Concrete Research* 29(8): 1131-1147.

[154] Richardson I. G. (2004). "Tobermorite/jennite- and tobermorite/calcium hydroxide-based models for the structure of C-S-H: applicability to hardened pastes of tricalcium silicate, beta-dicalcium silicate, Portland cement, and blends of Portland cement with blast-fumace slag, metakaolin, or silica fume." *Cement and Concrete Research* 34(9): 1733-1777.

[155] Ross S. M. (2000). *Introduction to probability and statistics for engineers and scientists.* Academic Press.

[156] Ruetz W. (1968). *A hypothesis for the creep of hardened cement paste and the influence of simultaneous shrinkage.* International conference on the structure of concrete, London, England.

[157] Salençon J. (1983). *Viscoélasticité.* Paris, Presses de l'Ecole Nationale des Ponts et Chaussées.

[158] Salençon J. (1990). "An introduction to the yield design theory and its applications to soil mechanics." *European Journal of Mechanics A-Solids* 9(5): 477-500.

[159] Sanahuja J. and Dormieux L. (2005). "Strength of a porous medium with a heterogeneous solid phase." *Comptes Rendus Mécanique* 333(11): 818-823.

[160] Sanahuja J., Dormieux L. and Chanvillard G. (2007). "Modelling elasticity of a hydrating cement paste." *Cement and Concrete Research* 37(10): 1427-1439.

[161] Schweiger H. F. (1994). "On the use of Drucker-Prager failure criteria for earth pressure problems." *Computers and Geotechnics* 16(3): 223-246.

[162] Scrivener K. and Van Damme H. (2004). "Construction materials: From innovation to conservation." *Mrs Bulletin* 29(5): 308-310.

[163] Shahsavari H., Buehler M.J. and Ulm F.-J.. "Benchmark of calculation of mechanical properties of tobermorite", manuscript in preparation.

[164] Sherwood J. D. (1997). "Packing of spheroids in three-dimensional space by random sequential addition." *Journal of Physics A-Mathematical and General* 30(24): L839-L843.

[165] Shimizu S., Yanagimoto T. and Sakai M. (1999). "Pyramidal indentation load-depth curve of viscoelastic materials." *Journal of Materials Research* 14(10): 4075-4086.

[166] Sloane N. J. A. (1998). "Kepler's conjecture confirmed." *Nature* 395(6701): 435-436.

[167] Sneddon I. N. (1965). "The relation between load and penetration in the axisymmetric boussinesq problem for a punch of arbitrary profile." *International Journad of Engineering Science* 3(1): 47-57.

[168] Sneddon I. N. (1977). *Application of integral transforms in the theory of elasticty.* Wien - New York, Springer Verlag.

[169] Sprung S. and Siebel E. (1991). "Assessment of the suitability of limestone for producing Portland limestone cement (PKZ)." *Zement-Kalk-Gips* 44(1): 1-11.

[170] Stillwell N. A. and Tabor D. (1961). "Elastic recovery of conical indentation." *Proceedings of the Physical Society of London* 78: 169-179.

[171] Straub L. G. (1930). "Plastic flow in concrete arches." *Proceedings of the american society of civil engineers* 56: 49-114.

[172] Sullivan E. (2006). *World economic growth may ease slightly.* http://www.cement.org/exec/International%20Flash%20(Oct.%202006).pdf

[173] Tabor D. (1948). "A simple theory of static and dynamic hardness." *Proceedings of the royal society of London. Series A, Mathematical and Physical Sciences* 192(1029): 247-274.

[174] Tabor D. (1951). *The hardness of metals.* Oxford, Clarendon Press.

[175] Taggart J. (1977). "Polishing technique for geologic samples." *American Mineralogist* 62: 824-827.

[176] Tamtsia B. T. and Beaudoin J. J. (2000). "Basic creep of hardened cement paste - A re-examination of the role of water." *Cement and Concrete Research* 30(9): 1465-1475.

363

[177] Taylor H. F. W. (1997). *Cement chemistry*. London, Thomas Telford.

[178] Taylor H. F. W. and Newbury D. E. (1984). "Calcium hydroxide distribution and calcium silicate hydrate composition in tricalcium silicate and beta-dicalcium silicate pastes." *Cement and Concrete Research* 14(1): 93-98.

[179] Tennis P. D. and Jennings H. M. (2000). "A model for two types of calcium silicate hydrate in the microstructure of Portland cement pastes." *Cement and Concrete Research* 30(6): 855-863.

[180] Ting T. C. T. (1966). "The contact stresses between a rigid indenter and a viscoelastic half-space." *Journal of Applied Mechanics* 88: 845-854.

[181] Tweedie C. A., Constantinides G., Lehman K. E., Brill D. J., Blackman G. S. and Van Vliet K. J. (2007). "Enhanced stiffness of amorphous polymer surfaces under confinement of localized contact loads." *Advanced Materials* 19: 2540-2546.

[182] Tweedie C. A. and Van Vliet K. J. (2006). "Contact creep compliance of viscoelastic materials via nanoindentation." *Journal of Materials Research* 21(6): 1576-1589.

[183] Ulm F.-J. and Acker P. (1998). "Le point sur le fluage et la recouvrance des bétons." *Bulletin de liaison des Ponts et Chaussées spécial* XX: 73-82.

[184] Ulm F. J., Constantinides G. and Heukamp F. H. (2004). "Is concrete a poromechanics material? - A multiscale investigation of poroelastic properties." *Materials and Structures* 37(265): 43-58.

[185] Ulm F.-J., Delafargue A. and Constantinides G. (2005). *Experimental microporomechanics*. in Applied micromechanis of porous materials. L. Dormieux and F.-J. Ulm. Wien, New York, Springer: 207-288.

[186] Ulm F.-J., Le Maou F. and Boulay C. (1999). "Creep and shrinkage coupling: new review of some evidence." *Revue française de génie civil* 3: 21-37.

[187] Ulm F.-J., Vandamme M., Bobko C., Ortega J. A., Tai K. and Ortiz C. (2007). "Statistical indentation techniques for hydrated nanocomposites: Concrete, bone, and shale." *Journal of the American Ceramic Society* 90(9): 2677-2692.

[188] U.S. Bureau of Reclamations (1956). *Creep of concrete under high intensity loading.* Report n. C-820. Denver, Colorado.

[189] U.S. Department of Transportation, Federal Highway Administration, http://www.fhwa.dot.gov/pavement/pccp/pubs/04150/chapt6.cfm

[190] U.S. Department of Transportation (2006). *2006 Status of the nation's highways, bridges, and transit: Conditions and Performance.*

[191] Vandamme M. and Ulm F.-J. (2006). "Viscoelastic solutions for conical indentation." *International Journal of Solids and Structures* 43(10): 3142-3165.

[192] VanLandingham M. R., Chang N. K., Drzal P. L., White C. C. and Chang S. H. (2005). "Viscoelastic characterization of polymers using instrumented indentation. I. Quasi-static testing." *Journal of Polymer Science Part B-Polymer Physics* 43(14): 1794-1811.

[193] Velez K., Maximilien S., Damidot D., Fantozzi G. and Sorrentino F. (2001). "Determination by nanoindentation of elastic modulus and hardness of pure constituents of Portland cement clinker." *Cement and Concrete Research* 31(4): 555-561.

[194] Verbeck G. J. and Helmuth R. H. (1969). *Structures and physical properties of cement paste.* Fifth international congress cement chemistry, Tokyo, Japan.

[195] Vuk T., Tinta V., Gabrovsek R. and Kaucic V. (2001). "The effects of limestone addition, clinker type and fineness on properties of Portland cement." *Cement and Concrete Research* 31(1): 135-139.

[196] Wang W. and Lu K. (2002). "Nanoindentation measurement of hardness and modulus anisotropy in Ni3Al single crystals." *Journal of Materials Research* 17(9): 2314-2320.

[197] Whittmann F. H. (1982). *Creep and shrinkage mechanisms.* in: Creep and shrinkage in concrete structures. Z. P. Bazant and F. H. Whittmann. New York, John Wiley & Sons Ltd: 129-161.

[198] Yang S., Zhang Y. W. and Zeng K. Y. (2004). "Analysis of nanoindentation creep for polymeric materials." *Journal of Applied Physics* 95(7): 3655-3666.

[199] Zaoui A. (2002). "Continuum micromechanics: Survey." *Journal of Engineering Mechanics* 128(8): 808-816.

[200] Zhang C. Y., Zhang Y. W., Zeng K. Y. and Shen L. (2005). "Nanoindentation of polymers with a sharp indenter." *Journal of Materials Research* 20(6): 1597-1605.

[201] Zhang C. Y., Zhang Y. W., Zeng K. Y. and Shen L. (2006). "Characterization of mechanical properties of polymers by nanoindentation tests." *Philosophical Magazine* 86(28): 4487-4506.

[202] Zhang C. Y., Zhang Y. W., Zeng K. Y., Shen L. and Wang Y. Y. (2006). "Extracting the elastic and viscoelastic properties of a polymeric film using a sharp indentation relaxation test." *Journal of Materials Research* 21(12): 2991-3000.